

#### **Archive ouverte UNIGE**

https://archive-ouverte.unige.ch

Thèse 2025

**Open Access** 

This version of the publication is provided by the author(s) and made available in accordance with the copyright holder(s).

Microtubule flux dysregulation causes primary microcephaly

\_\_\_\_\_\_

Ivanova, Daria

#### How to cite

IVANOVA, Daria. Microtubule flux dysregulation causes primary microcephaly. Doctoral Thesis, 2025. doi: 10.13097/archive-ouverte/unige:185717

This publication URL: <a href="https://archive-ouverte.unige.ch/unige:185717">https://archive-ouverte.unige.ch/unige:185717</a>

Publication DOI: <u>10.13097/archive-ouverte/unige:185717</u>

© This document is protected by copyright. Please refer to copyright holder(s) for terms of use.

Section de médicine

Département de physiologie cellulaire et métabolisme

Professeur Patrick Meraldi

# MICROTUBULE FLUX DYSREGULATION CAUSES PRIMARY MICROCEPHALY

#### **THÈSE**

présentée aux Facultés de médecine et des sciences de l'Université de Genève pour obtenir le grade de Docteur ès sciences en sciences de la vie, mention Biosciences moléculaires

par

**Daria Ivanova** 

Thèse Nº 342

**GENÈVE** 

2025



## DOCTORAT ÈS SCIENCES EN SCIENCES DE LA VIE DES FACULTÉS DE MÉDECINE ET DES SCIENCES MENTION BIOSCIENCES MOLÉCULAIRES

#### Thèse de Mme Daria Ivanova

intitulée ::

## « Microtubule flux dysregulation causes primary microcephaly. »

Les Facultés de médecine et des sciences, sur le préavis de Monsieur Patrick MERALDI, Professeur ordinaire et directeur de thèse (Département de Physiologie Cellulaire et Métabolisme), Madame Miriam Carolin STOEBER, Professeure assistante (Département de Physiologie Cellulaire et Métabolisme), Madame Ivana GASIC, Professeure assistante (Département de Biologie Moléculaire et Cellulaire), Madame Alexis BARR, Professeure (MRC Laboratory of Medical Sciences (LMS), 6.12B, Imperial College London, Hammersmith Hospital Campus, Londres, Angleterre) autorisent l'impression de la présente thèse, sans exprimer d'opinion sur les propositions qui y sont énoncées.

Genève, le 16 mai 2025

Thèse - 342 -

Le Doyen Faculté de médecine

1. C. uu

La Doyenne Faculté des sciences

N.B. - La thèse doit porter la déclaration précédente et remplir les conditions énumérées dans les "Informations relatives aux thèses de doctorat à l'Université de Genève".



# Contents

| Summary  | 4 -                                  |
|--|--------------------------------------|
| Résumé   | 5 -                                  |
| ntroduction  | 7 -                                  |
| Development of human brain   | 7 -                                  |
| Evolutionary development of human brain  | 7 -                                  |
| Early embryonic brain development  | 7 -                                  |
| Neurodevelopmental disorders of cortical development   | 14 -                                 |
| Current hypotheses of microcephaly disease origins   | 18 -                                 |
| Models to study microcephaly   | 19 -                                 |
| Drosophila melanogaster  | 20 -                                 |
| Mus musculus   | 20 -                                 |
| WDR62 and its functions  | 21 -                                 |
| Mitosis  | 23 -                                 |
| Mitotic spindle components and spindle architecture at metaphase   | 24 -                                 |
|  |                                      |
| Motor proteins and microtubule associated proteins (MAPs)  | 28 -                                 |
| Motor proteins and microtubule associated proteins (MAPs)  |                                      |
|  | 31 -                                 |
| Microtubule Flux   | 31 -                                 |
| Microtubule Flux   | 31 -                                 |
| Microtubule Flux  Prophase  Prometaphase   | 31 - 35 - 35 - 37 - 39 -             |
| Microtubule Flux  Prophase  Prometaphase  Metaphase  | 31 -<br>35 -<br>37 -<br>39 -<br>45 - |
| Microtubule Flux  Prophase  Prometaphase  Metaphase  Anaphase  | 31 35 37 39 45 48 -                  |
| Microtubule Flux  Prophase  Prometaphase  Metaphase  Anaphase  Lagging chromosome correction   | 313537394548 -                       |
| Microtubule Flux  Prophase  Prometaphase  Metaphase  Anaphase  Lagging chromosome correction  Telophase and cytokinesis  | 31353739454850 -                     |
| Microtubule Flux  Prophase  Prometaphase  Metaphase  Anaphase  Lagging chromosome correction  Telophase and cytokinesis  Asymmetric cell division                              | 31 35 37 39 45 48 50 52 54 -         |
| Microtubule Flux  Prophase  Prometaphase  Metaphase  Anaphase  Lagging chromosome correction  Telophase and cytokinesis  Asymmetric cell division  Mitotic exit and interphase |                                      |

| Transient lagging chromosomes cause primary microcephaly 61 -                                 |
|---|
| Additional results to "Transient lagging chromosomes cause primary microcephaly" 106 -        |
| WDR62 depletion leads to aberrant microtubule dynamics 106 -                                  |
| Other primary microcephaly genes lead to transient lagging chromosomes 109 -                  |
| USP28 might be important for 53BP1 upregulation in siWDR62 110 -                              |
| Persistent lagging chromosomes lead to 53BP1 appearance 111 -                                 |
| WDR62 depletion does not lead to abnormal nuclear shape 113 -                                 |
| WDR62 depletion leads to increased cell cycle timing but normal cell cycle partitioning 114 - |
| WDR62 localizes katanin at spindle poles to ensure synchronous chromosome segregation 117 -   |
| Discussion 142 -  |
| Origins of poleward microtubule flux disruption in WDR62 depletion 142 -                      |
| Lagging chromosomes in primary microcephaly and their recognition by Aurora B 144 -           |
| 53BP1 appearance and its consequences 146 -   |
| Rescue of downstream transient lagging chromosomes consequences by siCamsap1 149 -            |
| Current primary microcephaly hypotheses 150 -   |
| Why does the WDR62 depletion only affects brain size? 152 -                                   |
| Microcephaly and brain evolution 153 -  |
| Cytoskeleton in context of physiology and disease 154 -                                       |
| Materials and Methods 155 -   |
| Annex of other published articles 164 -   |
| The biophysical mechanism of mitochondrial pearling 164 -                                     |
| Acknowledgements 215 -  |
| References 217 -  |

# Summary

Primary microcephaly (MCPH) is an inborn neurodevelopmental disorder that leads to reduction of brain size in the newborns. The impaired neuronal progenitor proliferation is at the origin of this disease and it leads to impaired cognitive abilities which last throughout the lifetime of the patient. Many different genes are known to be mutated in primary microcephaly, majority of which play a role in the regulation of the mitotic spindle and cytoskeleton. Loss of the most frequently mutated microcephaly genes, WDR62 and ASPM, has been shown to cause slower poleward microtubule flux during cell division and result in transient lagging chromosomes during anaphase. The precise role of these gene loss in primary microcephaly, however, remains unknown.

In order to understand the origins of WDR62-dependent primary microcephaly and elucidate general mechanisms of cell division disruption in primary microcephaly, I investigated the mitosis and cell division in human cells and larvae of Drosophila melanogaster. In my study I found that transient lagging chromosomes lead to an Aurora B-dependent activation of 53BP1 and p21. This activation also impairs cell proliferation in human cells by prolonging the duration of the entire cell cycle. The codepletion of a protein CAMSAP1/Patronin, which protects microtubules, together with WDR62 depletion rescues normal microtubule flux rates, prevents lagging chromosomes during cell division, and leads to normal cell proliferation in human cells.

To correlate the findings in human cell culture with microcephaly disease, I took advantage of the Drosophila melanogaster model. As it is the case in humans, WDR62 depletion in Drosophila also causes a smaller brain phenotype and decreased cognitive abilities. In the brains of Drosophila larvae, co-depletion of WDR62 together with the Camsap1 orthologue Patronin can rescue the small brain and impaired cognitive ability.

This work allows us to postulate that transient lagging chromosomes in anaphase and their 53BP1/p21-dependent response are important drivers of primary microcephaly. The elucidated mechanism suggests the importance of microtubule flux and dynamics in the regulation of neuronal progenitor proliferation. Through this study we can better understand the origins of primary microcephaly and bring us closer to therapeutic advances.

# Résumé

La microcéphalie primaire est une maladie neurodéveloppementale résultant en une taille du cerveau réduite chez les nouveau-nés. Cette maladie est la conséquence d'une défaillance dans la prolifération des cellules souches du cerveau, et entraîne un retard mental irréversible. Différentes mutations ont pu être identifiées dans cette maladie, la majorité de ces gènes étant impliqués dans les mécanismes de division cellulaire et le cytosquelette. Il a été démontré que la perte des deux gènes les plus souvent mutés dans la microcéphalie, WDR62 et ASPM, provoquait un ralentissement dans la vitesse du flux des microtubules et avait pour conséquence un retard transitoire des chromosomes pendant l'anaphase. Le rôle précis de ces gènes reste inconnu.

Pour comprendre les origines de cette maladie, provoquée entre autres par la perte de WDR62, et pour comprendre les mécanismes de la microcéphalie, j'ai investigué le processus de mitose et de division cellulaire dans les cellules humaines et les larves de Drosophila melanogaster. Dans mes expériences, j'ai mis en évidence le fait que les chromosomes retardataires transitoires sont reconnus par le gradient d'Aurora B et activent les protéines 53BP1 et p21. Cette activation entraîne un ralentissement de la vitesse de prolifération des cellules. La co-déplétion de Camsap1/Patronin, une protéine qui inhibe la dépolymérisation des microtubules, restaure le flux des microtubules, prévient les chromosomes retardataires pendant la division cellulaire, ce qui permet une prolifération normale des cellules humaines.

Pour comprendre si ces effets sont causatifs de la maladie, j'ai testé l'influence de la déplétion de ces gènes chez la Drosophila melanogaster. Comme c'est le cas chez les humains, la déplétion de WDR62 chez la Drosophile a engendré des cerveaux plus petits que la normale et a eu une influence sur leurs capacités cognitives. Ce travail nous a permis de postuler que les chromosomes retardataires transitoires et le mécanisme de leur reconnaissance par 53BP1-p21 sont des facteurs pathogéniques importants de la microcéphalie primaire. Le mécanisme proposé montre l'importance du flux et de la dynamique des microtubules dans la prolifération des cellules souches du cerveau. Avec cette étude, nous pouvons mieux comprendre les origines de la microcéphalie primaire et avancer vers un futur traitement thérapeutique.

# **Preface**

The human brain, in all its complexity, is the result of a long and complex neurological development. From the early embryonic stages, a series of processes including neuronal cell proliferation, differentiation, and migration are important in order to shape the foundation of our cognitive functions. If these processes are disrupted, it can lead to various neurological disorders. Therefore, understanding the mechanisms that govern brain development is very important to uncover the causes of neurodevelopmental disorders.

In this thesis, I first provide an overview of brain formation, exploring the cellular and molecular mechanisms which guide its development from the embryonic stages to birth. After that I examine neurodevelopmental disorders that arise from faulty brain development processes, with a particular focus on primary microcephaly—a condition leading to abnormally small brain due to decrease in neuronal progenitor pool. I discuss the current scientific background and most common hypotheses regarding its origins.

In the final section of my introduction I will describe the mechanisms of mitosis and the cell cycle, two processes that are extremely important for neurodevelopment. Indeed, precise mitotic regulation is important for neurodevelopment and genetic integrity. Similarly, the regulation of the cell cycle plays an important role, as disruptions in proliferation appear to be a common denominator among many neurodevelopmental disorders. These two processes are deeply interconnected, often influencing one another in order to shape our brain.

Through this work, I would like to understand how defects in mitosis and the cell cycle contribute to primary microcephaly. The understanding of these molecular mechanisms will allow us to gain a deeper comprehension of how even minor disruptions in mitosis and cell cycle can lead to profound consequences, resulting in this disease.

1

# Introduction

# Development of human brain

#### Evolutionary development of human brain

The human brain is the most complex organ in the known universe, which has been shaped by many years of evolution. But what makes our brain so different? Interestingly, our brain is built in a way that has the highest neuronal concentration in the smallest amount of space (Herculano-Houzel et al. 2009, Dicke & Roth 2016). This can be compared to rodents which, if they had the same number of neurons as a human (85 billion), would have a brain weighing more than 35 kg, a value beyond all known brain masses (Herculano-Houzel et al. 2006).

Our brain is not the biggest and does not contain the most neurons in absolute terms, but the combination of its economic size and high concentration of neurons makes the primate brain unique in its kind (Herculano-Houzel et al. 2009). Although the human brain is not the largest in size in the animal kingdom, among primates it stands out for its exceptional size. Compared to a gorilla, our brain is around three-fold bigger (Isler & van Schaik 2014), despite having approximately the same gestation time (Wildman et al. 2011). This means that the human brain needs to increase in mass and the number of neurons dramatically during its development.

The exceptional process of human brain development is discussed in the next chapter.

#### Early embryonic brain development

#### Gastrulation

From fertilization, an embryo undergoes rapid changes and grows into an oval-shaped, two-layered blastocyst with over 120 cells in the first two weeks. The blastocyst contains an upper layer of epiblast cells and a lower layer of hypoblast cells (Sheng et al. 2015). Following the late blastocyst stage, the

gastrulation process transforms the embryo into a three-dimensional structure (Shoenwolf et al. 2000). Its beginning is marked by the appearance of a primitive streak, a narrow opening in the epiblast (reviewed in Stiles 2010). The epiblast cells start migrating to the primitive streak, passing through it and elongating it.

At the same time, the ingression of the epiblast cells into the primitive streak creates a circular cavity, known as the primitive pit (reviewed in Stiles 2010). The migrating cells build two new cell layers: the ones which migrate further away integrate into the hypoderm and build the endodermal layer, and the second set of cells builds a mesodermal layer (reviewed in Stiles 2010). The cells which remain in the epiblast form the endoderm, whose stem cells give rise to epidermal, ectodermal, and neuroectodermal stem cells (De Miguel et al. 2009). The latter are responsible for the formation of the central nervous system.

The differentiation of stem cells involves molecular cascades, which are initiated by the cells of the primitive streak end, called primitive node cells (reviewed in Stiles 2010). This signal is received by the cells migrating along the midline, which later become neuronal progenitor cells. Following the first signal, a second set of signals is produced by the primitive node, which determines the localization of the cells on the rostral-caudal axis of the embryonic nervous system (Patthey et al. 2008). The early migrating cells, therefore, receive the signal and consequently form the forebrain structure, while the late migrating cells will later form the hindbrain and spinal cord.

#### Formation of neural tube

At the end of gastrulation, the neuronal cells are positioned at the midline and build the so-called neuronal plate (reviewed in Stiles 2010). During the process of neurulation or dorsal induction, the cells form a neural tube (Papalopulu et al. 2007). To do so, first, the cells which find themselves in the middle of the neural plate will become anchored to the notochord, a structure formed above the primitive streak. After that, epidermal cells which are on the sides of the midline of the neural plate will start to move towards the center and shape the neuronal tube by bending the structure. The neural folds will get in contact with each other and the dispersion of the neural crest cells will divide the neural tube from the epidermis. The neural folds fuse in a tube starting from the inside towards the outside, leaving out the most anterior end, called the neural pore, which will later form the first brain structure (reviewed in Stiles 2010).

The neuronal progenitors, which are lining up the midline of the neural tube, migrate inside the hollow tube (Marin et al. 2006). Once the neuronal tube is closed, it will form the ventricular zone of the brain

(Fame et al. 2020). By the end of the 6th gastrulation week (GW), the neural pore forms three primary brain vesicles (O'rahilly & Müller 2008). The most anterior vesicle is called the prosencephalon and is the precursor of the forebrain. The middle structure is called the mesencephalon and forms midbrain structures, and the posterior vesicle forms the rhombencephalon, precursor of the hindbrain (reviewed in Stiles 2010). In the following days, the prosencephalon grows rapidly and the rostral part divides into two vesicles called the telencephalic vesicles, which will later become the two cerebral hemispheres (Tole et al. 2020). The caudal part of the prosencephalon divides into the diencephalic vesicles, which will later become the optical vesicle and the thalamus. The mesencephalon continues to grow without division to become the midbrain, and the rhombencephalon divides into the metencephalon, which will become the pons and cerebellum, and the myelencephalon, which will become the medulla.

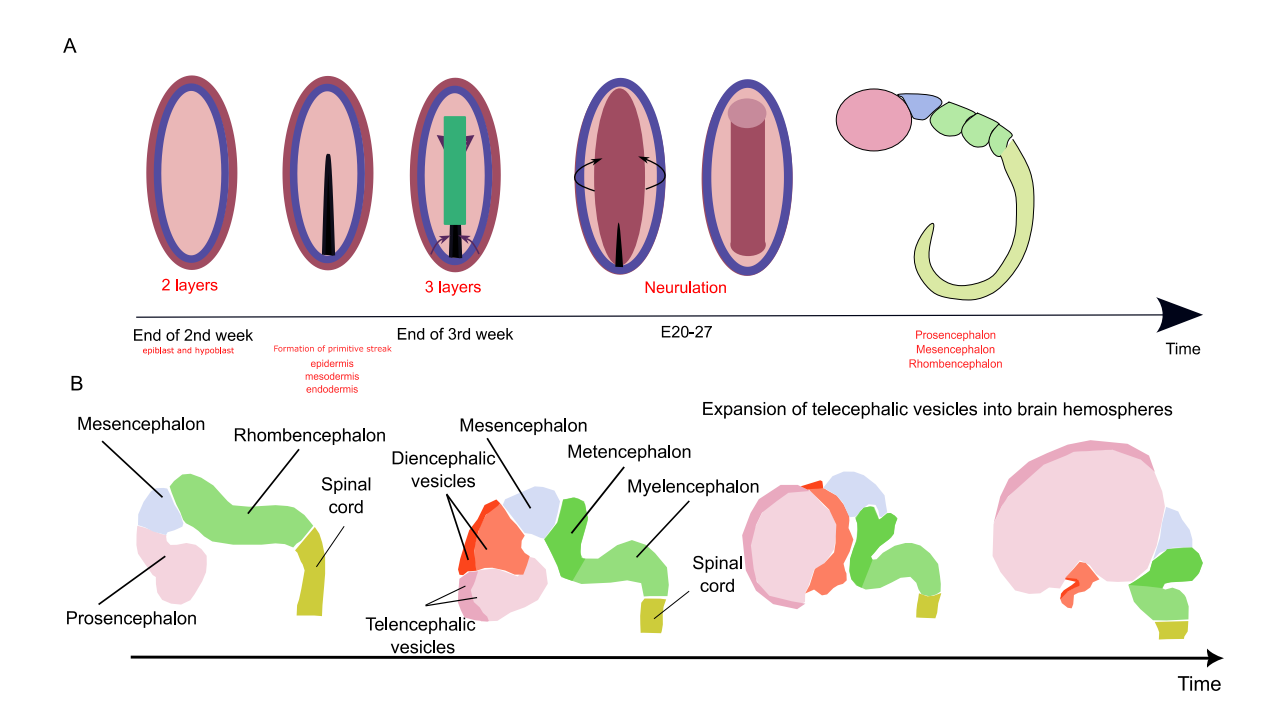


Figure 1: Early brain development from gastrulation to cortical expansion

- (A) From left to right represents time course: blastocyst containing epiblast (outer structure, dark pink) and hypoblast (blue), its transformation into three-layered structure and appearance of primitive streak (in black), formation of neuronal tube and cellular migration through it, closure of neuronal tube (neurulation), building of three primary brain vesicles.
- (B) From left to right represents time course: three primary brain vesicles, formation of telencephalic and diencephalic vesicles and division of rhombencephalon into metencephalon and myelencephalon, expansion of telencephalic vesicles to form cerebral hemispheres.

#### Neuronal patterning

During the early embryonic patterning, different protein gradients allow for the maturing of the embryonic brain. As mentioned previously, the prosencephalon becomes the diencephalon and telencephalon, which mature further through patterning by Shh (Sonic Hedgehog) and BMP (Bone Morphogenic Protein) (Rallu et al. 2002). The telencephalon contains a primitive sheet of neurons, which is called the pallium, where the creation of well-defined partitions of the brain starts (Medina et al. 2021). This is achieved through the differential molecular signals, which are present in different areas of the proliferative tissue.

The two most important transcription factors, Pax6 (Paired Box 6) and Emx2 (Empty Spiracles Homeobox 2), give rise to gradients throughout the proliferative zone of the neocortex, with Emx2 concentrating on the posterior and medial regions, while Pax6 is accumulating at the anterior part of the neocortex (Bishop et al. 2002). Thus, the Pax6-rich anterior part of the proliferative tissue gives rise to the motor cortex, and the Emx2-rich posterior part allows for the formation of the visual cortex (Bishop et al. 2000, Muzio 2003). The part with a mix of both transcription factors develops into the somatosensory cortex.

Indeed, studies performed in mice have shown that the blocking of Emx2 or Pax6 transcription factors leads to defective formation of the visual and motor cortexes, respectively (reviewed in Ypsilanti&Rubenstein 2016) Moreover, during the neocortex development, other gradient patterns emerge, such as the Coup-TF1 (Coup Transcription Factor 1) gradient in the caudal-lateral regions and the SP8 in the rostral-medial regions (Ip et al. 2010).

#### Fetal brain development

In human development, the fetal period is counted from the 9th GW to the end of gestation. During this period, the human brain undergoes dramatic changes, developing from a smooth structure to the characteristic patterns of gyri (ridges) and sulci (crevices). The process of formation of gyri and sulci is a highly ordered process, in which the primary sulci form grooves on specific brain regions, followed by the secondary and then tertiary branches (White & Hildgetag 2008). After that, the fissures start to form, the first one being the longitudinal fissure, separating both brain hemispheres (Nishikuni et al. 2013). During the following gestation weeks, other fissure formations follow, including the formation of the sylvian, parieto-occipital, and intraparietal fissures (Nishikuni et al. 2013, see Figure 3).

The changes in the anatomy of the brain are also reflected in the changes of its cellular composition. During the fetal development, neuronal production begins and different neuronal populations start to form distinct brain regions. During this period of time, the neuronal production and migration (described in detail below), taking rise in the ventricular zone (VZ), will create a six-layered cortical structure. Once positioned in the right place, the neurons will start the differentiation process, produce neurotransmitters and neurotrophic factors, and extend their axonal bodies, forming grey and white brain matter (Oliviera et al. 2013).

#### Neurogenesis and neuronal migration

The process of neurogenesis continues until birth, taking place in the subependymal region of the lateral ventricles (Malik et al. 2013). This process is initiated at the neuronal tube, which consists of neuroepithelial cells. These neuroepithelial cells (NE) will later give rise to glial cells and neurons. In order to reach the size of a newborn human brain, during the gestation period, billions of neurons must be produced (Lindercamp et al. 2009). This is unachievable with the pool of neural progenitors available after gastrulation. Thus, the first step of neuronal production is the increase in size of the cell population of neuronal progenitors (Florio et al. 2014). In order to do so, neuronal epithelial cells start to divide symmetrically and generate a zone, which is called the ventricular zone (VZ) (Egger et al. 2011). After generating a big enough pool of neuroepithelial cells, they start to divide asymmetrically, producing radial glial cells (RGC), which marks the start of neurogenesis (Paridaen & Huttner 2014). Radial glial cells are the progenitors for all the following neurons and glial cells. Similar to differentiated glial cells, these cells express glial markers and serve as a scaffold for neuronal migration (Sild & Ruthazer 2011). As the glial cells migrate in the inside-out fashion, they build a layer called the subventricular zone (SVZ). Additionally, some early produced neurons can then translocate (Nadarajah et al. 2001) to the upper layer.

Once an RGC switches to asymmetric cell division, it produces one intermediate progenitor (IP) and one postmitotic neuron, migrating outwards (Willadrsen et al. 2011). The intermediate progenitors migrate to the pial surface, supported by glial fibres. The newborn postmitotic neuron, originating from the ventricular and subventricular zones, will end up in the cortical plate (CP) of the cortex (Paridaen & Huttner 2014). The asymmetrically dividing RGC will also give rise to Cajal-Retzius cells (CRs), which will create a marginal zone (Kilb et al. 2016). These cells secrete an important extracellular protein, Reelin, which is important for the migration of neurons (Gil-Sanz et al. 2013). The Reelin downstream factors Dab1 (disabled-1 protein) and CAMs (cell adhesion molecules) regulate the

direction of migration of the neurons towards the pial surface, the change in migratory modes, the migration end, and the neuronal aggregation (Hirota 2017). The increased amount of Reelin in vertebrates compared to non-vertebrates (Goffinet et al., 1986) is hypothesized to be responsible for a migration drive over large distances.

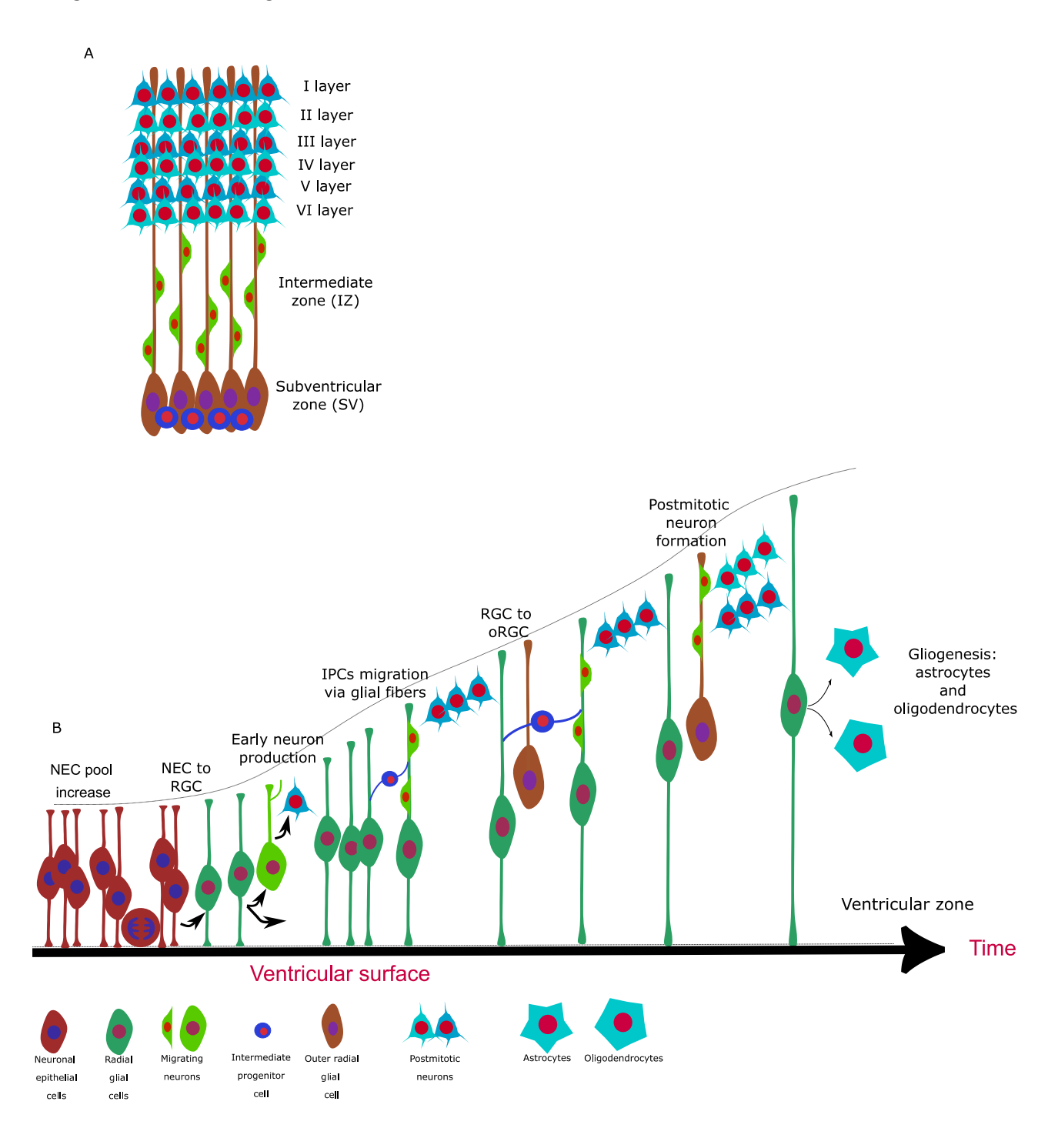


Figure 2: Cortical development and neuronal migration during human brain development

(A) Structure of a normal six layered brain: neurons migrate in inside out fashion from ventricular zone where they are born (figure B, under the subventricular zone) through subventricular and

- intermediate zone. They then constitute 6 brain layer from VI-I, I being the closest to the surface. Together, neurons constitute a cortical plate.
- (B) From left to right: Neuronal epithelial cells (NEC) start increasing their pool by means of symmetrical cell division. Over the course of time, NEC transform into radial glial cells (RGC). Early produced neurons are translocated. RGC proliferate and give rise to intermediate progenitor cells (IPCs). RGCs transform to outer RGCs which will give rise to postmitotic neurons. Neurons migrate using radial glial fibers as support. Gliogenesis allows to form astrocytes and oligodendrocytes from RGCs.

The developed brain is composed of the cerebrum, cerebellum, and brain stem. The biggest part of the human brain, the cerebrum, is divided into left and right cerebral hemispheres. Partially demarcated by sulci, the human cerebral cortex encompasses five lobes called the frontal, temporal, parietal, occipital, and limbic lobes. The most prominent sulci are the central sulcus, separating the frontal and parietal lobes; the Sylvian fissure, separating the temporal lobe from the frontal and parietal lobes; the parieto-occipital fissure, separating the parietal from the occipital lobes; and the cingulate sulcus, which separates the frontal lobe from the deeper lying limbic lobe. The diencephalon is divided into the thalamus, subthalamus, hypothalamus, and the brain stem, comprising the midbrain, pons, and medulla. In addition, the brain is cushioned by a series of cavities, filled with cerebral fluid, composing the so-called ventricular system. From outside, the brain is encapsulated by the three-layered meninges and protected by the skull.

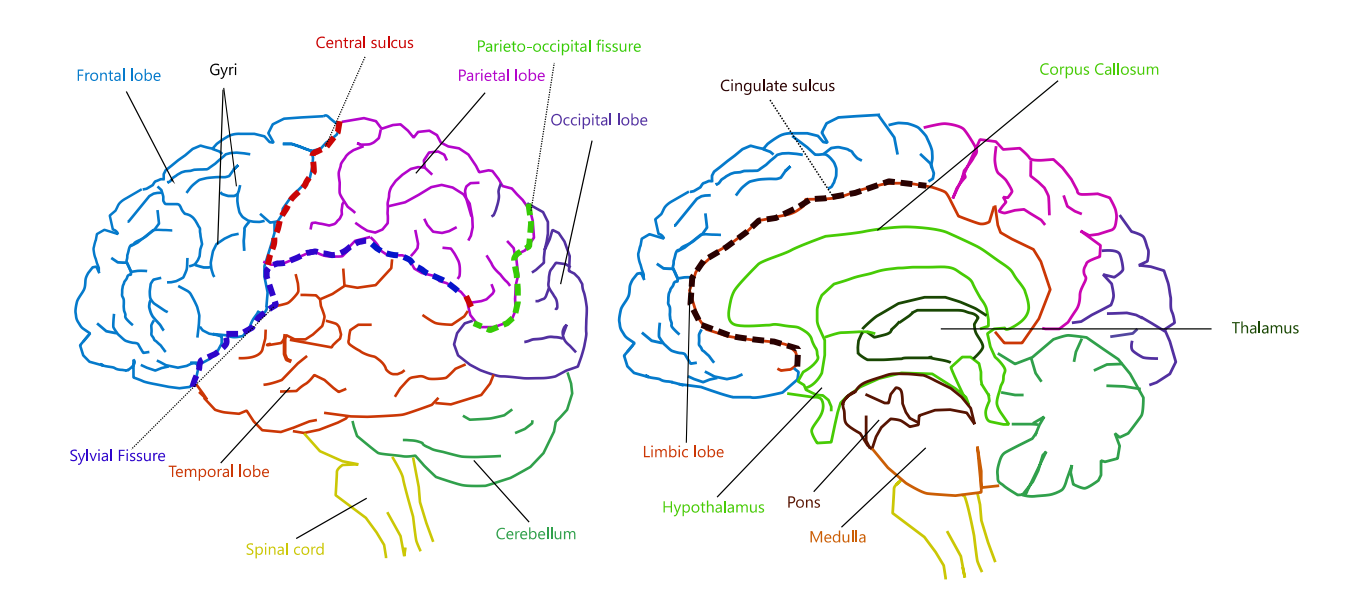


Figure 3: Anatomy of human brain

(A) Lateral saggital view. From left to rigt: frontal parietal, occipital, temporal occipital lobes, spinal cord and cerebellum. Central sulcus separates frontal from parietal lobe, parieto-occipital fissure separates parietal from occipital lobe and sylvian fissure separates frontal from parietal and temporal lobes. Gyri is a main structure of the brain.

(B) Median saggital view: Limbic lobe consists of hypothalamus, thalamus and corpus collosum. Above the spinal cord – pons and medulla. Cingulate sulcus separates frontal from limbic lobe.

## Neurodevelopmental disorders of cortical development

As I described previously, the development of human brain is a complex process that requires coordination of different cellular and molecular mechanisms. When the brain development is disrupted during the early stages of development, it can lead to neurodevelopmental disorders. Neurodevelopmental disorders are a group of conditions which arise from abnormal brain development. As the cerebral cortex is particularly vulnerable to internal and external influences during early development, it is often impacted in neurodevelopmental disorders. These disorders can be divided into several categories based on their underlying cause. For example, these disorders include disorders with defects in apoptosis and cell survival, abnormal brain patterning, impaired neuronal migration, and abnormal cell proliferation. In the following part, I will provide an overview of these disorders.

#### Disorders arising from defective cell survival

A disease such as Neu-Laxova syndrome arises due to apoptosis in neurons. This is a severe condition that leads to very small brains (microcephaly) and a smooth brain surface (agyria, lissencephraly, or microlissencephaly). It also affects the brainstem, spinal cord, and cerebellum. This disease is fatal, causing death in early infancy.

Recent research has linked Neu-Laxova syndrome to mutations in the PHGDH gene, which is crucial for the first step of L-serine production (Acuna-Hidalgo et al., 2014). Scientists believe the disease is caused by problems with neuron movement, stopping their development around 12–14 weeks of pregnancy. In addition, a defect in the neuronal migration resulting in arrest at the 12–14 weeks of embryogenesis has been proposed as the cause of the disease, while also an abnormal cell death causing depletion of neurons and their atrophy has been described (Kuseyri et al., 1993).

A study in mice, where cell death genes have been knocked out (Tybulewicz et al., 1991), has demonstrated a phenotypically similar brain to microlissencephaly.

#### Disorders arising from abnormal brain patterning

Another group of brain developmental disorders results from irregular brain patterning, as it is the case for various types of polymicrogyria. These conditions result in an abnormally thick brain surface, otherwise known as pachygyria. Pachygyria is often accompanied by small, fused folds (Jansen, 2005). In some cases, the cortex may exhibit an unusual four-layered structure or a complete lack of well-defined layers. In the four-layered form, tissue necrosis occurs following neuronal migration, leading to the fusion of gyri (Ferrer et al., 1986).

A closely related disorder, schizencephaly, is characterized by the formation of a cleft between the brain's outer (meningeal) and inner (ventricular) surfaces, with the cleft's edges lined by polymicrogyria (Shutterd, 2014).

#### Disorders arising from abnormal neuronal migration

As per the neuronal migration model, the earliest-born neurons migrate the least and form the deepest level of the brain, with each new division of the neuronal progenitor reaching further in the cortex (Nadarajah et al., 2002). Periventricular heterotopia is a disease of abnormal neuronal migration, where clumps of different neurons, including randomly oriented pyramidal neurons and interneurons, are found close to their generation side (Hannan et al., 1999; Kakita et al., 2002). Another disease, such as type 1 lissencephaly, a smooth brain disease, is a disease arising from severe neuronal migration defects, where affected cortexes are four-layered and have either completely absent or partial gyri (Wynshaw-Boris, 2010). Neuropathological analysis shows a disorganized outer pyramidal cell layer, followed by a cell-sparse and cell-dense region, hinting at the problem of neuronal migration from their origin layer. This disease, as other diseases in this spectrum, is caused in 40% of cases by Lis1 and DCX (Doublecortin) mutations (Wynshaw-Boris, 2010), both microtubule associated proteins (Smith et al 2000, Moores et al 2006).

#### Disorders of abnormal cell proliferation

Another type of neurodevelopmental disorder is disorders arising due to abnormal cell proliferation. One differentiates three diseases in this category: megalencephaly, which arises due to abnormal neuronal proliferation and migration in the postnatal brain (Leonardi et al., 2023);

hemimegalencephaly, or an asymmetric overdevelopment of one of the two hemispheres (Flores-Sarnat, 2002); and microcephaly, a disorder of an abnormally small brain.

#### Microcephaly

Microcephaly is a neurological disorder, which is defined by a 2-3 Standard Deviations (SD) reduced occipitofrontal head circumference (OFC) below the average. This disease can be acquired or genetic, named secondary and primary microcephaly respectively (reviewed in Passemard et al., 2013). Microcephaly is diagnosed in the second trimester, by birth, or later during infant development (Bromley, 1995). This disease can be accompanied by other symptoms such as visceral or skeletal malformations, facial dysmorphism, or present alone.

Secondary microcephaly can be acquired in a variety of ways, such as viral, bacterial, or parasitic intrauterine infection, irradiation, drug, alcohol, and toxins exposure, or as a result of different maternal diseases such as hyperphenylalaninemia. Secondary microcephalies most often occur in the first year of life and are associated with other developmental defects, such as motor and cognitive deterioration and seizures (Lim & Golden, 2020).

Primary microcephaly, on the other hand, can be both part of a syndrome or nonsyndromal, as an isolated condition. Syndromal microcephaly is known to be associated with at least 800 different disorders (Abuelo, 2007). Primary nonsyndromal microcephaly, or microcephaly primary hereditary (MCPH), is a rare neurodevelopmental heterogeneous familial disorder which accounts for 1:30,000 to 1:250,000 live births (reviewed in Passemard et al., 2013).

MCPH microcephaly can be diagnosed based on the size of the brain around the end of the second trimester of the pregnancy through ultrasound scan and around the third trimester by gyrification via fetal MRI (Pei et al., 2023). This disease is untreatable, but the symptoms can be attenuated through early therapy. This disease runs in around 100 families, and around 30 genes have been identified to be linked with it (OMIM base, 2025), most of which are associated with a loss-of-function of the respective protein.

One group of genes involved in microcephaly is DNA damage and repair genes. Indeed, one of the most prominent genes in this group is the first discovered microcephaly gene, Microcephalin (MCPH1). Microcephalin is required for the formation of DSB damage response foci and transcriptional regulation of other DNA damage response proteins such as Chk1 and BRCA1 (Xu et al., 2004).

Another group of genes is involved in transmembrane or intracellular transport. Indeed, mutations in several MCPH genes lead to disruption in vesicle transport from the Golgi to the plasma membrane and vesicle-mediated intracellular trafficking. Few other microcephaly proteins are involved in amino acid or protein synthesis (reviewed in Jayaraman et al., 2018).

Interestingly, most of the genes which were found to be linked with MCPH are responsible for cell division (Jayaraman et al., 2018). The precise mechanism of MCPH microcephaly, however, remains unknown and requires further study.

# Fatty acids transport DNA damage Transcription Signaling Cell division&Cell cycle

Figure 4: Pathways involved in primary microcephaly

Primary pathways where genes are mutated in primary microcephaly include cell division and cell cycle, cell signaling pathways, transcription, DNA damage and fatty acid transport. Genes involved in cell division and cell cycle constitute the highest number of primary microcephaly cases.

# Current hypotheses of microcephaly disease origins

As previously discussed, mutations in different sets of genes can cause primary microcephaly; however, the majority of these genes have been linked to mitotic cell division defects (Jaramayan et al 2018). How these, however, lead to microcephaly remains unclear.

In the past years, several different non-exclusive hypotheses were postulated regarding the origins of this disease and how mitotic dysregulation might lead to brain abnormality. Basto lab has found that, in contrast to the fly model where centrosome amplification causes tumorigenesis (Basto et al., 2008), in a mouse brain, centrosome amplification by overexpression of Polo-like kinase 4 leads to primary microcephaly by promoting aneuploidy. Indeed, in mammalian neuroblasts, PLK4 overexpression led to aneuploidy and neuronal progenitor pool depletion via p53-induced apoptosis (Martiens et al., 2013). In the absence of apoptosis, aneuploidy led to brain degeneration. With this work, an aneuploidy hypothesis of the primary microcephaly has been established, where p53 plays a central role in eliminating aneuploid cells and leading to increased apoptosis, resulting in depletion of neuronal progenitor pool.

Another common hypothesis, which has been dominating in the field, is that premature neuronal differentiation is driven by erroneous spindle orientation (reviewed in Noatynska et al 2012). Indeed, this hypothesis is based on the idea that neuronal progenitor cells need to change their spindle orientation to go from a symmetrical mode of division, which generates two neuronal progenitor cells, to an asymmetrical one, which generates one progenitor cell and one differentiated cell. This switch is physiological; however, if it happens preemptively, it can lead to neuronal progenitor pool depletion and ultimately microcephaly (reviewed in Noatynska et al 2012). Several papers have reported erroneous spindle orientation in mice (Lizzaraga et al., 2010) and Drosophila (Nair et al 2016). Lizzaraga et al., 2010, reported that CDK5RAP2 mutant mice exhibited microcephaly due to impaired mitotic progression caused by abnormal spindle orientation. The authors propose that CDK5RAP2 mutants are susceptible to cell cycle exit and death, which leads to the microcephaly phenotype (Lizzaraga et al., 2010). Similarly, the same lab has published data on spindle misorientation in NDE1deficient mice (Feng & Walsh, 2004), reporting a decrease in the cerebral cortex due to reduced cell division and altered neuronal cell fates. Similarly, ASPM depletion in the mouse brain was reported to lead to a deviation from perpendicular spindle orientation (to the ventricular surface of the neuroepithelium), resulting in increased asymmetric division and a decrease in the neuronal progenitor pool (Fish et al., 2006). In Drosophila, WDR62 depletion was reported to affect spindle orientation due to centrosome displacement (Nair et al., 2016). Also, Lis1/dynactin was reported to

affect astral microtubules, leading to spindle orientation defects at metaphase (Siller & Doe, 2008). Other studies, however, did not find spindle orientation defects upon WDR62 depletion (Guerreiro et al., 2021; Chen et al., 2014). The evidence of spindle misorientation in primary microcephaly remains contradictory.

Finally, some studies have shown prolonged mitosis resulting from severe centrosomal defects as a cause of primary microcephaly (Phan et al., 2021, Chen et al 2014). The publication from Chen et al 2014 has reported the increase of mitotic duration due to loss of interaction between Aurora A and WDR62 (Chen et al 2014), leading to the death of neuronal progenitor cells. In the publication from the Holland lab, the authors have found yet another pathway leading to primary microcephaly, a mitotic surveillance pathway (discussed more in the "53BP1 roles in mitosis" chapter). The authors have reported that mitotic surveillance pathway, which consists of the 53BP1 and USP28 complex, activates p53 and leads to increased apoptosis in the event of prolonged mitosis. This effect was a result of centrosomal defects in mice caused by a loss of CEP63 and SAS4 and leading to monopolar spindles. The activation of this pathway results in decreased brain size (Phan et al., 2021).

Overall, different pathways have been proposed to explain the origins of primary microcephaly; however, the results are contradictory. Further studies are needed to underpin the molecular mechanisms of primary microcephaly.

# Models to study microcephaly

The study of neurodevelopmental diseases, compared to studies of other human diseases, is complicated by the lack of accessibility of the brain for direct observations during its development. Therefore, it is crucial to establish alternative models using animals, which can be instrumental in studying brain development in vertebrates and complement the neuropathology studies. Different model animals, such as the mouse (Mus musculus) and the fruit fly (Drosophila melanogaster), have been used extensively in neurodevelopmental studies over the past years. Compared to in vitro studies of neurodevelopmental disorders, in vivo models give a unique advantage by analyzing the development in real time. Additionally, around 75% of all human disease-related genes can be found in Drosophila (Reiter, 2001), which allows the use of the Drosophila model in disease studies. In the next paragraph, I will briefly describe different models and the advantages and disadvantages of their use for studying MCPH microcephaly.

#### Drosophila melanogaster

Drosophila melanogaster is a widely used microcephaly model due to its fast breeding time, costeffectiveness, and genetic traceability. The genome of the fruit fly contains only about 13,600 genes (Rew, 2001), significantly fewer than humans. Additionally, the Drosophila model lacks human brain complexity, which makes it hard to compare the late stages of brain development to humans. However, most fundamental molecular pathways in neurodevelopment are conserved between Drosophila and humans. Indeed, some of the first fundamental studies of neuronal patterning and embryonic development were conducted in Drosophila (Nüsslein-Volhard and Wieschaus, 1984). In fact, even some of the first microcephaly genes have been discovered in Drosophila (Richmyre, 2007). As meantioned previously, the central nervous system of the fly is much simpler compared to humans, but this allows the study of core neuronal functions, such as glial cell functioning and glia-related disorders. Indeed, the second most commonly mutated gene in primary microcephaly, WDR62, has been studied in Drosophila glial cells (Lim et al., 2017; Shohayeb et al., 2020) and neuronal progenitor cells (Nair et al., 2016). Depletion of the MCPH1 protein Microcephalin, which gives the name to the microcephaly disease, has been shown to result in premature chromosome condensation in Drosophila (Richmyre, 2007), a phenotype which is in accordance with human patients (Trimborn et al., 2004).

Additionally, a wide variety of genetic tools are available in Drosophila, such as, for example, the reverse genetic approach using the GAL4/UAS system, often combined with RNAi. Briefly, once a fly containing Gal4 and another fly containing UAS RNAi sequence are crossed, the progeny receives both sequences. In the progeny, yeast Gal4 transcription factor binds to the UAS (Upstream Activated Sequence), which is inserted upstream of the gene of interest together with an inverted complementary repeat to the gene of interest. Gal4 activates the expression of the inverted repeat, which leads to the formation of a hairpin structure and sequence-specific RNAi silencing (reviewed in Duffy et al., 2002). Taken together, the cost-effectiveness, fast breeding time, and genetic traceability of the fruit fly, alongside a variety of genetic tools available, make Drosophila melanogaster a great model to study microcephaly.

#### Mus musculus

Mouse is one of the most widely used models for human diseases due to its high degree of homology in embryonic development and anatomy. Mice contain a similar number of genes as humans (20,000-

22,000) and around 85% of all genes are highly conserved between the two species (Makałowski et al., 1996). Despite its advantages, mouse models are costly and require a long breeding time. Additionally, in terms of brain development, the mouse brain is smooth compared to the human brain, which has gyri and sulci (Van Essen 2002). Many microcephaly studies, however, have been conducted in mice. Different MCPH genes have been studied extensively in mice, including the most commonly mutated MCPH gene ASPM (Bond et al., 2002; Fujimori et al., 2014) and the second most commonly mutated MCPH gene WDR62 (Chen et al., 2014; Zhou et al., 2018). Some of these advances will be discussed in the next chapter where I present the roles and functions of WDR62.

#### WDR62 and its functions

WDR62, first discovered in 2010 (Nicolas et al., 2010), is the second most commonly mutated gene in primary microcephaly (OMIM 2025). This gene has 32 exons and is localized on the chromosome 19q12. At least two splicing transcripts are known in the human genome: the first one consists of 1,523 amino acids or 1,511 amino acids, which excludes the first 12 nucleotides of exon 27 (Nicolas et al., 2010). WDR62 protein contains at least 15 WD-40 repeats (WDR), the fourth most abundant domain in the human genome (Afza et al., 2022). WDR domains are composed of serine—histidine and tryptophan—aspartate motifs (WD). The domain usually consists of  $\beta$ -propeller folds assembled in a donut shape (Stirnimann et al., 2010). WDR domains often act as scaffolds for large protein complexes, binding proteins and molecules through the donut hole. WD-40 domain proteins perform versatile functions in the cell and, as a result, are often perturbed in human pathologies, such as endometrial and colorectal cancers, as well as neurological disorders such as primary microcephaly (Zhang et al., 2014).

The involvement of WDR62 in microcephaly has been a subject of intensive research for the past 10 years. Indeed, WDR62 is the second most commonly mutated gene in microcephaly after ASPM. Over 40 pathogenic mutations have been published until now, most of them associated with a wide range of cortical malformations (OMIM 2025). A study by Bilguvar et al., researching the phenotypic changes in the brain after a frameshift mutation leading to a premature stop codon, has shown in nine individuals that all of them had extreme microcephaly, pachygyria, and hypoplasia of the corpus callosum, accompanied by lissencephaly, various degrees of cortical thickening, and loss of the grey—white junction. Sylvian fissures were observed in six patients; two showed signs of polymicrogyria, asymmetric in both hemispheres. Six had hippocampal dysmorphology, and one displayed cerebellum dysgenesis (Bilguvar et al., 2010). Missense and null mutations that have been found in two families

led to a simplified gyral pattern in the first case and additional cerebral cortex thickening in the second case (Nicolas et al., 2010), suggesting a more severe cortical delamination phenotype. Another study described a Sudanese family where two siblings were affected by microcephaly through a homozygous variant in exon 4 of WDR62. These siblings both suffered from primary microcephaly accompanied by lissencephaly, with the first one additionally exhibiting symmetrical widening of supra- and infratentorial cerebral ventricles, Sylvian fissures, and extra-axial cerebral fluid spaces (Bastaki et al., 2016). A further study describes an Indian family with a truncating nonsense mutation in exon 8. This mutation resulted in pachygyria and polymicrogyria (Bhat et al., 2011). In the study by Zombor et al. 2019, a missense mutation in exon 6 led to pachygyria, thickening of the cortex, and abnormal formation of the corpus callosum. Overall, the study has observed a more severe phenotype as a result of a very early premature stop codon compared to missense or frameshift mutations (Zombor et al., 2019).

A thorough postmortem study has shown the potential role of WDR62 in the proliferation of neurons and their migration. The brain of a 27-week-old patient was reported to be microcephalic with lissencephalic features. Both hemispheres were smooth, with poorly defined Sylvian fissures and few sulci. The cerebral cortex was reported to be largely abnormal, showing pyramidal neurons almost absent in layers II/III and patches of progenitor cells in the subventricular zone. This study has demonstrated profoundly dysfunctional neurogenesis in the developing human brain, more precisely in the outer subventricular zone and neuronal migration, following a mutation in the WDR62 gene (Yu et al., 2011).

In more fundamental work on WDR62 using mice and fruitfly models, it has been reported that WDR62 is crucial for neuronal differentiation and that depletion or deletion of WDR62 results in the premature differentiation of the neuronal progenitor pool and a decrease in brain size (Chen et al., 2014; Nair et al., 2016). During interphase, WDR62 localizes to stress granules, where it interacts with JNK2 and MMK7 and is hypothesized to regulate the fate of mRNA after stress (Wassermann et al., 2010), controlling the interplay between polysomes, stress granules, and processing bodies. During mitosis, WDR62 is phosphorylated by Aurora A, which leads to its localization at the spindle poles (Lim et al 2016). More precisely, WDR62 was shown to localize to the centrosome in some studies (Yu et al., 2010; Sgourdou et al., 2017; Nair et al., 2016) but to the microtubule minus ends in others (Guerreiro et al., 2021). WDR62 localization at the microtubule minus ends is maximal at metaphase and degrades by the end of anaphase. Upon mitotic exit, WDR62 localization becomes cytoplasmic (Guerreiro et al., 2021). WDR62 was also shown to be important for cilia formation, and the loss of WDR62 is known in ciliopathies. At the basal body of cilia, WDR62 was shown to recruit CPAP (Centrosomal P4.1-Associated Protein, CENP-J) (Shohayeb et al., 2020). Furthermore, it was

demonstrated that WDR62 is important for Cep170 localization. Moreover, it leads to the WDR62-CEP170-Kif2A cascade, which is fundemental for primary cilium disassembly (Zhang et al., 2019). Additionally, it has been shown that WDR62 regulates centrosome duplication and allows centriolar matrix proteins ASPM and Cep63 to be correctly localized in the S-phase (Jayaraman et al., 2016). However, another study has demonstrated that at the spindle poles WDR62 depletion does not alter ASPM localization (Guerreiro et al 2021). In Drosophila neuroblasts, depletion of WDR62 in interphase led to asymmetric localization of PLK4/PLP at the centrosomes and increased microtubule stability (Nair et al., 2016).

Once the cell enters mitosis, WDR62 was shown to be phosphorylated by PLK1, which allows its recruitment at the spindle poles (Miyamoto et al., 2017). Indeed, WDR62 is recruited by TPX2/Aurora A complex to the spindle poles where it acts as an adaptor for localization of the microtubule-severing enzyme Katanin (Huang et al., 2021). In the absence of WDR62, Katanin is mislocalized, leading to a decrease in poleward flux speed, a wider metaphase plate, and asynchronous chromosome segregation (Guerreiro et al., 2021).

In mouse neuronal progenitor cells, WDR62 was shown to colocalize with Aurora B and other CPC (Chromosome passanger complex) components, and depletion of WDR62 was shown to downregulate CPC components at the centromeres (Sgourdou et al., 2017). Depletion of WDR62 in Drosophila neuroblasts leads to a smaller brain phenotype, which can be rescued by co-depletion with Aurora A (Lim et al., 2017). Additionally, this study has shown the presence of WDR62 at microtubule plus ends, something that was not confirmed in other studies (Guerreiro et al 2021).

To summarize, research on the role of WDR62 in microcephaly and mitosis is extensive; however, some results are contradictory. Therefore, more work is needed to understand the precise cause of WDR62 related primary microcephaly and the function of WDR62 in mitosis. In the next chapters, I will introduce mitosis and its main processes.

### Mitosis

By the end of interphase, the cell has replicated a sufficient number of macromolecules and has replicated the DNA to produce two new cells. During the process of mitosis, the cell segregates the replicated DNA into two daughter cells, which is followed by cell division or cytokinesis. In the following chapter, I will first describe the components of the mitotic spindle, focusing on the

metaphase spindle. Further, I will go into details of certain mitotic high points before describing the process that leads to the formation of the metaphase spindle and its resolution at mitotic exit.

#### Mitotic spindle components and spindle architecture at metaphase

During mitosis, the cell needs to divide its genetic material equally to the two daughter cells. For this task, a cell assembles a structure called the mitotic spindle. This complex structure is composed of different types of microtubules and is anchored at the cellular cortex to provide the cell orientation and division axis. In the next paragraph, I will describe the different components of this fascinating machinery.

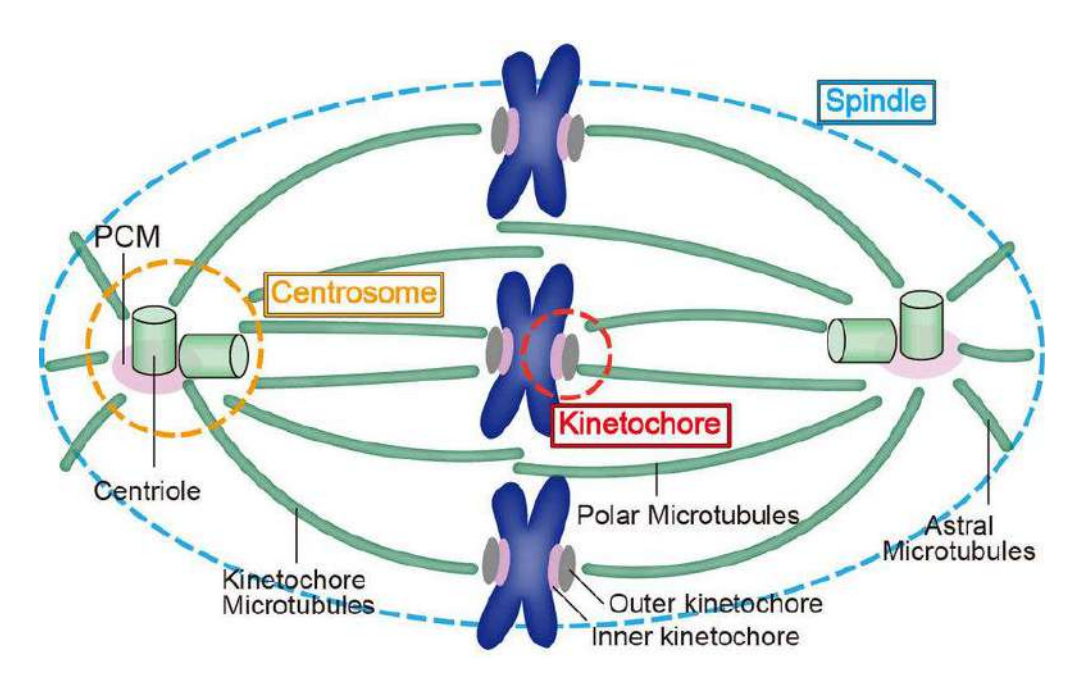


Figure 5: Mitotic spindle components and mitotic spindle structure at metaphase.

Mitotic spindle is composed of centriolar pair, embedded in the pericentriolar material, both structures together are called centrosome. Centrosome nucleates the majority of microtubules, such as kinetochore microtubules and astral microtubules. Kinetochore microtubules bind chromosomes at the outer kinetochore and the inner kinetochore is connected to the centromeric DNA.

Adopted from Ito et al 2020

#### K-Fibers

The mitotic spindle is assembled from a variety of different microtubule types with the role of segregating the chromosomes into two daughter cells (Walczak & Heald, 2008). The mitotic spindle is

a bipolar structure, composed of microtubules. Microtubules are polymer molecules, assembled from  $\alpha$  and  $\beta$  tubulin subunits. A microtubule is assembled from 13 protofilaments of  $\alpha\beta$ -tubulin heterodimers (see schematics, Tillney, 1973) in a head-to-tail fashion, giving them polarity. Polarity is essential for microtubules and allows for many different processes to take place, such as motion of the cargo but also for different growth speeds at the two ends of the microtubule (Rolls, 2022). Indeed, every microtubule grows by the addition of an  $\alpha\beta$  tubulin dimer and shrinks by its ejection (reviewed in Brouhard et al., 2018). Both the  $\alpha$  and  $\beta$  subunits of tubulin are associated with GTP, but only the  $\beta$ tubulin subunits undergo a hydrolysis reaction, resulting in a conformational change of the protein and microtubule lattice destabilization (reviewed in Nogales, 2001). This is achieved by a change in the conformation of the individual microtubule protofilament, which, upon GTP hydrolysis, changes from a straight sheet to a curved conformation (Müller-Reichert et al., 1998). This process is known as the dynamic instability of microtubules and will be discussed in the next chapters. The polarity of the microtubules is conventionally labeled as the plus-end (the growing end of the microtubule) and the minus-end (the shrinking end of the microtubule). On the mitotic spindle, the microtubules carrying the chromosomes apart are called k-fibers. K-fibers are kinetochore microtubules which have their plus-end embedded in the kinetochore and the minus-end anchored in the PCM matrix of the centrosome (reviewed in Tolic et al., 2018). These microtubules generate pulling forces on the chromosomes, and their attachments to the kinetochores (KT-MT attachments) are important to satisfy the SAC (spindle assembly checkpoint), allowing progression from metaphase to anaphase (Nezi & Mustacchio, 2009). K-fibers are assembled from 4-20 single microtubules providing a robust anchoring point and a strong pulling force on chromosomes (reviewed in Tolic et al., 2018). kMTs are the longest-lived and most stable microtubules, with a half-life of around 720 s in RPE cells, while other microtubule types such as for example interpolar microtubules display a half-life of only around 180 s (reviewed in Valdez et al., 2023). As mentioned before, every kMT is polarized, with the more stable minus-end being anchored in the microtubule organizing center (MTOC) and the plus-end being free to polymerize and depolymerize to explore the cell in space and time. This allows the kMTs to search and capture the kinetochores. How this is achieved will be discussed in the following chapters.

#### Interpolar microtubules

Besides K-fibers, the mitotic spindle contains other microtubules which do not bind directly to the kinetochore, such as interpolar microtubules and astral microtubules. One hypothesis says that these interpolar microtubules can arise during the early spindle formation, when, in a "search and capture" fashion (Kirschner & Mitchison 1986), the mitotic spindle grows in all directions. Interpolar

microtubules are known to be important during spindle formation at prometaphase. Indeed, the sliding of the antiparallel interpolar microtubules by Kinesin 5 allows for the generation of outward sliding force which will push centrosomes apart, allowing the spindle to become bipolar (Tanenbaum & Medema 2010). Interpolar microtubules extending from two opposite sides of the mitotic spindle can become crosslinked and generate an additional force during chromosome separation (reviewed in Tolic et al. 2018). Some interpolar microtubules are tightly coupled with K-fibers that are bound to the kinetochore, having the appearance of a bridge between the kinetochore and the K-fiber. Because of their function and their appearance, they are called bridging fibers (Kajtez et al. 2016). Interestingly, it was shown that if the K-fiber is ablated, the bridging fibers connected to the K-fiber move together, demonstrating the physical link between a K-fiber and a bridging fiber (reviewed in Simunic & Tolic 2016). Together with K-fibers, bridging fibers are indispensable for the biorientation of chromosomes at the metaphase plate before mitosis.

#### Astral microtubules

Another class of non-kinetochore microtubules are astral microtubules. Astral microtubules are anchored with their minus-end at the centrosome and grow out in an astral arrangement towards the cell cortex. Astral microtubules are nucleated from the spindle poles and, like other microtubules, undergo periods of growth and shrinkage. Once they reach the cortex, they interact with the cortical protein dynein, a minus-end-directed motor which generates an outward-directed force that determines the mitotic spindle orientation (reviewed in Valdez et al. 2023).

#### Kinetochore, centromere and chromosome

To ensure correct chromosome segregation by the mitotic spindle apparatus, kinetochores are searched for and captured by microtubules. Kinetochores are large protein assemblies with the primary function of creating a bond between the microtubule and chromosome (Maiato et al. 2004). These attachments need to be able to withstand considerable strength, which requires the kinetochore to be robust. In addition to its robustness, the kinetochore is also a hub for different cellular pathways, implicated in cell division and the cell cycle, functions which are carried out by many proteins constituting the kinetochore structure (Chan et al. 2005). Indeed, even the simplest kinetochore in Saccharomyces cerevisiae contains around 60 proteins (De Wulf et al. 2003). Most of these proteins are conserved in the majority of eukaryotes.

In vertebrates, kinetochores contain around 100 proteins, and they appear to be a disc-shaped structure containing inner and outer kinetochore plates, with the inner plate being oriented toward the centromeric region of the chromosome and the outer plate interacting with the plus end of the microtubule (reviewed in Cheeseman et al. 2014). Kinetochore composition is complex, and the inner kinetochore on its own can be divided into several parts. Indeed, the innermost part of the kinetochore, the inner centromeric region, is the intersection between the inter-sister chromatid and the inter-kinetochore. This part harbors proteins, such as the cohesin complex, CPC, Shugoshin 1/2 (Sgo1/2), and Haspin (Hindriksen et al. 2017). Further out lies the kinetochore-proximal centromere, and it contains proteins such as CENP-A and CENP-B. The outermost part contains CCAN (Constitutively Centromere Associated Network) proteins which connect the kinetochore with the centromere (reviewed in McAinch & Marston 2022). These proteins are composed of CENP family proteins and include CENP-C, CENP-H, CENP-I, CENP-K, CENP-L, CENP-M, CENP-N, CENP-O, CENP-P, CENP-Q, CENP-U, CENP-R, CENP-T, CENP-W, CENP-S, and CENP-X.

The outer kinetochore is composed of KMN network proteins (Knl1, Mis12 complex, and the NDC80 complex) as well as spindle assembly checkpoint proteins Bub1 and Mps1 (Varma & Salmon 2012). On top of the outer plate sits a fibrous corona, which only expands and becomes visible when the kinetochores are not attached to the microtubules, containing microtubule motors, such as CenpE, and spindle assembly checkpoint proteins such as the RZZ complex (Cooke et al. 1997). The fibrous corona has a role in generating lateral microtubule attachments and transforming them into end-on attachments, as discussed later (see chapter kinetochore-microtubule attachment). Also, the fibrous corona has been proposed as a microtubule nucleation site at the kinetochore (Wu et al. 2023).

The kinetochore binds to a centromere, which in vertebrates is a region spanning a part of the chromosome. This part contains a specialized centromeric histone protein H3 variant, CENP-A, with repetitive satellite DNA on it (Talbert & Henikoff 2022). In human cells, centromeres have different localizations depending on the chromosome. Metacentric chromosomes have a centromere in the middle, submetacentric chromosomes have centromeres in the middle region, and acrocentric chromosomes (chromosomes number 13, 14, 15, 21, and 22) have centromeres at one end of the chromosomal structure (Tseng 1995).

#### Microtubule organizing center (MTOC)

Many microtubules in mitosis and interphase are anchored at the microtubule organizing center (MTOC). During interphase, the MTOC is important for organelle organization and support as well as cilia genesis (Joshi 1994), while in mitosis, the MTOC mainly serves as a microtubule nucleation site

and, later on, as an anchoring site for the spindle microtubules (reviewed in Lüders 2021, Vineethakumari & Lüders 2022).

Centrosome is the microtubule organizing center (MTOC) of animal somatic dividing cells, is composed of paired barrel-shaped structures of nine microtubule triplets called centrioles (reviewed in Vineethakumari & Lüders 2022). These are surrounded by the pericentriolar material, a major anchoring site for different proteins, which includes a nucleator yTuRC, the function of which will be discussed later on. Centrioles are composed of a basal body and centriolar appendages at the distal end, the latter differentiating the old from the young centriole. The older centriole (also called the grandmother centriole) contains distal appendages and subdistal appendages, whereas the mother centriole contains only distal appendages. The two newborn centrioles are devoid of these appendages (reviewed in Uzbekov & Alieva 2018). For instance, Cep164 and OFD1 are examples of distal appendage protein and ODF2/cenexin, ninein and centriolin are examples of subdistal appendages (Ma et al 2023).

The centrosome duplicates once per cell cycle in a semi-conservative manner (Blanco-Ameijeiras et al. 2022). After cell division, each daughter cell inherits a centrosome, which is composed of an orthogonally oriented mother-daughter centriole pair (Wilhelm et al. 2019). During the G1 phase of the cell cycle, these centrioles elongate, and when the cell proceeds into the S-phase, each of the centrioles grows a procentriole. In the G2 phase, centrioles mature and start recruiting PCM component proteins in preparation for mitosis. Just before mitosis starts, centrosomes disengage, and when entering mitosis, they begin nucleating microtubules to build the mitotic spindle (Nigg & Stearns 2011).

#### Motor proteins and microtubule associated proteins (MAPs)

Microtubule plus- and minus-ends are characterized and modulated by different sets of Microtubule-Associated Proteins (MAPs hereafter). The better-characterized plus ends are highly dynamic and fast-growing microtubule ends. One of the most studied plus-end binding proteins is the EB (End Binding) family protein, which in mammals is composed of EB1, EB2, and EB3. EB proteins are important regulators of microtubule dynamics; they recognize the GTP microtubule state through their N-terminal calponin homology (CH) domains, promoting microtubule growth (Gimona et al. 2005, Mustyatsa et al. 2017). Another well-studied plus-end binding protein family includes APC (Adenomatous polyposis coli protein), Clip-170 (Cytoplasmic linker protein), and CLASPs (CLIP-associating proteins). In the majority of cases, these proteins act through EB and are implicated in

stabilizing microtubules and regulating microtubule polymerization by modulating the structure of the microtubule ends (Galjart 2005). Another important plus-end regulator is the Ch-TOG family of proteins, which favor new microtubule formation and are implicated in mitotic stability (Barr & Gergerly 2008).

At the less dynamic minus-end, a different set of proteins regulate microtubule stability and dynamics. This end is often capped by the γ-tubulin ring complex (γ-TURC) (Zheng 1995). However, during mitosis, not all microtubule minus ends are capped by γ-TURC, and free microtubule minus-ends can depolymerize, leading to the poleward microtubule flux, a conveyor-belt-like motion of tubulin dimers (Mitchison 1989), which is described in more detail below. Due to the misconception that microtubule minus-ends do not polymerize, they were understudied for decades. However, in the past years, different regulators of microtubule minus-ends have been identified. For instance, microtubule minus-end depolymerizers, such as Kinesin-13 family members (Kif2A, Kif2B, MCAK), have been investigated to understand their role in microtubule minus-end depolymerization (Ems-McClung & Walczak 2010). Kif2A was shown to be an important regulator of microtubule minus-ends in HEK293T (Guan et al. 2023), which is responsible for correct spindle architecture and length. Also, Kif2A plays a role in cilium disassembly in RPE-1 cells (Miyamoto et al. 2015).

Kif2A paralog MCAK is, on the other hand, both a minus and plus-end localizing kinesin with the larger pool at the kinetochores (Oguchi et al. 2011). Recent data from our lab has shown that MCAK is an important driver of poleward microtubule flux during mitosis and is downstream of a microtubule capping protein, Calmodulin-regulated Spectrin-associated protein 1 (Camsap1) (unpublished data).

Camsap1 is a member of the Camsap family of proteins, which in humans is composed of three members: Camsap1, Camsap2, and Camsap3 (Jiang et al. 2014). Its Drosophila ortholog, Patronin, has been extensively studied before and was found to be an important regulator of microtubule minusend depolymerization. Indeed, Patronin was found to antagonize the action of the microtubule depolymerizer Klp10a, an ortholog of Kif2A in Drosophila at the mitotic spindle poles (Goodwin & Vale 2010). This led to shorter mitotic spindles.

In the interphase of polarized cells, Patronin was shown to organize microtubule arrays in histoblast cells to form the abdomen of Drosophila (Panzade & Matis 2021), to be important for the formation of apical-basal polarity in epithelia (Khanal et al. 2016), and to be critical for axon regeneration in neurons (Chuang et al. 2014). Other members of Camsap (Baines et al. 2009) can bundle the microtubules and decorate them along the lattice as well as the microtubule minus-ends (Goodwin & Vale 2010, Meng et al. 2008), compared to the minus-end restricted localization of Camsap1. The main role of Camsap2 and Camsap3 is to promote the stability of microtubule minus-ends and the

microtubule lattice, being a seed for microtubule outgrowth (Jiang et al. 2014, Tanaka et al. 2012). The localization of Camsap2 and Camsap3 along the microtubule lattice allows them to facilitate the generation of non-centrosomal microtubules (Jiang et al. 2014). Additionally, Camsap2 and Camsap3 were shown to play a role in the reduction of tubulin dimer incorporation at the microtubule minusend (Hendershott & Vale 2014), while Camsap1 was identified as solely tracking minus-end protein with no clear function. In neuronal cells, Camsap family members are important for microtubule density and stability. Depletion of Camsap2 in neurons has a strong effect on axon formation and branching of dendrites (Yau et al. 2014). Camsap1 depletion was shown to affect neurite formation; however, Camsap1 depletion does not display a strong effect on neuronal function. However, in mitosis, Camsap1 seems to play a role. Unpublished data from our lab suggest that during mitosis, Camsap1 is important for microtubule flux regulation (in agreement with Jiang et al. 2019). Additionally, it has been shown that Camsap1 depletion does not alter spindle architecture. However, our data show that depletion of Camsap1 leads to chromosome segregation defects and was shown to regulate MCAK function at the spindle poles (unpublished data).

The microtubule minus-ends, which are protected by Camsap family proteins from depolymerization, can be generated from the microtubule cutting by severing enzymes (Jiang et al. 2017). Microtubule severing enzymes Katanin, Spastin, and Fidgetin belong to a subgroup of AAA ATPases that all utilize a common feature of using ATP hydrolysis as an energy source for large molecular remodeling (Roll-Mecak & McNally 2010). Both Katanin and Spastin are microtubule-stimulated AAA ATPases, as the N-terminal domain of Katanin and Spastin contains a Microtubule Interacting and Trafficking (MIT) domain. Through gradual unfolding of tubulin peptide chains, they lead to the loss of contact of the tubulin subunit with the lattice and its removal (Roll-Mecak & McNally 2010). Katanin is composed of two enzymatic subunits: the p80 regulatory subunit and the p60 subunit of AAA ATPase function (Rezabkova et al. 2017). The destabilization of the microtubule lattice by Katanin leads to the creation of two microtubule ends, which function as a substrate for microtubule depolymerization (Srayko et al. 2006).

Katanin is regulated via different proteins such as ASPM (Abnormal spindle-like microcephaly associated, Jiang et al. 2017) and WDR62 (WD40 repeat domain 62., Guerreiro et al. 2021, Huang et al 2021), both of which are most commonly mutated genes in primary microcephaly. ASPM is also a microtubule minus-end binding protein, which was reported to be important for spindle orientation during neurogenesis (Higgins et al. 2010). Additionally, ASPM was shown to be crucial for cytokinesis (Higgins et al. 2010) and to regulate the length of astral microtubules in HeLa (Gai et al. 2016). It was also shown that ASPM also functions as a spindle focusing factor during mitosis (Tungadi et al. 2017). ASPM is important for Katanin localization at the spindle poles. Together, they form an ASPM-Katanin

complex, which promotes the severing of microtubules (Jiang et al. 2017). Depletion of ASPM leads to the loss of Katanin at microtubule minus-ends, resulting in the decrease of poleward microtubule flux speed (Jiang et al. 2017). The microtubule poleward flux mechanisms, as well as chromosome segregation errors, will be described in the following chapters.

#### Microtubule Flux

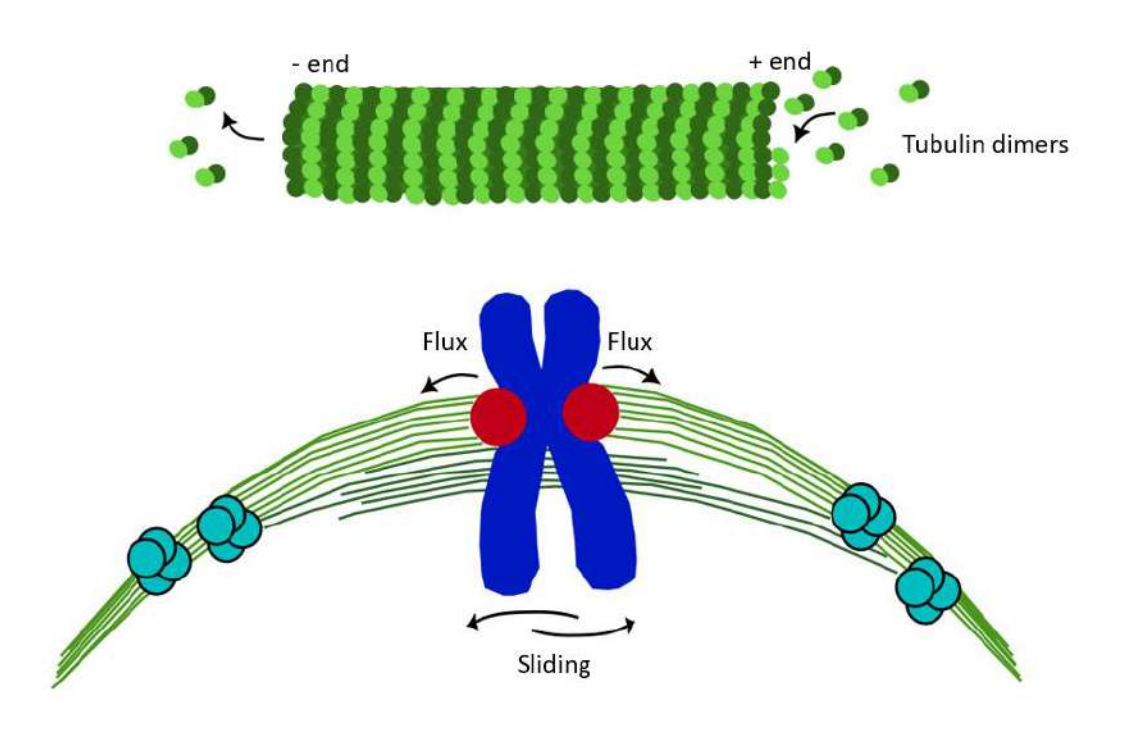


Figure 6: Poleward microtubule flux components

- (A) Polymerization of microtubule plus-end and depolymerization of microtubule minus-end
- (B) Crosslinking and sliding of the microtubules

Over the past decades, microtubules have been extensively studied due to their unique properties and implications in different diseases. Indeed, in every cell, tubulin has a very complex polymerization dynamic. In mammals, the half-life of tubulin in spindle microtubules is less than a minute (Gorbsky et al., 1990). These dynamics arise due to two phenomena: dynamic instability and microtubule poleward flux. Dynamic instability is an inherent property of every single microtubule, which regularly switches between shrinkage and growth states (Kirschner & Mitchison, 1984). On the other hand, poleward microtubule flux describes a property of spindle microtubules during mitosis and is characterized by the incorporation of tubulin dimers at the microtubule plus end, their conveyor belt-like fluxing through the microtubule, and their removal from the minus ends of the microtubule

(Mitchison, 1986). This phenomenon can be nicely visualized using photoactivable GFP tubulin cell lines (Samora & McAinch, 2011). If a stripe of tubulin on the mitotic spindle is activated through light, it will travel to the microtubule minus-ends until it is removed from the minus-ends. This phenomenon allows for the preservation of tension on the kinetochores and correct chromosome segregation during anaphase (Mitchison, 1986).

Microtubule flux is an ATP-driven process, which is dependent on three players:

- Plus-end microtubule-associated proteins that drive the polymerization
- Minus-end microtubule-associated proteins that are responsible for depolymerization
- Motor proteins and crosslinkers

Sliding of the crosslinked microtubules apart was shown to be crucial during mitosis (reviewed in McIntosh et al., 1969), especially for the regulation of mitotic spindle length. Before anaphase, several crosslinkers such as Eg5/Kinesin5 and kinesin-12/KIF15 were shown to be important for microtubule crosslinking. Eg5 (Kinesin 5) is a well-studied plus-end-directed protein which crosslinks antiparallel microtubules and slides them by pushing them apart. The accumulation of this protein at the antiparallel microtubules is length-dependent, and longer overlaps lead to a higher number of Eg5 (Shimamoto et al., 2015). Eg5 is important for the establishment of bipolarity during prometaphase (Whalley et al., 2015), however, it is dispensable for its maintenance (Kollu et al., 2009). Kif15 has a compensatory activity to Eg5, which maintains spindle bipolarity (Tannenbaum et al., 2009) and contributes to the outward force generation on the mitotic spindle. Other microtubules responsible for sliding are chromokinesin Kif4A, which binds microtubules and chromosomes and exerts pushing force on the chromosomes to help them congress on the metaphase plate (reviewed in Almeida & Maiato, 2018); and CenpE, which facilitates chromosome congression by promoting lateral kinetochore microtubule attachments (Shrestha et al., 2013). Another crosslinker of antiparallel microtubules is PRC1/Ase1, which similarly to Eg5 is length-dependent (Jagric et al., 2021). Kinesin-14 (HSET) is a minus-end-directed motor that, through microtubule crosslinking, allows efficient aster formation (Henkin et al., 2022). Finally, NuMa in complex with Dynein crosslinks microtubules for minus-end clustering and pole focusing (Hueschen et al., 2017).

Several plus-end-localizing proteins are important for promoting poleward microtubule flux through the polymerization of spindle microtubules. One of these proteins is TPX2, which in vitro was shown to stabilize early microtubule nucleation intermediates and promote microtubule growth (Zhang et al., 2017). TPX2 works synergistically with another important player at the plus-ends of the microtubules, chTOG. ChTOG was shown to promote microtubule growth at the spindle plus-ends (Roostalu et al., 2019), acting synergistically with TPX2, and counter-interacting the action of

XKCM1/MCAK depolymerizers. Additionally, as described above, another class of plus-end stabilizers at the plus-ends is CLASPs (CLIP-associating proteins).

At the minus-end, Kinesin-13 family proteins such as MCAK, which localizes at plus- and minus-ends, and Kif2a, which solely localizes at the minus-ends, are heavily implicated in depolymerizing activity (Wordeman, 2005). The mechanism of activity of Kinesin-13s has been investigated in vitro and showed that they bind to curved protofilaments and accelerate the rate of transition to a catastrophe state of the microtubule (Gardner et al., 2011). If the number of Kinesin-13 proteins is high enough, the catastrophe can be provoked without the addition of ATP; however, ATP increases the efficiency and makes it extremely catalytic (Wordeman, 2005). Another minus-end-binding depolymerizer is Kif18A, which is part of the Kinesin-8 family. This is a plus-end-directed protein, important for the regulation of kinetochore fiber length, responsible for its polymerization and depolymerization (Lin et al., 2018).

The spindle microtubules flux has different roles depending on the mitotic phase. It is driven by the activity of Eg5, Kif15, Kif4a, and CenpE on the antiparallel interpolar microtubules and is transmitted to the k-fibers through the crosslinkers NuMA and HSET (Steblyanko et al., 2020). The flux is further supported through the depolymerization activity of MCAK and Kif2A on the microtubule minus-ends and polymerization on the plus-ends by TPX2 and chTOG (reviewed in Borisic et al., 2021). In metaphase, microtubule poleward flux plays a role in chromosome alignment, correction of erroneous attachments, and centromere tension. Finally, in anaphase A, the poleward microtubule flux allows for microtubule shortening, which is 70% contributed from plus-end shortening (otherwise known as pacman) and 30% minus-end shortening (otherwise known as flux) (Barisic & Rajendraprasad, 2021). This is generated by the depolymerization of the minus-ends by Kif2A (Ganem et al., 2005; Rogers et al., 2004) and the plus-ends are proposed to be tension-dependently regulated by depolymerizing activity of MCAK (Steblyanko et al 2020). In Anaphase B, on the other hand, the most important role is played by the motors, sliding the bridging fibers. Microtubule plus-end-directed kinesin-6, -8, and -12 were shown to play an important role for sliding in Anaphase B (Brust-Mascher et al., 2011). These kinesins have been shown to be counterattracted by kinesin-4, its binding partner PRC1, and kinesin 5. In the absence of these three kinesins, chromosomes hyper-segregate, suggesting their role as a break during Anaphase B (reviewed in Barisic & Rajendraprasad, 2021).

Overall, in metaphase, three mechanisms seem to be important for the generation of poleward microtubule flux: antiparallel microtubule sliding and crosslinking, depolymerization from the minus end, and polymerization from the plus end (reviewed in Barisic & Rajendraprasad, 2021). However, the precise mechanism of flux regulation and to which extent these three mechanisms contribute

remains unknown. The first model of flux generation, postulated by Tim Mitchison in 1986 (Mitchison, 1986), which is based on the depolymerization of microtubule minus-ends with concomitant polymerization of microtubule plus-ends, has been challenged by studies showing the inability of astral microtubules to flux despite the depolymerization from the minus-end (Waterman-Storer et al 1998). In another study, the compression of mitotic spindles inhibited the activity of microtubule minus-end depolymerizers, during which the poleward flux was not affected (Dumont & Mitchison, 2009). A recent model has proposed the sliding of antiparallel microtubules by different motor proteins, described above, as the main force driving the microtubule flux. This flux is then transmitted to the k-fibers through the connection created by crosslinker proteins (Risteski et al., 2022). However, as it was shown previously and confirmed in our lab, disruption in solely microtubule minus-end depolymerization results in slower microtubule flux (Guerreiro et al., 2021). This result suggests that despite disproving the model of regulation of microtubule flux by minus-end depolymerization, the minus-end still plays some role in addition to the antiparallel microtubule sliding.

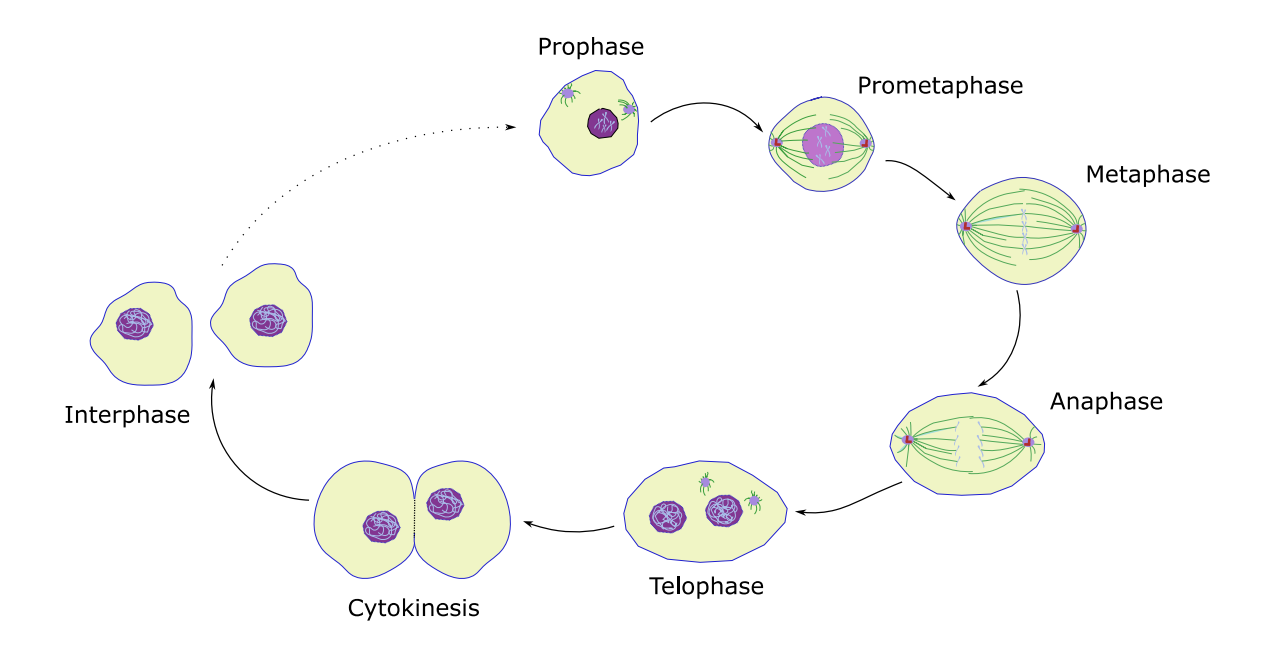


**Figure 7**: Mitotic stages

From left to right: cell enters mitosis in prophase, where DNA starts to condense and mitotic spindle starts to form. The nuclear envelope starts to break down. In prometaphase, mitotic spindle "searches and captures the chromosomes and aligns them at metaphase plate at metaphase. During anaphase, chromosomes are separated and during telophase new nuclear envelope is forming. Almost concomitantly, cell separates the cytoplasm in process of cytokinesis which leads to formation of two new cells.

#### **Prophase**

Prophase is the first step in mitosis, in which the cell condenses its chromosomes, the nuclear envelope breaks down, and the mitotic spindle machinery starts to form (reviewed in McIntosh, 2016). However, the preparation of DNA for mitosis starts long before mitosis itself. Indeed, already in S phase, DNA undergoes the process of chromatin cohesion alongside DNA replication (Rhodes et al., 2017). This process is mediated by four different proteins, which together assemble a Cohesin complex. Two of these proteins, Smc1 and Smc3, recruit Scc1 and Scc3 to form a ring structure that encloses the replicated chromosomes together (Wong, 2010). Once the cell is in prophase, sister chromatids begin to condense through the activity of a related family of chromosomal proteins, condensin I and condensin II (reviewed in McIntosh, 2016). These protein complexes are formed from a pair of Smc proteins (Smc2 and Smc4) and non-SMC regulatory subunit proteins (Hirano, 2006). The Condensin II complex starts to condense the DNA, which allows for more compact chromatin packaging, making the chromosomes visible in the light microscope (reviewed in McIntosh, 2016). In a parallel process to condensation, chromosomes undergo entanglement by the action of Topoisomerase II (Piskadlo & Oliveira, 2017). Through this process, cohesin is removed from the chromosome arms through the phosphorylation of Scc3 by Plk1 and histone H3 by the Aurora-B kinase. At the centromere, however, the chromosomes remain joined by the protective function of Shugosin (Marston, 2015).

During prophase, centrosomes are disjoined and transported to the opposite sides of the nucleus by the action of Eg5, dynein, and Kif15, with slight involvement of actin guiding the centrosomes to the opposite sides (reviewed in Kapoor, 2017). Around the same time as centrosome separate, the nuclear envelope starts to break down. Both of these events are achieved through the activation of CDK1. CDK1 phosphorylates Nek9, which allows its binding to PLK1. The phosphorylation activates Nek9 and drives its binding with Nek6 and Nek7 (Salaun et al., 2008). The complex then phosphorylates Eg5, allowing its recruitment to the centrosomes and the centrosome separation (Bertran et al., 2011). The complex activation cascade is important to synchronize the processes of nuclear envelope breakdown and centrosome separation.

Once the nuclear envelope is broken and chromosomes find themselves in the cytoplasm, PP2A is inhibited, and CDK1 starts to phosphorylate many targets important for subsequent steps (Álvarez-Fernández & Malumbres, 2014).

#### Spindle microtubule nucleation

The ultimate event of prophase is the start of mitotic spindle formation. To achieve the formation of the mitotic spindle, the cell needs to nucleate microtubules. This process requires the formation of tubulin oligomers, an energetically unfavorable structure. Higher eukaryotes use γTURC (γ-Tubulin Ring Complex), a complex that acts as a template for microtubule formation (reviewed in Valdez & Dumont, 2023). This cone-shaped complex is composed of γ-tubulin complex proteins 2–6, mitotic spindle organizing proteins 1 and 2 (MZT1 and MZT2), and actin, which together serve as a scaffold for microtubule formation (Chumova et al., 2021). This scaffold allows for the correct maintenance of 14 γ-tubulin subunits and serves as a template for microtubule building. Once nucleation starts, γTURC switches from an open 14-unit conformation to a 13-unit closed conformation (Brito et al., 2024). The process of microtubule nucleation by γTURC allows microtubules to overcome the kinetic barrier of microtubule nucleation (reviewed in Valdez & Dumont, 2023). Additionally, the ability of γTURC to nucleate microtubules allows the cell to nucleate microtubules at precise locations, thus controlling the nucleation sites. There are several microtubule nucleation sites in eukaryotic cells, with the largest pool of γTURC being located at the centrosome (Kuijpers et al., 2011).

At the onset of mitosis, the master regulator kinase CDK1 is activated by binding to Cyclin B (Ferrari, 2006), which in turn starts to phosphorylate different microtubule-associated proteins. Phosphorylation of MAP7 (Ensconsin), Stathmin, and MAP4 allows for the inhibition of their binding to the interphase microtubules, resulting in the disassembly of all interphase microtubules and increasing the pool of tubulin in the cytoplasm (Mchedlishvili et al., 2017). The availability of soluble tubulin allows γTURC to nucleate spindle microtubules (Mukherjee & Conduit, 2019).

The centrosomes expand their PCM (pericentriolar material) through the accumulation of various proteins, a process driven by Aurora A and PLK1 kinases (Cabral et al., 2019). Through the phosphorylation cascade driven by microtubule nucleation, effectors such as CEP192 and NEDD1, γTURC and chTOG (a protein that recruits tubulin subunits to γTURC) are localized at the centrosomes and give rise to microtubules (Gomez-Ferreria et al., 2012). Pericentrin, an important component of PCM, together with CDK5RAP2, anchors γTURC at the centrosome (Fong et al., 2008). Interestingly, despite the important role of centrosomes in nucleating microtubules, they are mostly dispensable for assembling the mitotic spindle (Basto et al., 2006).

Indeed, several other microtubule nucleation pathways exist. Microtubules can be nucleated from other microtubules by a process called branching microtubule nucleation (Alfaro-Aco et al., 2017). These are nucleated by yTURC at shallow angles alongside other microtubules (Alfaro-Aco et al., 2020).

An important facilitator of this process is a protein called Augmin, without which branching is reduced (Alfaro-Aco et al., 2020).

Another pathway of microtubule nucleation is kinetochore-driven nucleation, which was recently proven to be indispensable for bipolar spindle orientation and correct chromosome segregation (Wu et al., 2023). Nup-interactor ELYS and TPX2 localize yTURC to the kinetochore structure (Yokoyama et al., 2014). Finally, microtubules can be nucleated by another mechanism, which is centrosome-, microtubule-, or kinetochore-independent. This can be achieved by microtubule nucleation through the chromosome passenger complex (CPC) (Maresca et al., 2009). This complex is made of Aurora B kinase, INCENP (inner centromere protein), Borealin, and Survivin (Vader et al., 2006). Aurora B can phosphorylate microtubule depolymerizers in the vicinity of chromosomes, such as Stathmin or MCAK (KIF2C), which promotes microtubule formation and its capturing by kinetochores (reviewed in Barisic et al., 2021).

As the human cell enters mitosis, the majority of microtubules are nucleated first from centrosomes, but this is overtaken by microtubule branching nucleation once the bipolar spindle is established (reviewed in Barisic et al., 2021). Overall, all these pathways work synergistically to allow efficient microtubule nucleation and spindle structure and function maintenance.

#### Prometaphase

During prometaphase, a newly formed structure called the mitotic spindle has the important function of "searching and capturing" the chromosomes (reviewed in McIntoch, 2016). The model of this step was proposed by Kirschner and Mitchison in 1984, where it was hypothesized that mitotic spindle microtubules undergo periods of growth and shrinkage, and those which randomly connect to the kinetochore stabilize, while others depolymerize in the absence of a GTP cap. In this manner, one by one, all the kinetochores would be caught by microtubules and stabilized by tension in the event of correct attachment, while incorrect attachment would result in weak tension leading to detachment (Kirschner & Mitchison, 1984). However, this model was later deemed incomplete, as Wollman et al. described using Monte Carlo simulations that even the simplified search for a single target would take 23 minutes (average mitotic timing from nuclear envelope breakdown to anaphase onset in RPE cells), which is too long for an in-vivo cell (Wollman et al., 2005).

Indeed, other additional mechanisms seem to be in place to ensure the timely capture of the chromosomes by the mitotic spindle. As the chance of capturing the 200-nm kinetochore from a centrosome, which is positioned  $10-15~\mu m$  away, is low, a mechanism nucleating microtubules

outside the centrosomes must exist. The master regulator of non-centrosomal microtubule nucleation during mitosis is the RanGTP gradient, which ensures the capturing of chromosomes (Carazo-Salas et al., 2001). Briefly, Ran is a member of the Ras superfamily of small GTPases, which switch between GDP- and GTP-bound conformations. Ran interacts with the GTPase-activating factor of Ran (RanGAP) in the cytoplasm, which allows for the conversion of GTP to GDP. Close to the chromosome, RCC1 (Regulator of Chromosome Condensation 1), which localizes ubiquitously on the chromatin, drives the opposite conversion from Ran GDP to Ran GTP (Clarke & Zhang, 2008). Once in the GTP state, Ran binds to Importins, which release their inhibitory binding of several spindle assembly proteins around chromosomes, such as TPX2 (Grus & Vernos, 2004), Augmin (Kraus et al., 2023), and HURP (unpublished data of the lab), allowing for microtubule nucleation from pre-existing microtubules as well as from kinetochores. Recent work in Xenopus on TPX2 suggests that it undergoes phase separation and forms condensates with tubulin preferentially on the pre-existing microtubules (King & Petry, 2020), allowing for branching microtubule nucleation. Further, to form branching microtubules, TPX2 requires the presence of Augmin (Kraus et al., 2023), another RanGTP gradientmediated protein. Augmin itself is required for non-centrosomal microtubule nucleation (Goshima et al., 2008). The Augmin complex, composed of 8 HAUS (Homologous to Augmin Subunits) proteins, increases the density of the microtubule network, which is important for capturing kinetochores (Petry et al., 2013). Out of the 8 HAUS subunits of Augmin, Haus6 binds to microtubules, while others bind to the yTURC complex and recruit it to induce branching microtubule formation via NEDD1 (Zhu et al., 2008). Also, recent results from the lab have demonstrated that HURP (Hepatoma 23 Upregulated Protein), found in the vicinity of the chromosomes where it was known to stabilize kfibers, also binds and stabilizes branching microtubules (unpublished data).

In addition to the RanGTP gradient, microtubule nucleation at kinetochores depends on the activity of Pericentrin (Wu et al., 2023) and the Chromosome Passenger Complex (CPC). Indeed, in prometaphase, the CPC, which is made up of Inner Centromere Protein (INCENP), Survivin, Borealin, and Aurora B, localizes at the kinetochore and downregulates the activity of Mitotic Centromere-Associated Kinesin (MCAK or Kif2C) through inhibitory phosphorylation by Aurora B (Carmena et al., 2012). Different cellular pathways are important for microtubule nucleation in the vicinity of chromosomes, helping the chromosomes to be captured by microtubules.

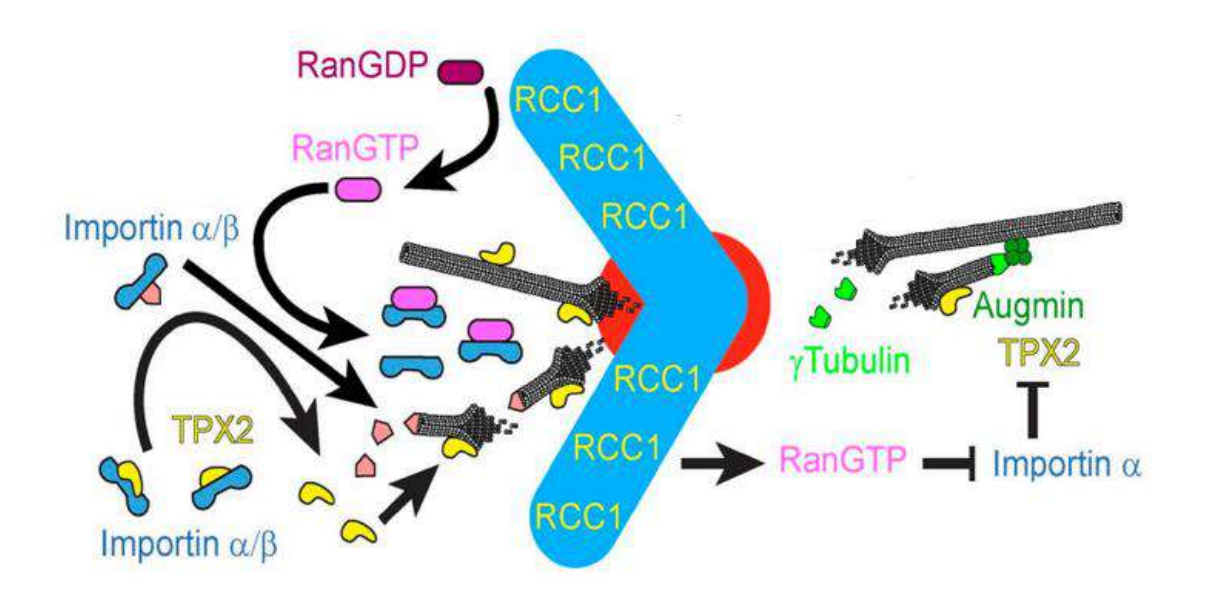


Figure 8: Mechanisms of RanGTP gradient for microtubule nucleation

RCC1 which is localizing at the chromosomes allows to increase the concentration of RanGTP in the vicinity of chromosomes. RanGTP gradient at the chromosomes allows microtubule polymerization by binding Importin from Importin – TPX2 complex and liberating TPX2. TPX2 allows for microtubule nucleation at kinetochore and from another microtubule through Augmin.

Adopted from Heald&Khodjakov et al 2015

#### Metaphase

Once the microtubules are nucleated, the process of kinetochore capturing begins. In this process, called chromosome alignment, chromosomes are brought to the middle of the cell (the metaphase plate) prior to chromosome segregation. In the next chapters, I will elaborate on the mechanisms of this process.

#### Generation of force by microtubules for chromosome alignment and biorientation

Microtubules can exert different types of forces on the organelles or other structures inside the cell. In the case of mitosis, these forces are needed to achieve precise chromosome segregation during anaphase. Once captured and attached to the microtubules, chromosomes need to move towards the cell equator (lemura et al., 2015). However, the starting position of the chromosomes will not be the same, as the location of different chromosomes inside the interphase nucleus is also not the same. The main chromosome mass is located in a central part in the vicinity of the spindle and can therefore

be directly bound by microtubules in a bi-directional fashion or transported to the cell equator, where they will be bound to the mitotic spindle. But part of the chromosomes will be on the periphery of the spindle, and they will be transported towards the equatorial plane of the cell (Risteski et al., 2021).

To align all the chromosomes on one plane prior to segregation, pulling and pushing forces must be exerted on them. Microtubules can exert a pushing force when the plus end is growing and new tubulin dimers are added. In reverse, the pulling force is exerted by the microtubule depolymerization at the minus end, putting it under tension (Valdez & Dumont, 2023). As for the microtubule sliding, this movement is powered by microtubule motors and can be pushing or pulling depending on the direction of the movement (Tolic-Nørrelykke, 2008).

Sliding movement can be excerted by plus-end directed motor CenpE which slides the chromosome by using another k-fiber as a walking substrate in order to congress them (Shaar et al., 1997; Craske, 2020). The poleward pulling force is exerted by dynein, which binds to kinetochores and brings them to the spindle pole, increasing their chance of being captured by the microtubule. This process is required for efficient chromosome congression too (Li et al., 2007). Depletion of dynein or its adapter proteins ZW10 and Spindly was found to be responsible for the misalignment of around 20% of chromosomes during chromosome congression (Li et al., 2007). After all the peripheral polar chromosomes reach the vicinity of the mitotic spindle, they are transported by chromokinesins Kid and Kif4a, which create a pushing force along the chromosome arms and away from the spindle poles (Almeida & Maiato, 2018). Additionally, mechanisms like spindle elongation and microtubule pivoting contribute to the reincorporation of the polar chromosomes into the mitotic spindle. Indeed, microtubules attached to the chromosomes, which find themselves on the periphery of the spindle, can pivot around the spindle pole and bring the chromosome into contact with the spindle surface (Koprivec et al 2024).

During metaphase, spindle length is kept constant also by the balance of pushing (in yeast - kinesin-5) and pulling forces (in yeast - kinesin-8) (Syrovatkina et al., 2013). When the spindle needs to elongate, like in Anaphase B, the pushing force from the central spindle prevails, and spindle poles are pushed apart (Sholey et al., 2016).

#### *Kinetochore microtubule attachments*

At the beginning of mitosis, none of the chromosomes are bound to the microtubules. The initial interaction between chromosomes and microtubules occurs in the majority of cases laterally, a process called "lateral attachment" (Shrestha & Draviam, 2013). In order to generate lateral

kinetochore-microtubule attachments, the kinetochore forms a structure called the "fibrous corona," containing proteins such as Dynein, Cenp-E, Cenp-F, and the Rod–ZW10–Zwilch (RZZ) complex (Kops & Gassmann, 2020). These proteins form a crescent-like shape around the kinetochore, creating a platform for microtubule capture. Over time, microtubule attachment to the fibrous corona of the kinetochore is gradually replaced by end-on attachment, and by the beginning of metaphase, all chromosomes are attached in an end-on fashion (Huitorel et al., 1988).

The process of lateral attachment and, later, end-on attachment depends on the kinetochore linking the centromere on the chromosome to the spindle microtubule (Cheeseman, 2014). The KMN network is a highly conserved central regulator of kinetochore-microtubule attachments and is composed of KNL1, Mis12, and NDC80 complexes (Cheeseman et al., 2006). The NDC80 complex, in turn, is composed of NDC80, Nuf2, Spc24, and Spc25 (Nilsson et al., 2012). These proteins form heterodimers in a two-by-two fashion, creating globular domains on each side (kinetochore and microtubule) and are connected through interactions of their coiled-coil shafts, forming a heterotetrameric rod structure (Valverde et al., 2016). The KMN network is highly regulated through different phases of cell division to prevent stable end-on attachments from forming too early (Varma & Salmon, 2012). During early mitosis, the KMN network is inhibited by the RZZ complex, as at this stage, incorrect kinetochore-microtubule attachments are more common (Barbosa et al., 2022). RZZ activity peaks at prometaphase and decreases at metaphase (Barbosa et al., 2022). The interaction between Dynein and RZZ is responsible for the removal of the RZZ complex from the kinetochore at metaphase, allowing the NDC80 complex to stabilize kinetochore-microtubule end-on attachments (Amin et al., 2018).

Additionally, phosphorylation of NDC80 by Aurora kinases is known to negatively regulate its binding affinity to the microtubules. Important for the correction of erroneous kinetochore-microtubule attachments, Aurora A phosphorylation of NDC80 at spindle poles is highest in prometaphase and decreases at metaphase. A small kinetochore protein, Bod-1 (Biorientation defective 1), was recently found to counteract premature dephosphorylation activity of PP2A on NDC80 (Schleicher et al., 2017). In metaphase, dephosphorylation of NDC80 by PP2A allows for the formation of stable kinetochore-microtubule attachments (Cheerambathur et al., 2017). Another phosphatase, PP1, directly interacts with KNL1, counteracting the activity of Aurora B kinase at the kinetochore (Liu et al., 2010).

Indeed, Aurora B is a master regulator of kinetochore-microtubule attachments, which localizes at the inner centromere, which is the intersection between the inter-sister chromatid and inter-kinetochore regions. It regulates the activity of different substrates, such as KMN network proteins Hec1 and MCAK

(kinesin-13), through their phosphorylation (DeLuca et al., 2018). High microtubule turnover, through the activity of Aurora B, helps resolve potentially erroneous attachments (Cimini et al., 2006).

#### Erroneous kinetochore microtubule attachments and their correction

But how do cells differentiate erroneous attachments from the correct ones? It has been proposed that an important feature of correct bi-orientation, compared to erroneous attachments, is the tension between sister kinetochores (Zhang et al., 2013). Indeed, if both kinetochores are bi-oriented, the tension of the linkage between the two sister kinetochores is higher compared to monotelic or syntelic attachments (Pennings, 2014). Whether Aurora B itself can sense the tension remains unclear. A so-called "spatial positioning model" proposes that the tension moves the chromosomes away from the Aurora B phosphorylation gradient, emanating from the inner centromere (Meadows et al., 2013). Once the kinetochores are attached to the microtubules, the tension pulls the kinetochore away from the inner centromere and prevents phosphorylation of the NDC80 complex by Aurora B. According to some studies, this region has been estimated to be around 80 nm (Krenn & Mussachio, 2015). However, other studies have found that a strong decrease in inter-kinetochore distances does not lead to spindle assembly checkpoint induction or microtubule detachment through Aurora B-dependent phosphorylation (Dudka et al., 2018).

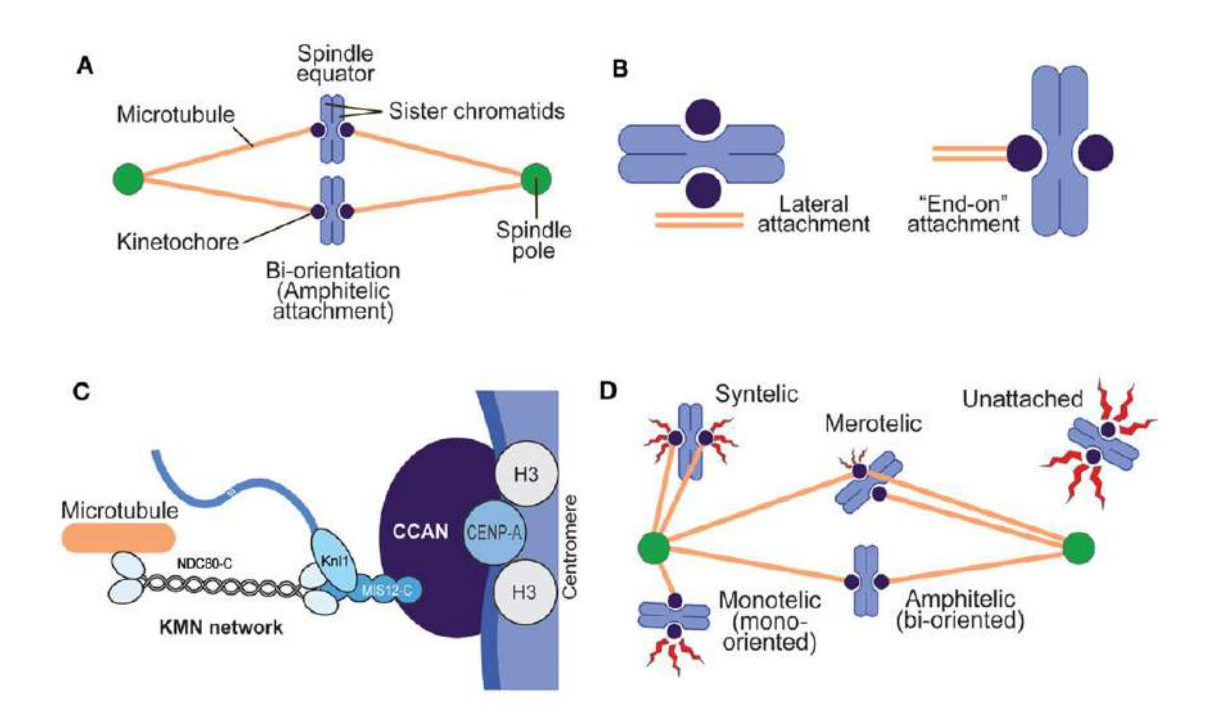


Figure 9: Mechanisms of kinetochore-microtubule attachments

- (A) Kinetochores are bound by microtubules emanating form spindle poles. The correct biorientation or amphitelic attachment is each kinetochore bound by one microtubule from the same pole.
- (B) Two main attachment types at mitotic spindle: "lateral" and "end-on" attachments. Lateral attachment to the microtubule lattice occurs in early stage of chromosome congression. These attachments are then converted into "end-on" attachments which are typical for the final stages of attachment.
- (C) Kinetochore microtubule attachment. The histone variant CENP-A is bound to CCAN subunits of inner kinetochore. KMN network constituted of MIS12, KNL1 and NDC80 binds to microtubule.
- (D) Correct (amphitelic) and erroneous kinetochore microtubule attachments. Kinetochore is attached monotelically when it is bound only from one side by a microtubule. Synthelically attached kinetochores are attached on two kinetochores by microtubules emanating from the same pole and are blocked polarly. Merotelically attached kinetochores are at the metaphase plate, but bound by microtubules emanating from the same pole.

Adapted from Krenn&Mussacchio 2015

#### Spindle assembly checkpoint

Chromosome segregation is an event requiring utmost precision to segregate the genetic material equally into two daughter cells. To do so, a cell may require time to correct erroneous kinetochoremicrotubule attachment and to establish bi-orientation of chromosomes (Lampson & Grishchuk 2017). In order to give the cell time to correctly attach its chromosomes, the Spindle Assembly Checkpoint (SAC) has evolved. SAC translates the mechanical state of the cell (MT-KT attachments) into biochemical signals. It is activated by default at the beginning of every mitosis with the main purpose of preventing the ubiquitination of anaphase inhibitors by the APC/C ubiquitin ligase, the event which is required for anaphase initiation (see Anaphase, Lara-Gonzales et al. 2021). SAC is composed of budding uninhibited by benomyl (BUB) proteins, a Ser/Thr kinase monopolar spindle protein 1 (MPS1), and the non-kinase components mitotic arrest deficient proteins MAD1 and MAD2 (reviewed in Musacchio & Salmon 2007). In the event of chromosome misalignment, MPS1 binds to the NDC80 complex on the unattached kinetochore and, at the same time, phosphorylates Knl1 (Hiruma et al. 2015). Once phosphorylated, Knl1 recruits the Bub1-Bub3 complex, which facilitates MPS1 mediated phosphorylation events, allowing the recruitment of the Mad1-Mad2 complex (Mora-Santos et al. 2016). The phosphorylation of Mad1 by Mps1 leads to inhibition of CDC20, a co-factor of APC/C, by forming an inhibitory complex (consisting of CDC20, MAD2, BUBR1/Mad3, and BUB3), otherwise known as the MCC (mitotic checkpoint complex) (Sudakin et al. 2001). The inhibitory complex prevents the recognition of the D-box motif (destruction box motif) on CDC20, which, under normal circumstances, targets the protein for degradation (Eitan et al. 2006). Incorporation of Cdc20 inside the MCC stabilizes Securin and Cyclin B, which prevents premature chromosome segregation (Kim et al. 2011). The kinetochore therefore plays a crucial role in SAC activity in human cells, as the

kinetochore-independent pool of MCC is small and cannot delay chromosome segregation sufficiently in the case of perturbation (Meraldi et al. 2004).

#### Aurora B relocalization to central spindle during anaphase

An important event at anaphase onset is the re-localization of Aurora B from the centromere to the central spindle. Once all the chromosomes are correctly aligned, Aurora B needs to be quickly removed since its presence on the centromere indicates erroneous attachment (Krenn & Mussacchio 2015).

An AAA+ATPase, Cdc48/p97, is an important ubiquitin-dependent chaperone that regulates this process in mitosis, as well as others in mitosis and interphase (Meyer & Popp 2008). Binding through its N-terminal region to different substrates, this complex uses ATP hydrolysis to induce conformational changes (Meyer & Popp 2008). The majority of the substrates of p97 are ubiquitinated during ER-associated degradation, chromatin-associated degradation, or ribosome-associated degradation (Stach et al. 2017). For these actions, Cdc48/p97 associates with different adaptor proteins, which are hypothesized to be specific for each ubiquitination process (Stach et al. 2017). To translocate Aurora B from centromeres to the central spindle, Cdc48/p97 associates with the heterodimer Ufd1-Npl4 (Dobrynin et al. 2011). For this process, Aurora B is first ubiquitinated by the CUL3/KLHL9/KLH13 complex (Sumara et al. 2007). The Cdc48/p97 complex with Ufd1 and Npl4 recognizes ubiquitinated Aurora B and physically extracts it from the centromeres (Dobrynin et al. 2011). The localization of Aurora B at the central spindle requires the action of the UBA-containing protein UBASH3B, which can bind to both Aurora B and MKLP-2, the latter kinesin driving the physical translocation of Aurora B (Krupina et al. 2016).

The re-localization of Aurora B to the central spindle prior to anaphase is important in several ways. First of all, Aurora B determines the positioning of the future cleavage furrow (Goto et al. 2003). Additionally, Aurora B creates a phosphorylation gradient with the highest concentration at the central spindle, dissipating in the direction of the spindle poles. This gradient is also a sensor for chromosome separation during anaphase (Afonso et al. 2014), which is discussed in the following chapters.

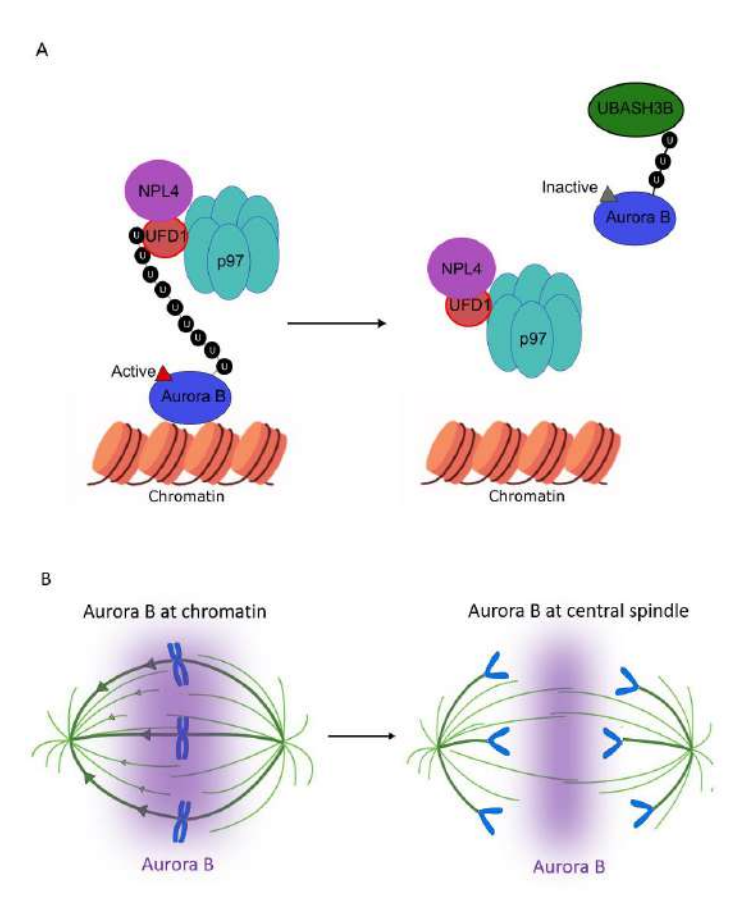


Figure 10: Aurora B re-localization from chromosomes to central spindle

- (A) Aurora B is re-localized to the central spindle at the anaphase onset by the action of CDC48/p97-UFD1-NPL4 complex. This complex extracts the whole chromosome passenger complex including Aurora B from the chromatin. The inactive Aurora B is then transported to the central spindle by the action of UBASH3B.
- (B) Two Aurora B states: at chromatin during metaphase and at central spindle during the anaphase.

Spindle images adopted from E.Doria

#### Anaphase

Once all the chromosomes are correctly attached, the spindle assembly checkpoint must be silenced rapidly to avoid abnormal mitotic timing, which can lead to cell death or cell arrest in the following G1 (Brito & Rieder 2006; Y. Uetake & Sluder 2010). This process is called "stripping" and requires the activity of the minus-end directed motor dynein, which is recruited to the kinetochore by the RZZ-Spindly complex (Wang et al. 2014). Dynein transports Mad1-Mad2, Spindly, and the RZZ complex towards the spindle poles, where they are likely disassembled (Silva et al. 2014). As Mad2 and BubR1 are responsible for silencing the APC/C-CDC20 complex, in their absence, the complex is activated (Ge

et al. 2009). The APC/C-CDC20 complex, in turn, ubiquitinates Securin, an inhibitor of Separase (Li et al. 2007). Activated Separase is able to cleave the cohesion complex, holding together the sister chromatids. Additionally, APC/C-CDC20 ubiquitylates Cyclin B by targeting its D-box motif (Yamano et al. 2004), which is necessary to downregulate CDK1 activity and to allow the chromosome segregation.

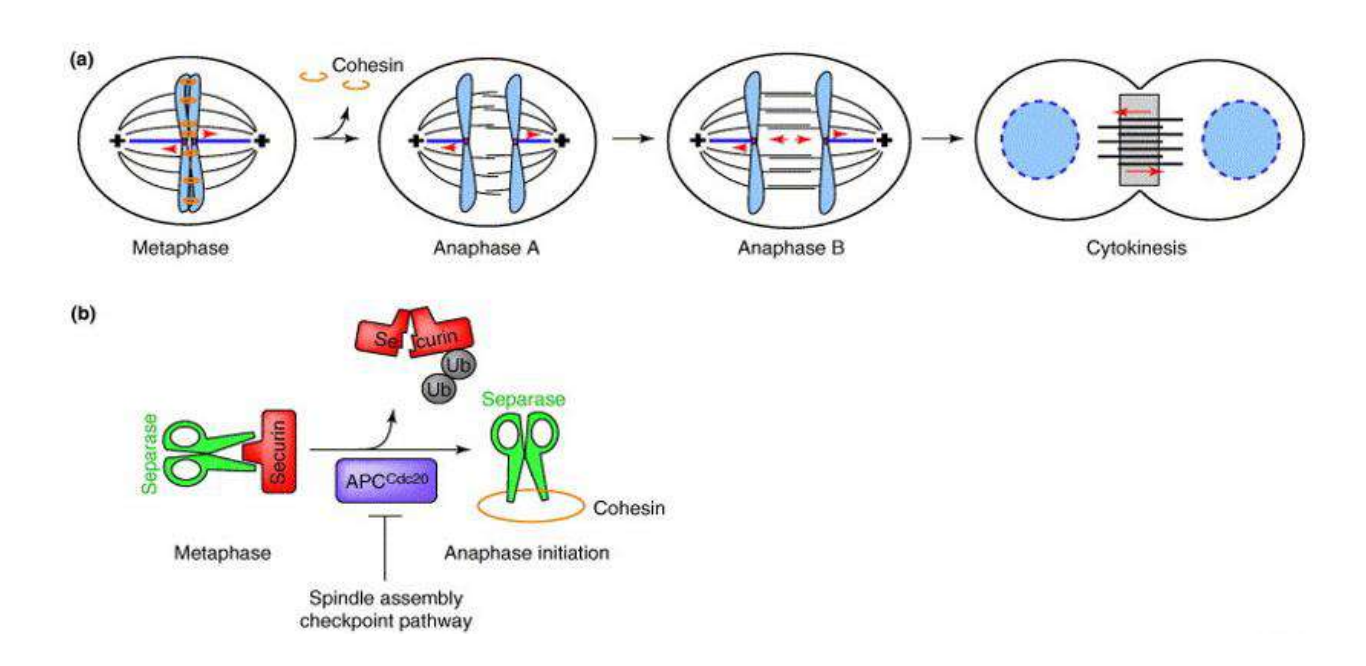


Figure 11: Metaphase to anaphase progression

- (A) During the metaphase to anaphase transition, cohesin removal from the chromosomes allows for their separation during anaphase. During Anaphase B, chromosomes are primarily pulled by microtubule depolymerization and during anaphase B, they are additionally separated through sliding of antiparallel microtubules.
- (B) At the anaphase onset, APC/C Cdc20 targets securin for degradation. This allows separase to cleave cohesin, allowing for anaphase initiation.

Adopted from Gramont&Cohen-Fix 2005

#### Anaphase A and B

After separation of the sister chromatids, chromosomes start moving apart in two distinct steps: Anaphase A and Anaphase B. These two phases happen one after the other in some organisms (Fitzharris et al., 2012), while in others, these two steps occur simultaneously (Pearson et al., 2001).

In Anaphase A, the chromosomes move toward the spindle poles. This is achieved through the poleward microtubule flux at the minus-ends of the microtubules and Pacman depolymerization of the plus-ends (Mitchison et al., 1986; Cassimeris et al., 1987). Indeed, during this movement, the

chromosomes are carried towards the spindle poles by microtubules. It has been shown early on that the severing of the k-fiber stops the chromosome movement during anaphase, while ablation of the chromosome arm does not affect the poleward chromosome movement (McNeill and Berns, 1981; Uretz et al., 1954). This process is proposed to be powered by CENP-E, which in vitro was found to be important for depolymerization-dependent chromosome movements (Lombillo et al., 1995). At the plus-end, Kif18A affects the velocity of kinetochores through reduction of plus-end dynamics. At the minus-end, depletion of severing enzymes, such as fidgetin (Mukherjee et al., 2012) and katanin (Guerreiro et al., 2021), was shown to decrease poleward flux speed. Indeed, in human cells during Anaphase A, microtubule plus-end depolymerization is important for 80% of chromosome movement, while poleward flux at the minus-ends is important for around 20% of chromosome movement (Ganem et al., 2005).

During Anaphase B, the spindle poles start to elongate from each other. In different organisms, this process seems to be regulated differently. In *S. Cerevisiae*, this process requires the pulling forces emanating from astral microtubules (Palmer et al., 1992), through either motor protein-induced pulling of astral microtubules by dynein or depolymerization of astral microtubules (Pavin & Tolić-Nørrelykke, 2013). In human cells, this process requires the sliding of antiparallel microtubules in the spindle midzone, which seems to require a change in overlap length throughout the anaphase. Indeed, some studies have shown that overlap length decreases during the anaphase-telophase transition in long-nosed potoroo epithelial kidney cells (PtK1) (Mastronarde et al., 1993). Other studies, however, have demonstrated that tubulin subunits are added at the plus-end of antiparallel interpolar microtubules during late anaphase (Saxon & McIntoch, 1987).

The spindle pole elongation during Anaphase B is governed by the protein regulator of cytokinesis 1 (PRC1), which is important for antiparallel microtubule crosslinking and stability. PRC1 acts as a negative regulator of spindle elongation and prevents overelongation of the spindle poles (Pamula et al., 2019). Similarly, Kif4A is also required for the termination of spindle elongation, and in its absence, the spindle elongates abnormally (Hu et al., 2011).

Once all chromosomes are separated, the cell can continue with telophase and cytokinesis.

#### Errors during anaphase and chromosome segregation

In order to maintain genomic stability, cells must guarantee the correct transmission of DNA into the daughter cells. However, this process is not completely error-free. Indeed, despite the laborious process of chromosome alignment and checkpoint control, around 1% of all chromosomes are mis-

segregated during anaphase (Santaguida & Amon, 2015). Different types of errors exist. These include chromosome bridges, where chromatin stretch is tethered between the two segregating DNA masses, and lagging chromosomes (Jiang et al., 2024) or laggards, a part or whole chromosome which remains at the equatorial plate throughout anaphase (Bizard & Hickson, 2018). Laggards can lead to aneuploidy, which is defined as the loss or gain of part or whole chromosomes (Bizard & Hickson, 2018). Aneuploidy is at the heart of tumorigenesis and other diseases, and in order for the cell to maintain genome integrity, it needs to be repaired (Passerini & Storchová, 2016).

The majority of mis-attached chromosomes are repaired before anaphase by the repair mechanism, which is under the control of the spindle assembly checkpoint, as described previously. SAC controls the kinetochore microtubule attachments and is not satisfied until all kinetochores are correctly attached (Musacchio, 2015). However, one type of attachment is not sensed by the SAC, which allows it to escape the surveillance and lets the cell progress into anaphase. The merotelically attached chromosomes are attached from the same spindle pole by two microtubules, which, from the point of view of tension, allows it to satisfy the spindle assembly checkpoint (Nezi & Musacchio, 2009). If the cell progresses into anaphase with this type of attachment, it will move slowly apart, "lagging" behind the main nuclear mass (Gregan et al., 2011). These chromosomes are at high risk of being excluded from the main nuclear mass at the nuclear envelope reformation and becoming a micronucleus (reviewed in Cimini, 2023). A micronucleus is a small nucleus separated from the cytoplasm by the nuclear envelope. Micronuclei are known to be a hub for DNA mutations resulting from DNA replication errors and extensive genomic rearrangements through the action of topoisomerases. This process is known as chromothripsis, leading to the loss of genetic information, a process that was found in a variety of cancers (Jones & Jallepalli, 2012).

Lagging chromosomes can also be transient. Indeed, a previous study in the lab has shown that in the depletion of WDR62, transient lagging chromosomes can be found during anaphase. These are the chromosomes that are lagging behind at one point during anaphase but are incorporated back into the main nucleus before the end of anaphase. These lagging chromosomes, compared to persistent lagging chromosomes, do not lead to micronuclei formation (Guerreiro et al., 2021).

#### Lagging chromosome correction

Lagging chromosomes are an event that is more common than previously thought (Orr et al., 2021; Sen et al., 2021). Indeed, in the study, Orr et al. found around 10% of lagging chromosomes in RPE-1 cells, and Sen et al. estimated around 30% of lazy kinetochores in RPE-1 cells. Orr et al. have shown

that out of 10% of lagging chromosomes, only 6% have displayed micronuclei after mitosis. Additionally, the overall rate of chromosome mis-segregation was estimated by Santaguida & Amon, 2015, at around 1% in human non-transformed cells (Santaguida & Amon, 2015). Therefore, a correction mechanism must exist to surveil lagging chromosomes and prevent their mis-segregation. Cimini et al. was one of the first studies to propose the existence of anaphase correction mechanism based on the observation that in anaphase B, merotelically attached chromosomes end up in the correct cell, and the ones which do not usually have similar pulling forces exerted from both spindle poles (Cimini et al., 2003, 2004). By preventing interpolar MT sliding, Orr et al. have demonstrated an increase in the rate of lagging chromosomes, leading to the understanding that anaphase spindle elongation is crucial for lagging chromosome correction (Orr et al., 2021). Additionally, this study has shown that it is Aurora B, which at the central spindle, seems to be important for lagging chromosome correction. Indeed, inhibition of the midzone-based Aurora B phosphorylation gradient leads to an increase in lagging chromosomes and a 3-fold increase in micronucleus formation (Orr et al., 2021).

Despite some body of evidence demonstrating the involvement of Aurora B in the anaphase correction mechanism, the precise mechanism still remains under debate. Indeed, Aurora B is known to be involved in the major error correction mechanism in pre-anaphase cells, where it localizes at the kinetochore to destabilize erroneous kinetochore-microtubule attachments which do not demonstrate strong enough tension (Lampson & Grishchuk, 2017). In anaphase, some authors propose a similar mechanism, which relies on destabilization of kinetochore-microtubule attachments. Sen et al. demonstrated by imaging of phospho-specific KNL1 p-Serine24 antibody, an established marker for Aurora B-dependent destabilization of kinetochore-microtubule attachments (Welburn et al., 2010; Sen et al., 2021), that lazy kinetochores had a higher fluorescent signal of pKNL1 compared to timely segregated ones. Authors propose that severely lazy kinetochores, the ones with the balanced attachment from the two spindle poles, are destabilized. If the attachment is unbalanced, the microtubule from the correct spindle side will pull the kinetochore stronger, resulting in the incorrect attachment side being closer to the Aurora B gradient, destabilizing it. However, this model has been challenged by several other studies. For instance, some authors have found no detachment of merotelicly attached kinetochore microtubules during anaphase (Cimini et al., 2004). Also, kinetochore-microtubules have a lower turnover rate in anaphase which can potentially prevent the microtubule destabilization (Gorbsky & Borisy, 1989). Some authors have proposed an alternative mechanism, in which Aurora B is important for stabilization of kinetochore-microtubule attachments during anaphase. Indeed, Aurora B was shown to phosphorylate different kinetochore proteins and by this promote the kinetochore-microtubule attachments. Plk1 phosphorylation at Thr210, previously shown in metaphase (Paschal et al 2012), was also found in anaphase. Additionally, another

two pre-anaphase microtubule stabilization markers, phosphorylation of Astrin and Dam1, were also shown to be phosphorylated by anaphase Aurora B gradient in yeast (Keating et al., 2009). In addition to microtubule phosphorylation, Aurora B gradient in anaphase has been demonstrated to phosphorylate chromosomes. Indeed, Papini et al. have shown that H3.3 Ser10 phosphorylation on anaphase chromosomes reduces with anaphase progression and that lagging chromosomes display stronger H3.3 Ser10 localization compared to non-lagging chromosomes in HeLa cells (Papini et al., 2021).

But why would the Aurora B gradient control chromosome separation? In the process of nuclear envelope reformation, Aurora B has an inhibitory effect on the nuclear envelope assembly factors (Warecki et al., 2018). Indeed, since the assembly of the nuclear envelope is a gradual process starting with chromosomes located at the spindle poles, phosphorylation by the Aurora B gradient and persistence of chromosomes in its vicinity provides more time for correct segregation of the chromosomes (Afonso et al., 2014). This process is crucial to allow the chromosomes to segregate into a correct daughter nucleus and prevent formation of micronuclei, as they are a common site for chromothripsis and DNA damage (Jones & Jallepalli, 2012). Micronuclei, in turn, can activate the p53dependent signaling pathway resulting in the reduction of cell proliferation (Fonseca et al., 2019). Also, Hervé et al. have shown that mis-segregation of chromosomes leads to nuclear envelope deformation, activating the p21/p53-dependent mechanosensitive checkpoint (Hervé et al., 2025). Therefore, it seems like cells need to avoid chromosome mis-segregation at all costs. Indeed, even lagging chromosomes on their own have been proposed to activate p53. As described in Hinchcliffe et al., lagging or misaligned chromosomes acquire H3.3 Ser31 phosphorylation, which in the interphase nucleus leads to p53 activation (Hinchcliffe et al., 2016). Despite the absence of a direct link with the Aurora B gradient in this paper, one can hypothesize its involvement in this process. Indeed, it is possible that Aurora B phosphorylation works as a sort of an analog transmitter, marking the potentially lazy kinetochores.

#### Telophase and cytokinesis

Once chromosomes are separated to two opposite sides at a specific distance from each other (around 8 µm in Drosophila, Afonso et al., 2014), the cell enters telophase. This is a stage in which DNA is decondensed and the nuclear envelope reforms around the DNA, making two nuclei in the two daughter cells (Ashraf et al., 1980). Prior to the telophase, Repo-Man targets PP1 phosphatase to chromosomes by forming a complex. The PP1-Repo-Man complex dephosphorylates the mitotic marks of histone H3: Thr3, Ser10, and Ser28 (Qian et al., 2011), allowing mitotic exit. Another

phosphatase PP2A also seems important for mitotic exit, as the depletion of PP2A leads to its delay (Schmitz et al., 2010). Additionally, throughout anaphase and prior to telophase, cells degrade B-Cyclins, as their absence is crucial for the anaphase-to-telophase transition (Sigrist et al., 1995). For nuclear envelope reformation in telophase, the downregulation of CDK1 is important, as CDK1 phosphorylates Lamin B and prevents premature nuclear reformation (Tseng & Chen, 2011). Moreover, the anaphase-to-telophase transition is controlled by the Aurora B gradient at the central spindle, as described in the previous chapter. In yeast, the Aurora ortholog IpI1 is also important for restricting the decondensation of chromosomes to telophase (Vas & Clarke, 2008).

Almost concomitant with chromosome decondensation and nuclear envelope reformation, the cell begins cytokinesis. Cytokinesis is the process of partitioning the cell content into the two daughter cells (Glotzer, 1997). In order to achieve that, the central region of the anaphase spindle starts to form the midbody, an actomyosin ring. Formation of the actomyosin ring is directed by the mitotic spindle through centralspindlin, which binds to Ecl2, activating active Ras homolog family member A (RhoA) and forming an equatorial RhoA zone (reviewed in Green et al., 2011). Active RhoA recruits formins, which nucleate actin, and citron kinase, which promotes Myosin II activation (Piekny et al., 2005). Additionally, septin filaments are recruited to the actomyosin ring (Eggert et al., 2006). All of these filaments are bound by the filament-crosslinker Anillin (D'Avino, 2009; Piekny & Maddox, 2010) and form an actomyosin ring complex. The actomyosin ring constriction mechanism still remains not fully understood. Some models propose that constriction is executed through the sliding of myosindependent filaments, while others show that actin treadmilling is the driving force for this process (reviewed in Green et al., 2012). Once the ring is formed, the cell is split into two in the process of cell abscission. The constriction of the actomyosin ring leads to the formation of the midbody from the central spindle. As the midbody matures, the contractile ring becomes the midbody ring as many contractile ring proteins, such as Anillin, septins, citron kinase, and RhoA, are retained there (reviewed in Green et al., 2012). Additionally, some central spindle proteins also accumulate there, creating a densely packed region. Some of these proteins were shown to be important for the midbody abscission regulation (Singh & Westermark, 2011; Dionne et al., 2015), while others are hypothesized to localize there as a strategy for elimination from the cell (Addi et al., 2020). Midbody abscission is regulated by ESCRT-I and ESCRT-III complex proteins (Henne et al., 2011), which are sequentially recruited to the intercellular bridge. At the same time, the dodecameric ring-shaped AAA+ ATPase B VPS4, a co-factor of ESCRT-III, colocalizes to the abscission side (Elia et al., 2011). Together, they create a filamentous structure from both sides of the midbody, allowing it to progressively decrease its diameter through regularly spaced electron-dense ripples in the plasma membrane (Mullins & Biesele, 1977). Finally, microtubules of the mitotic spindle are disassembled through the action of Spastin

(Vietri, 2015). At the end of cytokinesis, there are two daughter cells, one still containing a midbody, which can be abscised following cytokinesis or remain as a part of the cell.

#### Asymmetric cell division

#### Drosophila Neuroblasts

Asymmetric cell division is a mechanism used by stem cells to give rise to two daughter cells with different cell fates (Mukherjee et al., 2015). This type of cell division is common in the differentiation process of stem cells to proliferative tissue. For example, in Drosophila, both neuroblast type I and neuroblast type II divide asymmetrically along the apical-basal axis hundreds of times to generate brain tissue (Prehoda, 2009). In the case of type I neuroblasts, the most frequently found in the central brain, these cells divide to generate a neuroblast and a precursor cell, the ganglion mother cell (GMC). This ganglion mother cell will, in turn, divide into two neurons or two glial cells. In the case of neuroblast II, the neuroblast will divide into a neuroblast and an intermediate neural progenitor (INP), which in turn will generate several GMCs that, after several cell divisions, will generate neurons and glial cells (Homem & Knoblich, 2012). There are around 100 type I neuroblasts and 8 type II neuroblasts in the Drosophila brain, together generating the neuronal cortex (Walsh & Doe, 2017). Neuroblasts initially delaminate from the neuroepithelium to undergo symmetric cell division (Wodarz & Hattner, 2003). In larval neuroblasts, one part differentiates into a basal part, which will become a GMC in the case of neuroblast I, and an apical part, which will retain stem cell capacity. The neuroblast polarity is not present throughout the cell cycle but only in mitosis (reviewed in Prehoda, 2009). At prophase, the GMC fate determinant proteins such as Numb, Prospero, and Brat start to be displaced from the apical cortex, so that at metaphase they are restricted to the basal cortex (Crews, 2019). Prospero and Brat, on one hand, are sequestered by the other basal cortex protein Miranda, which in turn is transferred to the basal cortex by the activity of Myosin VI (Slack et al., 2007). Numb, on the other hand, does not require Miranda for its localization to the basal cortex, but it interacts with Pon (Partner of Numb), which allows for its more efficient localization to the basal cortex (Shan et al., 2018).

But what restricts GMC fate determinant proteins to the basal cortex? It is known that the direct upstream factor in this process is the apical polarity factor atypical protein kinase C (aPKC). This kinase is important in restricting the localization of Miranda to the basal cortex (Atwood & Prehoda, 2009). Indeed, in the aPKC mutants, Miranda is localized uniformly on both sides of the cortex (Lee et al., 2006c). It has been shown that both Numb and Miranda are phosphorylated by aPKC, and this phosphorylation is required for their localization to the basal cortex. The recruitment of aPKC,

however, requires the activity of Par proteins, such as Bazooka (Par-3) and Par-6, and is regulated by cell cycle progression. Briefly, it is proposed that the mitotic kinase Aurora A recruits Par-6 to the apical cortex (Wirtz-Peitz et al., 2008), and Inscutable (Kraut et al., 1996) recruits Baz apically in mitosis. The Baz in turn recruits the Rho GTPase Cdc42, which binds to Par-6 through its semi-CRIB domain, interacting only with the GTP-bound form of the Rho GTPase (Peterson et al., 2004). The lethal giant larvae protein (LgI), localized to the basal cortex, binds to the aPKC-Par6 complex and excludes it from the membrane, preventing the translocation of aPKC to the basal cortex. Finally, in order to achieve asymmetrical cell division, the mitotic spindle must be positioned according to the apical-basal polarity axis (reviewed in Gallaud et al., 2017). The primary connection protein between the polarity protein Baz (Bazooka) and Pins (Partner of Inscutable) is Inscutable. Pins binds to Gai (Yu et al., 2003), which interacts with Dynein-binding protein Mud (NuMA in mammals) on the mitotic spindle. This mechanism allows for the correct positioning of the mitotic spindle with regard to the apical-basal polarity axis (reviewed in Gallaud et al., 2017).

#### Mammalian brain

Cell polarity is equally important during the formation of the mammalian brain. In the mammalian brain, as in the Drosophila brain, progenitor cells, after the generation of the progenitor pool, need to divide asymmetrically to generate postmitotic neurons (O'Shea et al., 2004). Here, I will describe the mechanisms of apical-basal polarity in the generation of excitatory neurons, the most common neuronal type found in the mammalian brain.

Excitatory neurons result from the differentiation of the cortical neuronal stem cells, which produce most of the cells in the mammalian cortex: astrocytes, oligodendrocytes, and different types of excitatory neurons (Kon et al., 2017). To do so, neuronal progenitor cells first differentiate into radial glial cells (RGCs), which will later divide asymmetrically. When RGCs divide asymmetrically, they generate another RGC and a neuron (Wodarz & Hunter, 2003). As described previously, the RGC will continue dividing and generating different intermediate progenitors and neurons. The differentiating cell resulting from the asymmetric division of the RGC will inherit an apical domain (in contrast to Drosophila, where the differentiating cell inherits a basal domain) and delaminate from the ventricular surface through the transcriptional repression of cadherins (Rousso et al., 2012; Itoh et al., 2013). In this process, many proteins have been conserved between Drosophila and mammals. Par3 was shown to bind to Numb, which results in the phosphorylation of Numb by aPKC (Nishimura & Kaibuchi, 2007), repressing the activity of Numb. Par-3 is asymmetrically distributed in the two daughter cells, suggesting that the asymmetric distribution of Par-3 leads to the selective inhibition of Numb and,

therefore, different cell fates. On the basal cortex, beta-3 integrin was shown to be important for radial glial cell identity (Fietz et al. & Hutter, 2010) in the ferret; however, these data were not confirmed in mice (Haubst et al., 2006). Additionally, Cyclin D2 was shown to localize at the basal cortex (Glickstein et al., 2009), and its absence resulted in the loss of self-renewal identity in the radial glial cells (Tsunekawa et al., 2012).

Extrinsic factors play an important role in cell fate regulation. Indeed, conserved in Drosophila, the Notch-Delta pathway has been shown to be crucial for the maintenance of stem characteristics in radial glial cells in mammals (Yoon & Gaiano, 2005). The radial glial cells possess a Notch receptor, which is distributed along the whole cell membrane. The ligand Delta-like 1 is expressed in differentiated cells in the ventricular zone, and it is sensed by a Crumbs complex located in the RG subapically, activating Notch signaling (reviewed in Shitamukai & Matsuzaki, 2012). High Notch signaling in the RG cells has been shown to be important for the maintenance of stem cell fate (Mase et al., 2021).

Finally, other secreted molecules have been shown to contribute to the cell fate decisions in radial glial cells, such as retinoic acid secreted from the meninges (which is important for the first transition from neuroepithelial stem cells to radial glia), Sonic Hedgehog for peripherally migrating interneurons, and Reelin secreted from Cajal-Retzius cells, which promotes the Notch-Delta pathway (Lakoma et al., 2011).

The complexity of brain formation and asymmetric cell division for neuronal differentiation described for both the Drosophila and mammalian brains leads us to conclude that there are major evolutionary conserved pathways, which allow us to study them in different model organisms and relate them to human brain formation.

#### Mitotic exit and interphase

Once a cell undergoes division, it proceeds through the cell cycle, which is partitioned into different phases. In eukaryotic cells, there are four cell cycle phases. In the pre-replication phase, or gap phase 1 (G1), the cell prepares for replication, undergoing a complex signaling process to allow a smooth transition into the replication phase. This phase is the longest and, in human epithelial cells, lasts around 10 hours. Afterward, the cell enters the S-phase, or replication phase, where it duplicates its DNA for approximately 3 hours. Upon completion of DNA replication, the cell enters the second gap phase, G2, where it prepares for cell division. The final stage of the cell cycle is mitosis, during which the cell undergoes a precise process of chromosome segregation and cytokinesis. Both the S-phase and M-phase must alternate in time to allow the cell to duplicate its chromosomes in S-phase and

segregate them in M-phase in an orderly fashion. Outside of a proliferative cell cycle, another phase exists—called the G0 phase—which is defined as a state where the cell does not proliferate due to intrinsic or extrinsic factors but maintains its capacity for proliferation (reviewed in Schafer, 1998).

The switching between different cell cycle stages is driven by the activity waves of cyclin-dependent kinases (CDKs). As the name suggests, CDKs must be activated by their regulatory subunit, cyclin. The synergy between these molecules drives the cell cycle progression (Malumbres, 2014). For cells to exit GO and re-enter the proliferative cell cycle, cyclin D must be expressed. The transcription of cyclin D depends on various factors, including mitogenic growth factors and the MAP kinase pathway in response to growth factors binding to the cell surface (Musgrove, 2006). This activation leads to the stabilization of AP-1 and the activation of cJun and cFos (Güller et al., 2008), resulting in elevated translation of cyclin D through the activity of the mTOR pathway and self-phosphorylation. When cyclin D levels reach a critical threshold, cells resume proliferation (Baldin et al., 1993). Once activated, cyclin D binds to CDK4 and CDK6, propelling the cell toward S-phase (Qie & Diehl, 2016). A primary substrate of cyclin D is the RB protein, a master regulator of G1 progression (Qie & Diehl, 2016). Before RB is phosphorylated by the CDK4/6-cyclin D complex (in its hypo-phosphorylated state), it binds to the E2F complex and prevents activation of DP proteins, which are important for the transcription of S-phase entry genes. Phosphorylation of RB by the CDK4/6-cyclin D complex releases its binding to E2F and initiates the transcription of S-phase entry genes, such as cyclin E and cyclin A, which activate CDK2 and help maintain pRB phosphorylation status while progressing into S-phase (Giacinti & Giordano, 2006). Progression into S-phase is also regulated by Cip family proteins (Nakayama, 1998). Depending on their phosphorylation status, these proteins (p21, p27, and p57) can either activate the D-CDK complex or, when unphosphorylated, inhibit it, as seen during serum starvation (Besson et al., 2008).

If DNA damage has accumulated in the M or G1 phases, the cell must address it by prolonging G1. Once DNA damage is sensed by ATR/Chk1 or ATM/Chk2 (more details on DNA damage recognition are in the chapter "DNA Damage"), these proteins phosphorylate the N-terminus of p53, abolishing its inhibition by MDM2 and increasing its transcriptional activity (Abraham, 2001). One of the main cell cycle regulators activated in response to DNA damage is the Cip family protein, CDK inhibitor p21. P21 binds to cyclins A and E, and this inhibition of cyclins A and E results in diminished phosphorylation of pRB and prolonged G1 timing (Gartel et al., 1996).

However, if no damage is present, cells will progress to S-Phase. Actually, cells begin preparing for DNA duplication already long before the start of S-phase. Several origin recognition complex (ORC) proteins, such as ORC1-6, CDT1, and CDC6, assemble at the origin of replication sequence (Sivaprasad

et al., 2006). Once loaded, these proteins allow the MCM 2-7 (minichromosome maintenance complex) helicases to dock, forming the pre-replication complex and completing the origin licensing (Nishitani et al., 2004). At the G1-S transition, origins of replication are activated by CDK2/cyclin A and CDC7/DBF4 through phosphorylation of pre-RC components (Nishitani et al., 2004). This phosphorylation facilitates the recruitment of helicase activators, such as GINS and CDC45. Once activated, the MCM 2-7 complex unwinds the DNA, and single-stranded DNA is stabilized by the RPA protein (Remus et al., 2009). The unwound DNA becomes accessible to DNA polymerases to initiate DNA synthesis.

Once genome replication is finished, cyclins E, CDT1, and CDC6 are degraded to prevent initiation of a new pre-RC. Additionally, the MCM 2-7 complex is phosphorylated, excluding it from the nucleus (Tsuji et al., 2006). Furthermore, Geminin binds to CDT1, preventing its localization to replication origins. Following S-phase, the cell progresses into G2, where it prepares for mitosis (Caillat, 2012).

The G2-M checkpoint ensures that DNA replication has been completed before the cell proceeds into mitosis (Stark & Taylor, 2004). The main kinase regulator of G2 is CDK1, which binds to the cyclin B regulatory subunit. In G2, CDK1 is inhibited by phosphorylation of Thr14 and Tyr15 residues through Wee1 and Myt1 kinases (Schmidt et al., 2017). At the end of G2, phosphorylation of Plk1 by Aurora A and Bora complex activates CDC25 family proteins, which in turn activate CDK1 (Seki et al., 2008). The autocatalytic activity of CDK1 allows further self-activation and deactivation of Wee1 (Mulard, 2008).

By phosphorylating Bora for degradation, Aurora A is released, and the nuclear pool of Aurora A is free to bind to the TPX2 complex at the mitotic spindle (Mulard, 2008).

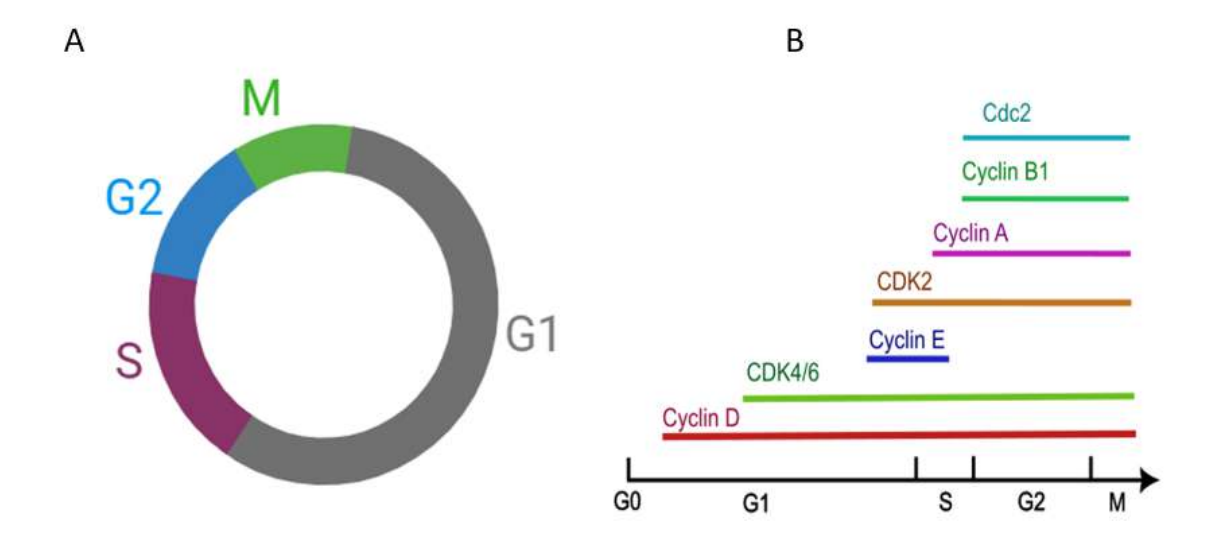


Figure 12: Cell cycle

- (A) Different phases of cell cycle: after mitosis, cell goes in Gap phase 1 (G1) in which it remains until S phase where the cell replicates its DNA. Finally, prior to mitosis, cells go into Gap phase 2 (G2).
- (B) Transitions between cell cycle phases are regulated by CDK/Cyclin complexes.

### DNA damage and response

Throughout the cell cycle, DNA can accumulate thousands of lesions due to its susceptibility to various external and intrinsic factors that induce DNA damage. These lesions are major drivers of gene mutations, tumorigenesis, and apoptosis (Dasika, 1999). Fortunately, eukaryotic cells have evolved mechanisms to combat this damage by employing DNA repair processes such as mismatch repair (MMR), base excision repair (BER), nucleotide excision repair (NER) for single-strand breaks, and homologous recombination (HR) and non-homologous end joining (NHEJ) for the repair of DNA double-strand breaks (Sirbu & Cortez, 2013). Here, I will describe the DNA damage repair mechanisms that follow DNA strand breaks.

Single- and double-strand damage and repair

As mentioned previously, DNA damage can occur on either the single strand or both strands, depending on the nature of the damage. Single-strand breaks (SSBs) are the most common type of strand breaks in the genome. These breaks arise, among other causes, from oxidative damage by

reactive oxygen species (ROS) and can lead to replication fork stalling or collapse during S-phase (Sirbu & Cortez, 2013). SSBs are repaired by the SSB repair mechanism, which includes SSB detection, DNA end processing, DNA gap filling, and DNA ligation (Caldecott, 2008).

On the other hand, double-strand breaks (DSBs) occur when both DNA strands are broken within a distance of less than 30 base pairs (Rass et al., 2022). Although DSBs are much less frequent, they are highly cytotoxic. In fact, failure to repair even one double-strand break can lead to apoptosis (Pierce et al., 2001). There are two major pathways for the repair of double-strand breaks: homologous recombination (HR) and non-homologous end joining (NHEJ). But how do cells choose between these pathways to repair a double-strand break?

When a DNA lesion is present, the cell typically cannot proceed further in the cell cycle and must arrest to allow more time for DNA damage repair. Depending on the nature of the DNA damage and the cell cycle stage, the cell can be arrested either in the G1/S transition, catalyzed by ATM and dependent on p53 activation, or in the G2/M transition, where ATR inhibits the activation of the CDK1/Cyclin B complex (Dasika et al., 1999).

The cell has two primary repair pathways to choose from. In HR, the DNA damage repair machinery uses a sister chromatid as a template for repair, meaning this process is restricted to the S- and G2-phases. In HR, the MRN complex (MRE11, Rad50, NBS1) recognizes the DNA strands, recruits ATM to the damage site, and activates the downstream repair mechanisms. The DNA ends are resected, and RAD51 recruits the homologous template, allowing DNA polymerase to synthesize the missing piece (Jasin & Rothstein, 2013). Other HR repair subtype pathways include alternative end joining and single-strand annealing, but these are beyond the scope of this thesis.

In contrast, NHEJ is active throughout the entire cell cycle and is therefore the predominant repair pathway, used in approximately 80% of all double-strand breaks. NHEJ is faster and does not require extensive DNA resection or a homologous sequence (Pannunzio et al., 2017). A key regulator of NHEJ is p53-binding protein 1 (53BP1), an important player in DSB signaling and one of the first interactors identified with p53. 53BP1 is a large protein, consisting of 1972 amino acids, containing BRCA repeats and several phosphorylation sites for the ATM kinase (Adams & Carpenter, 2006). 53BP1 prevents DNA end resection, a key process that promotes HR, thereby directing the repair process toward NHEJ. During G1 phase, ATM is sequestered at the damage site, phosphorylating histone H2AX (yH2AX) and creating a platform for the recruitment and activation of various proteins, such as 53BP1 and Chk2. Once Chk2 is activated, it disperses throughout the nucleus, activating different targets that inhibit cell cycle progression. Through this mechanism, Chk2 activates p53, which in turn activates p21, delaying progression into S-phase (reviewed in Panier & Boulton, 2014).

Another critical role of 53BP1 in DSB repair is serving as a scaffold for the recruitment of additional DNA damage repair proteins to the damaged chromatin. ATM-phosphorylated histones (yH2AX) recruit 53BP1, which in turn recruits chromatin modulators, such as EXPAND1 (MUM1), RIF1 (RAP1-interacting factor 1), and PTIP (PAX transactivation domain-interacting protein, also known as PAXIP1) (reviewed in Panier & Boulton, 2014). Additionally, 53BP1 plays a crucial role in amplifying ATM kinase signaling when DNA damage levels are low. It has been shown that in the absence of 53BP1, low levels of DNA damage lead to insufficient phosphorylation of ATM targets, including p53, CHK2, and BRCA, which can result in genomic instability (Fernandez-Capetillo et al., 2002).

#### 53BP1 roles in mitosis

As described above, 53BP1 plays several key roles in the regulation of DSBs. However, recent studies have uncovered additional functions of 53BP1 outside of DNA repair. For instance, 53BP1 acts as a mitotic surveillance protein, monitoring mitotic defects and contributing to the formation of mitotic stress bodies through phase separation with Lamin A/C and RIF1. These bodies do not colocalize with yH2AX (Bleiler et al., 2023). It has also been reported that 53BP1 localizes at the kinetochore when phosphorylated by Aurora B, where it plays a role in the resolution of merotelic microtubule attachments (Wang et al., 2017).

Moreover, loss of centrosomes or prolonged mitotic duration activates 53BP1, leading to the recruitment of the deubiquitinase USP28. Together, 53BP1 and USP28 form a focus that triggers p53-p21-dependent cell cycle arrest (Fong et al., 2016; Meitinger et al., 2016; Lambrus et al., 2016). Notably, the memory of extended mitosis can be passed to daughter cells through 53BP1 activity. In the case of prolonged mitosis, 53BP1 forms a complex with USP28 and p53 in daughter cells, leading to G1 arrest and activating a mechanism referred to as the "mitotic stopwatch" (Meitinger et al., 2024). This mitotic stopwatch mechanism appears to require PLK1, which promotes timely 53BP1 release from kinetochores and its subsequent activation for this process (Burigotto et al., 2023).

Therefore, 53BP1 is not only a central protein in double-strand break repair but also plays a critical role in mitotic surveillance.

## Aims of this study

Mitosis is a fundamental process, allowing the cell to segregate its genetic content into two daughter cells. Proper regulation of mitosis is therefore crucial to allow the generation of healthy progenitor cells. Errors in mitosis can lead to a variety of different diseases, including cancers and neurodevelopmental disorders. In my PhD, I have aimed to explore the importance of mitotic regulation in physiological and pathological contexts.

Indeed, spindle dynamics in mitosis have been deeply studied for decades; however, gaps remain, especially in the roles of minus-end proteins in mitotic progression and disease. Therefore, in my PhD, I have had the following aims:

- Clarify the role of microtubule minus-end binding proteins in mitosis
- Understand the mechanisms of WDR62-induced primary microcephaly and how dysregulation of poleward microtubule flux can result in this disease

For the last aim, I have collaborated with my colleague Dr. Elena Doria to understand the mechanisms of WDR62-induced microcephaly. We have found that WDR62 depletion leads to transient lagging chromosomes, which leads to 53BP1 foci formation and p21 activation, resulting in cell cycle proliferation delay and microcephaly in Drosophila melanogaster.

### Results

# Transient lagging chromosomes cause primary microcephaly

As previously mentioned in the introduction, WDR62 and ASPM are two most commonly mutated genes in a neurodevelopmental disorder Primary Microcephaly. While the precise reason of this disease remains unclear, it is known that both these proteins are important for loading of Katanin at the microtubule minus-ends during mitosis. Katanin in turn is important for microtubule severing and its mis-localization following WDR62 or ASPM depletion leads to decrease in microtubule flux speed (Jiang et al 2019, Guerreiro et al 2021).

Our preprint describes the consequences of WDR62 depletion in human RPE cells. Indeed, we find that WDR62 depletion leads to transient lagging chromosomes and activation of 53BP1-p21 dependent cell cycle delay, leading to decreased brain size in Drosophila Melanogaster larvae. The co-depletion of WDR62 with Camsap1, on the other hand, rescues the microtubule flux and its downstream consequences, including the brain size.

This paper is a direct continuation of Guerreiro et al 2021 (see below). I am a first co-author of this paper together with my colleague Elena Doria. While I have initiated the measurements of transient lagging chromosomes and 53BP1 in WDR62 depletion, Elena has started the work on Camsap1 depletion.

Following experiments have been performed solely by me: Figure 1A, B, C, D, E, F, G, H; Figure 2D,E, O; Figure 4F, G, H; Figure 5C, H, I, J, K, L.

Following experiment have been performed together with Elena Doria: Figure 2A, B, C, D, E, F, G; Figure 3G, H, I, L; Figure 4A, B, C, D; Figure 5A, B.

Following experiments have been performed solely by Elena Doria: Figure 2H, I, J, K, L, M, N; Figure 3A, B, D, E, F, J, K; Figure 4E, Figure 5E, F, G.

Transient lagging chromosomes cause primary microcephaly

\*Elena Doria<sup>1,2</sup>, \*Daria Ivanova<sup>1,2</sup>, Alexandre Thomas<sup>1,2</sup> and Patrick Meraldi<sup>1,2</sup>

<sup>1</sup>Department of Cell Physiology and Metabolism, Faculty of Medicine, University of Geneva, 1211

Geneva 4, Switzerland

<sup>2</sup>Translational Research Centre in Onco-hematology, Faculty of Medicine, University of Geneva, 1211

Geneva 4, Switzerland

\* Equal contribution

Correspondence to: patrick.meraldi@unige.ch - ORCID: 0000-0001-9742-8756

#### ABSTRACT

Primary microcephaly results from the impaired neuronal progenitor proliferation, causing reduced brain size and impaired cognitive abilities. Loss of the most frequently microcephaly genes, *WDR62* and *ASPM*, slows down poleward microtubule flux and results in transient lagging chromosomes in anaphase. Whether these defects cause primary microcephaly is unknown. Here we show that transient lagging chromosomes elicit an Aurora-B-dependent activation of 53BP1 and p21, impairing cell proliferation. Co-depletion of the microtubule depolymerase inhibitor CAMSAP1/Patronin in a WDR62 depletion background, restores normal flux rates, suppresses lagging chromosomes, and allows normal cell proliferation in human cells, while rescuing the small brain and the cognitive defects in fly larvae. We postulate that transient lagging chromosomes in anaphase and 53BP1/p21-dependent response they elicit, are a major driver of primary microcephaly.

#### INTRODUCTION

Autosomal recessive primary microcephaly (microcephaly primary hereditary [MCPH]) leads to smaller brain size in new-borns due to exhaustion of neuronal progenitor cells (1). Recessive loss-of-function mutations in 30 different genes, most of which involved in cell cycle and cell division, are linked to this disease. This includes genes encoding key regulators of centriole biogenesis (*PLK4*, *SAS6*, *STIL*, *SAS4*, *CEP152* and *CEP135*), pericentriolar proteins (*CDK5RAP2*, *PCNT*, *TUBGCP4* and TUBGCP6), microtubule-associated proteins and microtubule-motors of the mitotic spindle (*ASPM*, *WDR62*, *MAP11*, *KIF11* and *KIF14*), kinetochore proteins (*KNL1* and *CENP-E*), and regulators of DNA damage/condensation/replication (*MCPH1*, *ORC1*, *ORC4*, *ORC6*, *CDC45*, *NCAPH*, *NCAPD2* and *NCAPD3*) (2–5). The common denominator between those genes remains unknown. For the cell division genes, several non-exclusive hypotheses have been postulated: (1) chromosome segregation errors that lead to aneuploidy and result in neuronal progenitor pool depletion via p53-induced apoptosis (6); (2) erroneous spindle orientation that drives premature neuronal differentiation depleting the neuronal progenitor pool (7–9), (3) or centrosomal defects that prolong mitosis, causing an activation

of 53BP1 that triggers a p53-dependent cell proliferation defect (10). However, loss of function of WD Repeat-Containing Protein 62 (WDR62, MCPH2) and the abnormal spindle-like microcephaly associated gene (ASPM, MCPH5), which account for over 80% of all microcephaly cases (11), has not been conclusively linked to aneuploidy, spindle mis-orientation or a mitotic delay in human cells (12–14).

Instead, WDR62 and ASPM regulate microtubule dynamics by recruiting the microtubule-severing enzyme Katanin to mitotic spindle poles (14–16). Impairment of either protein results in insufficient microtubule minus-end depolymerization and reduced poleward microtubule flux rates (14–16), a conveyor belt-like movement that drives tubulin subunits towards the minus ends at spindle poles (17). We previously showed that human WDR62 depletion does not delay mitosis but instead leads to transient lagging chromosomes in anaphase that are nevertheless incorporated into the daughter nuclei (14). Whether these transient chromosome segregation defects are linked to microcephaly remains unknown.

Here, we show that transient lagging chromosomes in anaphase in WDR62- and ASPM-depleted human cells elicit an Aurora-B dependent response that activates 53BP1 in the ensuing G1 phase, impairing cell proliferation. We hypothesized that such mild segregation defects, which are frequently seen after the loss of most MCPH genes, could be a common origin for the reduced proliferation of neuronal progenitor cells. To test this hypothesis, we co-depleted CAMSAP1, a member of the Patronin/CAMSAP family, which inhibits spindle-associated microtubule depolymerases of the kinesin-13 family at spindle poles (18–22). CAMSAP1/Patronin co-depletion in a WDR62 RNAi background suppressed the appearance of transient lagging chromosomes and the cell proliferation delay seen in human cells and *Drosophila melanogaster* neuroblasts, and rescued microcephaly in fly larvae. We postulate that transient lagging chromosomes in anaphase are a major cause of primary microcephaly.

#### RESULTS

Depletion or deletion of WDR62 in human tissue culture cells leads to decreased microtubule depolymerization at spindle poles, slower poleward microtubule flux rates, and transient lagging chromosomes in anaphase (14). Such chromosomes (also called lazy chromosomes) transiently lag behind the DNA masses during anaphase in WDR62-depleted cells but, unlike persistent lagging chromosomes, are incorporated into the daughter nuclei without the formation of micronuclei (14, 23). Transient lagging anaphase chromosomes were visible in live WDR62-depleted cells stained with SiR-DNA (a cell was considered to have a transient lagging chromosome if a chromosome arm was sticking out of the DNA mass by >2 μm as the two DNA masses were separated by >6 μm; p = 0.0191 in paired t-test; Figure 1A and B and Supplementary Figure 1A and B for siRNA validation). These lagging chromosomes reflected asynchronous kinetochore movements, since such laggards were also visible in WDR62-depleted RPE1 cells expressing kinetochore (GFP-CENP-A) and centrosome (GFP-Centrin1) markers (p = 0.0087 in paired t-test; Supplementary Figure 1C and D). Transient lagging chromosomes have so far not thought to lead to DNA damage. Nevertheless, since primary microcephaly is genetically also linked to DNA damage signalling, we tested whether WDR62 depletion activated such pathways. We stained non-transformed retina pigment epithelial cells expressing human telomerase (hTert-RPE1) for γH2AX and 53BP1 after control or WDR62 depletion, or after treatment with the DNA-damaging agent Doxorubicin. Both form nuclear foci upon activation: while γH2AX labels double-strand breaks (24), 53BP1 is involved in double-strand break repair, but also in p53 stabilization after long mitotic delays (25-29). This drives the expression of the cyclin-dependent kinase inhibitor p21, a key p53 target, resulting in cell cycle delay or arrest (30). Using automatic image analyses (Supplementary Figure 1E), we analysed hundreds of interphase cells per experiment for the presence of γH2AX or 53BP1-positive nuclei. In each independent experiment, WDR62 depletion increased the proportion of cells with 53BP1-positive nuclei, leading on average to an increase from 31% (siControl) to 42% (siWDR62; overall p < 0.0001 in Fischer's exact test, Fig. 1C and D). In contrast, WDR62 depletion did not increase the proportion of γH2AX-positive cells (Supplementary Figure 1F and G). WDR62depleted cells typically displayed single nuclear 53BP1-positive foci, while doxorubicin-treated cells

(condition representing DNA damage) displayed dozens of 53BP1 foci (Figure 1C). Quantitative immunofluorescence measurements on the same cells indicated that WDR62-depleted cells also had elevated nuclear p21 levels (p < 0.0001 in Fisher's exact test; Figure 1C and E), implying a cell cycle delay. When we labelled control- or WDR62-depleted cells with cell proliferation pulse-chase marker CFSE (Carboxyfluorescein succinimidyl ester, Supplementary Figure 1H for methodology), and let them proliferate for 5 days, we found WDR62-depleted cells underwent half a cell division less than control-depleted cells (p = 0.0029 in one way ANOVA; in comparison serum starved cells underwent 2 cell division less; Figure 1F and G). This implied that WDR62-depletion activates the 53BP1-p53-p21 signalling pathway and that it delays cell proliferation independently of double-strand breaks. Consistently, WDR62 depletion did not significantly delay cell proliferation in a p21 knockout in RPE1 cell line, while delaying cell proliferation in the parental cell line (p = 0.0141 in one way ANOVA; Figure 1H).

#### Transient lagging chromosome induce 53BP1 foci and delay the cell cycle via Aurora B signalling.

53BP1 is activated in the absence of DNA damage, but also if cells are delayed in mitosis, for example after centrosome loss (27–29). Aneuploidy can also activate p53 (31). WDR62 depletion, however, does not lead to a mitotic delay or micronuclei, nor does it affect centrosome numbers (14). Metaphase spreads over 40 cells in 3 replicates indicated that WDR62-depleted RPE1 cells had generally the same chromosome numbers as control-depleted RPE1 cells; in contrast cells treated with Reversine, an inhibitor of the spindle assembly checkpoint kinase Mps1 that induces aneuploidy, displayed severe aneuploidy ((32); Supplementary Figure 2A and B). To exclude low levels of aneuploidy and quantify individual chromosomes at single cell level, we compared control- and WDR62-depleted cells by single cell DNA sequencing. We found that within a population of 384 cells, WDR62 depletion and control-depleted cells had the same chromosome distribution (Figure 2A, and supplementary Figure 2C), indicating that WDR62 depletion does not induce aneuploidy. We next reasoned that 53BP1 activation could be either linked to the transient lagging chromosomes or to an unrelated cell-cycle function of WDR62. To distinguish between the two possibilities, we tested whether the appearance of 53BP1 foci in 53BP1 foci-negative cells correlated with the presence of transient lagging chromosomes in the

preceding anaphase. Monitoring live WDR62-depleted 53BP1-GFP RPE1 cells in the presence of the chromosome marker SiR-DNA (33), revealed that the appearance of 53BP1 nuclear foci in hitherto 53BP1-negative G1 cells was nearly always preceded by a transient lagging chromosome in anaphase (p = 0.0105 in student t-test; Figure 2B and C). This suggested that transient lagging chromosomes are linked to 53BP1 foci formation. Consistently, ASPM-depleted cells also displayed transient lagging chromosomes (p = 0.0005 in paired t-test) and 53BP1 foci (p < 0.0001 in Fischer's test with Bonferroni correction; Figure 2D-G, and supplementary Figure 2D and E for siRNA validation).

Why would transient lagging chromosomes in anaphase activate 53BP1? One possibility is that transient lagging chromosomes are exposed longer to the activity gradient of the mitotic kinase Aurora B at the spindle mid-zone (34), an activity known to delay nuclear envelope reformation (35, 36), which has been proposed to activate p53 in the presence of permanent lagging chromosomes (37). Two predictions of such a model are that partial Aurora B depletion should prevent 53BP1 foci formation and the cell cycle delay found in WDR62-depleted cells. Partial inhibition of Aurora B with 50 nM Barasertib, a condition that did not prevent cytokinesis but reduced the Aurora B-dependent localization of its substrate MCAK at kinetochores by 60% ((38) Supplementary Figure 2F and G), indeed abolished the increase in 53BP1-positive nuclei in WDR62-depleted cells (Fig. 2H and I). Moreover, when we extracted cell cycle duration (time between two mitoses) from long-term live cell imaging under the same experimental conditions (50 nM Barasertib was too toxic for the 5-day CFSE assay), we found that WDR62 depletion led to a 9-hour cell cycle delay that was suppressed by partial Aurora B inhibition (p = 0.0115 in one-way Anova test, Figure 2J and supplementary Figure 2H and I). This indicated that the 53BP1 foci formation and the cell cycle delay in WDR62-depleted cells depends on Aurora B activity.

A third prediction was that maintaining Aurora B on anaphase chromosomes should lead to more 53BP1-positive cells and a reduced proliferation. Aurora B is extracted from chromosomes at anaphase onset via Cdc48/p97 and the de-ubiquitinase UBASH3B, allowing its transport to the spindle midzone (36, 39, 40). Partial depletion of the Cdc48/p97 co-factor NPL4, or of UBASH3B, delayed chromosomal Aurora-B extraction in anaphase (p = 0.040 and p = 0.0034 and in Mann-Whitney test,

Figure 2K-M, Supplementary Figure 2J-M), and led, as predicted, to more 53BP1-positive cells (Figure 2H - N) and a reduced cell proliferation (Figure 2O), despite the absence of a mitotic delay or lagging chromosomes (Supplementary Figure 2N-P and data not shown). Consistent with our model, the increase in 53BP1 positive cells after NPL4 or UBASH3B depletion was suppressed by partial Aurora B inhibition (Figure 2N). We thus hypothesized that a deregulation of poleward microtubule flux in WDR62-depleted cells favours the appearance of transient lagging chromosomes in anaphase that activate 53BP1 via Aurora B in the next G1 phase, delaying cell cycle progression.

## Co-depletion of CAMSAP1 rescues poleward microtubule flux rates and lagging chromosomes in WDR62-depleted cells.

To test this hypothesis, we aimed to restore normal poleward microtubule flux rates in WDR62-depleted cells. One promising candidate was the depletion of CAMSAP1, a member of the CAMSAP protein family, which we found to localize to spindle poles in mitotic cells (Figure 3A and B). CAMSAP1-3 proteins and their *Drosophila melanogaster* ortholog Patronin inhibit the microtubule depolymerizing activity of kinesin-13s; moreover, *PATRONIN* mutations increase poleward microtubule flux rates in flies (18–20). In RPE1 cells, CAMSAP1 depletion increased poleward microtubule flux rates in metaphase by 50% and doubled the percentage of cells displaying transient lagging chromosomes (Figure 3C-F). This suggested that both a reduction and an increase in poleward microtubule flux can impair efficient anaphase chromosome movements. Co-depletion of CAMSAP1 and WDR62, in contrast, restored normal poleward microtubule flux rates (Figure 3G-K) and rescued the transient lagging chromosome phenotype (Figure 3L). We conclude that the reduction of poleward microtubule flux causes lagging chromosomes in WDR62-depleted cells, and that efficient anaphase chromosome movements require a balanced microtubule flux rate.

## Co-depletion of CAMSAP1 in WDR62-depleted cells suppresses activation of the 53BP1 and p21 and restores normal cell proliferation.

We next found by quantitative immunofluorescence that CAMSAP1 co-depletion also suppressed the appearance of 53BP1 foci and the accumulation of nuclear p21 in WDR62-depleted cells (Figure 4A-

C). Moreover, co-depletion of CAMSAP1 in a WDR62 siRNA background also restored normal cell proliferation, as quantified with the 5-day CFSE assay (Figure 4D). This confirmed our hypothesis that reduced poleward microtubule flux rates and transient lagging chromosomes activate 53BP1 and drive p21 expression to induce a cell proliferation delay.

Nevertheless, we also noted that cells depleted of CAMSAP1 alone, neither accumulated p21 (Figure 4C) nor experienced a cell proliferation defect (Figure 4D), despite transient lagging chromosomes (Figure 3F) and an increased proportion of cells with 53BP1-foci (Figure 4B and C). How was this possible? Re-examining both live-cell SiR-DNA and GFP-53BP1 movies revealed key differences: (1) while transient lagging chromosomes in WDR62-depleted cells persisted in anaphase for a median time of 3.5 mins, the corresponding median time in control-, CAMSAP1-, or CAMSAP1/WRD62-depleted cells was only 2 mins (p < 0.0001 in Mann-Whitney test); (2) 53BP1 foci appeared on average 1 hour after an aphase in WDR62-depleted cells, but only after 2 hours in CAMSAP1-depleted cells (p = 0.0001in Mann Whitney test, Figure 4E and F). This suggested that the response to transient lagging chromosomes is gradual and that the probability to rapidly activate 53BP1 (and most likely activate p21) increases the longer transient lagging chromosomes persist, consistent with the fact that unperturbed cells often experience transient lagging chromosomes for brief periods without impairing cell proliferation. To test this idea, we recorded dual-colour live-cell SiR-DNA and GFP-53BP1 movies at high temporal resolution and found that the timing of 53BP1 foci appearance, whether control- or WDR62-depleted, was indeed inverse correlated to the duration of transient lagging chromosomes (r = -0.4410, p = 0.0039 in Spearman correlation test, Figure 4G and H). We conclude that poleward microtubule flux defects lead to transient lagging chromosomes that, if not rapidly resolved, will activate 53BP1 and p21 to delay cell proliferation.

#### Patronin co-depletion restores brain size and cognitive function in WDR62-depleted fly larvae

Given that primary microcephaly is caused by an exhaustion of neuronal progenitor cells, and that an extension of the cell cycle timing in murine progenitors causes a premature cell differentiation (41), we hypothesized that the proliferation impairment we observed, could explain the origin of microcephaly in organisms lacking WDR62. To test this hypothesis, we turned to *Drosophila melanogaster* larvae,

where *WDR62* mutations cause a cell cycle delay and a brain size reduction (*42*). We used the UAS/Gal4 system (*43*) to express UAS-*WDR62* and UAS-*Patronin* RNAi constructs (*WDR62* RNAi and *Patronin* RNAi hereafter, Supplementary Figure 3B) to knock-down their respective mRNA specifically in the brain (*44*, *45*). We first tested whether Patronin co-depletion counteracts the effects of WDR62 RNAi on brain lobe size. To compare brain size of larvae of similar age, we staged egg-laying and stained the resulting third instar larvae with the DNA-marker DAPI and the neuroblast-specific polarity marker Miranda ((*46*); Figure 5A and supplementary Figure 3C). Consistent with previous studies, brain size (p < 0.0001) and neuroblast numbers in the central brain (p = 0.0041 in one-way Anova) was decreased by roughly one quarter in *WDR62* RNAi compared to control conditions (Figure 5A-C). *PATRONIN* RNAi had no effect on its own but led to larger brain lobes and restored neuroblast numbers in a *WDR62* RNAi background (Figure 5A-C), indicating a rescue of the microcephaly phenotype. Miranda staining also allowed us to probe the polarity of the neuroblasts and spindle orientation vs the polarity axis ((*46*); supplementary Figure 3C and D). We observed the typical Miranda crescents in all conditions and found no change in spindle orientation (Figure 5D and supplementary Figure 3D), indicating that the brain size phenotypes occurred independently of cell polarity or spindle orientation.

To test whether WDR62, PATRONIN and WDR62 + PATRONIN RNAi also led to transient lagging chromosomes in anaphase, we applied these depletions in a strain expressing the microtubule-marker Jupiter-GFP and the chromosome marker His2Av-mRFP (47, 48), extracted the live brain from the larvae, and monitored neuroblast divisions by live cell imaging (Figure 5E). As in human cells both PATRONIN and WDR62 RNAi led to transient lagging chromosomes in anaphase, while their codepletion suppressed this phenotype (Figure 5E and F). Similar to human cells, lagging chromosomes persisted twice as long in WDR62-depleted neuroblasts than in PATRONIN-depleted or WT cells (Figure 5F and G; p = 0.0043, Kruskal-Wallis test). Moreover, as RPE1 cells, WDR62-depleted neuroblasts had a normal mitotic timing (Supplementary Figure 3E), but a longer cell cycle (Figure 5H). In contrast, WDR62 + PATRONIN RNAi led to a shorter cell cycle, which could partially explain the resulting larger brain size (Figure 5H). We conclude that the depletions of PATRONIN and WDR62 in in situ neuroblasts fully phenocopy the orthologous depletion in human RPE1 cells.

At the functional level, to test whether the reduction in brain size in WDR62-depleted cells impairs larval cognitive functions, we performed two basic behavioural assays. In the first assay we recorded larvae on agar plates as they searched for food (Figure 5J and supplementary figure 3C). Wild-type larvae optimize their search strategy by turning by 90° after 3-4 contractions (49). In contrast, WDR62 RNAi-treated larvae turned much less frequently, leading them to unidirectional movements (11 median contraction per turn, p < 0.0001; Figure 5J and supplementary Figure 3C). This defect was rescued by Patronin co-depletion (3 median contractions per turn; Figure 5J and supplementary Figure 3C). Second, we plated larvae on agar plates containing in one half fructose and in the other half no fructose and recorded the position of the larvae after 5 minutes. As previously described, wild-type larvae selectively chose the fructose containing half-plate (76%; (50)); in contrast, WDR62 RNAi larvae showed a much weaker preference for fructose (57% p = 0.0319 in Fischer's exact test; Figure 5I and J, supplementary Figure 3D). This cognitive defect was again rescued by Patronin co-depletion (77%, Figure 5J). We concluded that co-depletion of Patronin rescues the microcephaly phenotype induced by WDR62 depletion in terms of brain size, neuroblast depletion and basic cognitive functions.

#### **DISCUSSION**

Loss of function of WDR62 or ASPM causes over 80% of the primary microcephaly cases (II). These cases, however, are not due to the postulated cellular origins for primary microcephaly: excessive mitotic duration, loss or gain of chromosomes, or spindle orientation defects (6, 8–10, 51). Instead, our *in vitro* and *in vivo* results indicate that a deregulation of microtubule minus-end dynamics, which leads to transient lagging chromosomes that elicit an Aurora-B dependent activation of 53PB1 and the p53-target p21, impairs cell cycle progression thus limiting the number of neuronal progenitor cells (see model Figure 5K). We postulate that this response is due to a surveillance mechanism that reacts to chromosomes that are not segregated in time with the rest of the chromosome mass in anaphase, complementing the mitotic surveillance mechanism that checks whether cells have remained for too long in mitosis (26–29, 52). Given that loss of many cell division genes associated to primary microcephaly leads to transient lagging chromosomes, we speculate that this mechanism could be a frequent cause of this disease.

One major difficulty when evaluating the potential cellular causes of primary microcephaly, has been the lack of effective rescue experiments that could validate the hypotheses. Indeed, it is difficult to correct for aneuploidy, spindle orientation defects or excessive mitotic timing without introducing additional mitotic defects that may have confounding effects. Here however, by combining WDR62 and CAMSAP1 depletion and restoring normal minus-end microtubule dynamics, we could rescue all the downstream effects of WDR62 depletion at the cellular level, establishing a causal chain of events. The fact that this co-depletion suppressed lagging chromosomes and the cell cycle delay in neuroblasts, while restoring their numbers and basic cognitive function in WDR62-depleted fly larvae, backs the hypothesis that defects in microtubule minus-end dynamics cause primary microcephaly in WDR62-depleted flies. Our data also imply that the speed of poleward microtubule flux needs to be balanced, as both an increase and a decrease in speed will lead to asynchronous anaphases, consistent with a recent study (53). Nevertheless, the rescue after WDR62/CAMSAP1 co-depletion is not perfect: co-depletion of WDR62 and Patronin results in larvae with larger brain size. One potential cause could be the shorter neuroblast cell cycle we observed in this genetic background, which will generate more descendants. These neuroblasts, however, did not resemble tumour cells, as their cell polarity was preserved.

Work in the last 15 years have shown that cells not only possess different mitotic surveillance mechanisms: a spindle checkpoint for kinetochore-microtubule attachment in metaphase (54), a surveillance mechanisms for aneuploidy (55), but also a mitotic duration surveillance mechanism, which blocks the cell cycle when cells spent more than 90 minutes in mitosis, whether they experience chromosome segregation errors or not (26–29, 52). Here, we propose the existence of another, complementary surveillance mechanism that monitors chromosome movements in anaphase and activates 53BP1 in the presence of transient lagging chromosomes. This mechanism is distinct from the mitotic timing and aneuploidy surveillance systems, as WDR62-depleted cells have a normal mitotic timing and no increased aneuploidy. It allows cells to react to erroneous kinetochore-microtubule attachments that cannot be detected by the spindle checkpoint and do not extend mitotic timing, such as chromosomes with merotelic kinetochore-microtubule attachments, which often transiently lag in anaphase (one kinetochore bound by microtubules from both spindle poles; (56)). Previous studies had

shown that Aurora B can promote their rapid correction or later delay nuclear envelope reformation to prevent micronuclei formation (23, 57, 58). Here we postulate that cells also react to the intermediate case: transient lagging chromosomes that are not immediately corrected but do not end up as micronuclei. This surveillance mechanism is linked to the proximity of anaphase chromatin to Aurora-B activity and not the lagging per se, as it can be activated in Npl4- or UBASH3B-depleted cells without lagging chromosomes. Whether this 53BP1 activation depends on the ability of Aurora-B to delay nuclear envelope reformation (35, 36), or its ability to phosphorylate chromatin proteins of lagging chromosomes (37), remains to be seen. The net result is that such a surveillance mechanism prevents the proliferation of cells having experienced such as intermediate lagging chromosome, which contribute to chromosome compaction and nuclear architecture defects in the absence of aneuploidy and impair post-natal growth in mice (59). We also postulate that this surveillance mechanism relies on a gradual response: lagging chromosomes that persist only 1-2 minute, such as in CAMSAP-1 depleted cells, lead to a weak response that does not impair cell proliferation; in contrast transient lagging chromosomes that persist for 3-4 minutes, as seen in WDR62 depleted cells, are associated with a rapid 53BP1 foci formation and p21 activation. Such a semi-permissive mechanism also fits with the observation that short-lived transient lagging chromosomes can be observed in 20-30% of wild-type RPE1 cells.

Finally, we speculate that primary microcephaly might be caused by the frequent incapacity to satisfy this surveillance mechanism in time, due to transient lagging chromosomes. This disease is caused by the loss of over 30 different genes, many of which are linked to cell division and chromosome segregation. Although it is likely that several cellular mechanisms can contribute to neuronal progenitor exhaustion, we note that transient lagging chromosome are likely to appear in most of those genetic backgrounds, such as defective centriole biogenesis, impaired centrosome function, or loss of microtubule associated proteins, microtubule motors or kinetochore proteins, and might thus represent a common cellular origin. These mild defects would be sufficient to affect the expansion of neuronal progenitor cells, which have very short cell cycle, without impairing the overall development of the other organs. The mildness of these defects may also explain why patients having lost WDR62 or APSM

do not display an elevated risk for cancer development, unlike patients with a predisposition to an an an analysis and (60).

#### **ACKNOWLEDGEMENTS**

We thank A. Khodjakov (State University of New York), R. Medema (Netherland Cancer Institute), E.Nagoshi (University of Geneva) and R.Giet (University of Rennes) for reagents, the HumanaFly facility and M. Savitskiy (University of Geneva) for drosophila support, the Bioimaging Facility and N. Liaudet (University of Geneva) for microscopy support; the Flow Cytometry Core Facility (University of Geneva) for FACS support; S. Barbieri (University of Geneva) for help with data analysis, H. Maiato (University of Porto), Iva Tolic (Ruđer Bošković Institute), M. Gotta and her laboratory (University of Geneva), and members of the Meraldi laboratory for critical discussions. This work in the Meraldi laboratory is supported by the Swiss National Science Foundation project grants (208052 & 215124) and the University of Geneva.

#### **Competing interests**

The authors declare no competing interests.

#### **Author contributions:**

The project was initiated by E.D., D.I. and P.M. and directed by P.M.; E.D. and D.I. performed all experiments; A.T. contributed to the drosophila experiments; E.D., D.I. and P.M. analyzed and interpreted all the results; E.D., D.I., A.T. and P. M. wrote the manuscript.

Figure 1 Doria, Ivanova et al.

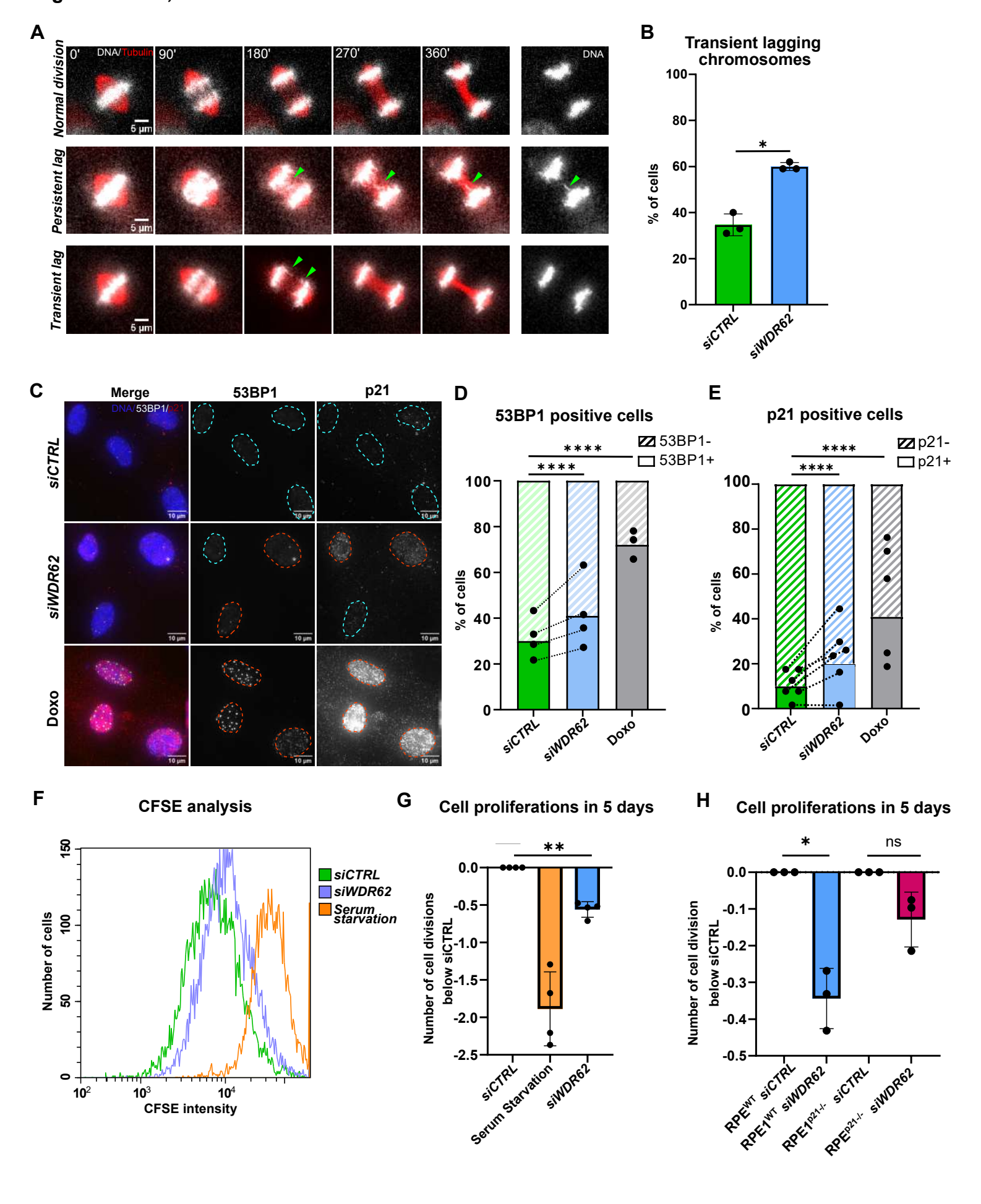


Figure 1: WDR62 depletion leads to 53BP1 and p21 activation and a proliferation delay. (A) Timelapse single-plane images RPE1 cells stained with SiR-Tubulin (red) and SpY-DNA (white) showing examples of transient or persistent lagging chromosomes (green arrows). Scale bars = 5 µm. (B) Quantification of transient lagging chromosomes in siWDR62-treated RPE1; N = 3 independent experiments; n = 83-115 cells, \*p = 0.0191, student two-tailed t-test. (C) Immunofluorescence images of interphase RPE1 cells treated with siCTRL, siWDR62 or Doxorubicin, and stained with DAPI, 53BP1 and p21 antibodies. Blue dotted lines represent 53BP1-negative nuclei, red dotted lines represent 53BP1-positive nuclei. Scale bars =  $10 \,\mu m$ . (**D**) Quantification of 53BP1 positive cells. Connected dots represent paired experiment. N = 4 independent experiments, n = 648 - 1440 cells; \*\*\*\*p < 0.0001, Fisher's exact test with Bonferroni correction (E) Quantification of p21 positive cells. Connected dots represent paired experiment. Blue dotted lines represent p21-negative nuclei, red dotted lines represent p21-positive nuclei. N = 6, n = 570-1010 cells; \*\*\*\*p < 0.0001, Fisher's exact test with Bonferroni correction (F) Example of FACS CFSE analysis data (G) Quantification of cell divisions after 5 days compared to control depletion based on CFSE intensity, N = 4, n = 18194 - 82963 cells; \*\*p = 0.0029, one-way ANOVA test. (H) Quantification of cell divisions after 5 days when compared to control depletion based on CFSE intensity in RPE1 WT or p21<sup>-/-</sup> cells, N = 3, n = 27693 - 29379 cells; \*p = 0.0141, one-way ANOVA test. All error bars represent SEM.

Figure 2 Doria, Ivanova et al.

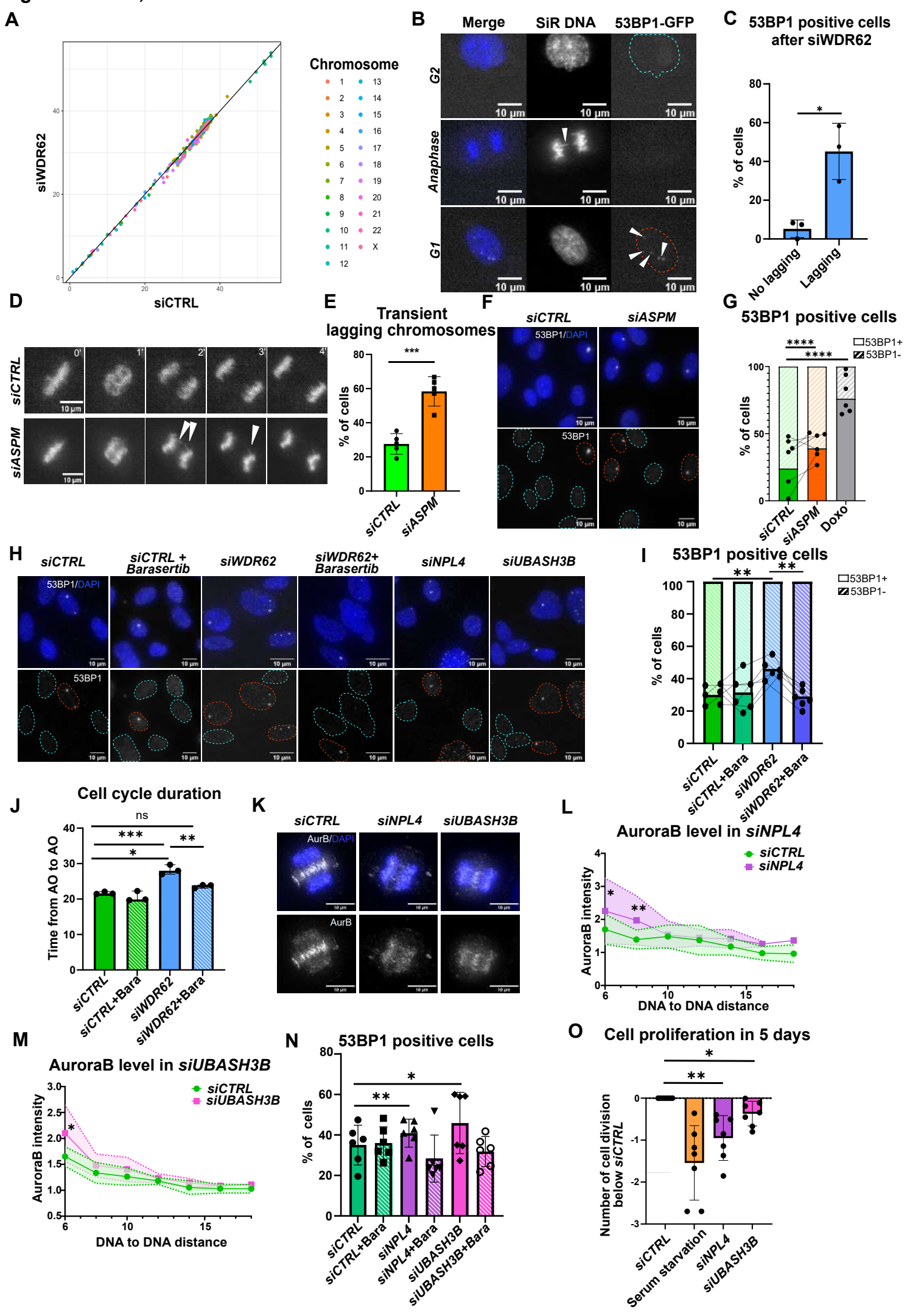


Figure 2: Transient lagging chromosomes activate 53BP1 via Aurora B (A) Scatter-plot of chromosome copy number comparing the coverage of individual chromosomes in WDR62- vs. controldepleted cells. Numbers indicate the normalized number of reads per chromosome. The diagonal indicates that the chromosome numbers in each dataset are highly correlated (B) Time lapse images of RPE-1 53BP1-GFP cell treated with siWDR62 in G2 (top row, blue dotted circle 53BP1-negative), anaphase (middle row) and in the ensuing G1 phase (bottom row, red dotted circlle 53BP1-positive). White arrow indicates transient lagging chromosome. Scale bars = 10 µm (C) Quantification of siWDR62-treated 53BP1-GTP positive cells after a cell division with or without lagging chromosomes. N = 3; n = 60 cells; \*p = 0.0105, student two-tailed t-test. (**D**) Time lapse imaging of RPE1 cells stained with SiR-DNA undergoing mitosis. Arrows indicate transient lagging chromosomes in anaphase. Scale bars = 10 µm (E) Quantification of lagging chromosome in SiR-DNA stained live RPE-1 cells treated with siCTRL or siASPM. N = 5; n = 41-115 cells; \*\*\*p = 0.0005, paired t-test. (F) Immunofluorescence images of siCTRL- or siASPM-treated RPE-1 cells stained for 53BP1 and DAPI. Blue dotted circles represent 53BP1- nuclei, red ones 53BP1 positive nuclei. (G) Quantification of 53BP1 positive cells after siCTRL (n=1556 cells), siASPM (n=1224 cells) or Doxorubicine (n=681 cells) treatment. N = 6, n = 681-1556 cells; connected dots represent paired experiment. \*\*\*\*p < 0.0001, Fisher's exact test with Bonferroni correction. (H) Immunofluorescence images of RPE-1 cells treated with indicated treatments and stained for 53BP1 and DAPI. Light blue dotted circles represent 53BP1- nuclei, red ones 53BP1 positive nuclei. Scale bars =  $10 \mu m$  (I) Quantification of 53BP1 positive cells after siCTRL, siCTRL + barasertib, siWDR2, siWDR62 + barasertib treatments. N = 6, n = 1516-1883 cells; connected dots represent paired experiments. siCTRL vs siWDR62 p = 0.0082, siWDR62 vs siWDR62 + barasertib p = 0.0051, one-way Anova test. (J) Quantification of cell cycle duration (anaphase to anaphase) after indicated treatments. N = 3, n = 103 - 129 cells. siCTRL vs siWDR62 p = 0.0134, siWDR62 vs siWDR62+ barasertib p = 0.0085, one-way Anova test. (**K**) Immunofluorescence of RPE-1 cells after *siCTRL*, siNPL4 or siUBASH3B treatment stained for AuroraB and DAPI. Scale bars = 5  $\mu$ m (L and M) AuroraB intensity quantification in anaphase RPE-1 cells treated with siCTRL, siNPL4 or siUBASH3B. Y-axes indicate Aurora B intensity on DNA normalized to background; x-axes indicates the distance between the two DNA masses reflecting anaphase progression, dotted lines represent 95% confidence intervalls,

n = 77 -113 cells; \*p = 0.0369, \*\*p = 0.0034 (L) and \*p = 0.400 (M), Mann-Whitney test (N) Quantification of 53BP1 positive cells after indicated treatment. N=8, n = 1900-2790 cells, siCTRL vs siNPL4 p = 0.0094, siCTRL vs siUBASH3B p = 0.0274, one-way Anova test (O) Quantification of cell divisions after 5 days when compared to control depletion based on CFSE intensity in NPL4- and UBASH3B-depleted cells, N = 7, n = 38699 - 7511 cells; siCTRL vs siNPL4 p = 0.0083, siCTRL vs siUBASH3B p = 0.0382, one-way Anova test. All error bars represent SEM.

Figure 3 Doria, Ivanova et al. В C Depletion efficency Photoactivation assay Poleward flux Intensity normalized to ctrl Final time Time 0 Time 1 SICTRL Speed (µm/min) 1.0 0.5 Photoactivation distance 4 3 5 µm 5 µm 2 siCAMSAP1 sicamsap1 siCTRI SICAMSAPT SICTRL Ε F G WDR62 CAMSAP1 CAMSAP1 WDR62 Lagging chromosomes Centrin & CENP-A Normal division SICTRL 80 percentage (%) 60-5 µm 5 µr 40 20 siCAMSAP1 SICAMEARY 5 µm 5 µm 5 µm 5 µm WDR62 signal **CAMSAP1** signal siWDR62 2.5 Fold increase Fold increase 5 µm 5 µm 5 µm 0.5 SiCANS INDRES sicams ap1 sicamsap1 SICTRIL siNDR62 siCTRL siNDR62 sic Answir J K Poleward flux Photoactivation 2.0 Speed (µm/min) 1.0 0.5 SICTRL 5µm 5µm 5µm 5µm 5µm siCAMSAP1 sicamsap1 0.0 siNDR62 siCTRL SiCAMSAP1 5µm 5µm 5µm 5µm 5µm **Transient lagging** L chromosomes siWDR62 100 5µm 5µm 5µm 5µm 5µm percentage of cells (%) siCAMSAP1 +siWDR62 5µm 5µm 5µm 5µm 5µm SICANSAP162

sicamsap1

siCTRL

SIND R62

Figure 3: CAMSAP1 co-depletion rescues the transient lagging chromosomes in WDR62-depleted cells (A) Immunofluorescence of RPE-1 cells treated with siCTRL or siCAMSAP1 stained for CAMSAP1 and DAPI. (B) Quantification of normalized CAMSAP1 level in RPE-1 cells treated with siCTRL (n=55 cells) and siCAMSAP1 (n=47 cells). N = 3, n = 47-55 cells, p = 0.0103, student twotailed t-test. (C) Scheme of photoactivation assay for microtubules poleward flux measurement. (D) Quantification of microtubule poleward flux speed in RPE-1 PAGFP-atubulin cells treated with siCTRL and siCAMSAP1. N= 3, n = 33-39 cells, p = 0.0008, paired t-test. (E) Stills of RPE-1 GFP-Centrin1/GFP-CENPA cells in a normal anaphase or an anaphase with a transient lagging kinetochore. (F) Quantification of transient lagging chromosomes in 15 minutes live cell movies of RPE1 GFP-Centrin1/GFP-CENPA cells treated with siCTRL or siCAMSAP1, n = 66-71 cells, p = 0.0071, paired ttest. (G) Immunofluorescence images of RPE-1 cells treated with siCTRL, siCAMSAP1, siWDR62, or siCAMSAP1 + siWDR62, stained for CAMSAP1 (left panels), WDR62 (right panels) and DAPI. (H) Quantification of normalized CAMSAP1 levels in RPE-1 cells treated with indicated siRNAs. N=3, n = 66-95 cells, siCTRL vs siCAMSAP1 p = 0.0008, siCTRL vs siCAMSAP1 + siWDR62 p = 0.0013 in one-way Anova test. (I) Quantification of normalized WDR62 levels in RPE-1 cells treated with indicated siRNAs. N=3, n = 66-95 cells, siCTRL vs siCAMSAP1 \*\*\*\*p < 0.0001 in one-way Anova test. (J) Live cell images RPE-1 PAGFP-atubulin cells treated with siCTRL, siCAMSAP1, siWDR62, siCAMSAP1+siWDR62 before and after photoactivation (K) Quantification of microtubule poleward flux speeds in RPE-1 PAGFP-atubulin cells treated with siCTRL, siCAMSAP1, siWDR62, siCAMSAP1+siWDR62. N = 3, n = 28-47 cells, \*\*\*\*p < 0.0001, one-way Anova test. (L) Percentage of RPE-1 GFP-Centrin1/GFP-CENPA cells with transient lagging chromosomes after indicated siRNA treatments. Lagging chromosomes were quantified as shown in (E); N = 6-7; n = 54-73 cells; siCTRL $vs\ siCAMSAP1\ p=0.0062,\ siCTRL\ vs\ siWDR62\ p=0.0025,\ siWDR62\ vs\ siCAMSAP1+siWDR62\ p=0.0025,\ siWDR62\ p=0.0025,\ siW$ 0.0015, in one-way Anova test. All scale bars = 5  $\mu$ m.

Figure 4 Doria, Ivanova et al.

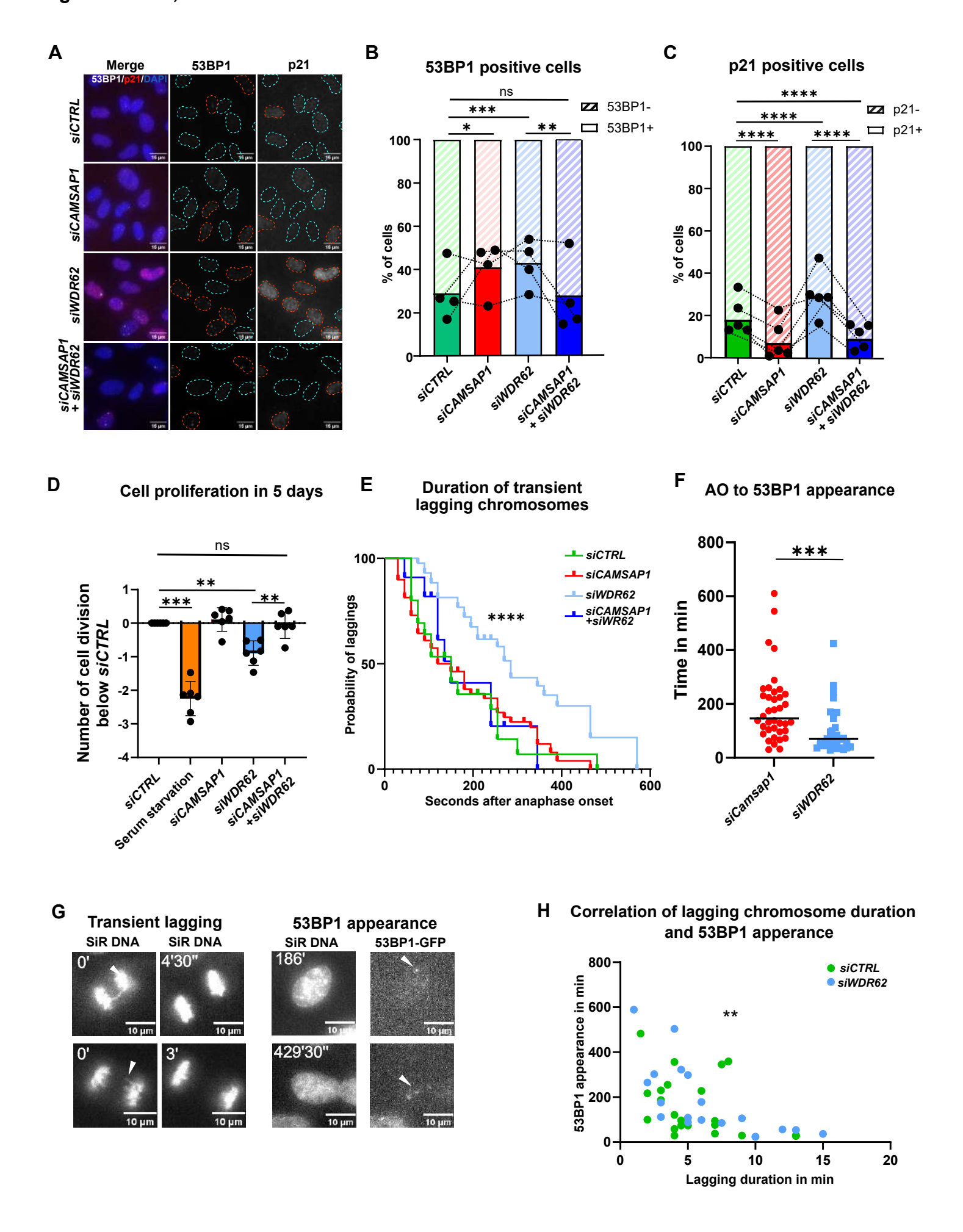


Figure 4: Camsap1 co-depletion rescues WDR62 RNAi phenotype. (A) Immunofluorescence images of interphase RPE1 cells treated with siCTRL, siCAMSAP1, siWDR62, siCAMSAP1+siWDR62 and Doxorubicin, stained with DAPI, 53BP1 and p21 antibodies. Blue dotted circles represent 53BP1negative nuclei, red ones 53BP1-positive nuclei. Scale bars = 10 µm. (B) Quantification of 53BP1 positive cells after indicated siRNA treatments. Connected dots represent paired experiment. N = 4, n = 648 - 1440 cells; siCTRL vs. siWDR62, p = 0.0006; siCTRL vs. siCAMSAP1, p = 0.0381; siWDR62vs. siCAMSAP1 + siWDR62, p = 0.0018, Fisher's exact test with Bonferroni correction. (C) Quantification of p21 positive cells in indicated siRNA treatments. Connected dots represent paired experiment. Blue dotted circles represent p21-negative nuclei, red one p21-positive nuclei. N = 5, n = 1020 - 1330 cells; \*\*\*\*p < 0.0001; Fisher's exact test with Bonferroni correction. (**D**) Quantification of cell divisions versus control depletion in CFSE assay in indicated treatments, N = 6, n = 69504-72579 cells;  $siCtrl\ vs$  serum starvation p = 0.0006,  $siCTRL\ vs$ . siWDR62, p = 0.0097:  $siWDR62\ vs$ . siCAMSAP1 + WDR62, p = 0.0022, one-way Anova test; error bars represent SEM. (E) Quantification of persistence of transient lagging chromosomes in live RPE1 GFP-CenpA/GFP-Centrin1 cells after indicated treatments, N = 4, n = 43 - 59 cells; siCAMSAP1 vs siWDR62 \*\*\*\*p < 0.0001 in Mann-Whitney test. (F) Time of 53BP1 foci appearance in siCAMSAP1 and siWDR62-treated RPE1 GRP-53BP1 live cells having experienced a lagging chromosome, N = 14, n =33-38 cells; \*\*\*p = 0.0001, Mann-Whitney test. (G) Live-cell imaging stills of WDR62-depleted GFP-53BP1 RPE1 cells stained with SiR-DNA; displayed is a cell with a rapidly resolved lagging chromosome (upper panels) or a slowly resolved lagging chromosome in anaphase (lower panel) with the corresponding panel showing the first appearance of a GFP-53BP1 focus (H) Scatter-plot of time of 53BP1 appearance vs persistence of transient lagging chromosomes, N = 15, n = 41 cells; r = -0.4410, \*\*p = 0.0039, Spearman correlation test.

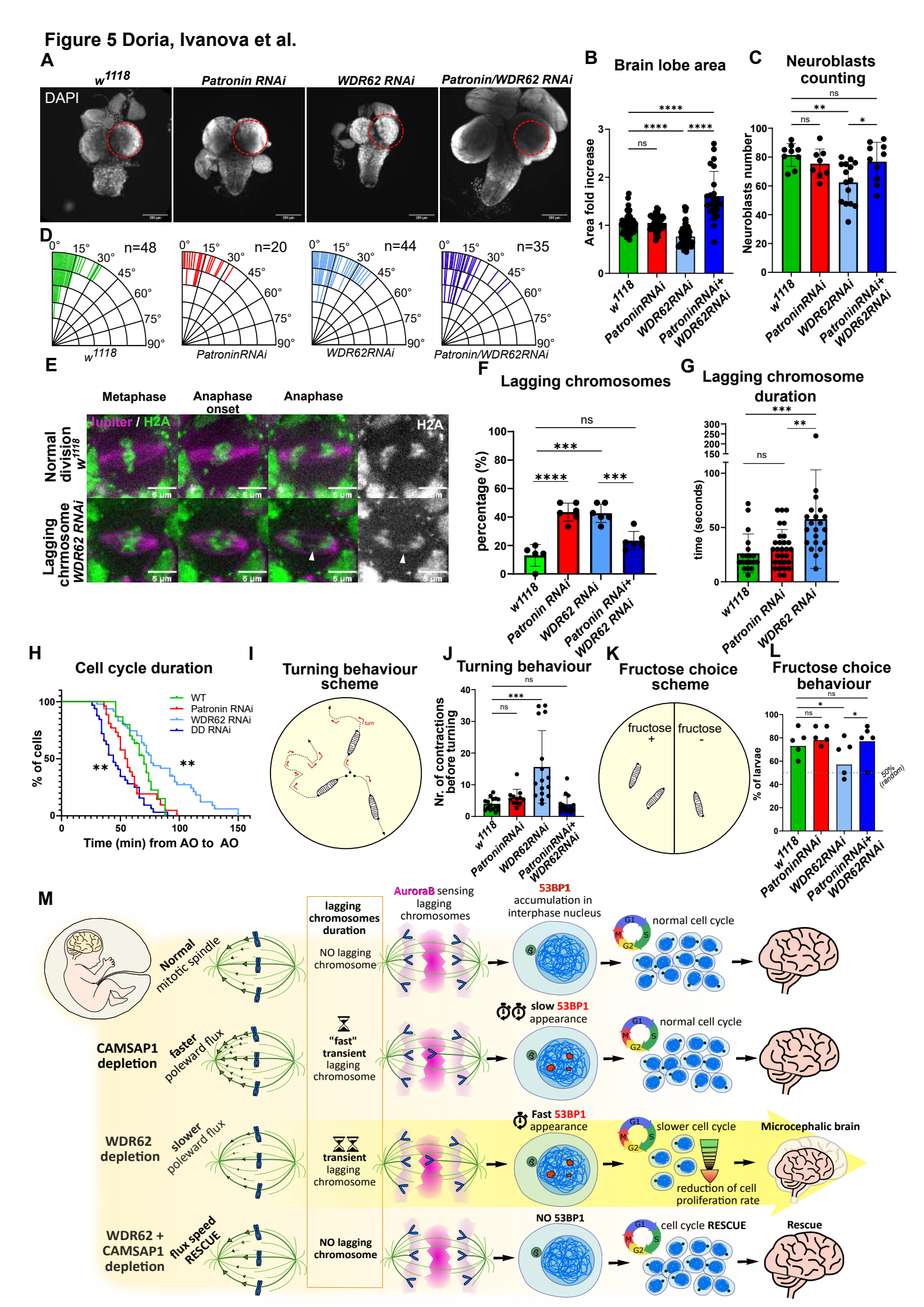


Figure 5: Co-depletion of Patronin rescues small brain phenotype in WDR62 RNAi background (A) Brains extracted from D. melanogaster larvae of w<sup>1118</sup>, PatroninRNAi, WDR62RNAi, and PatroninRNAi + WDR62RNAi, stained with DAPI. The dotted red circle represents the area of the right lobe from w<sup>1118</sup> brain superposed on PatroninRNAi, WDR62RNAi, PatroninRNAi+ WDR62RNAi brains. (**B**) Brain lobes area quantification of *D. melanogaster* larvae brains extracted from  $w^{1118}$  (n= 73 lobes), PatroninRNAi (n= 56), WDR62RNAi (n= 76), PatroninRNAi+ WDR6RNAi (n= 23) larvae., w<sup>1118</sup> vs WDR62RNAi p < 0.0001,  $w^{1118}$  vs PatroninRNAi + WDR62RNAi p < 0.0001, WDR62RNAi vs PatroninRNAi + WDR62RNAi p < 0.0001, one-way Anova test. (C) Quantification of neuroblast stained with Miranda antibodies in brains extracted from w<sup>1118</sup> (n= 9 brains), PatroninRNAi (n= 8), WDR62RNAi (n= 15), PatroninRNAi + WDR6RNAi (n= 10) larvae,  $w^{1118}$  vs WDR62RNAi p = 0.0041, WDR62RNAi vs PatroninRNAi + WDR62RNAi p = 0.0324, one-way Anova test. (D) Quantification ofthe spindle orientation angles (as determined in Fig.5E) in neuroblasts from D. melanogaster larvae brain lobes from w<sup>1118</sup> (n= 48 cells), PatroninRNAi (n= 20), WDR62RNAi (n= 44), PatroninRNAi+ WDR6RNAi (n=35) larvae, all non-significant, Kruskal-Wallis test. (E) Live cell imaging of WT (upper panel) or WDR62 RNAi neuroblasts in live larval brains in the Jupiter-Tomato/GFP-H2A strain. White arrow indicates lagging chromosome (F) Quantification of lagging chromosomes in indicated genetic background, n = 34-79 cells, W118 vs *PATRONIN RNAi* p < 0.0001, W118 vs *WDR62 RNAi* p < 0.0001,  $WDR62\ RNAi\ vs\ PATRONIN + WDR62\ RNAi\ p = 0.0004$  in one-way Anova test (G) Quantification of the duration of lagging chromosomes in W118 (n = 19 cells), PATRONIN RNAi (n = 29 cells) and  $WDR62\ RNAi\ (n=21\ cells)$  neuroblasts, W118 vs  $WDR62\ RNAi\ p=0.0004$ ,  $PATRONIN\ vs\ WDR62$ RNAI p = 0.0043, Kruskal-Wallis test (H) Quantification of cell cell cycle times in neuroblasts with indicated genetic background, n = 44 - 76 cells, W118 vs WDR62 RNAi p = 0.0096, W118 vs PATRONIN+WDR62 RNAi p = 0.0015, Log-rank Mantel-Cox test with Bonferroni correction (I) Scheme of larvae turning behaviour assay: the number of larva contraction before each change in direction was determined (see Supplementary Fig3E for examples of tracking). (J) Quantification of the contractions before change of direction in w<sup>1118</sup> (n=16 larvae), PatroninRNAi (n=12), WDR62RNAi (n= 16), Patronin RNAi+ WDR6RNAi (n= 15) larvae. w<sup>1118</sup> vs PatroninRNAi, w<sup>1118</sup> vs WDR62 RNAi p = 0.0001, WDR62 RNAi vs PatroninRNAi + WDR62RNAi p < 0.0001, Kruskal-Wallis test. (**K**) Scheme

of larvae fructose choice assay: the proportion of larvae on the half containing fructose was counted after 5 minutes of free movements (See Supplementary Fig5D for examples of tracking). (J) Quantification of larvae number on the Fructose-containing half after 5 minutes of movements of w<sup>1118</sup> (n=68 larvae), *PatroninRNAi* (n=58), *WDR62RNAi* (n=54), *PatroninRNAi*+ *WDR6RNAi* (n=53) larvae. w<sup>1118</sup> vs *PatroninRNAi*, w<sup>1118</sup> vs *WDR62RNAi* P = 0.0319, *WDR62RNAi* vs *PatroninRNAi*+ + *WDR62RNAi* P = 0.0390, Fisher's exact test. (M) Proposed model for the origin of primary microcephaly origin: We postulate that cells can can detect lagging chromosomes via the Aurora B activity gradient. If these lagging chromosomes are only briefly in contact with Aurora B, as is the case in many wild-type or more frequently in CAMSAP1-depleted cells (fast poleward microtubule flux speed), this may lead to a transient activation of 53BP1, but not an activation of p21. If these lagging chromosomes remain longer, as is the case in WDR62-depleted cells (slow poleward microtubule flux speed) this will lead to a rapid 53BP1 activation and p21 induction resulting in a cell cycle delay which can exhaust the neuroprogenitor cell pool. Re-equilibrating poleward microtubule flux rates by codepleting CAMSAP1 and WDR62 prevents transient lagging chromosomes and rescues the primary microcephaly phenotype.

#### SUPPLEMENTARY MATERIAL

#### MATERIALS AND METHODS

# Cell culture and drug treatments

hTert-RPE1 (ATCC: CRL-4000), hTert-RPE1-53BP1-GFP (kind gift of Réné Medema, Princess Maxima Center, Utrecht (*61*)), hTert-RPE1 GFP-Centrin1/GFP-CENPA (kind gift from A. Khodjakov, State University of New York), and hTert-RPE1 PAGFP-α-tubulin cell lines (*62*) were cultured in Dulbecco's Modified Eagle's Medium (DMEM; Thermo Fisher Scientific: 61965-026), supplemented with 10% FCS (Labforce, S181T), 100 U/ml penicillin and 100 mg/ml streptomycin (Life, 15140122). All cells were cultured at 37°C with 5% CO2 in a humidified incubator. For live-cell imaging, cells were cultured in eight-, four-, or two-well lbidi chambers (Vitaris) in Leibovitz's L-15 medium (Thermo

Fisher Scientific, 21083027) supplemented with 10% FCS before imaging for maximum 12 h in the absence of CO<sub>2</sub>. The following drugs were added to the culture or imaging medium: 10 μM MG132 (Sigma Aldrich, C2211-5MG) for 30 min, 100 nM Doxorubicin (Sigma, D1515) for 12 h, 50 nM Aurora B inhibitor Barasertib (AZD1152, S1147, Selleckchem), 50 nM SiR-Tubulin (Spirochrome, SC002) for 2 h, 100 nM SiR DNA (Spirochrome, SC007) for 2 h, 100 nM SpY DNA (Spirochrome, SC101) for 5 h.

# siRNA and plasmid transfections

For protein depletions, cells were transfected for 48 h in case of single depletions and 72 h in case of the double depletions with 20 nM siRNAs using Opti-MEM (Invitrogen, 31985-047) and Lipofectamine RNAiMAX (Invitrogen, 13778075) according to the manufacturer's instructions. For the double depletions, a double amount of Lipofectamine RNAiMAX was used. The medium was replaced 24 h after transfection. The following sense strands of validated siRNA duplexes were used (all Qiagen unless indicated): siASPM (16), 5'-GCU AUA UGU CAG CGU ACU ATT-3'; siCamsap1 (validated in Supplementary Figure 3) 5'-CAUCGAGAAGCUUAACGAATT-3'; siWDR62 (Dharmacon; (14)), 5'-AGA CAA AGG UGA CGA GCA C-3'; siNPL4 (39), 5'-CAGCCUCCUCCAACAAAUCdTdT-3'; siUBASH3B – 1 (40), 5'-CCGCTTAAGGATGCTAACATT-3', siUBASH3B – 2 (40), ), 5'-AAGAGAGTTGTTCTTAGGTTA-3' mixed 1:1 and as a negative control siCTRL (AllStars Negative Control siRNA; Qiagen, 1027281, Proprietary).

## **Immunofluorescence**

To stain for WDR62, 53BP1, p21, yH2AX, Aurora B, NPL4, UBASH3B hTert-RPE1 cells were fixed at -20°C for 7 min with ice-cold methanol stored at -20°C. To stain for CAMSAP1, MCAK, hTert-RPE1 cells were fixed at room temperature for 15 minutes with a solution containing 4% Formaldehyde (Applichem, A3592), 2mM of PIPES (Applichem, A1079.0500), pH 6.8, 1mM of EGTA (Applichem, A0878.0100), and 0.2% -Triton X-100 (Applichem, A4975.0100). To stain for α-tubulin cells were washed 30 seconds in a 37°C warm buffer containing 80mM M KOH-PIPES, 10mM MgC12 (Applichem, 131396.1211), 5mM EGTA, 0.5% Triton-X and fixed at room temperature for 10 minutes in a 12.5% Glutaraldehyde (Sigma Aldrich, G5882), 80mM KOH-PIPES, 10mM MgC12, 5mM EGTA

and 0.5% Triton-X solution. Cells were washed for 7 minutes in a freshly prepared 0.1% NaBH4 (Sigma Aldrich, 16940-66-2) in PBS quenching solution. The samples were washed twice for 2 minutes in PBS. After all fixations cells were rinsed with PBS and blocked 1 hour in blocking buffer (PBS + 3% BSA (LabForce, S181T) and 1% N<sub>3</sub>Na (Applichem, A1430). After blocking, cells were washed thrice for 5 minutes with PBS and incubated 1 hour with the primary antibody diluted in blocking buffer. Next, cells were washed twice in PBS and incubated 1 hour with the secondary antibody diluted in blocking buffer. Coverslips were mounted on microscopes slides with DAPI Vectashield mounting medium (Vector Laboratories, H1200).

The following primary antibodies were used: recombinant human anti-α-tubulin (1:500; (63)), rabbit anti-CAMSAP1(1:1500; Novus Biologicals NBP1-26645), rabbit anti-WDR62 (1:1000; Bethyl A301-560A), rabbit anti-MCAK (1:1000; (64)), rabbit anti-53BP1 (1:1000; Cell Signalling Technology 4937), mouse anti-p21 (1:1000; Cell Signalling Technology 2947), mouse anti-yH2Ax (1:2000; EMD Millipore, 05-636), mouse anti-AuroraB (1:2000; BD Biosciences 611083), rabbit anti-NPL4(1:500; Novus Biologicals NBP1-82166), rabbit anti-UBASH3B (1:500; Proteintech 19563-1-AP). For secondary antibodies, Alexa Fluor–conjugated antibodies (1:400; Invitrogen) were used. The pictures used for the analysis were acquired using 60× and 100× (NA 1.4) oil objectives on Olympus DeltaVision wide-field microscope (GE Healthcare) equipped with a DAPI/FITC/TRITC/Cy5 filter set (Chroma Technology Corp.) and Coolsnap HQ2 CCD camera (Roper Scientific) running Softworx (GE Healthcare). Alternatively, they were also acquired using a HC PL APO CS2 63x/1.40 Oil objective on a Leica Stellaris 5 confocal microscope equipped with 405 nm, 488nm, 561nm and 638 nm lasers and two Hybrid S detectors (HyD S1 and HyD S2) running LAS X software (version: 4.5.0.25531).

## Live-cell imaging

To monitor mitotic progression and chromosome segregation, hTert-RPE1 and hTert-RPE1-53BP1 GFP cells were seeded into Ibidi chambers (Vitaris) and treated with siRNAs as described above. Prior to imaging, cells were supplemented with L15 medium containing SiR DNA (Spirochrome #SC007) according to manufacturer protocole and recorded on a Nikon Eclipse Ti-E wide-field microscope (Nikon) equipped with a GFP/mCherry/Cy5 filter set (Chroma Technology Corp.), an Orca Flash 4.0

complementary metal-oxide-semiconductor camera (Hamamatsu), and an environmental chamber using NIS software (Nikon). For normal movies cells were imaged in the GFP and Cy5 channels for 12 h at 37°C, at 1-min 30 sec or 2 min intervals, in 17 steps of 1  $\mu$ m Z-stacks, using a 60× (NA 1.51) oil objective and 2 × 2 binning. To correlate the persistence of lagging chromosomes (SiR-DNA) and the timing of appearance of GFP-53BP1 foci, a first movie was recorded in the Cy5 channel for 1 h at 37°C at 30 sec intervals, in 17 steps of 1  $\mu$ m Z-stacks, using a 60× (NA 1.51) oil objective and 2 × 2 binning. The movie was stopped and restarted at the same positions using both the GFP and Cy5 channels for 12 h at 37°C at 3 min intervals, in 17 steps of 1  $\mu$ m Z-stacks, using a 60× (NA 1.51) oil objective and 2 × 2 binning. For cell cycle duration measurement, hTert-RPE1 cells were seeded into Ibidi chambers and treated with siRNAs as described above. Prior to imaging, cells were supplemented with Leibovitz's L-15 Medium and recorded on the same Nikon Eclipse Ti-E wide-field microscope using brightfield illumination for 30h at 37°C, at 3 min interval, in single plane, using a 10× objective and 2 × 2 binning.

# Anaphase kinetochore tracking assay

hTert-RPE1 GFP-centrin1/GFP-CENPA were treated with the reported siRNAs, and metaphase cells imaged for 15 min every 15 s using a 100× (NA 1.4) oil objective on an Olympus DeltaVision wide-field microscope (GE Healthcare) equipped with an environmental chamber maintained at 37°C and a GFP/RFP filter set (Chroma Technology Corp.). Z-stacks of 15-µm thickness with z-slices separated by 0.5 µm were imaged in the GFP channel with 2 × 2 binning to track kinetochores from metaphase until late anaphase. 4D images (XYZT) obtained were deconvolved in conservative mode and cropped using Softworx (GE Healthcare). The kinetochores and the poles were segmented using Imaris (Bitplane) during metaphase and anaphase. The kinetochores positions over time were analysed using a Matlab code ((14), https://github.com/AmandaGuerreiro/WDR62 2020).

## Poleward microtubule flux measurement

hTert-RPE1 PA-GFP- $\alpha$ -tubulin cells were incubated with 10  $\mu$ M MG132 for 30 minutes and imaged for 1 hour. Single focal planes of 150-nm pixel size were acquired using a 60× (NA 1.4) CFI Plan Apochromat oil objective on a Nikon A1r point scanning confocal microscope equipped with a 37°C heating chamber and running NIS elements software. A 3-pixel-thick and 100-pixel-long ROI parallel

to the DNA and close to spindle centre was photoactivated with a 500-ms, 405-nm laser pulse at 50–100% intensity depending on the PA-GFP-α-tubulin expression levels and imaged every 20 seconds for 4 min in a single focal plane. The photoactivated mark was tracked manually for 120 s with Fiji (ImageJ). Distance between the photoactivated mark and the corresponding spindle pole was tracked in time and the displacement of the photoactivated mark over time was calculated.

# Single cell sequencing

Cells were arrested in G1 phase using the CDK4/6 inhibitor Palbociclib (Cayman Chemical Company: 16273) at 100 nM for 12 hours. Cells were next sorted as single cells into a 384-well plate by FACS using the MoFlo Astrios cell sorter at the FACS facility of the Medical Faculty of the University of Geneva. At the single cell core facility of the ONCODE institute facility, nuclei in each well were digested with NlaIII, after which the genomic fragments (following end processing) were ligated to barcoded adapters containing a unique molecular identifier (UMI), cell-specific barcode, and T7 promoter allowing linear amplification by in vitro transcription (IVT). Libraries were sequenced on an Illumina Nextseq 500 at 16M reads. At the University of Geneva Bioinformatics facility, the raw fastq files were mapped to GRCH38 using the Burrows—Wheeler aligner. The mapped data were analyzed using custom scripts in R (available at GitHub: https://github.com/DIvanova-EDoria/master.git), which parsed for library barcodes, removed reads without a NlaIII sequence and removed PCR-duplicated reads. To perform quality control of the sequences, the following gates were set: minimum count: 10000 reads, maximum count: 75000 reads. The data which did not fail the QC were normalized to simulate the same amount of reads in every cell as following: 10000 \* value / sum(value).

# Metaphase spreads

Cells were incubated with 1mM Nocodazole (Sigma Aldrich, M1404-2MG) for 1h at 37C. Mitotic cells were shaken off, centrifuged and resuspended in 0.56% KCl (Applichem, A3582.0500) at room temperature for 6 min, before resuspending them dropwise in a 5 ml 3:1 MeOH/ CH3COOH (AppliChem, A2369) solution. The excess of supernatant was removed and 20ul of cells suspension was added dropwise on cooled microscopy slides (Epredia, 1.0mm) and left to dry in humid air chamber

for 1h. The metaphase spreads were mounted using DAPI Vectashield and Epredia cover slips 22x22 mm.

# CFSE labelling for cell proliferation assay

To measure cell proliferation over 5 days, hTert-RPE1, hTert-RPE1-PCNA-mRuby and hTert-RPE1-PCNA-mRuby p21 KO 2a (both kind gifts of Prof A. Barr, Imperial College London) cells were trypsinized, centrifuged, washed once with PBS, and resuspended in PBS at a concentration of  $1 \times 10^6$  cells/ml in the presence of 1  $\mu$ M CFSE (BioLegend, 423801) for 20 min at 37 °C. The CFSE was quenched by adding 5 times the original staining volume of cell culture medium for 10 min. After a final washing step, a fraction of the cells was resuspended in PBS with 20mM Tris (Applichem, A1379.5000) and 0.1% FCS and quantified by flow cytometry for reference (see below). The remaining cells was seeded and treated with siRNAs for 5 days. After 5 days of incubation, CFSE signal intensity was measured using 488 nm laser on Beckman Coulter Cytoflex.

# Image processing and 53BP1, p21 and γH2AX quantifications

Immunofluorescence images were first converted to z-stack (sum slices) using ImageJ/Fiji and opened in QuPath 0.4.3 (65). To quantify 53BP1, p21 or γH2AX, nuclei were segmented using the DAPI channel. To detect 53BP1 foci, a code was used to determine foci with a minimal area of 0.2 μm² and an intensity higher than the mean nuclear intensity plus 2 standard deviations. For p21 or γH2AX intensities, an automatized QuPath analysis was used to analyse p21 or γH2AX levels in segmented nuclei. The background was subtracted, and cells were counted as positive if their intensity was higher than the mean plus one standard deviation of the intensity in *siCTRL*-treated cells. Time-lapse movies were analysed manually with NIS Elements software to quantify mitotic timing and presence of 53BP1 foci, taking into account cells 4h after mitosis. Time-lapse movies were also analysed manually with NIS Elements software to quantify the presence of transient lagging chromosomes. These were quantified as present when DNA clouds in anaphase were > 6um apart and the lagging was > 2um long. For siRNA immunofluorescence quantification, 3D images were analysed manually with

ImageJ/Fiji. Aurora B intensity in anaphase was quantified using surface tool on DNA signal Imaris (Bitplane) 10.

All the data were plotted using GraphPad Prism 8.2.1.

# D. melanogaster strains

The following sources of different D. melanogaster lines were used in this study:

| Source          | Strain                            | ID   |
|-----------------|-----------------------------------|--|
| Régis Giet lab  | w; InscuteableGal4/Cyo (II)       | Bloomington <i>Drosophila</i> Stock centre: 8751 |
| Régis Giet lab  | w; Jupiter-GFP, His2Av-mRFP (III) | (47, 48)   |
| NIG-Fly         | w; UAS-Wdr62-RNAi (III)           | 7337-R1  |
| VDRC            | w; UAS-PatroninRNAi (II)          | 108927   |
| Emi Nagoshi lab | w <sup>1118</sup> <del>/-</del>   |  |

D. melanogaster fruit flies were raised at 25 °C in standard medium.

## Immunofluorescence of *D. melanogaster* brain larvae

3rd instar larvae were collected 120h after an egg laying of 5h. Larval brains were dissected in testis buffer (TB, 183 mM KCl, 47 mM NaCl, 10 mM Tris, and 1 mM EDTA, pH 6.8 MT) and brains were fixed at room temperature for 20 min in TB + 10% FA and 0.01% Triton-X. Brains were washed 2 times x 15 minutes in PBS and then 2 times x 15 minutes in PBS + 0.1% Triton-X. Brains were blocked for 1 hour in PBSTB (1% BSA, 0.1% Triton-X in PBS). Brains were incubated with the primary antibodies in PBSTB for 1 hour at room temperature. After 1 wash with PBS, brains were incubated with secondary antibodies in PBSTB for 1 hour at room temperature. After washes, samples were mounted on microscope slides with DAPI Vectashield mounting medium (to avoid brain deformation, for brain size measurements, spacer were used while mounting microscope slides).

The following primary antibody was used: rat anti-Miranda (1:500, Abcam, ab197788). For secondary antibodies, Alexa Fluor–conjugated antibodies (1:400; Invitrogen) were used. For neuroblast counting and spindle orientation experiments, images were acquired using a HC PL APO CS2 40x/1.40 air objective on a Leica stellaris 5 confocal microscope equipped with 405 nm, 488nm, 561nm and 638 nm lasers and two Hybrid S detectors (HyD S1 and HyD S2) running LAS X software (version: 4.5.0.25531). For brain size image acquisitions, a Nikon Eclipse Ti-E wide-field microscope (Nikon) equipped with a GFP/mCherry filter set (Chroma Technology Corp.), an Orca Flash 4.0 complementary metal-oxide-semiconductor camera (Hamamatsu), and an environmental chamber using NIS software was used.

To measure brain lobe sizes, the average diameter of one brain lobe was calculated as the mean of two measurements in orthogonal orientation (length + width / 2) using Fiji. The brain lobe shape was approximated to a circle shape and the area was calculated with the formula:  $Area=(\pi \times diameter^2)/4$  The number of neuroblasts in the central brain was calculated as the number of Miranda positive cells, manually using FIJI, and the average of the two lobes was reported. For spindle orientation, Fiji from ImageJ software was used to calculate the angle between the spindle poles axis and a line perpendicular to Miranda signal.

## Live cell imaging of *D. melanogaster* brain larvae

3rd instar larvae were collected 120h after an egg laying of 5h. Larval brains were dissected in Schneider's Drosophila Medium (Gibco, 21720024) and transferred in testis buffer into Ibidi chambers (Vitaris). Brains were then imaged on Nipkow spinning disk microscope equiped with EC Plan-Neofluar 10x / 0.3 Ph1 M27 WD=5.2mm and LCI Plan-Neoflur 63x / 1.3 Imm Korr DIC for Water Silicone Glycerole immersion WD=0.15-0.17 objectives and 405 nm, 488nm, 561nm and 638 nm lasers. For transient lagging chromosome and mitotic timing experiment, a 63x glycerol objective was used; metaphase cells were selected and recorded every 6 sec using 488nm and 561nm lasers until they were in late anaphase. QC gate of  $1\mu m$  was used to differentiate a transient lagging chromosome. For

cell cycle duration, a 10x objective was used and brains were acquired using 488nm and 561nm lasers every 2 min with a z-step of 1µm for a total of 31 steps.

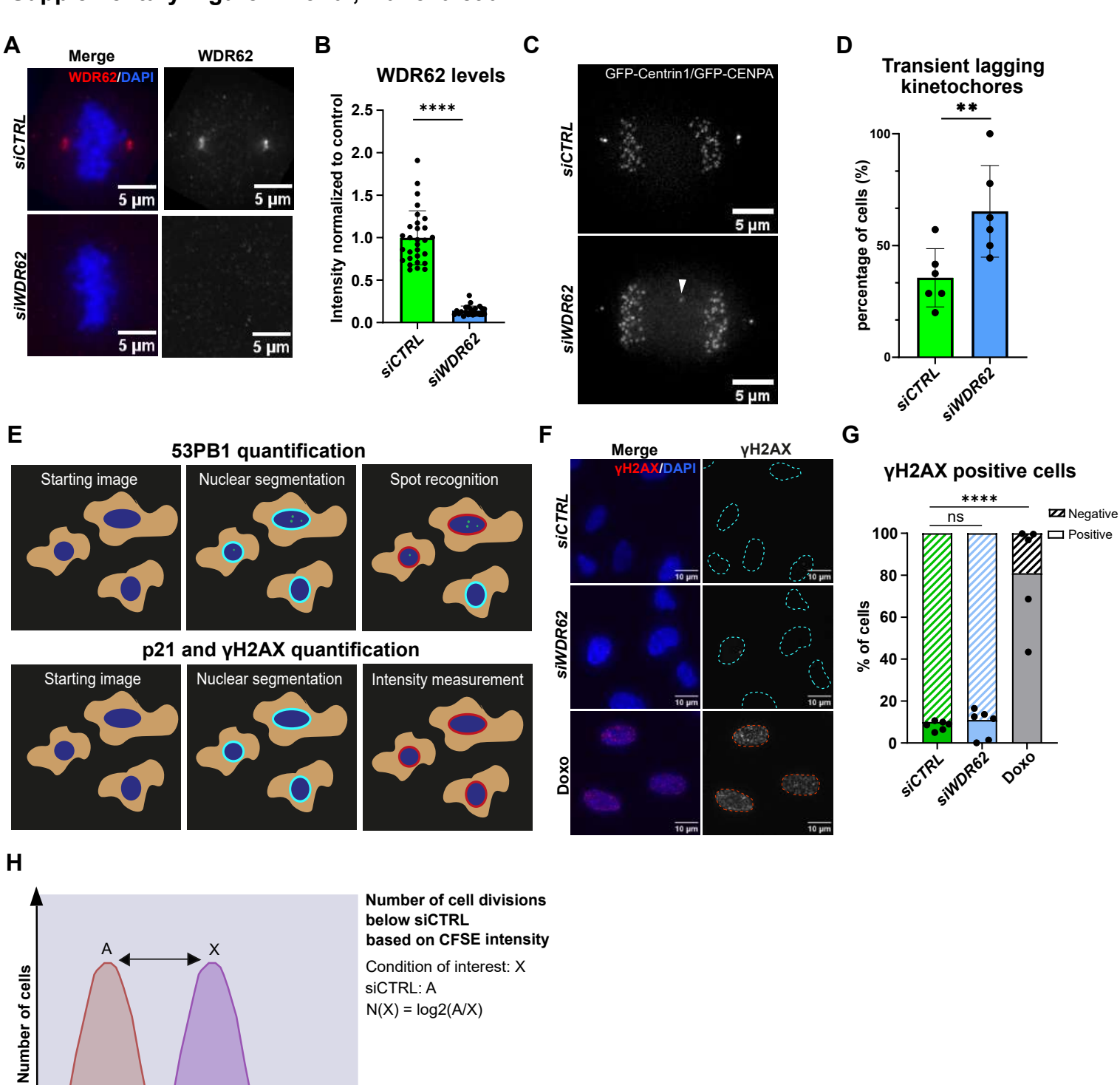
# **Cognitive tests**

For the running assay, all 3<sup>rd</sup> instar larvae were recorded directly after collection on a 0.8% agar 10 cm (500 ml water, 4 g agar (Roth, Karlsruhe)) surface. Prior to recording, larvae were briefly washed with PBS. Turning frequency is indicated as the number of peristaltic movements a larva needs to make before turning. Movies of 5 min were made and analysed by hand selecting a 1 min interval. For fructose assay, all 3<sup>rd</sup> instar larvae were recorded directly after collection on a 0.8% agar 10 cm (500 ml water, 4 g agar (Roth, Karlsruhe)) surface, containing in one half 0.2M Fructose (Sigma Aldrich, F0127, 3.6g in 100 ml 0.8% agar) and no fructose in the other half. Prior to recording, larvae were briefly washed with PBS. Fructose preference was evaluated by setting the larvae in the middle of the dish and allowing them to choose a side. The movements were recorded, and the final choice was analysed by the end of 5 min.

# SUPPLEMENTARY FIGURES

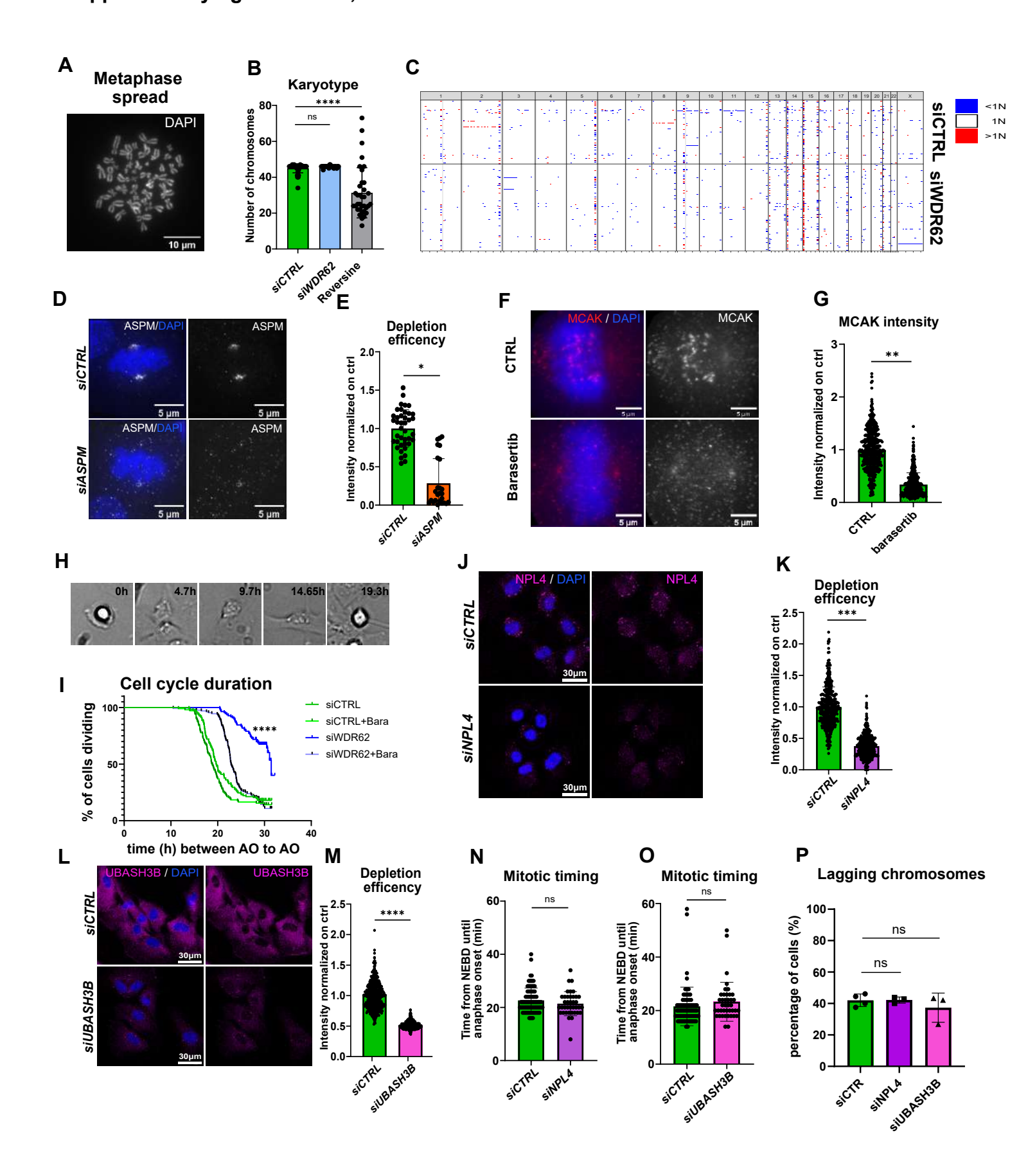
# Supplementary Figure 1 Doria, Ivanova et al.

**CFSE** intensity



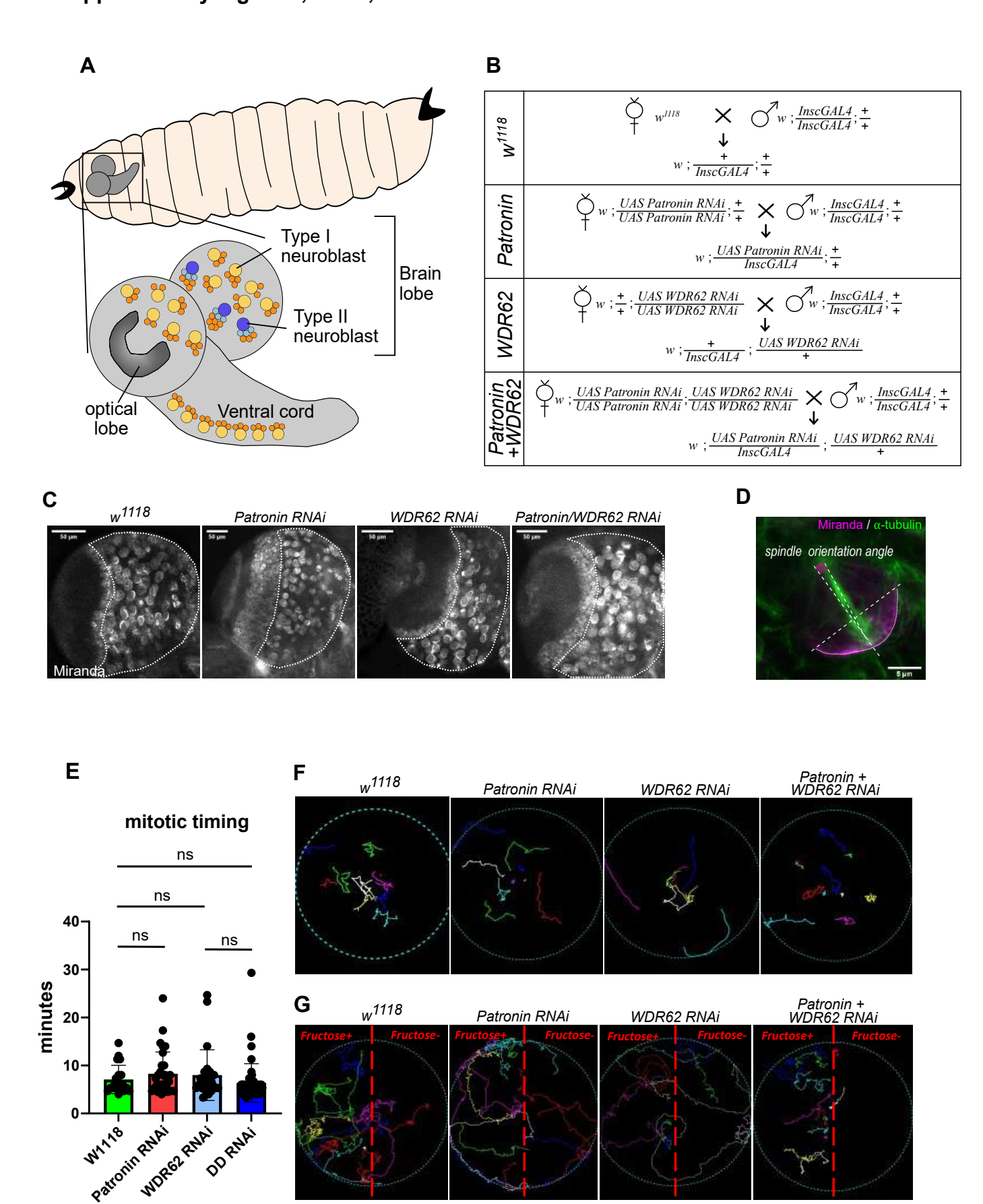
Supplementary Figure 1: WDR62 depletion, and quantification of γH2AX, 53BP1 and p21 (A) Immunofluorescence images of metaphase RPE1 cells treated with siCTRL and siWDR62 and stained with DAPI and WDR62 antibodies. Scale bars =  $5 \mu m$ . (B) Quantification of WDR62 levels in RPE1 cells treated with siCTRL or siWDR62 cells normalized to siCTRL values. N = 4 independent experiments, n = 49-81 cells, \*\*\*\*, p < 0.0001, unpaired t-test. Error bars represent SEM. (C) Live stills of GFP-centrin1/GFP-CENP-A RPE1 anaphase cells treated with siCTRL or siWDR62. White arrow indicates transient lagging chromosome in siWDR62-treated cell. (D) Quantification of GFP-Centrin1/GFP-CENP-A RPE1 cells with transient lagging chromosomes in anaphase after siCTRL or siWDR62 treatment. N= 6; n = 54-55 cells; \*\* p = 0.0015 in paired t-test. Note that the data represented here are a duplicate of the quantification in Figure 3L. (E) Schematic representation of automated 53BP1 (upper panel) and p21/yH2AX analysis (lower panel). Nuclei were segmented using DAPI staining, and, for 53BP1, foci were counted as positive if the spots displayed an intensity than was higher than the nuclear mean plus 2 standard deviations; for p21/yH2AX the intensity of nuclei in corresponding channel were measured and counted as positive if their intensity was higher than the mean plus one standard deviation in siCTRL-treated cells. (F) Immunofluorescence images of interphase RPE1 cells, treated with siCTRL, siWDR62 or 100 nM Doxorubicin, stained with DAPI and γH2AX antibody. Blue dotted circles represent γH2AX-negative nuclei, red ones γH2AX-positive nuclei. Scale bars = 10 µm. (G) Quantification of yH2AX positive cells after siCTRL, siWDR62 or Doxorubicin treatment. N = 6, n = 834 - 2234 cells; siCTRL vs. Doxorubicin, \*\*\*\*, p < 0.0001, Fisher's exact test with Bonferroni correction. (H) Schematic representation the Carboxyfluorescein succinimidyl ester (CFSE) assay: CFSE is a cell-permeable dye that covalently couples to intramolecular molecules via its succinimidyl group; since after a CFSE pulse its intensity decreases by half after each cell division, it can be used as a pulse-chase assay to quantify cell proliferation. In all our assays we compared the indicated siRNA-treatments to control depletion. To calculate the number of cell divisions above serum starvation we determined by FACS the peak intensity of a control-depleted cells (A) and divided it by the peak intensity of the condition of interest (X). The log2 of (A/X) indicates the number of divisions cells have undergone in comparison to control-depleted cells.

# Supplementary figure 2 Doria, Ivanova et al.



Supplementary Figure 2: ASPM, NPL4, UBASH3B siRNA validation and characterization (A) Chromosomes spread of RPE-1 cells stained with DAPI. Scale bar = 10 µm (B) Quantification of chromosomes number of RPE-1 cells treated with siCTRL, siWDR62 or Reversine. N = 7; n = 35-42 cells; siCTRL vs Reversine \*\*\*\*p < 0.0001, Kolgomornov-Smirnov test with Bonferroni correction (C) Heat map of chromosome parts copy number variations across 384 control-depleted or 384 WDR62depleted RPE1 cells (**D**) Immunofluorescence images of RPE-1 cells treated with *siCTRL* or *siASPM*, and stained for ASPM and DAPI. Scale bars =  $5 \mu m$  (E) Quantification of ASPM levels in RPE-1 cells treated with siCTRL and siASPM. ASPM intensity was normalized to siCTRL in each replicate. N = 3, n = 26-40 cells; p= 0.0230, student t-test. (F) Immunofluorescence image of RPE-1 cells treated with DMSO (CTRL), Barasetrib and stained for MCAK and DAPI. Scale bars =  $5 \mu m$  (G) Quantification of MCAK levels on kinetochores in RPE-1 cells treated with DMSO (CTRL) and Barasertib. MCAK intensity was measured on 10 kinetochores randomly selected per cell, MCAK values were normalized on the average intensity of the CTRL in each replicate. N = 3, n = 438-458 kinetochores, p = 0.0022, student t-test. (H) Phase-constrast live cell movies of RPE1 cells, illustrating how the cell cycle duration was determined using the time period between two anaphase onsets (I) Quantification of cell cycle time in the overall pool of cells subject to the indicated treatments. N = 3, n = 110-129 cells, \*\*\*\*p < 0.0001, Log-rank Mantel-Cox test with Bonferroni correction (J) Immunofluorescence images of RPE-1 cells treated with siCTRL or siNPLA stained for NPLA and DAPI. Scale bars = 5  $\mu$ m (**K**) Quantification of NPL4 levels in RPE-1 cells treated with siCTRL or siNPL4. NPL4 intensity was normalized to siCTRL in each replicate. N = 3, n = 419-430 cells; p = 0.0002, student t-test. (L) Immunofluorescence images of RPE-1 cells treated with siCTRL or siUBASH3B stained for UBASH3B and DAPI. Scale bars = 5 μm (M) Quantification of UBASH3B levels in RPE-1 cells treated with siCTRL or siUBASH3B. UBASH3B intensity was normalized to siCTRL in each replicate. N =3, n = 429-442 cells; \*\*\*\*p < 0.0001, student t-test. (N and O) Quantification of mitotic timing of RPE-1 cells treated with siCTRL, (N) siNPL4 or (O) siUBASH3B, based on SiR-DNA live cell movies. Mitotic time is calculated from nuclear envelope break down till anaphase onset. N = 3, n = 39-90 cells. ns in student t-test (P) Quantification of transient lagging chromosomes in live PRE-1 cells stained with SiR-DNA and treated with siCTRL, siNPL4 or siUBASH3B. ns in one-way ANOVA test.

# Supplementary Figure 3, Doria, Ivanova et al.



Supplementary Figure 3: (A) *D. melanogaster* larva brain scheme, (B) *D. melanogaster* crosses used for the experiments reported in Figure 5. Wild-type (w<sup>1118</sup>), *PatroninRNAi*, *WDR62RNAi*, *PatroninRNAi*+ *WDR6RNAi* flies were crossed with *InscGAL4* flies in order to obtain larvae expressing the RNAi in type I and type II neuroblasts. (C) Extracted *D. melanogaster* larvae brains from w<sup>1118</sup>, *PatroninRNAi*, *WDR62RNAi*, *PatroninRNAi*+ *WDR6RNAi* and stained for Miranda and DAPI. The dotted white line highlights the shape of lobes. (D) Immunofluorescence from a larva brain stained for Miranda and α-tubulin. Dotted lines represent the pole-to-pole axe and the cellular axe perpendicular to the Miranda signal (spindle orientation angle). The magenta line represents the angle between the 2 axes. (E) Quantification of mitotic time (nuclear envelope breakdown till anaphase) in neuroblasts of indicated genetic background. Errors bars indicate SEM. (F and G) Examples of tracking of w<sup>1118</sup>, *PatroninRNAi*, *WDR62RNAi*, *PatroninRNAi*+ *WDR6RNAi* larvae movements on agar plates. Each colour is a single larva tracking. In (D) the agar plates are composed of a half agar Fructose+ and the other half agar Fructose-.

#### REFERENCES

- 1. D. Jayaraman, B.-I. Bae, C. A. Walsh, The Genetics of Primary Microcephaly. *Annu. Rev. Genom. Hum. Genet.* **19**, 1–24 (2018).
- 2. R. S. O'Neill, T. A. Schoborg, N. M. Rusan, Same but different: pleiotropy in centrosome-related microcephaly. *Mol. Biol. Cell* **29**, 241–246 (2018).
- 3. E. A. Nigg, L. Čajánek, C. Arquint, The centrosome duplication cycle in health and disease. *FEBS letters* **588**, 2366–2372 (2014).
- 4. M. Nano, R. Basto, Cell Division Machinery and Disease. *Adv. Exp. Med. Biol.* **1002**, 19–45 (2017).
- 5. T. P. Phan, A. J. Holland, Time is of the essence: the molecular mechanisms of primary microcephaly. *Genes Dev.* **35**, 1551–1578 (2021).
- 6. V. Marthiens, M. A. Rujano, C. Pennetier, S. Tessier, P. Paul-Gilloteaux, R. Basto, Centrosome amplification causes microcephaly. *Nature cell biology* **15**, 731–740 (2013).
- 7. C.-T. Chen, H. Hehnly, Q. Yu, D. Farkas, G. Zheng, S. D. Redick, H.-F. Hung, R. Samtani, A. Jurczyk, S. Akbarian, C. Wise, A. Jackson, M. Bober, Y. Guo, C. Lo, S. Doxsey, A Unique Set of Centrosome Proteins Requires Pericentrin for Spindle-Pole Localization and Spindle Orientation. *Curr. Biol.* **24**, 2327–2334 (2014).

- 8. S. B. Lizarraga, S. P. Margossian, M. H. Harris, D. R. Campagna, A.-P. Han, S. Blevins, R. Mudbhary, J. E. Barker, C. A. Walsh, M. D. Fleming, Cdk5rap2 regulates centrosome function and chromosome segregation in neuronal progenitors. *Development* **137**, 1907–1917 (2010).
- 9. J. L. Fish, Y. Kosodo, W. Enard, S. Pääbo, W. B. Huttner, Aspm specifically maintains symmetric proliferative divisions of neuroepithelial cells. *Proceedings of the National Academy of Sciences of the United States of America* **103**, 10438–10443 (2006).
- 10. T. P. Phan, A. L. Maryniak, C. A. Boatwright, J. Lee, A. Atkins, A. Tijhuis, D. C. Spierings, H. Bazzi, F. Foijer, P. W. Jordan, T. H. Stracker, A. J. Holland, Centrosome defects cause microcephaly by activating the 53BP1-USP28-TP53 mitotic surveillance pathway. *EMBO J.* **40**, e106118 (2021).
- 11. S. Rasool, J. M. Baig, A. Moawia, I. Ahmad, M. Iqbal, S. S. Waseem, M. Asif, U. Abdullah, E. U. H. Makhdoom, E. Kaygusuz, M. Zakaria, S. Ramzan, S. ul Haque, A. Mir, I. Anjum, M. Fiaz, Z. Ali, M. Tariq, N. Saba, W. Hussain, B. Budde, S. Irshad, A. A. Noegel, S. Höning, S. M. Baig, P. Nürnberg, M. S. Hussain, An update of pathogenic variants in ASPM, WDR62, CDK5RAP2, STIL, CENPJ, and CEP135 underlying autosomal recessive primary microcephaly in 32 consanguineous families from Pakistan. *Mol. Genet. Genom. Med.* **8**, e1408 (2020).
- 12. J. N. Pulvers, J. Bryk, J. L. Fish, M. Wilsch-Bräuninger, Y. Arai, D. Schreier, R. Naumann, J. Helppi, B. Habermann, J. Vogt, R. Nitsch, A. Tóth, W. Enard, S. Pääbo, W. B. Huttner, Mutations in mouse Aspm (abnormal spindle-like microcephaly associated) cause not only microcephaly but also major defects in the germline. *Proc. Natl. Acad. Sci.* **107**, 16595–16600 (2010).
- 13. E. A. Tungadi, A. Ito, T. Kiyomitsu, G. Goshima, Human microcephaly ASPM protein is a spindle pole-focusing factor that functions redundantly with CDK5RAP2. *J. Cell Sci.* **130**, 3676–3684 (2017).
- 14. A. Guerreiro, F. D. Sousa, N. Liaudet, D. Ivanova, A. Eskat, P. Meraldi, WDR62 localizes katanin at spindle poles to ensure synchronous chromosome segregation. *J Cell Biol* **220**, e202007171 (2021).
- 15. J. Huang, Z. Liang, C. Guan, S. Hua, K. Jiang, WDR62 regulates spindle dynamics as an adaptor protein between TPX2/Aurora A and katanin. *J Cell Biology* **220**, e202007167 (2021).
- 16. K. Jiang, L. Rezabkova, S. Hua, Q. Liu, G. Capitani, A. F. M. Altelaar, A. J. R. Heck, R. A. Kammerer, M. O. Steinmetz, A. Akhmanova, Microtubule minus-end regulation at spindle poles by an ASPM–katanin complex. *Nat Cell Biol* **19**, 480–492 (2017).
- 17. M. Barisic, G. Rajendraprasad, Y. Steblyanko, The metaphase spindle at steady state Mechanism and functions of microtubule poleward flux. *Semin Cell Dev Biol* **117**, 99–117 (2021).
- 18. G. A. Pavlova, A. V. Razuvaeva, J. V. Popova, E. N. Andreyeva, L. A. Yarinich, M. O. Lebedev, C. Pellacani, S. Bonaccorsi, M. P. Somma, M. Gatti, A. V. Pindyurin, The role of Patronin in Drosophila mitosis. *Bmc Mol Cell Biology* **20**, 7 (2019).
- 19. M. C. Hendershott, R. D. Vale, Regulation of microtubule minus-end dynamics by CAMSAPs and Patronin. *Proc National Acad Sci* **111**, 5860–5865 (2014).
- 20. S. S. Goodwin, R. D. Vale, Patronin Regulates the Microtubule Network by Protecting Microtubule Minus Ends. *Cell* **143**, 263–274 (2010).

- 21. K. Jiang, S. Hua, R. Mohan, I. Grigoriev, K. W. Yau, Q. Liu, E. A. Katrukha, A. F. M. Altelaar, A. J. R. Heck, C. C. Hoogenraad, A. Akhmanova, Microtubule Minus-End Stabilization by Polymerization-Driven CAMSAP Deposition. *Dev. Cell* **28**, 295–309 (2014).
- 22. J. Atherton, K. Jiang, M. M. Stangier, Y. Luo, S. Hua, K. Houben, J. J. E. van Hooff, A.-P. Joseph, G. Scarabelli, B. J. Grant, A. J. Roberts, M. Topf, M. O. Steinmetz, M. Baldus, C. A. Moores, A. Akhmanova, A structural model for microtubule minus-end recognition and protection by CAMSAP proteins. *Nat. Struct. Mol. Biol.* **24**, 931–943 (2017).
- 23. O. Sen, J. U. Harrison, N. J. Burroughs, A. D. McAinsh, Kinetochore life histories reveal an Aurora-B-dependent error correction mechanism in anaphase. *Dev. Cell* **56**, 3405 (2021).
- 24. E. P. Rogakou, D. R. Pilch, A. H. Orr, V. S. Ivanova, W. M. Bonner, DNA double-stranded breaks induce histone H2AX phosphorylation on serine 139. *J. Biol. Chem.* **273**, 5858–68 (1998).
- 25. L. B. Schultz, N. H. Chehab, A. Malikzay, T. D. Halazonetis, P53 Binding Protein 1 (53bp1) Is an Early Participant in the Cellular Response to DNA Double-Strand Breaks. *J. Cell Biol.* **151**, 1381–1390 (2000).
- 26. Y. Uetake, G. Sluder, Prolonged prometaphase blocks daughter cell proliferation despite normal completion of mitosis. *Current biology: CB* **20**, 1666–1671 (2010).
- 27. B. G. Lambrus, V. Daggubati, Y. Uetake, P. M. Scott, K. M. Clutario, G. Sluder, A. J. Holland, A USP28–53BP1–p53–p21 signaling axis arrests growth after centrosome loss or prolonged mitosis. *J. Cell Biol.* **214**, 143–153 (2016).
- 28. F. Meitinger, J. V. Anzola, M. Kaulich, A. Richardson, J. D. Stender, C. Benner, C. K. Glass, S. F. Dowdy, A. Desai, A. K. Shiau, K. Oegema, 53BP1 and USP28 mediate p53 activation and G1 arrest after centrosome loss or extended mitotic duration. *J. Cell Biol.* **214**, 155–166 (2016).
- 29. C. S. Fong, G. Mazo, T. Das, J. Goodman, M. Kim, B. P. O'Rourke, D. Izquierdo, M.-F. B. Tsou, 53BP1 and USP28 mediate p53-dependent cell cycle arrest in response to centrosome loss and prolonged mitosis. *eLife* **5**, e16270 (2016).
- 30. W. S. El-Deiry, T. Tokino, V. E. Velculescu, D. B. Levy, R. Parsons, J. M. Trent, D. Lin, W. E. Mercer, K. W. Kinzler, B. Vogelstein, WAF1, a potential mediator of p53 tumor suppression. *Cell* **75**, 817–825 (1993).
- 31. S. L. Thompson, D. A. Compton, Proliferation of an euploid human cells is limited by a p53-dependent mechanism. *J Cell Biol* **188**, 369–381 (2010).
- 32. S. Santaguida, A. Tighe, A. M. D'Alise, S. S. Taylor, A. Musacchio, Dissecting the role of MPS1 in chromosome biorientation and the spindle checkpoint through the small molecule inhibitor reversine. *J Cell Biol* **190**, 73–87 (2010).
- 33. G. Lukinavičius, C. Blaukopf, E. Pershagen, A. Schena, L. Reymond, E. Derivery, M. Gonzalez-Gaitan, E. D'Este, S. W. Hell, D. W. Gerlich, K. Johnsson, SiR-Hoechst is a far-red DNA stain for live-cell nanoscopy. *Nature communications* **6**, 8497 (2015).
- 34. B. G. Fuller, M. A. Lampson, E. A. Foley, S. Rosasco-Nitcher, K. V. Le, P. Tobelmann, D. L. Brautigan, P. T. Stukenberg, T. M. Kapoor, Midzone activation of aurora B in anaphase produces an intracellular phosphorylation gradient. *Nature* **453**, 1132–1136 (2008).

- 35. O. Afonso, I. Matos, A. J. Pereira, P. Aguiar, M. A. Lampson, H. Maiato, Feedback control of chromosome separation by a midzone Aurora B gradient. *Science (New York, NY)*, 1251121 (2014).
- 36. K. Ramadan, R. Bruderer, F. M. Spiga, O. Popp, T. Baur, M. Gotta, H. H. Meyer, Cdc48/p97 promotes reformation of the nucleus by extracting the kinase Aurora B from chromatin. *Nature* **450**, 1258–1262 (2007).
- 37. E. H. Hinchcliffe, C. A. Day, K. B. Karanjeet, S. Fadness, A. Langfald, K. T. Vaughan, Z. Dong, Chromosome missegregation during anaphase triggers p53 cell cycle arrest through histone H3.3 Ser31 phosphorylation. *Nat. Cell Biol.* **18**, 668–675 (2016).
- 38. W. Lan, X. Zhang, S. L. Kline-Smith, S. E. Rosasco, G. A. Barrett-Wilt, J. Shabanowitz, D. F. Hunt, C. E. Walczak, P. T. Stukenberg, Aurora B Phosphorylates Centromeric MCAK and Regulates Its Localization and Microtubule Depolymerization Activity. *Curr. Biol.* **14**, 273–286 (2004).
- 39. G. Dobrynin, O. Popp, T. Romer, S. Bremer, M. H. A. Schmitz, D. W. Gerlich, H. Meyer, Cdc48/p97–Ufd1–Npl4 antagonizes Aurora B during chromosome segregation in HeLa cells. *J. Cell Sci.* **124**, 1571–1580 (2011).
- 40. K. Krupina, C. Kleiss, T. Metzger, S. Fournane, S. Schmucker, K. Hofmann, B. Fischer, N. Paul, I. M. Porter, W. Raffelsberger, O. Poch, J. R. Swedlow, L. Brino, I. Sumara, Ubiquitin Receptor Protein UBASH3B Drives Aurora B Recruitment to Mitotic Microtubules. *Dev. Cell* **36**, 63–78 (2016).
- 41. F. Calegari, W. B. Huttner, An inhibition of cyclin-dependent kinases that lengthens, but does not arrest, neuroepithelial cell cycle induces premature neurogenesis. *J. Cell Sci.* **116**, 4947–4955 (2003).
- 42. A. R. Nair, P. Singh, D. S. Garcia, D. Rodriguez-Crespo, B. Egger, C. Cabernard, The Microcephaly-Associated Protein Wdr62/CG7337 Is Required to Maintain Centrosome Asymmetry in Drosophila Neuroblasts. *Cell reports*, doi: 10.1016/j.celrep.2015.12.097 (2016).
- 43. A. H. Brand, N. Perrimon, Targeted gene expression as a means of altering cell fates and generating dominant phenotypes. *Development* **118**, 401–415 (1993).
- 44. E. Derivery, C. Seum, A. Daeden, S. Loubéry, L. Holtzer, F. Jülicher, M. Gonzalez-Gaitan, Polarized endosome dynamics by spindle asymmetry during asymmetric cell division. *Nature* **528**, 280–285 (2015).
- 45. N. R. Lim, B. Shohayeb, O. Zaytseva, N. Mitchell, S. S. Millard, D. C. H. Ng, L. M. Quinn, Glial-Specific Functions of Microcephaly Protein WDR62 and Interaction with the Mitotic Kinase AURKA Are Essential for Drosophila Brain Growth. *Stem Cell Rep.* **9**, 32–41 (2017).
- 46. S. X. Atwood, K. E. Prehoda, aPKC Phosphorylates Miranda to Polarize Fate Determinants during Neuroblast Asymmetric Cell Division. *Curr. Biol.* **19**, 723–729 (2009).
- 47. S. Heeger, O. Leismann, R. Schittenhelm, O. Schraidt, S. Heidmann, C. F. Lehner, Genetic interactions of separase regulatory subunits reveal the diverged Drosophila Cenp-C homolog. *Genes Dev.* **19**, 2041–2053 (2005).
- 48. X. Morin, R. Daneman, M. Zavortink, W. Chia, A protein trap strategy to detect GFP-tagged proteins expressed from their endogenous loci in Drosophila. *Proc. Natl. Acad. Sci.* **98**, 15050–15055 (2001).

- 49. W. Song, M. Onishi, L. Y. Jan, Y. N. Jan, Peripheral multidendritic sensory neurons are necessary for rhythmic locomotion behavior in Drosophila larvae. *Proc. Natl. Acad. Sci.* **104**, 5199–5204 (2007).
- 50. J. Bittern, M. Praetz, M. Baldenius, C. Klämbt, Long-Term Observation of Locomotion of Drosophila Larvae Facilitates Feasibility of Food-Choice Assays. *Adv. Biol.* **6**, e2100938 (2022).
- 51. J.-F. Chen, Y. Zhang, J. Wilde, K. C. Hansen, F. Lai, L. Niswander, Microcephaly disease gene Wdr62 regulates mitotic progression of embryonic neural stem cells and brain size. *Nature communications* 5, 3885 (2014).
- 52. F. Meitinger, H. Belal, R. L. Davis, M. B. Martinez, A. K. Shiau, K. Oegema, A. Desai, Control of cell proliferation by memories of mitosis. *Sci. (N. York, NY)* **383**, 1441–1448 (2024).
- 53. P. Risteski, J. Martinčić, M. Jagrić, E. Tintor, A. Petelinec, I. M. Tolić, Microtubule poleward flux as a target for modifying chromosome segregation errors. *Proc. Natl. Acad. Sci.* **121**, e2405015121 (2024).
- 54. A. D. McAinsh, G. J. P. L. Kops, Principles and dynamics of spindle assembly checkpoint signalling. *Nat Rev Mol Cell Bio*, 1–17 (2023).
- 55. S. Hervé, A. Scelfo, G. B. Marchisio, M. Grison, K. Vaidžiulytė, M. Dumont, A. Angrisani, A. Keikhosravi, G. Pegoraro, M. Deygas, G. P. F. Nader, A.-S. Macé, M. Gentili, A. Williart, N. Manel, M. Piel, Y. A. Miroshnikova, D. Fachinetti, Chromosome mis-segregation triggers cell cycle arrest through a mechanosensitive nuclear envelope checkpoint. *Nat. Cell Biol.* 27, 73–86 (2025).
- 56. D. Cimini, B. J. Howell, P. S. Maddox, A. L. Khodjakov, F. Degrassi, E. D. Salmon, Merotelic kinetochore orientation is a major mechanism of aneuploidy in mitotic mammalian tissue cells. *J Cell Biol* **153**, 517–527 (2001).
- 57. B. Orr, F. D. Sousa, A. M. Gomes, O. Afonso, L. T. Ferreira, A. C. Figueiredo, H. Maiato, An anaphase surveillance mechanism prevents micronuclei formation from frequent chromosome segregation errors. *Cell Reports* 37, 109783 (2021).
- 58. H. Maiato, S. Silva, Double-checking chromosome segregation. *J Cell Biology* **222**, e202301106 (2023).
- 59. C. L. Fonseca, H. L. H. Malaby, L. A. Sepaniac, W. Martin, C. Byers, A. Czechanski, D. Messinger, M. Tang, R. Ohi, L. G. Reinholdt, J. Stumpff, Mitotic chromosome alignment ensures mitotic fidelity by promoting interchromosomal compaction during anaphase. *J. Cell Biol.* **218**, 1148–1163 (2019).
- 60. S. Matsuura, Y. Matsumoto, K. Morishima, H. Izumi, H. Matsumoto, E. Ito, K. Tsutsui, J. Kobayashi, H. Tauchi, Y. Kajiwara, S. Hama, K. Kurisu, H. Tahara, M. Oshimura, K. Komatsu, T. Ikeuchi, T. Kajii, Monoallelic BUB1B mutations and defective mitotic-spindle checkpoint in seven families with premature chromatid separation (PCS) syndrome. *Am. J. Méd. Genet. Part A* **140A**, 358–367 (2006).
- 61. A. Janssen, M. van der Burg, K. Szuhai, G. J. P. L. Kops, R. H. Medema, Chromosome Segregation Errors as a Cause of DNA Damage and Structural Chromosome Aberrations. *Science* **333**, 1895–1898 (2011).

- 62. A. Toso, J. R. Winter, A. J. Garrod, A. C. Amaro, P. Meraldi, A. D. McAinsh, Kinetochore-generated pushing forces separate centrosomes during bipolar spindle assembly. *J Cell Biol* **184**, 365–372 (2009).
- 63. A. Guerreiro, P. Meraldi, AA344 and AA345 antibodies recognize the microtubule network in human cells by immunofluorescence. *Antib Reports* **2**, e17 (2019).
- 64. A. C. Amaro, C. P. Samora, R. Holtackers, E. Wang, I. J. Kingston, M. C. Alonso, M. A. Lampson, A. D. McAinsh, P. Meraldi, Molecular control of kinetochore-microtubule dynamics and chromosome oscillations. *Nature cell biology* **12**, 319–329 (2010).
- 65. P. Bankhead, M. B. Loughrey, J. A. Fernández, Y. Dombrowski, D. G. McArt, P. D. Dunne, S. McQuaid, R. T. Gray, L. J. Murray, H. G. Coleman, J. A. James, M. Salto-Tellez, P. W. Hamilton, QuPath: Open source software for digital pathology image analysis. *Sci. Rep.* **7**, 16878 (2017).

# Additional results to "Transient lagging chromosomes cause primary microcephaly"

In our preprint, we describe a mechanism of WDR62 dependent primary microcephaly. We believe that transient lagging chromosomes caused by perturbations of poleward microtubule flux at the microtubule minus-ends are at the core of this disease. We find that recognition of transient lagging chromosomes relies on Aurora B gradient during anaphase. The increase in transient lagging chromosomes leads to 53BP1-p21 dependent cell cycle delay and ultimately results in smaller brain.

The following results are complimentary to the preprint "Transient lagging chromosomes cause primary microcephaly", where I try to go in a more detail about the microtubule dynamics in WDR62 depletion, nuclear form, 53BP1 mechanism and cell cycle delay. Furthermore, I investigate depletion of other microcephaly genes for presence of transient lagging chromosomes.

# WDR62 depletion leads to aberrant microtubule dynamics

Previously, we have published that WDR62 depletion leads to Katanin mis-localization at the microtubule minus-ends, which leads to a decrease in microtubule poleward flux at the minus-ends. To verify this result, I have depleted WDR62 in the hTert-RPE1 PA (photoactivatable) GFP-α-tubulin cell line (Toso et al. 2009). As shown in the schematic, a thin 3-pixel-thick and 100-pixel-long ROI parallel to the DNA of GFP-Tubulin on the mitotic spindle was photoactivated with a 500-ms, 405-nm laser pulse at 50–100% intensity, depending on the PA-GFP-α-tubulin expression levels. The cell was then imaged every 20 seconds for 4 min in a single focal plane. As can be seen in Figure 1A, this acquisition allowed us to follow the movement of photoactivated GFP-Tubulin on the mitotic spindle as a readout of microtubule poleward flux (incorporation of tubulin dimers at the microtubule plus end, their conveyor belt-like fluxing through the microtubule, and their removal from the minus-ends of the microtubule, Mitchison et al. 1986). We have repeated this experiment for the siRNA Control depletion and siWDR62 depletion and have confirmed that WDR62 depletion leads to slower poleward microtubule flux, as can be seen in Figure 1A. As has been shown previously (Guerreiro et al. 2021), MG132 arrest in metaphase does not change the spindle length; therefore, we have concluded that with constant spindle length, WDR62 depletion leads to slower poleward microtubule flux.

In Guerreiro et al. 2021, we have found that WDR62 depletion increases microtubule stability. To understand more deeply the mechanisms of WDR62-dependent microtubule stability, we have decided to investigate KT-MT occupancy. It was described previously that a decrease in microtubule stability induced by BAL27862 leads to decreased KT-MT occupancy (Dudka et al. 2018). As WDR62 depletion was shown to increase microtubule stability (Guerreiro et al. 2021), we decided to test if this would result in an increased number of microtubules per k-fiber. To do so, we have used transmission electron microscopy (EM), which has been the gold standard for quantifying microtubule number in each k-fiber (Wendell et al. 1993, Dudka et al. 2018). To do so, cells in mitosis were enriched and separated from interphase cells using mitotic shake-off. The cells were then fixed, embedded in epon resin, and sliced into thin sections. The sections were visualized, and chromosomes were located (see an example of a section view, Figure 1C, Dudka et al. 2018). The microtubules close to the chromosomes were imaged, and k-fibers were quantified in post-imaging analysis. The k-fiber was identified as a k-fiber if it was within 1 µm from the chromosome, having at least 7 microtubules separated from each other by not more than 80 nm (Figure 1C) as proposed previously (Dudka et al 2018). Using these gates, the number of microtubules per k-fiber was quantified in siRNA Control and siWDR62. As can be seen from the quantification, surprisingly, the number of microtubules per k-fiber almost does not differ in siWDR62 compared to siRNA Control, despite increased microtubule stability in siWDR62 cells. This result suggests that the microtubule stability of siWDR62-depleted cells must result from another mechanism.

To understand if microtubule stability in siWDR62-depleted cells is only a feature of kinetochore microtubules, we have decided to analyze the number of non-kinetochore microtubules. For this, I have used the hTert-RPE1 eGFP- $\alpha$ Tubulin cell line and SiR-Tubulin. Indeed, SiR-Tubulin is known to bind only the microtubules with slow kinetics, which are either k-fibers or not free microtubules (David et al. 2019). Therefore, by co-staining the hTert-RPE1 eGFP- $\alpha$ Tubulin cell line with SiR-Tubulin, I was able to discriminate the unstable non-kinetochore microtubules. The ratio of GFP-Tubulin to SiR-Tubulin is used in this case as a proxy for the number of non-kinetochore microtubules. To understand how the number of non-kinetochore microtubules changes depending on their localization on the spindle, I have analyzed the pole-to-pole profile of SiR-Tubulin, which reflects mostly the k-fibers, and GFP-Tubulin, which reflects all microtubules. As can be seen from the quantification (Figure 1G), siWDR62-depleted cells display a higher amount of non-kinetochore microtubules compared to control, leading us to hypothesize that WDR62 depletion also leads to changes in non-kinetochore microtubules.

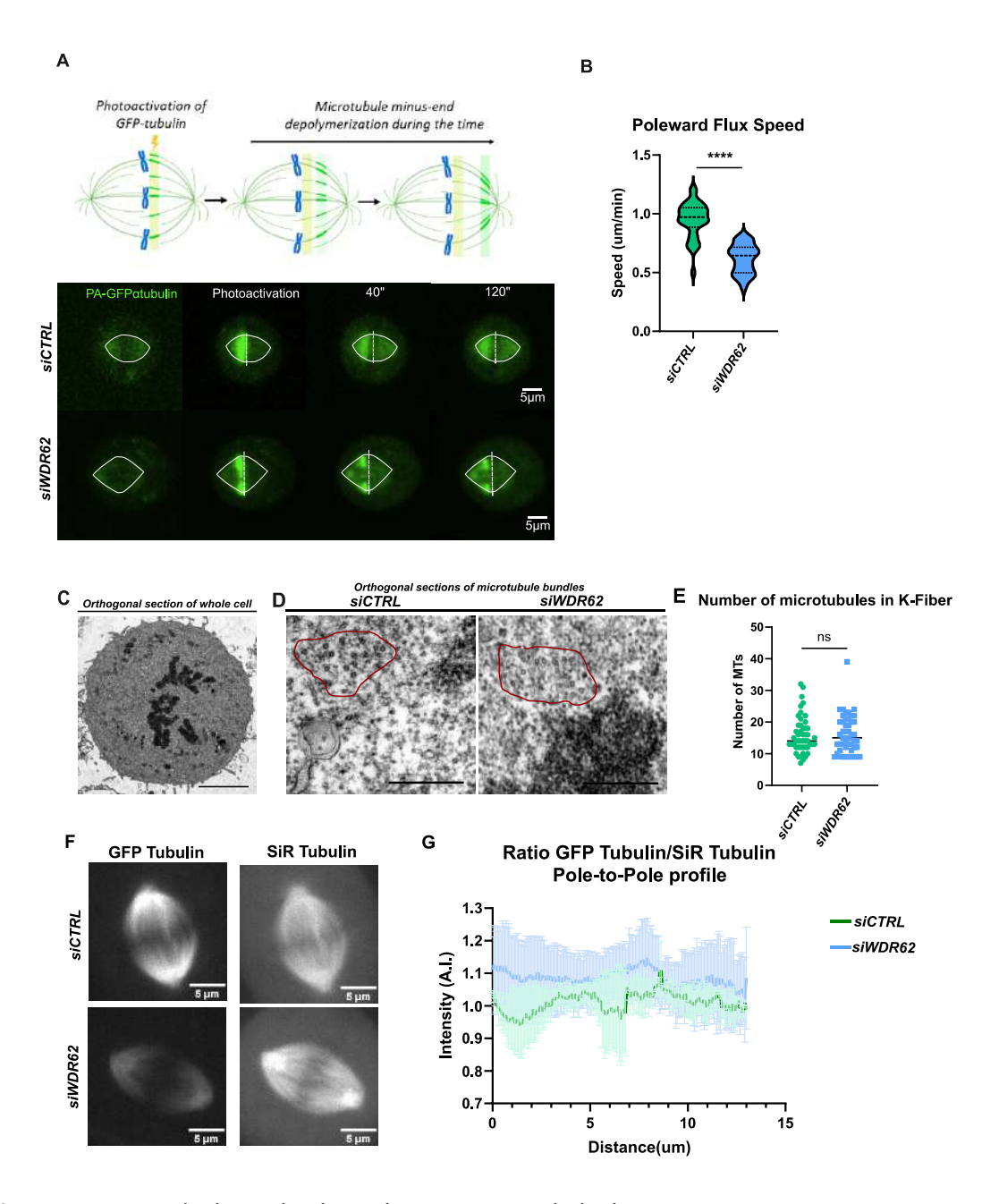


Figure 1: WDR62 depletion leads to aberrant microtubule dynamics

- (A) Schematic example and images of photoactivable RPE- PAGFP Tubulin mechanism. A thin strip of tubulin is activated using 488nm laser and the movies are recorded while following displacement of activated tubulin strip.
- (B) Difference in speed of poleward microtubule flux in WDR62 depleted cells compared to control. N = 3, n = 28-47 cells, \*\*\*\*p < 0.0001, student t-test.
- (C) Transmission electron microscopy orthogonal section of hTERT- RPE cells. Example of whole cell at low magnification. Scale bars =  $5 \mu m$ .
- (D) Orthogonal sections of hTERT- RPE cells treated with siCTRL and siWDR62, blocked in metaphase with 10  $\mu$ M MG132 and imaged by transmission electron microscopy. Images show individual KT fibres (red ROIs). KT fibres were defined as a set of at least 7 parallel MTs, in the vicinity of chromatin and not more than 80 nm separated from one another. Scale bar= 500 nm.
- (E) Quantification of microtubule number per k-fiber in siCTRL vs siWDR62 cells. N = 7, n = 6-7 cells per experiment and condition, p = ns, student t-test.

- (F) Examples of RPE aTubulin GFP cells treated with siCTRL and siWDR62. On the left aTubulin GFP and on the right SiR tubulin channels in metaphase. Scale bar= 5um
- (G) Pole to pole intensity profile ratio between GFP Tubulin and SiR Tubulin. Green siCTRL, blue siWDR62. The bold line represents the mean values as a function of space and shaded area represents standard deviations. N=3 independent experiments, 5 cells per condition and experiment.

#### Other primary microcephaly genes lead to transient lagging chromosomes

There are more than 30 different genes that are implicated in primary microcephaly, with 60% of them being related to cell division and the cell cycle (Jaramayan et al 2018). However, how they lead to primary microcephaly still remains unknown. As we have described, WDR62 and ASPM depletion both lead to transient lagging chromosomes, which causes an increase in the number of 53BP1-positive cells (Guerreiro et al. 2021, Doria & Ivanova 2024 et al, BioRxiv). We therefore wanted to test if the depletion of other MCPH-related genes can cause transient lagging chromosomes. To do so, we have depleted CDK5RAP2 (MCPH3), first identified in 2000 as an MCPH gene (Moynihan et al. 2000), in hTERT-RPE1 cells. CDK5RAP2 is a protein that allows the centrosomal localization of γ-tubulin and promotes microtubule nucleation (Fong et al. 2008).

To visualize chromosome segregation, we used SiR-DNA dye and imaged the cells every minute using a 60× objective. Post-imaging analysis identified almost a two-fold increase in the presence of transient lagging chromosomes in siCDK5RAP2 cells, as can be seen in Figure 2B. Additionally, we have depleted a centriolar assembly protein, SAS6, which has also been identified in primary microcephaly as MCPH14 (Khan et al. 2014). Following SAS6 depletion, I also determined a significant increase in transient lagging chromosomes.

Overall, these data suggest that transient lagging chromosomes might be a common feature of several microcephaly gene depletions in which mitosis and microtubule genes have been mutated.

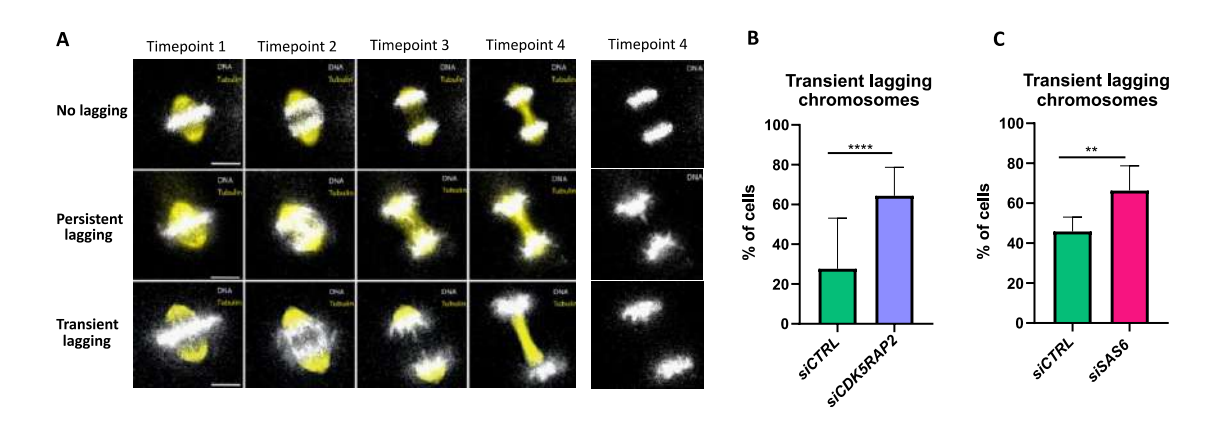


Figure 2: Other primary microcephaly genes can lead to transient lagging chromosomes

- (A) Examples of persistent, transient and non-lagging chromosomes during anaphase. Time interval: 1 min. SiR Tubulin in yellow, SiR DNA in grey. Scalebar:  $5 \mu m$ .
- (B) Quantification of % of cells displaying transient lagging chromosomes in siCTRL vs siCDK5RAP2. N = 3 independent experiments, 5-25 cells per experiment. \*\*\*\*p < 0.0001, Fisher's exact test.
- (C) Quantification of % of cells displaying transient lagging chromosomes in siCTRL vs siSAS6. N = 3 independent experiments, 6-14 cells per experiment. p=\*\*, Fisher's exact test.

#### USP28 might be important for 53BP1 upregulation in siWDR62

To investigate more deeply the mechanism of WDR62-induced transient lagging chromosomes, we wanted to test the mechanism of 53BP1 appearance. It has been found recently that 53BP1 has an additional role beyond the canonical DNA damage response, which is mitotic surveillance (Meitinger et al. 2021, 2024; Lambrus et al. 2016; Fong et al. 2016). In these studies, it has been shown that 53BP1 colocalizes with USP28 for mitotic surveillance mechanisms.

To test if USP28 was also involved in the transient lagging chromosome recognition mechanism, we took advantage of USP28 KO in hTERT-RPE cells (a kind gift from Franz Meitinger, Meitinger et al. 2024). In USP28 KO cells, we depleted WDR62 and tested if this would decrease the number of 53BP1-positive cells. Indeed, the depletion of WDR62 in the USP28 -/- background led to a decrease in the number of 53BP1-positive cells compared to siWDR62 in the parental cell line. While this result is yet preliminary, it seems like USP28 is important for 53BP1 accumulation in WDR62-depleted cells. This result, however, needs to be strengthened by additional independent replicates.

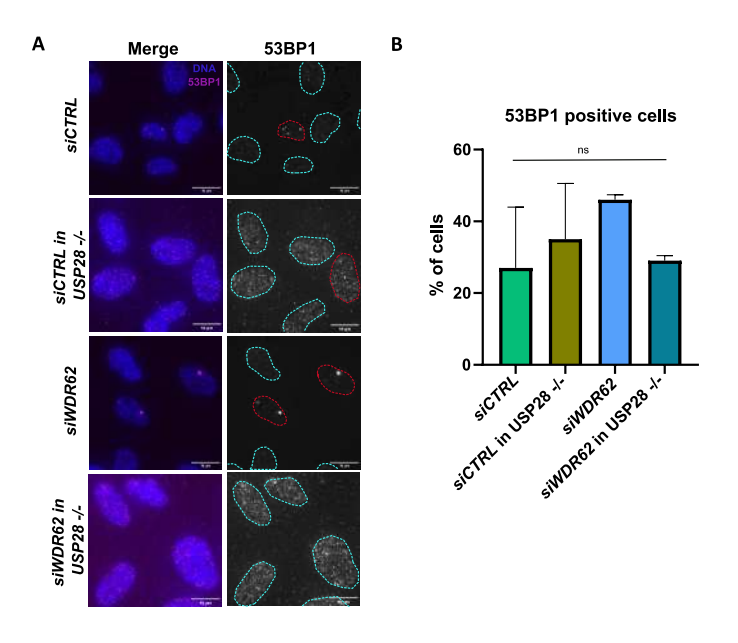


Figure 3: USP28 is important for 53BP1 upregulation in siWDR62

- (A) Example images of 53BP1 staining in siCTRL and siWDR62 in parental cell line and siCTRL and siWDR62 in USP28  $^{-/-}$  cell line. Light blue dotted ROIs represent 53BP1 negative nuclei, red ones 53BP1 positive nuclei. Scale bars = 10  $\mu$ m.
- (B) Quantification of 53BP1 positive cells (in %) in siCTRL and siWDR62, in the parental cell line and in the USP28 -/- cell line. N=2 independent experiments, 300 cells per experiment and experiment. p=ns, student t-test.

#### Persistent lagging chromosomes lead to 53BP1 appearance

Previously, it has been shown that persistent lagging chromosomes are recognized by the Aurora B gradient (Orr et al. 2021, Papini et al. 2021). However, the involvement of 53BP1 in persistent lagging chromosomes and its dependence on the Aurora B gradient remain unclear. Here, we take advantage of the inhibitor Reversine (an MPS-1 inhibitor) to block the spindle assembly checkpoint and generate persistent lagging chromosomes. Indeed, as described previously (see Introduction), the spindle assembly checkpoint is important for the recognition of erroneously attached chromosomes. MPS-1 plays a central role in SAC, binding to the NDC80 complex on the unattached kinetochore, phosphorylating Knl1 (Hiruma et al. 2015), and recruiting Bub1-Bub3, which ultimately leads to the recruitment of the Mad1-Mad2 complex (Mora-Santos et al. 2016). Erroneous attachments are known to generate persistent lagging chromosomes (Thompson & Compton 2011).

Once MPS-1 was inhibited, we measured the occurrence of persistent lagging chromosomes using live-cell imaging with SiR-DNA. As can be seen in Figure 3A, most of the cells displayed persistent lagging chromosomes compared to control hTERT-RPE1 cells. Using hTERT-RPE1-53BP1-GFP (a kind gift from René Medema, Princess Máxima Center, Utrecht; Janssen et al. 2011), we decided to investigate the appearance of 53BP1 foci following persistent lagging chromosomes and if it can be rescued using the Aurora B inhibitor Barasertib. As can be seen in Figure 3B, the majority of persistent lagging chromosomes (around 90%) led to 53BP1 appearance. The treatment of MPS-1-inhibited RPE cells with Barasertib, on the other hand, led to an almost three-fold decrease in 53BP1 appearance. This result allows us to hypothesize that Aurora B is involved in the recognition of various types of lagging chromosomes, confirming previously published results (Papini et al. 2021, Orr et al. 2021). Additionally, most of the cells displayed micronuclei after cell division, a sign of persistent lagging chromosomes (Krupina et al 2021).

An interesting observation we made was that 53BP1 never localized in a micronucleus and was always found in the main nuclear body. As previously described in Crasta et al. 2012, where the authors examined the recruitment of DNA damage proteins to micronuclei, many micronuclei display an abnormal laminar structure, making it impossible to recruit DNA damage response proteins, such as

53BP1. In our study, we decided also to test this in our cells and stained the hTERT-RPE1 cells treated with Reversine for nucleoporin. Indeed, as can be seen in Figure 3C, the micronucleus was devoid of nucleoporin (NUP62). Quantifications of nucleoporin intensity demonstrated that micronuclei have lower nucleoporin intensity compared to the main nucleus, signifying a defective envelope (Marelli et al 2021).

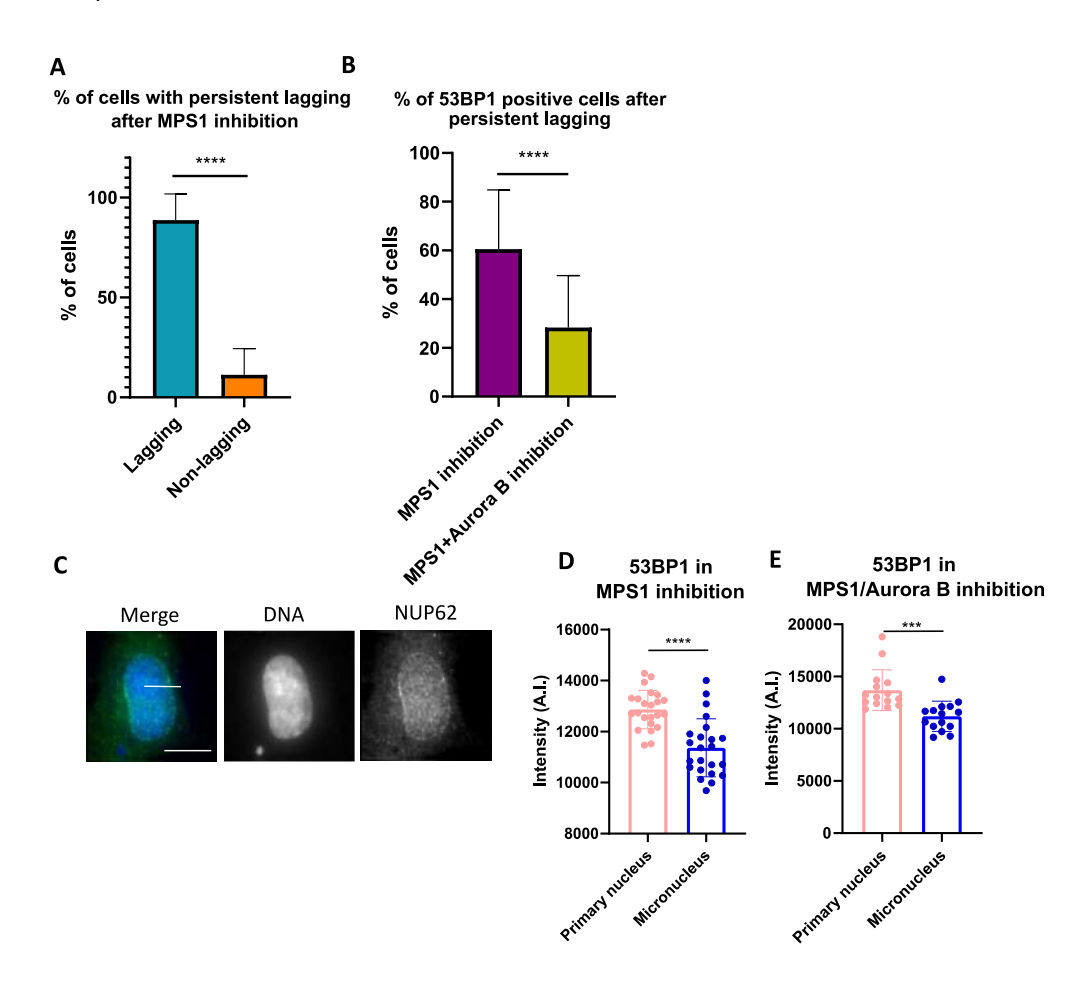


Figure 4: Persistent lagging chromosomes lead to 53BP1 appearance

- (A) Quantification of percentage of RPE1 cells displaying persistent lagging chromosomes after MPS-1 inhibition with Reversine. N=4 independent experiments, 5-10 cells per condition and experiment. \*\*\*\*p < 0.0001, Fisher's exact test.
- (B) Quantification of the percentage of 53BP1 positive cells, in the population that displayed persistent lagging chromosomes, in MPS-1 inhibition with Reversine vs MPS-1 inhibition with Reversine and partial Aurora B inhibition with Baracertib. N=4 independent experiments, 5-10 cells per condition and experiment. \*\*\*\*p < 0.0001, Fisher's exact test.
- (C) Example images of micronucleus staining for nuclear pore marker NUP62. Scale bars =  $10 \mu m$ .
- (D) 53BP1 intensity in primary nucleus vs micronucleus in MPS-1 inhibited cells with Reversine. \*\*\*\*p < 0.0001, student t-test.
- (E) 53BP1 intensity in primary nucleus vs micronucleus in MPS-1 inhibited cells with Reversine and partial Aurora B inhibition with Baracertib. p=\*\*\*, student t-test.

#### WDR62 depletion does not lead to abnormal nuclear shape

A recent publication from the Fachinetti lab (Hervé et al. 2024) demonstrated that mis-segregating chromosomes lead to abnormal nuclear shapes, which activates a mechanosensitive checkpoint, ultimately triggering p53-p21-dependent cell cycle arrest. To determine whether the proliferation defect in WDR62-depleted cells could result from mechanosensitive checkpoint activation, we quantified nuclear shape abnormalities in these cells compared to siCTRL cells.

To assess nuclear shape, we categorized nuclei into three distinct morphological groups, as described by Janssen et al. (2022). First, we evaluated nuclear circularity, a commonly used metric for assessing nuclear abnormalities in different diseases (Tataki et al 2017). A perfectly round nucleus has a circularity value of 1, whereas irregularly shaped nuclei exhibit lower circularity values. As shown in Figure 4A, WDR62-depleted cells exhibited a slight decrease in circularity compared to control cells; however, this difference was not very big compared to control cells (0.85 to 0.83).

Next, we assessed nuclear eccentricity, a symmetry-based parameter used to distinguish oval-shaped nuclei from irregular shapes (Nikonenko and Bozhok, 2015). Eccentricity is defined as the ratio of the major and minor axes of the nucleus, with values ranging from 0 (perfectly circular) to 1 (highly elongated). Our measurements revealed that both siCTRL and siWDR62 cells had an eccentricity index of 0.8, indicating that their nuclear shapes were similarly elongated.

Finally, we analysed nuclear solidity, which is defined as the ratio of nuclear area to convex nuclear area. This parameter is a powerful indicator of nuclear membrane curvature, providing insight into the presence of blebbing and invaginations (Driscoll et al. 2012, Janssen et al. 2022). A nucleus with a smooth contour, free of invaginations or blebbing, has a solidity value of 1. As shown in Figure 4C, WDR62-depleted cells exhibited only a slight reduction in solidity compared to control cells.

Taken together, these measurements indicate that WDR62 depletion results in only minor nuclear shape alterations, which are unlikely to account for the pronounced reduction in cell proliferation. Therefore, we propose that mechanosensitive checkpoint activation is not the primary cause of the WDR62-dependent, 53BP1-p21-mediated cell cycle delay.

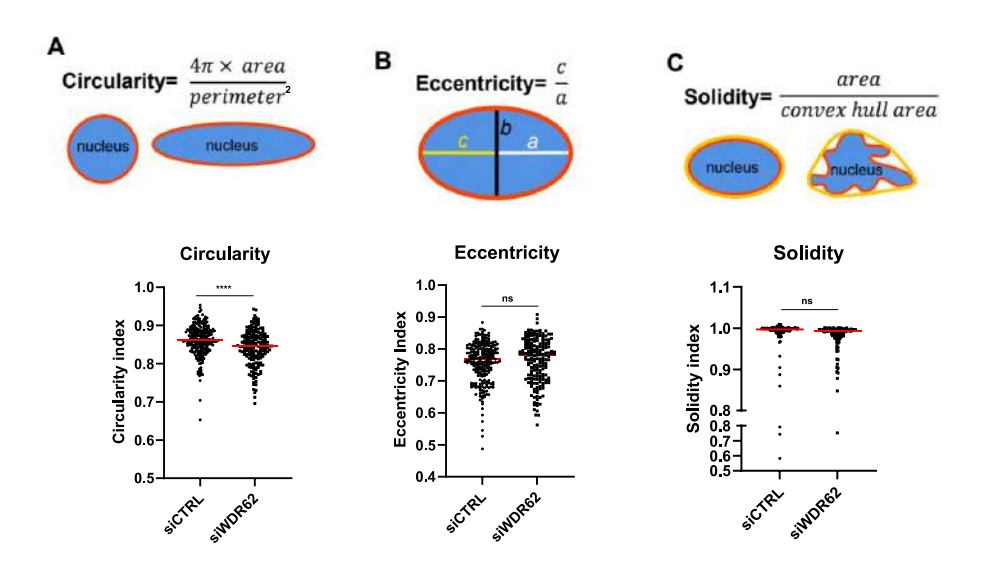


Figure 5: WDR62 depletion does not lead to abnormal nuclear shape

- (A) Nuclear circularity formula and schematics. Quantification of circularity in siCTRL vs siWDR62 RPE cells. \*\*\*\*p < 0.0001, student t-test. N=4 independent experiments, 200 cells per condition and experiment.
- (B) Nuclear eccentricity formula and schematics. Quantification of eccentricity in siCTRL vs siWDR62 RPE cells. p=ns, student t-test. N=4 independent experiments, 200 cells per condition and experiment.
- (C) Nuclear solidity formula and schematics. Quantification of solidity in siCTRL vs siWDR62 RPE cells. p=ns, student t-test. N=4 independent experiments, 200 cells per condition and experiment.

## WDR62 depletion leads to increased cell cycle timing but normal cell cycle partitioning

In our study (Doria & Ivanova et al 2024, BioRxiv), we demonstrated that WDR62 depletion leads to a reduction in cell proliferation over five days (see Figure 1G). To determine whether the siWDR62-dependent cell cycle delay results from a slower progression through the cell cycle or an increased number of cells entering the resting G0 phase, we assessed the proliferation marker Ki-67. Ki-67 is a multifunctional protein involved in cell cycle regulation and heterochromatin organization (Sun & Kaufman, 2018). It is also a widely used proliferation marker, known to be present during G1, S, and G2 phases but absent in G0 (Menon et al., 2019). Leveraging this characteristic, we used Ki-67 as a proxy for the proportion of G0 cells in WDR62-depleted and control conditions. As shown in Figure 5B, WDR62 depletion led to a decrease in the number of Ki-67-positive cells, indicating an increase in G0-arrested cells.

In our previous study (Doria & Ivanova et al 2024, BioRxiv), we also demonstrated that the cell proliferation defect caused by WDR62 depletion can be rescued by co-depleting WDR62 with Camsap1

(see Figure 4D). However, Ki-67 levels were only partially restored upon co-depletion of WDR62 and Camsap1 (Figure 5B). This suggests that while G0 arrest contributes to the reduced proliferation of WDR62-depleted cells, a general slowdown of the cell cycle also plays a role. To further characterize the WDR62-dependent cell cycle delay, we examined the phosphorylation status of RB, a key regulator of S-phase entry. Reduced RB phosphorylation is known to prolong G1 phase (Gartel et al., 1996). To assess whether WDR62 depletion leads to a prolonged G1 phase, we quantified the number of phospho-RB-positive cells. As shown in Figure 5C, no significant difference was observed between siWDR62, siCamsap1, and double depletion conditions, indicating that WDR62 depletion does not cause an RB-dependent G1 delay. To determine whether another cell cycle phase was prolonged in WDR62-depleted cells, we analysed cell cycle phase distribution using propidium iodide (PI) staining. PI binds to DNA, allowing for fluorescence-activated cell sorting (FACS)-based DNA content analysis. In this assay, G0/G1-phase cells exhibit a diploid (2N) DNA content, G2/M-phase cells are tetraploid (4N), and S-phase cells have an intermediate DNA content (between 2N and 4N) depending on their progression through DNA replication (see example in Figure 5D). Our measurements showed no significant differences in cell cycle phase distribution between WDR62-depleted and control cells.

Taken together, these findings suggest that WDR62 depletion does not lead to the prolongation of a specific cell cycle phase but rather causes a general cell cycle slowdown while maintaining normal phase distribution.

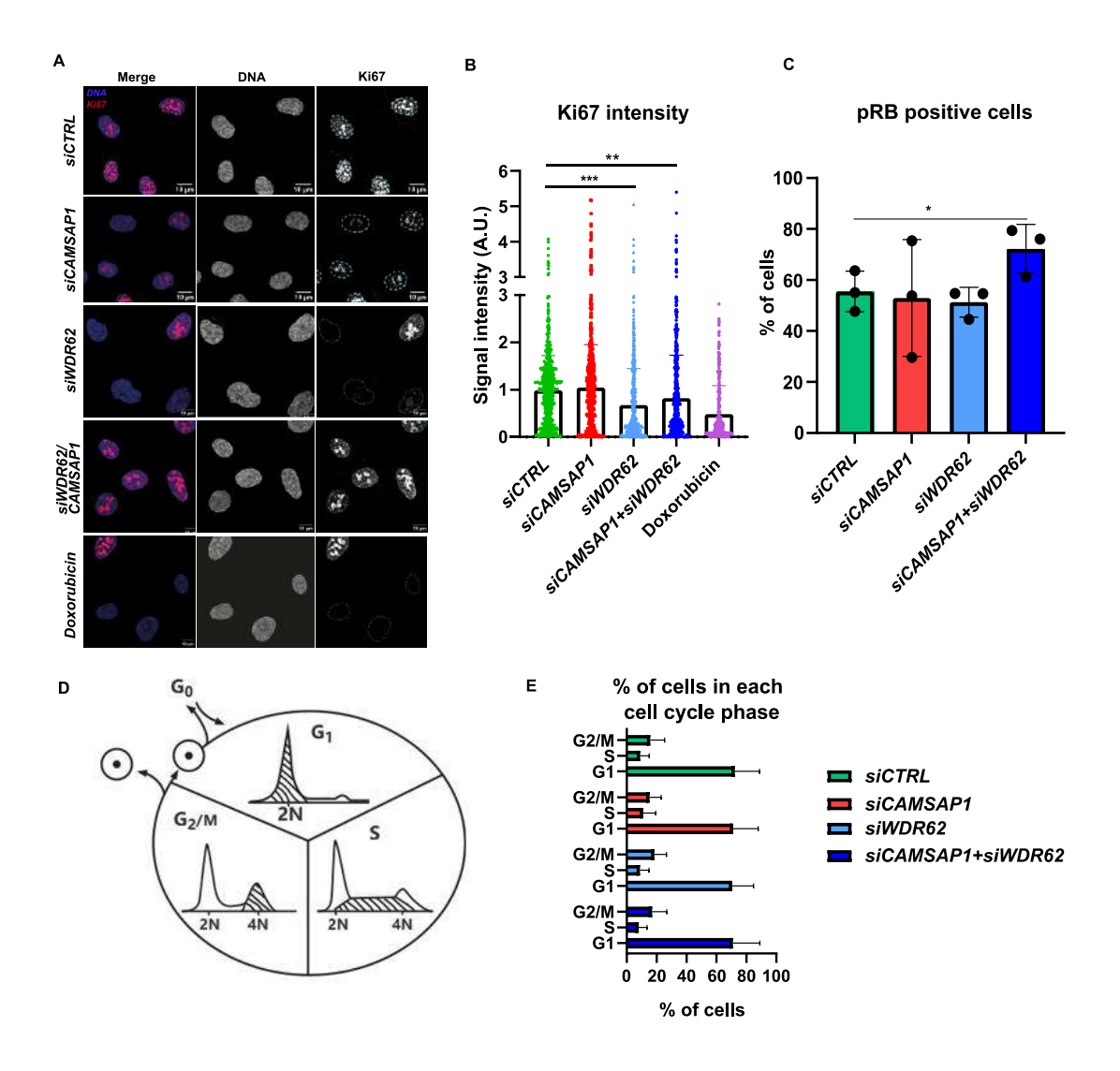


**Figure 6**: WDR62 depletion leads to less proliferation, but does not change the distribution of cells within each cell cycle phase.

- (A) Representative images of Ki-67 staining in hTERT- RPE1 cells treated with siRNA Control, CAMSAP1, WDR62, CAMSAP1/WDR62 co-depletion and Doxorubicin 100nM treatment. Light blue dotted circles represent nuclei. Scale bar=10 um.
- (B) Quantifications of Ki-67 signal in hTERT- RPE1 cells treated with siRNA Control, CAMSAP1, WDR62, CAMSAP1/WDR62 co-depletion and Doxorubicin 100nM treatment. siCTRL vs siWDR62, p = \*\*\*; siCTRL vs siWDR62/CAMSAP1, p = \*\*, one-way Anova test. N=4, 200 cells in total.
- (C) Quantifications of the % of cells positive for pRB signal in hTERT- RPE1 cells treated with siRNA Control, CAMSAP1, WDR62, CAMSAP1/WDR62 co-depletion. siCTRL vs siWDR62/CAMSAP1, p = \*, Fisher's exact test. N=3, 200 cells per condition and experiment.
- (D) Scheme to represent the principle of propidium iodide staining. From Zarbochová et al 2009.
- (E) Quantification of the percentage of cells in each cell cycle phase, as extracted from cell cycle profiles in siRNA Control, CAMSAP1, WDR62, CAMSAP1/WDR62 co-depletion. N=3 independent experiments, 10000 cells per experiment and condition.

## WDR62 localizes katanin at spindle poles to ensure synchronous chromosome segregation

As previously discussed, WDR62 recruits Katanin to sever microtubule minus-ends at the mitotic spindle. The initial studies on WDR62 localization in our lab were conducted by Amanda Guerreiro, a former PhD student in Patrick Meraldi's group.

During the first year of my PhD, I contributed to the revision of her first-author paper, "WDR62 localizes Katanin at spindle poles to ensure synchronous chromosome segregation." My specific contributions to this publication included analyzing the occurrence of transient lagging chromosomes (Figures 6B, C; S5) and measuring spindle size (Figure S3C).



#### **ARTICLE**

# WDR62 localizes katanin at spindle poles to ensure synchronous chromosome segregation

Amanda Guerreiro<sup>1</sup>, Filipe De Sousa<sup>1,2</sup>, Nicolas Liaudet<sup>3</sup>, Daria Ivanova<sup>1</sup>, Anja Eskat<sup>1</sup>, and Patrick Meraldi<sup>1,4</sup>

Mutations in the WDR62 gene cause primary microcephaly, a pathological condition often associated with defective cell division that results in severe brain developmental defects. The precise function and localization of WDR62 within the mitotic spindle is, however, still under debate, as it has been proposed to act either at centrosomes or on the mitotic spindle. Here we explored the cellular functions of WDR62 in human epithelial cell lines using both short-term siRNA protein depletions and long-term CRISPR/Cas9 gene knockouts. We demonstrate that WDR62 localizes at spindle poles, promoting the recruitment of the microtubule-severing enzyme katanin. Depletion or loss of WDR62 stabilizes spindle microtubules due to insufficient microtubule minus-end depolymerization but does not affect plus-end microtubule dynamics. During chromosome segregation, WDR62 and katanin promote efficient poleward microtubule flux and favor the synchronicity of poleward movements in anaphase to prevent lagging chromosomes. We speculate that these lagging chromosomes might be linked to developmental defects in primary microcephaly.

#### Introduction

The goal of the mitotic spindle is to faithfully segregate sister chromatids into two daughter cells (Walczak et al., 2010). The bipolar spindle relies on dynamic microtubules to attach and align sister-chromatids on the metaphase plate, before pulling them apart toward each spindle pole during anaphase (Prosser and Pelletier, 2017). Microtubules are polar polymers composed of tubulin dimers, with minus-ends embedded into spindle poles and plus-ends attached to kinetochores. Microtubules are dynamic, changing in a stochastic manner between growth and shrinkage, allowing them to explore their 3D environment (Akhmanova and Steinmetz, 2015; Prosser and Pelletier, 2017). Once microtubules bind kinetochores, they become more stable and form bundles called kinetochore fibers (k-fibers). These fibers still remain dynamic, as their plus-ends undergo periods of relative growth and shrinkage, resulting in oscillatory movements of bipolarly attached sister-kinetochores along the spindle axis (Jaqaman et al., 2010; Skibbens et al., 1993). At the same time, microtubules within k-fibers undergo a conveyor belt-like movement called poleward microtubule flux that is driven by microtubule motors acting on kinetochore and nonkinetochore microtubules, which over time results in new tubulin dimer incorporation at their plus-ends, concomitant with tubulin dimer removal at minus-ends (Mitchison, 1989; Steblyanko

et al., 2020). The entire segregation machinery is controlled by the spindle assembly checkpoint, which ensures that cells initiate anaphase only once all kinetochores are attached to spindle microtubules (Joglekar, 2016).

Mitotic spindle defects are associated with severe human pathologies. In cancer, errors in chromosome segregation are frequent and contribute to high genetic instability (Levine and Holland, 2018). The most frequent cause for the gain or loss of entire chromosomes is the presence of merotelic kinetochoremicrotubule attachments (one sister-kinetochore bound by microtubules of both poles; Gregan et al., 2011). Such erroneous attachments arise in a stochastic manner, but persist when microtubule dynamics are perturbed, preventing their correction (Bakhoum et al., 2009a; Godek et al., 2015). They can also accumulate after transient spindle defects, such as the formation of monopolar, multipolar, or bipolar spindles with incorrect geometry (Kaseda et al., 2012; McHedlishvili et al., 2012; Nam and van Deursen, 2014; Silkworth et al., 2012; 2009; Ganem et al., 2009). Autosomal recessive primary microcephaly (microcephaly primary hereditary [MCPH]) is the second major disease linked to genetic defects in the chromosome segregation machinery (Jayaraman et al., 2018; Nano and Basto, 2017). This developmental disease leads to severe underdevelopment of the

<sup>1</sup>Department of Cell Physiology and Metabolism, Faculty of Medicine, University of Geneva, Geneva, Switzerland; <sup>2</sup>Radiation Oncology Division, Geneva University Hospitals, Geneva, Switzerland; <sup>3</sup>Bioimaging Facility, Faculty of Medicine, University of Geneva, Geneva, Switzerland; <sup>4</sup>Translational Research Centre in Onco-hematology, Faculty of Medicine, University of Geneva, Switzerland.

Correspondence to Patrick Meraldi: patrick.meraldi@unige.ch; A. Eskat's present address is Clinical Trials Center, University Hospital Zurich, Zurich, Switzerland.

© 2021 Guerreiro et al. This article is distributed under the terms of an Attribution–Noncommercial–Share Alike–No Mirror Sites license for the first six months after the publication date (see http://www.rupress.org/terms/). After six months it is available under a Creative Commons License (Attribution–Noncommercial–Share Alike 4.0 International license, as described at https://creativecommons.org/licenses/by-nc-sa/4.0/).





neocortex, resulting in a small brain and mental retardation. Many MCPH mutations result in premature stop codons or low expression of genes encoding mitotic spindle components. These include proteins at centrosomes, spindle poles or kinetochores, and components of the DNA-damage pathway. Centrosomes are the main microtubule organizing centers of metazoan cells. They are composed of two barrel-shaped centrioles surrounded by pericentriolar material that acts as primary microtubule nucleation center during mitosis (Conduit et al., 2015). Although centrosomes are nonessential for cell division, they increase the fidelity of chromosome segregation, focus spindle poles, regulate spindle microtubule dynamics, and act as anchors for spindle orientation and positioning during asymmetric cell divisions (Basto et al., 2006; Meraldi, 2016; Sir et al., 2013; Dudka et al., 2019).

The cellular origins for primary microcephaly are most likely diverse. They include spindle orientation defects, chromosome segregation errors and aneuploidy, or accumulation of DNA damage (Jayaraman et al., 2018; Nano and Basto, 2017). Their common end point is exhaustion of dividing neuronal stem cells, either because they differentiate too early or because they undergo apoptosis. One important question is why such general cell cycle defects would mostly lead to brain developmental defects (Woods and Basto, 2014). One possibility is that cell fate determination is particularly sensitive to spindle orientation defects and/or that neuronal stem cells are particularly prone to apoptosis in the presence of aneuploidy or DNA damage (Gogendeau et al., 2015; Lancaster and Knoblich, 2012; Nano and Basto, 2017; Noatynska et al., 2012). A second key question is how mutations in different types of centrosomal proteins lead to primary microcephaly. A first large class of mutants is linked to genes required for centrosome duplication (SAS6, CPAP, CEP63, CEP152, CEP135, STIL, and CDKRAP2/CEP215; Nigg et al., 2014; O'Neill et al., 2018), which can impair the entire centrosome. A second class of mutations is found in genes involved in spindle pole organization, including ASPM, the microtubulesevering enzyme complex katanin, CDK5RAP2, CDK6, and WDR62 (Bilgüvar et al., 2010; Bond et al., 2002; 2005; Hu et al., 2014; Hussain et al., 2013; Mishra-Gorur et al., 2014; Nicholas et al., 2010; Yu et al., 2010). WDR62 (also called MCPH2), is the second most frequently mutated gene associated with primary microcephaly. The precise cellular function of the WDR62 protein and its localization remain under debate. WDR62 has been proposed to be associated with spindle poles, centrosomes, and/or spindle microtubules (Jayaraman et al., 2016; Kodani et al., 2015; Lim et al., 2016; Yu et al., 2010; Lim et al., 2015). Its localization is controlled by the protein kinase aurora-A, which phosphorylates WDR62 at mitotic onset to recruit it at centrosomes/spindle poles (Chen et al., 2014; Lim et al., 2016, 2015). At the functional level, human or murine WDR62 has been implicated in centriole duplication in conjunction with ASPM (Jayaraman et al., 2016), cilia formation when interacting with CPAP/IFT88 (Shohayeb et al., 2020), and cilia disassembly when interacting with CEP170 and KIF2A (Zhang et al., 2019). Loss of WDR62 has been reported to affect spindle orientation (Bogoyevitch et al., 2012; Miyamoto et al., 2017), spindle formation and mitotic progression without spindle orientation defects (Chen et al., 2014), or centrosome duplication and cilia formation (Jayaraman et al., 2016).

Here, we investigated the cellular functions of WDR62 in malignant and nontransformed human epithelial cell lines using both short-term siRNA depletions and long-term CRISPR/Cas9 gene knockouts. Our results indicate that WDR62 localizes to microtubule ends at spindle poles, but that it is not associated with centrosomes. We demonstrate that WDR62 and the microtubule-severing enzyme katanin are mutually dependent to localize at spindle poles. Loss of WDR62 stabilizes spindle microtubules due to insufficient microtubule minusend depolymerization, while leaving plus-end microtubule dynamics unaffected. At the level of the spindle, WDR62 loss leads to a severe reduction of poleward microtubule flux in metaphase, concomitant with asynchronous poleward movements in anaphase that result in lagging chromosomes. We propose that these lagging chromosomes could be linked to developmental defects in primary microcephaly.

#### Results

#### WDR62 localizes to the microtubules at spindle poles

To study the function of WDR62 in mitosis, we first investigated its precise localization on the mitotic spindle. Previous studies reported that it binds to centrosomes (Jayaraman et al., 2016; Kodani et al., 2015; Yu et al., 2010), while others suggested a potential binding to microtubules (Lim et al., 2016; 2015). To localize WDR62, we used both malignant HeLa cells and nonmalignant human retinal pigment epithelial cells expressing telomerase (hTert-RPE1), two cell lines widely used for mitotic studies. Cells were stained for centrin-1 (centriole marker), α-tubulin (microtubule marker), WDR62, and DAPI (chromosome marker). Using both deconvolution wide-field microscopy (RPE1) and 3D stimulated emission depletion (STED) superresolution microscopy (HeLa), we found that WDR62 was not enriched at centrioles, but rather localized to spindle poles, possibly as part of the pericentriolar material, or in association with the microtubules terminating at spindle poles (Fig. 1, A and B).

To differentiate between the two possibilities, RPE1 cells were submitted to an ice-cold treatment for 6 min. Such treatment depolymerizes free microtubules and partially depolymerizes spindle microtubules, resulting in their detachment from the pericentriolar material. We found that WDR62 was exclusively bound to the dissociated spindle microtubules (Fig. 1 C). In contrast, the pericentriolar marker pericentrin was still associated with centrosomes (Fig. 1 D). This suggested that WDR62 does not bind centrosomes but is rather associated with microtubule ends terminating at spindle poles.

To confirm this hypothesis, we used 8 nM of the microtubule-stabilizing drug taxol on HeLa cells to form multipolar spindles with centrosome-free and centrosome-associated spindle poles (Fig. 1 E; Jordan et al., 1993). Immunofluorescence analysis confirmed that WDR62, but not pericentrin, was present in the extra spindle poles free of centrosomes and centrioles (Fig. 1, E and F). We conclude that WDR62 is located at microtubule ends terminating at spindle poles, independently of centrosomes.



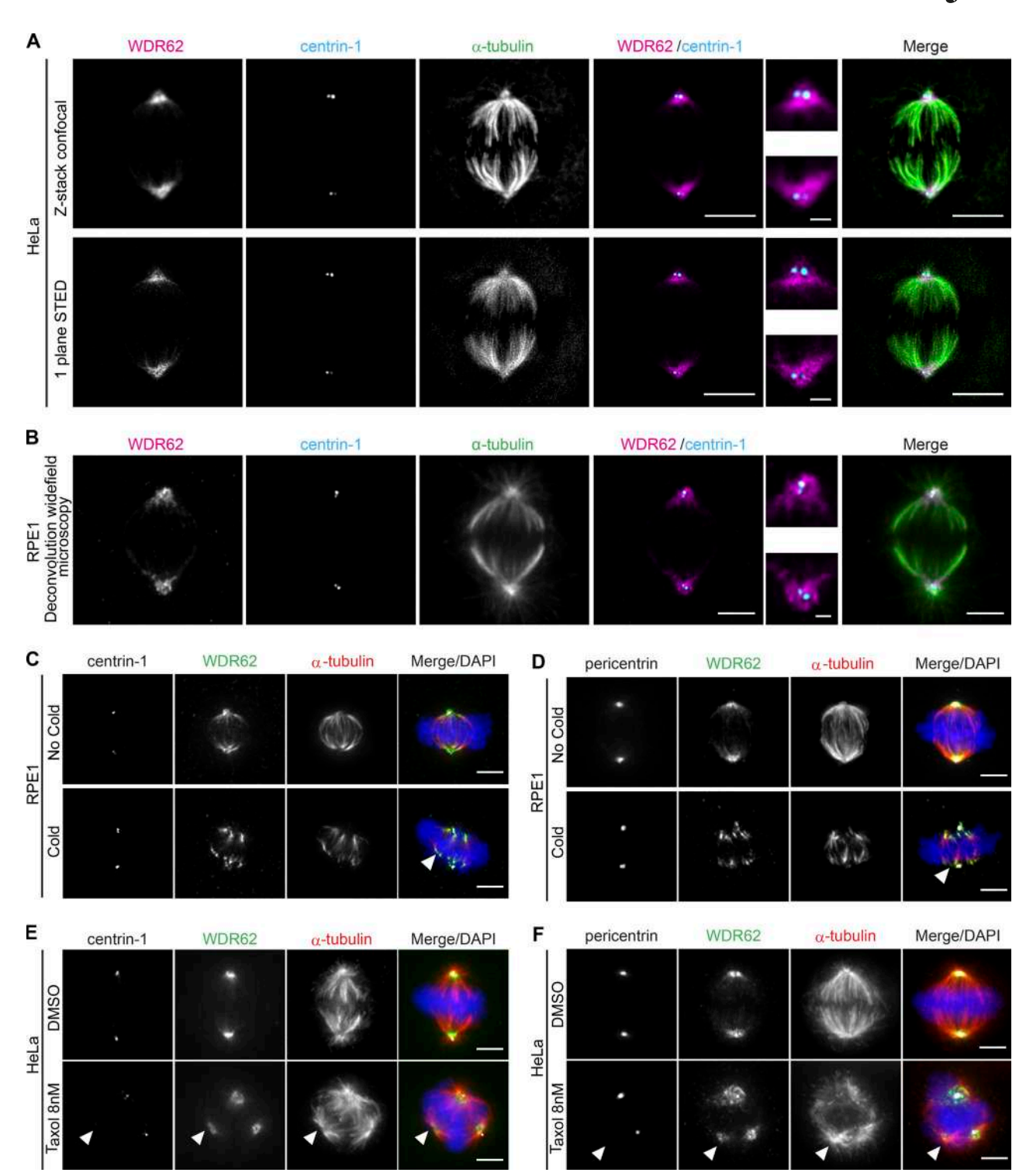


Figure 1. **WDR62 localizes to microtubules at spindle poles. (A and B)** Immunofluorescence images of metaphase. HeLa cells recorded by confocal (z-stack) and STED (one-plane) microscopy (A) or RPE1 cells recorded by deconvolution wide-field microscopy (one plane; B); cells were stained with  $\alpha$ -tubulin, centrin-1, and WDR62 antibodies. Insets show spindle poles. **(C and D)** Immunofluorescence images of metaphase RPE1 cells, treated with or without a cold treatment and stained with DAPI, WDR62 and  $\alpha$ -tubulin antibodies, and centrin-1 (C) or pericentrin (D) antibodies. Arrows indicate depolymerized microtubule minus-ends. **(E and F)** Immunofluorescence images of metaphase HeLa cells treated either with DMSO or 8 nM taxol for 12 h, stained with DAPI, WDR62 and  $\alpha$ -tubulin antibodies, and centrin-1 (E) or pericentrin (F) antibodies. Arrowheads indicate centriole- and pericentrin-free spindle poles. Scale bars = 5  $\mu$ m; 1  $\mu$ m (inset).



#### Loss of WDR62 increases spindle microtubule stability

Given the localization of WDR62 on microtubules at spindle poles, we tested how WDR62 loss affects spindle microtubule dynamics. Previous studies had linked WDR62 to microtubule stability, reporting that it could promote astral microtubule assembly (Miyamoto et al., 2017) and drive the disassembly of microtubules in the cilium via the microtubule depolymerase KIF2A (Zhang et al., 2019). To probe WDR62 function in human cells, we either knocked out the WDR62 gene by CRISPR/Cas9 in HeLa cells expressing the chromosome marker H2B-GFP (WDR62<sup>-/-</sup>; genomic sequencing confirmed the presence of an 11-base deletion in the first exon, Fig. S1 A) or depleted it for 48 h by siRNA (siWDR62) in RPE1 cells. Immunofluorescence indicated that these approaches led to an ~90% depletion (siWDR62) or a complete loss of WDR62 (WDR62<sup>-/-</sup>; Fig. S1, B and C). We subjected cells with or without WDR62 to ice-cold treatment (6 min for RPE1; 20 min for HeLa) to reveal the cold resistance of metaphase k-fibers. This resistance, in turn, reflects kinetochoremicrotubule stability. Cells were classified into three categories based on 3D visualization after α-tubulin staining: an intact metaphase spindle with almost all k-fibers present (class 1), a metaphase spindle with several missing and detached k-fibers at microtubule minus- or plus-ends (class 2), and a deteriorated spindle with most k-fibers lost (class 3; Fig. 2 A). Both WDR62 depletion in RPE1 cells and WDR62 deletion in HeLa cells increased k-fiber cold resistance in metaphase when compared with control depletion or the parental cell line (Fig. 2, B and C). To exclude off-target effects, we created stable RPE1 cells expressing eGFP or an siRNA-resistant exogenous WDR62-eGFP that localized correctly at spindle poles (Fig. 2 D). RNAi-resistant WDR62-eGFP, but not eGFP alone, rescued cold sensitivity after siWDR62 treatment, suggesting that WDR62 is required for k-fiber destabilization (Fig. 2 E).

To corroborate these findings, we used an unbiased spindle stability quantification assay in RPE1 cells. To visualize k-fibers, cells were labeled with SiR-tubulin, a tubulin live dye that binds to microtubules with a turnover rate of >10 s (Lukinavičius et al., 2014; David et al., 2019), at a concentration that does not change k-fiber dynamics (Dudka et al., 2019). Cells were arrested in metaphase with the proteasome inhibitor MG132 and treated with a 200 ng/ml pulse of the microtubule-depolymerizing drug nocodazole. Spindle decay was monitored live over 15 min, as previously described (Fig. 2 F; Dudka et al., 2019; Wilhelm et al., 2019). This assay indicated that k-fibers were significantly more stable after WDR62 depletion (Fig. 2 G), consistent with the cold treatment results.

Previous studies had reported that WDR62 is necessary for efficient centrosome duplication (Jayaraman et al., 2016; Kodani et al., 2015). We therefore tested, in both HeLa WDR62<sup>-/-</sup> and RPE1 cells treated with control or WDR62 siRNA, whether the change in microtubule stability could be due to impaired centrosome duplication. By counting the number of centrioles in metaphase with centrin-1 antibodies, we found that WDR62 loss or acute depletion was not associated with a significant centriole loss (Fig. 2, H–J). This indicates that WDR62 is either not involved in centrosome duplication or that it plays only a minor role in this process. We conclude

that it promotes k-fiber destabilization independently of centriole numbers.

#### WDR62 is required for katanin localization at spindle poles

WDR62 has been shown to interact with two different regulators of microtubule stability: the microtubule-depolymerase KIF2A at cilia (Zhang et al., 2019) and ASPM (MCPH5), another microcephaly-associated gene product, whose presence was reported to promote the localization of the microtubule-severing enzyme katanin (KATNB1) at spindle poles (Bond et al., 2002; 2003; Jayaraman et al., 2016; Jiang et al., 2017). We immunostained control- and siWDR62-treated cells for katanin, ASPM, KIF2A, and MCAK (a KIF2A paralog that acts at spindle poles and kinetochores) and quantified their levels at spindle poles. WDR62 depletion did not alter ASPM, KIF2A, or MCAK levels at spindle poles; katanin levels, however, were decreased by >70% (Fig. 3, A-E). Katanin levels at spindle poles were also dramatically reduced in WDR62<sup>-/-</sup> HeLa cells (-74%; Fig. S2 A) and could be rescued with siRNA-resistant WDR62-eGFP in siWDR62-treated RPE1 cells (Fig. 3, F and G) or with exogenous WDR62-eGFP in HeLa WDR62<sup>-/-</sup> cells (Fig. S2 B). This demonstrated that the katanin decrease at spindle poles is not an offtarget effect. Immunoblotting indicated that WDR62 depletion in RPE1 cells did not affect global KATNB1 levels (Fig. 3, H and I), but only prevented its correct localization at spindle poles. In line with these results, KATNB1 depletion stabilized spindle microtubules even more than WDR62 depletion in the spindle decay assay (Fig. S2, C and D).

We next tested whether, conversely, ASPM or KATNB1 depletion would impact WDR62 abundance at spindle poles (Fig. 3, J-L). Both siRNA treatments efficiently depleted either protein within 48 h (Fig. S2, E and F). Quantitative analysis indicated that ASPM depletion led to a 48% increase in WDR62 levels at spindle poles (Fig. 3, J and L). We conclude that WDR62 does not require ASPM to localize to spindle poles. In contrast, KATNB1 depletion decreased WDR62 levels at spindle poles by 52% (Fig. 3, K and L). This result had two potential explanations: (1) either KATNB1 and WDR62 are mutually dependent on each other for their recruitment at spindle poles, or (2) this reduction reflects a reduced number of microtubule minus-ends at spindle poles (each katanin cut generates an additional minus-end). To differentiate between the two, we stained KATNB1- and WDR62depleted cells for NuMA, a minus-end marker (Elting et al., 2014; Sikirzhytski et al., 2014; Gordon et al., 2001), and found a reduction of 30% and 34% in NuMA abundance at spindle poles (Fig. S2, G-I). Although we cannot exclude that WDR62 also specifically regulates NuMA recruitment, the results indicate that the strong reduction of WDR62 and KATNB1 in siKATNB1- or siWDR62-treated cells is specific, as it goes beyond the reduction seen with the minus-end marker NuMA. We conclude that WDR62 and katanin mutually depend on each other for spindle pole localization.

#### WDR62 loss impairs microtubule minus-end depolymerization

How does the loss of katanin at spindle poles affect the mitotic spindle? Some studies have reported that WDR62 is necessary for correct spindle orientation (Bogoyevitch et al., 2012; Hu and



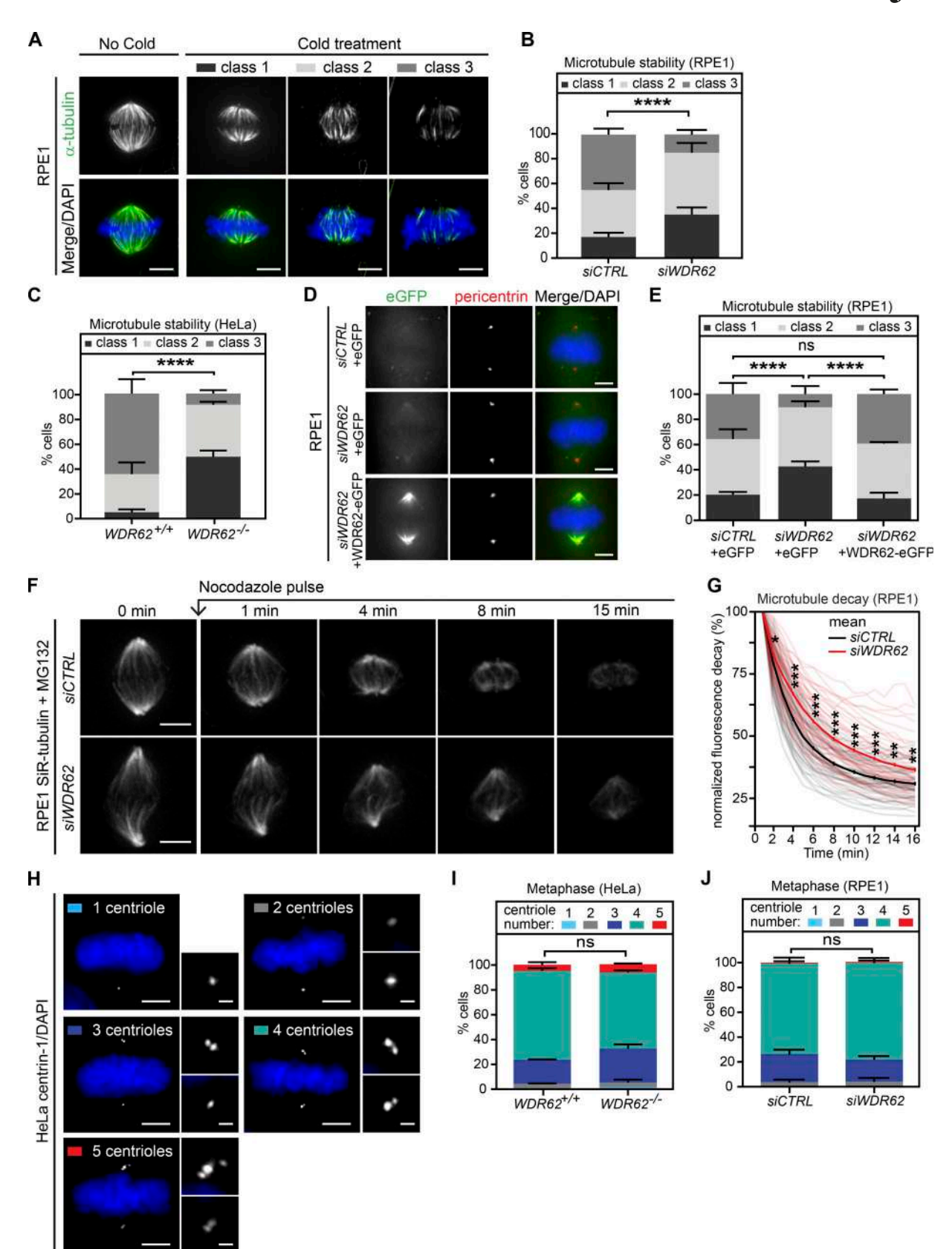


Figure 2. **WDR62 loss increases spindle microtubule stability.** (A) Immunofluorescence images of cold-treated metaphase RPE1 cells, stained with  $\alpha$ -tubulin antibodies and DAPI. Cells were categorized into three representative classes based on k-fiber integrity in 3D. (B and C) Quantification of cold-stable assay in metaphase RPE1 cells treated with *siCTRL* or *siWDR62* (B) or metaphase HeLa *WDR62*<sup>+/+</sup> or *WDR62*<sup>-/-</sup> cells (C); stack bars indicate mean percentages of class 1, 2, and 3 spindles as depicted in A: N = 3 independent experiments, n = 184 - 188 cells per condition (B) or n = 207 - 215 cells (C); error bars represent mean



 $\pm$  SEM; \*\*\*\*\*, P < 0.0001,  $\chi^2$  test. **(D)** Immunofluorescence images of RPE1 cells expressing eGFP or WDR62-eGFP treated with *siCTRL* or *siWDR62* and stained with pericentrin antibodies and DAPI. **(E)** Quantification of cold-stable assay in RPE1 eGFP or WDR62-eGFP metaphase cells treated with *siCTRL* or *siWDR62* as in B and C: N = 3, n = 183-206 cells; \*\*\*\*, P < 0.0001,  $\chi^2$  test. **(F)** Time-lapse sequences of MG132-arrested RPE1 metaphase cells treated with *siCTRL* or *siWDR62*, labeled with SiR-tubulin, and treated with 200 ng/ml nocodazole at t = 0. **(G)** Quantification of the spindle microtubule decay over time in RPE1 metaphase cells treated with *siCTRL* or *siWDR62*: N = 3, N = 55-58 cells; thick lines represent mean; thin lines represent single experiments; \*, P < 0.05; \*\*, P < 0.01; \*\*\*, P < 0.001, repeated two-tailed paired t test. **(H)** Immunofluorescence images of metaphase HeLa cells stained with centrin-1 antibodies and DAPI. Cells were categorized according to centriole numbers. **(I and J)** Quantification of centriole numbers in metaphase *WDR62*<sup>+/+</sup> or *WDR62*<sup>-/-</sup> HeLa cells (I) or RPE1 cells treated with *siCTRL* or *siWDR62* (J): stack bars indicate mean percentage of cells with corresponding centrioles numbers; error bars represent mean  $\pm$  SEM; N = 1, N = 200 cells;  $\chi^2$  test. Scale bars = 5  $\mu$ m; 2.5  $\mu$ m (inset).

Jasper, 2019; Miyamoto et al., 2017; Ramdas Nair et al., 2016; Xu et al., 2014), while others did not observe such an effect (Chen et al., 2014; Jayaraman et al., 2016). Since spindle orientation depends on a correct interaction between astral microtubules and the cell cortex, we first analyzed whether WDR62 or KATNB1 depletion affects the density of astral microtubules. Our quantification of the  $\alpha$ -tubulin signal behind the spindle poles indicated that both WDR62 and KATNB1 depletion led to 25–33% reduction in astral microtubule density (Fig. 4, A and B). This implied a modified balance in the distribution of microtubules in the spindle, with a partial reduction in astral microtubules and a higher k-fiber stability.

Next, we investigated the functional consequences of these changes, by monitoring spindle orientation. Since wild-type epithelial cells orient their spindle parallel to the growth surface, spindle orientation defects result in a higher median angle between the growth surface and the spindle axis (Fig. 4 C; Toyoshima and Nishida, 2007). However, both WDR62 and KATNB1 depletion in RPE1 cells did not increase the median spindle orientation angle, but if anything, led to a decrease in the angle (Fig. 4, D and E). The lack of spindle orientation defects was not due to incomplete protein depletion, since a similar phenotype was visible in HeLa WDR62<sup>-/-</sup>cells (Fig. S3 A). Both depletions, however, increased spindle length (Fig. 4, F and G), which could explain the reduced median spindle angle. Moreover, during the recording of the spindle decay assay, we often observed buckling of spindle microtubules between the two poles, implying a compression of microtubules as they push against the mitotic spindle (Fig. 4 H; Tolić et al., 2019). Overall, we conclude that neither WDR62 nor KATNB1 depletion results in a spindle orientation defect, but rather leads to buckling microtubules that arise due to the resistance of the mitotic spindle to outward pushing forces. This raised the hypothesis that spindles without WDR62 have an insufficient depolymerization at microtubule minus-ends, due to the absence of katanin.

To test this hypothesis, we quantified the rate of poleward microtubule flux in control-, WDR62-, and KATNB1-depleted RPE1 cells expressing photoactivatable (PA)-GFP- $\alpha$ -tubulin. This process is driven by microtubule motors in the spindle but requires microtubule minus-end depolymerization at spindle poles and new tubulin subunit incorporation at kinetochores (Buster et al., 2007; Mitchison, 1989; Steblyanko et al., 2020; Ganem et al., 2005). By photoactivating tubulin on k-fibers in metaphase cells arrested with the proteasome inhibitor MG132, when spindle length is constant (Fig. S3 C), one can read out the rate of minus-end depolymerization from the speed of poleward

microtubule flux. Our quantification indicated that flux speeds were halved in WDR62- or KATNB1-depleted cells when compared with a control depletion (Fig. 4, I and J; and Videos 1, 2, and 3), indicating that KATNB1 loss at spindle poles reduces minus-end microtubule depolymerization by half.

## WDR62 loss does not affect k-fiber plus-end dynamics but leads to wider metaphase plates

Having established that WDR62 depletion reduces k-fiber minus-end depolymerization, we tested whether it also influences their plus-ends and to which extent the dynamics of both ends are mechanically coupled. We used an automated kinetochore-tracking assay based on RPE1 cells expressing the kinetochore/centromere marker CENP-A (Jagaman et al., 2010), as kinetochore movements on the metaphase plate reflect the dynamic instability of k-fiber plus-ends. Sister-kinetochores undergo semiregular oscillatory movements along the spindle axis, from which it is possible to extract key mechanochemical parameters of sister-kinetochores and k-fiber plus-ends (Fig. 5 A; Olziersky et al., 2018), as follows. (1) Interkinetochore distances, which depend on the sum of the forces pulling the two sister-kinetochores apart, and the mechanical stiffness of the centromeric DNA. WDR62 or KATNB1 depletion did not change interkinetochore distances; in contrast, depletion of the centromeric cohesin subunit CAPD2 increased interkinetochore distances, as previously observed (Figs. 5 B and S4 A; Jaqaman et al., 2010). (2) The autocorrelation of kinetochore movements reveals the average (half-)period and regularity of the oscillations (Fig. 5 C). These parameters reflect the dynamic instability of k-fibers, as the half-period indicates how frequently k-fibers switch between growth and shrinkage, while regularity indicates whether k-fibers behave in a consistent manner. WDR62 or KATNB1 depletion had at best only marginal effects on these parameters, while CAPD2 depletion led to shorter half-periods (Fig. 5 D). (3) The average speed of the kinetochore motions, which was slightly higher after WDR62 depletion, unchanged in KATNB1-depleted cells, and markedly decreased after CAPD2 depletion (Fig. 5 E). (4) The width of the metaphase plate, which reflects the ability of the spindle to balance the forces on sister-kinetochores and to align chromosomes on a tight metaphase plate as cells progress toward anaphase (Jagaman et al., 2010). WDR62 depletion, as well as CAPD2 depletion (positive control), led to wider metaphase plates. (Fig. 5 F; Jaqaman et al., 2010). These wider plates persisted throughout metaphase until anaphase onset (Fig. 5, G and H). A similar trend could also be observed in katanin-depleted cells at the level of the maximal metaphase plate width and



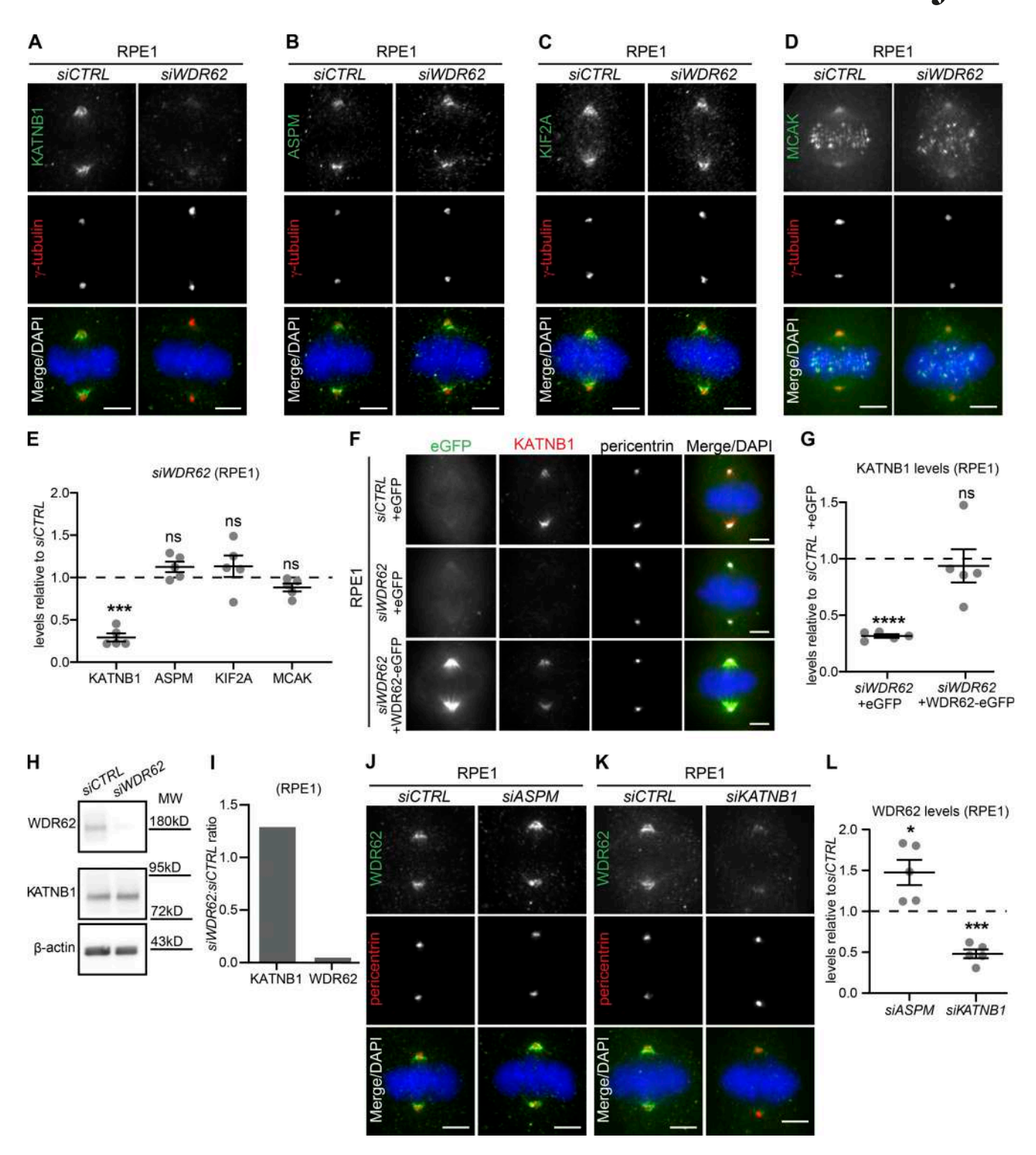


Figure 3. **WDR62** is **required for katanin localization at spindle poles. (A–D)** Immunofluorescence images of metaphase RPE1 cells treated with *siCTRL* or *siWDR62*, stained with DAPI, antibodies against γ-tubulin, and KATNB1 (A), ASPM (B), KIF2A (C), or MCAK (D). **(E)** Quantification of protein levels at spindle poles in *siWDR62* relative to *siCTRL*: N = 5; n = 286-328 cells; dot plot represents median per experiment; bars represent mean ± SEM; \*\*\*\*, P < 0.001, two-tailed paired t test. **(F)** Immunofluorescence images of RPE1 eGFP or WDR62-eGFP metaphase cells transfected with indicated siRNA, stained with KATNB1 and pericentrin antibodies, and DAPI. **(G)** Quantification of KATNB1 levels at spindle poles as shown in F: N = 5, n = 263-279 cells; dot plot represents median per experiment; bars represent mean ± SEM; \*\*\*\*\*, P < 0.0001, one-way ANOVA. **(H)** Western blot of asynchronous RPE1 cell lysates treated with *siCTRL* or *siWDR62* and probed against WDR62, KATNB1, and β-actin (loading control). **(I)** Quantification of immunoblot shown in H of KATNB1/β-actin and WDR62/β-actin ratio signal in *siWDR62* relative to *siCTRL*. N = 1. **(J and K)** Immunofluorescence images of metaphase RPE1 cells treated with indicated siRNA, stained with WDR62, pericentrin antibodies, and DAPI. **(L)** Quantifications of WDR62 levels at spindle poles in *siASPM* and *siKATNB1* relative to *siCTRL*: N = 5; n = 320-339 cells; dot plot represents median per experiment; bars represent mean ± SEM; \*, P < 0.005; \*\*\*, P < 0.001, two-tailed paired t test. All scale bars = 5 μm.



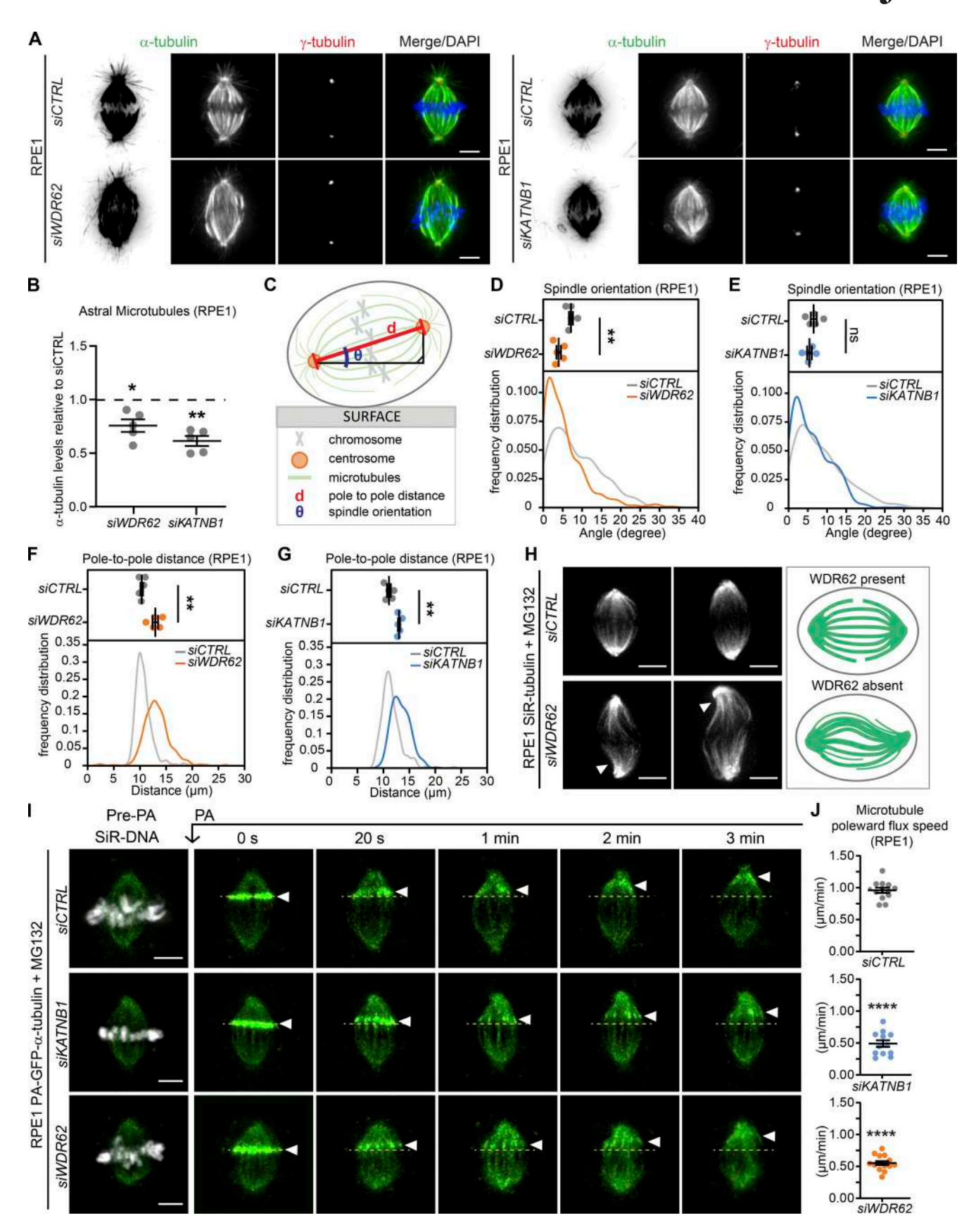


Figure 4. **WDR62 loss impairs microtubule minus-end depolymerization. (A)** Immunofluorescence images of RPE1 cells treated with indicated siRNAs stained with antibodies against  $\alpha$ - and  $\gamma$ -tubulin and DAPI. **(B)** Quantification of astral microtubules in siWDR62 and siKATNB1 relative to siCTRL; N=5, n=244-281 cells; dot plot represents median per experiment; bars represent mean  $\pm$  SEM; \*, P < 0.05; \*\*, P < 0.01, two-tailed paired t test. **(C)** Scheme



representing mitotic spindle orientation as the angle from the surface ( $\theta$ ) and the pole-to-pole distance (d). (**D–G**) Quantification of spindle orientation (D and E) and pole-to-pole distances (F and G) in siCTRL-, siKATNB1-, and siWDR62-treated RPE1 metaphase cells. Dot plots show medians per experiment; curves the frequency distribution; N = 5; n = 315-323 cells; bars represent mean  $\pm$  SEM; \*\*, P < 0.01 in two-tailed unpaired t test. (**H**) Immunofluorescence image of siCTRL- or siWDR62-treated MG132 arrested RPE1 cells labeled with SiR-tubulin, and representative spindle architecture scheme indicating microtubule buckling in the spindle of siWDR62-treated cells. (1) Time-lapse images of RPE1 PA-GFP- $\alpha$ -tubulin cells treated with indicated siRNAs and MG132, labeled with SiR-DNA, and photoactivated (PA) at t = 0. (J) Quantification of the microtubule poleward flux speed ( $\mu$ m/min): N = 3, n = 12-14 cells; dot plots represent each cell; bars represent mean  $\pm$  SEM; \*\*\*\*, P < 0.0001, two-tailed paired t test. All scale bars = 5  $\mu$ m. See also Video 1, Video 2, and Video 3.

metaphase plate width at anaphase onset, but the difference was too small to be significant within our sample size (Fig. 5, G and H).

We conclude that reduced minus-end depolymerization at spindle poles has only very little effect on the dynamics of k-fiber plus-ends, indicating that the two extremities can be experimentally uncoupled from each other. Nevertheless, WDR62 depletion led to persistently wider metaphase plates, implying an impaired ability to position the chromosomes in the equatorial plane of the spindle.

### WDR62 is required for synchronous poleward anaphase movements

Our results were reminiscent of models based on data from Drosophila melanogaster cells that postulated that poleward microtubule flux equalizes forces within the mitotic spindle and favors synchronous poleward anaphase movements (Matos et al., 2009). However, so far all the studies addressing the role of poleward microtubule flux in anaphase relied on knock-downs that affected both microtubule minus- and plusend dynamics (such as the depletion of KIF2A and MCAK or the depletion of the plus-end binding protein CLASP and MCAK; Ganem et al., 2005; Matos et al., 2009). This prevented definite conclusions on the role of flux, since changes in plusend microtubule dynamics affect the fidelity of chromosome segregation on their own (Bakhoum et al., 2009a; Godek et al., 2015). WDR62 depletion allows more precise experimental testing of the role of poleward microtubule flux in chromosome segregation, since it purely affects minus-end depolymerization.

We first analyzed the overall behavior of control- and WDR62-depleted RPE1 cells expressing the chromosome marker H2B-GFP. Our results indicated that WDR62 depletion did not greatly affect the timing of chromosome segregation, as WDR62depleted cells spent only 3 min more between nuclear envelope breakdown and anaphase (Fig. 6 A); nevertheless, WDR62 depletion led to a 22% increase in the number of cells displaying lagging chromosomes (35% vs. 13% after control depletion; Fisher's exact test, P < 0.0001; Fig. 6 B and Videos 4, 5, and 6). In contrast, it did not significantly affect the percentage of chromosome bridges, which were rare in both conditions (Fisher's exact test, P = 0.16; Fig. 6 B). The lagging chromosomes we observed in WDR62-depleted cells were very transient and only rarely led to the formation of micronuclei (Fig. 6 B). Since exogenous WDR62-GFP led to lagging chromosomes on its own (not depicted), we could not analyze the rescue experiment. Nevertheless, to test for off-target effects, we monitored chromosome segregation in HeLa or HeLa H2B-GFP, comparing the parental WDR62<sup>+/+</sup> cells to WDR62<sup>-/-</sup> cells. While mitotic timing was unchanged after WDR62 loss (Fig. S5 A), the percentage of cells displaying lagging chromosomes was significantly higher in both knockouts (Fig. S5, B and C; P > 0.0001 and 0.0002 in  $\chi^2$  test; note that the percentages of bridges were again not significantly changed, P = 0.34 and 0.24). The difference in the incidence of lagging chromosomes was smaller than in RPE1 cells (13% in both cases), most likely because of the already high level of lagging chromosomes in the parental HeLa cells. Since the same effect could be observed after siRNA depletion and two independent CRISPR/Cas9 knockouts in two different cell lines, we conclude that WDR62 loss leads to lagging chromosomes.

In theory, lagging chromosomes can originate from an inefficient correction of merotelic kinetochore-microtubule attachments, possibly due to an overstabilization of k-fibers (Bakhoum et al., 2009b; Gregan et al., 2011; Thompson and Compton, 2008). To test for this hypothesis, we treated cells with the Eg5 inhibitor monastrol to achieve a monopolar spindle configuration, before releasing them from monastrol arrest. This configuration results in a high incidence of syntelic (both sister-kinetochores attached to the same pole) and merotelic attachments (Lampson et al., 2004). The time cells take to align the chromosome on the metaphase plate reflects their ability to correct syntelic attachment, while the percentage of lagging chromosomes reflects persistent merotelic attachments (Lampson et al., 2004). WDR62-depleted RPE1-H2B-GFP cells released from monastrol arrest aligned their chromosomes as rapidly as control-depleted cells and had an incidence of lagging chromosomes that was only marginally higher than controldepleted cells, and similar to that observed in cells not treated with monastrol (Fig. 6, C and D). This indicated that WDR62 does not have a major impact on the correction of erroneous kinetochore-microtubule attachments. A second possible explanation for the lagging chromosomes could be that buckling microtubules "push back" on segregating chromosomes. We therefore tested whether microtubule buckling in metaphase could be a predictor for lagging chromosomes in anaphase. Our analysis of live RPE1 eGFP-CENP-A/eGFP-centrin-1 stained with SiR-tubulin and depleted of WDR62, however, indicated that microtubule buckling in metaphase did not correlate with lagging chromosomes, rather the opposite (Fig. S5 D).

Finally, we tested for asynchrony in poleward anaphase movements due to a reduction in poleward microtubule flux (Matos et al., 2009). To quantify the synchronicity of anaphase movements (Matos et al., 2009; Pereira and Maiato, 2010; Vukušić et al., 2019), we tracked kinetochores in RPE1 eGFP-CENP-A/eGFP-centrin-1 cells and quantified speeds of anaphase A (movements toward the poles) and B (movements of the poles relative to each other) and the spread of the chromosomes during their movements toward the poles. While KATNB1 depletion reduced anaphase A speeds and increased



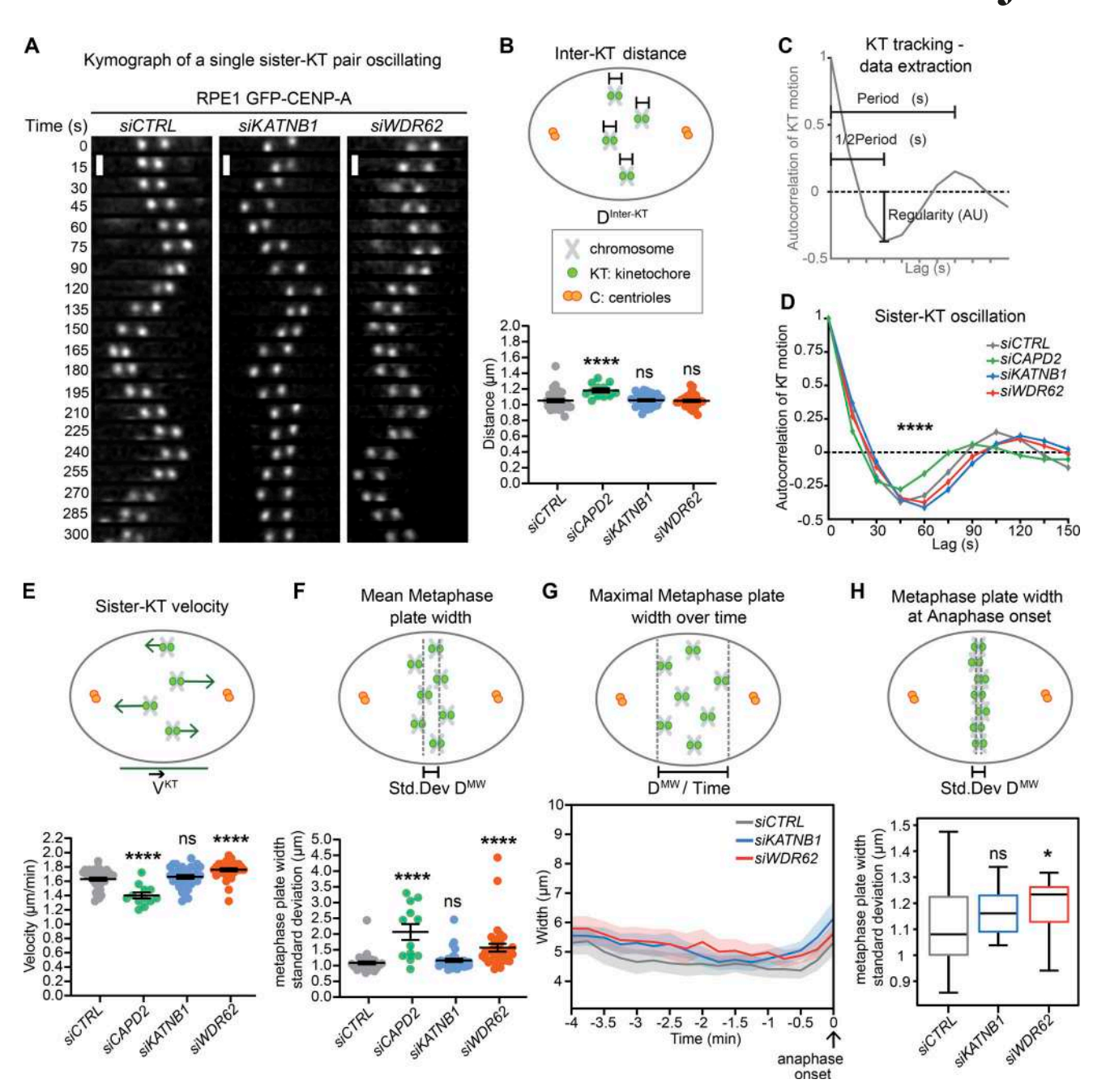


Figure 5. **WDR62 loss leaves k-fiber plus-end dynamics intact but leads to wider metaphase plates. (A–H)** Automated sister-kinetochore tracking of RPE1 GFP-centrin1/GFP-CENPA cells treated with indicated siRNA. Shown are kymographs single, oscillating sister-kinetochores, scale bars = 1  $\mu$ m (A); quantification of the interkinetochore distances (B); schematic illustrating the parameters of sister-kinetochore oscillation autocorrelation curves (C); autocorrelation curves of sister-kinetochore oscillations along spindle axis (D); sister-kinetochore velocities (E); mean metaphase plate width (F); maximal metaphase plate width over time (G); and mean metaphase plate width at anaphase onset (H). N = 3-5, n = 35 (siCTRL), 12 (siCAPD2), 34 (siKATNB1), and 33 (siWDR62) cells; dot plots represent each cell with bars displaying mean  $\pm$  SEM; box plot represent mean  $\pm$  SD; \*, P < 0.05; \*\*\*\*, P < 0.0001, one-way ANOVA. AU, arbitrary units.

anaphase B speeds when compared with control-depleted cells, WDR62 loss did not change either of them (Fig. 6, E and F). In contrast, both WDR62 and KATNB1 depletion led to a wider spread of the kinetochore half-plates in their movements toward the spindle pole, indicating that both proteins are important for the synchronicity of poleward anaphase movements (Fig. 6 G, Video 7, and Video 8). Our results therefore validate the hypothesis that minus-end depolymerization required

for flux plays an important role in equalizing forces in the spindle to ensure synchronous anaphase movements.

#### Discussion

Most genes associated with primary microcephaly have a general impact on cell division. The exact cellular function of WDR62/MCPH2 is, however, still unclear. Based on our data, we



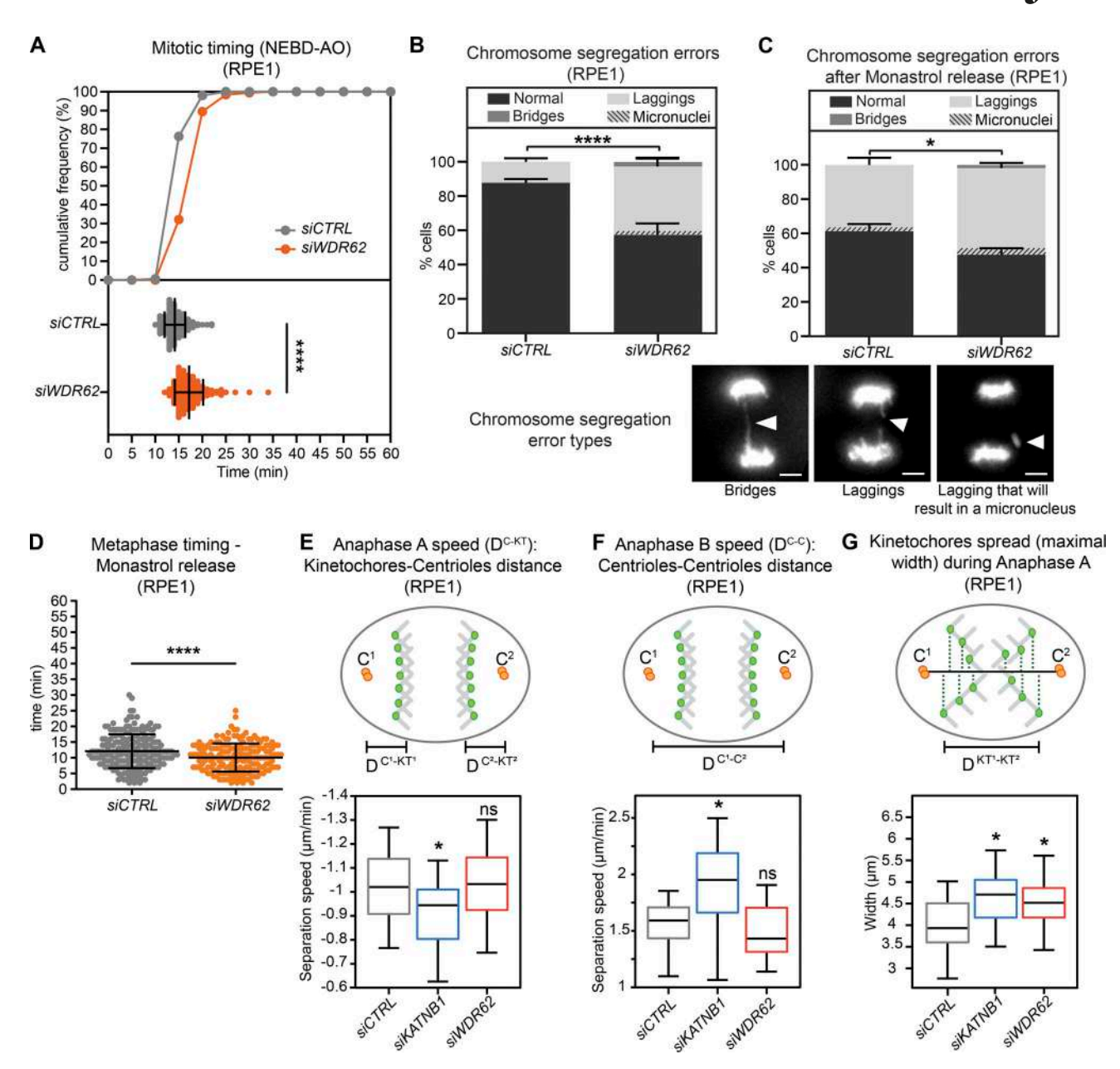


Figure 6. **WDR62** is required for synchronous poleward anaphase movements. (A) Mitotic timing from nuclear breakdown (NEBD) until anaphase onset (AO) of RPE1 EB3-GFP/H2B-mCherry cells treated with siCTRL or siWDR62, shown as cumulative frequency diagram or dot plot representing each cell with bars displaying mean  $\pm$  SEM; N = 3, n = 156-203 cells; \*\*\*\*, P < 0.0001, two-tailed paired t test. (B and C) Percentage of chromosome segregation errors from RPE1 EB3-GFP/H2B-mCherry cells, either unsynchronized (B) or after monastrol release (C). Stack bars represent normal anaphase, anaphase with lagging chromosomes, or anaphase with chromosome bridges as shown on representative images; scale bars = 5  $\mu$ m; gray stripes represent a cell with a lagging chromosome that will result in micronucleus; error bars represent mean  $\pm$  SEM; N = 5, n = 125-209 cells for B; N = 3, n = 209-234 cells for C; \*\*\*\*\*, P < 0.0001; \*, P = 0.042 by  $\chi^2$  test. (D) Timing from monastrol arrest release until anaphase onset from C; dot plot represents each cell; bars represent mean  $\pm$  SEM; \*\*\*\*\*, P < 0.0001, two-tailed paired t = 44 cells. (E-G) Automated spindle pole and KT of RPE1 GFP-centrin1/GFP-CENPA cells treated with indicated siRNA. Shown are anaphase A speed, derived from the distance between kinetochores and centrioles (DC-KT) over time (E); anaphase B speed, derived from the intercentrosome distance (DC-C) over time (F); and the maximal spread of kinetochores during their movements toward the poles in anaphase A for each condition (G); N = 3, n = 20 cells; bars represent mean  $\pm$  SD; \*, P < 0.05, one-way ANOVA. See also Video 4, Video 5, Video 6, Video 7, and Video 8.

propose that WDR62 ensures the correct localization of the katanin complex at spindle poles. The correct localization of this microtubule-severing activity at spindle poles ensures dynamic microtubules, prevents an overstabilization of k-fibers, and allows for efficient poleward microtubule flux rates. Finally, we demonstrate that loss of WDR62 or katanin impairs the synchronicity

of anaphase poleward movements resulting in lagging chromosomes (see model, Fig. 7).

Our data indicate that WDR62 is localized at spindle poles, at or in the immediate vicinity of microtubule minus-ends, where it plays an essential role in the recruitment of katanin. This microtubule-severing complex fails to localize to spindle poles in



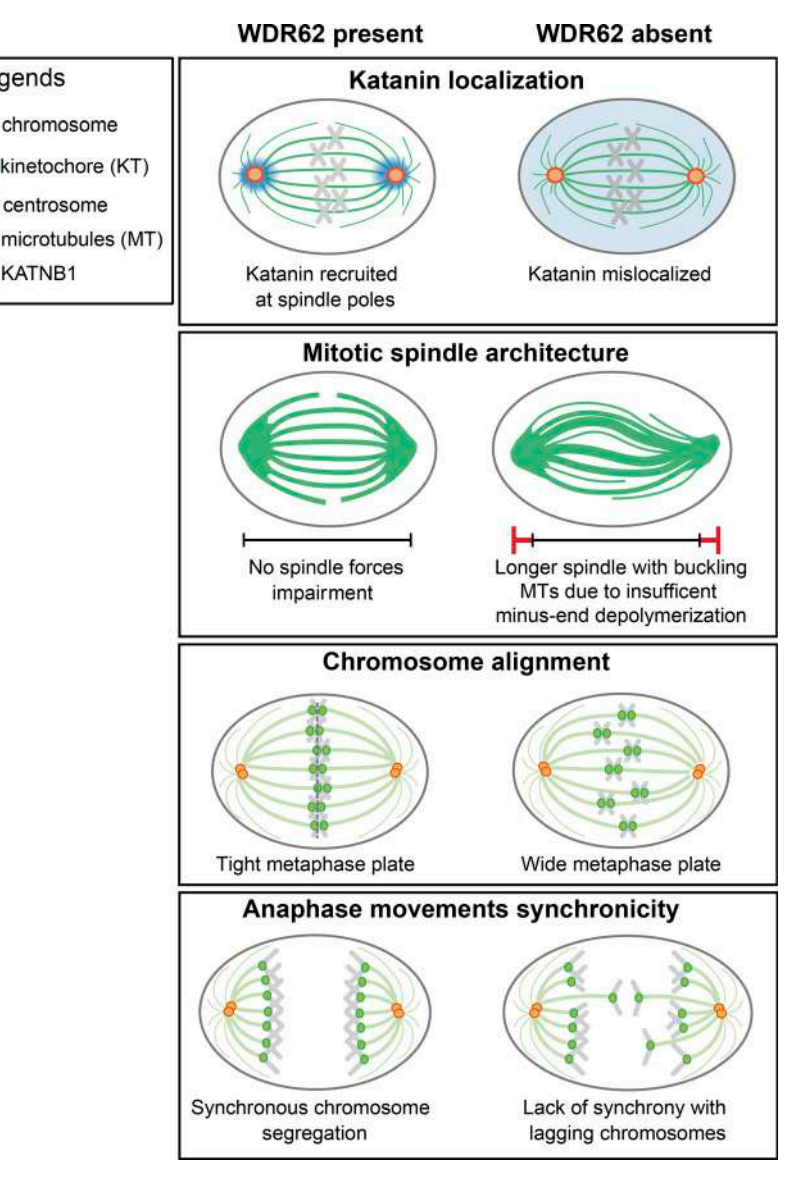


Figure 7. WDR62 localizes KATNB1 at spindle poles to ensure synchronous anaphase. Model of how WDR62 ensures efficient minus-end depolymerization by localizing katanin at spindle poles to ensure tight metaphase plates and synchronous anaphase movements.

both HeLa and RPE1 cells when WDR62 is depleted or lost, and our complementation assay indicates that katanin mislocalization is not caused by an off-target effect. Immunoblotting confirms that WDR62 controls only katanin localization, not the overall protein abundance. We propose that a deregulation of katanin is a major pathway causing primary microcephaly in humans. Indeed, this pathology can be caused by mutations in the KATNB1 gene itself (Mishra-Gorur et al., 2014) or by the loss of two microcephaly genes required for the enrichment of katanin at spindle poles: ASPM (Jiang et al., 2017) and WDR62 (this study). Our conclusions are reinforced by a parallel study demonstrating that recombinant WDR62 can recruit katanin to sever microtubules in vitro (Huang et al., 2021). Our dependence experiments indicate that WDR62 does not require ASPM to localize to spindle poles and that vice versa ASPM is unaffected by WDR62 depletion, indicating that they recruit katanin via separate pathways. A previous study based on mouse embryonic fibroblasts reported that ASPM and WDR62 form a complex at the mother centriole and play a crucial role in centrosome

Legends

chromosome

KATNB1

kinetochore (KT) centrosome

> duplication (Jayaraman et al., 2016). While our data do not exclude a direct interaction between ASPM and WDR62, we found no evidence for strong centrosome duplication defects after WDR62 loss or depletion, nor was WDR62 enriched at centrioles. Rather, we found that WDR62 preferentially localizes to spindle microtubule parts that terminate at spindle poles, possibly at microtubule minus-ends. This is consistent with previous studies reporting that WDR62 is found at microtubule nucleation sites associated with centrosomes or not (Bogovevitch et al., 2012).

> At the functional level we demonstrate that WDR62 loss differentially affects spindle microtubules: it increased k-fiber stability while reducing the density of astral microtubules. Since WDR62 itself does not localize to astral microtubules, we speculate that this latter effect is indirect. One possibility could be that the increased incorporation of tubulin dimers into k-fibers diminishes the pool of free tubulin dimers, decreasing tubulin incorporation in astral microtubules. Our results are also consistent with a loss of katanin at spindle poles, as full katanin



depletion results in an equivalent yet stronger pattern. These results, however, diverge from a previous study reporting that WDR62<sup>-/-</sup> mouse embryonic fibroblasts show a mild decrease in microtubule stability (Chen et al., 2014). The same study reported a mitotic arrest and unattached kinetochores in WDR62-/-, while our WDR62-depleted RPE1 or WDR62-deleted HeLa cells showed only a mild delay in mitotic progression, raising the possibility that human and murine cells might react differently to the loss of WDR62. One remarkable aspect is that WDR62 exclusively affected microtubule minus-end dynamics, reducing the rate of poleward microtubule flux, while leaving the k-fiber plus-end dynamics unaffected. We conclude that the two extremities of k-fibers can be regulated independently and are not necessarily mechanically coupled. Second, the results indicate that k-fiber stability is also determined by microtubule minus-end turnover, highlighting the emerging importance of minusend binding proteins (Akhmanova and Steinmetz, 2019; Jiang et al., 2017; 2014) and attenuating the prevalent view that k-fiber dynamics is primarily controlled by microtubule plusend dynamics (Akhmanova and Steinmetz, 2015).

How does the decrease in minus-end turnover in cells lacking WDR62 affect the function of the mitotic spindle? First, we find an increase in spindle length and buckling microtubules. Buckling is most likely the consequence of compressive forces that arise in the spindles when lengthening spindle microtubules are not severed (Tolić et al., 2019). Consistently, we also find buckling microtubules in cells depleted of KATNB1. In contrast to previous studies (Bogoyevitch et al., 2012; Miyamoto et al., 2017), but consistent with others (Chen et al., 2014; Jayaraman et al., 2016), we find no spindle orientation defects in cells lacking WDR62, in line with mouse experiments in which spindle orientation defects are not a major driver of primary microcephaly (Insolera et al., 2014). We also note that the increase in the average angle after WDR62 loss was either small (2°; Miyamoto et al., 2017) or based on only 12-14 cells in two independent experiments (Bogoyevitch et al., 2012), vs. >300 cells in five independent experiments in two different cell lines in the present study. We conclude that WDR62 depletion does not cause a major spindle orientation phenotype in a 2D tissue culture. This is surprising, given the reduction in astral microtubule density, which is critical for spindle orientation control. It is, however, possible that the increased spindle length seen in WDR62- or katanin-depleted cells compensates for the reduction in astral microtubules, allowing a sufficient interaction between cell cortex and astral microtubules. The consequences might be different in early murine neuronal stem cells that express low levels of the spindle-associated aurora-A activator TPX2 (Kufer et al., 2002), which controls the balance between spindle and astral microtubules (Vargas-Hurtado et al., 2019).

Nevertheless, the most striking phenotype we observe is that WDR62 loss leads to wider metaphase plates and asynchronous poleward anaphase movements. The increased kinetochore spread in anaphase results in lagging chromosomes that are integrated very late into the daughter nuclei. The monastrol-release experiments imply that these lagging chromosomes are not the results of an inefficient correction of erroneous

kinetochore-microtubule attachments due to hyperstable kfibers (Gregan et al., 2011; Lampson and Grishchuk, 2017). This suggests that inefficient error correction might correlate more with changes in microtubule plus-end turnover than with overall k-fiber stability (Bakhoum et al., 2009a), consistent with the observation that k-fiber stability and plus-end turnover are not necessarily correlated (Amaro et al., 2010). We postulate that in WDR62-depleted cells, asynchronous anaphase movements and lagging chromosomes are a direct consequence of reduced poleward microtubule flux rates. The decrease in flux rate is most likely due to the inability of WDR62depleted cells to efficiently sever microtubules at spindle poles, resulting in a jam that slows down the motor-driven flux machinery (Steblyanko et al., 2020) and leads to buckling microtubules. Our data suggest that lagging chromosomes are caused by the reduction in flux rates, and that microtubule buckling is separate symptom of the same condition. A link between efficient microtubule flux rate and chromosome segregation had been predicted by mathematical models, which postulated that poleward flux equalizes the pulling forces within the mitotic spindles (Matos et al., 2009). Consistent with a role for flux in force equalization, we find that WDR62 depletion does not change the anaphase A or B speeds, but specifically increases the spatial spread of kinetochores in metaphase and during anaphase. We postulate that a main function of WDR62 is to localize katanin on the spindle poles to ensure synchronous anaphase movements via poleward microtubule flux.

Interestingly, depletion of katanin itself led to a very similar but not equivalent phenotype. In metaphase, katanin depletion led to the same reduction in poleward microtubule flux, microtubule buckling, and even a stronger microtubule stabilization, indicating that unlike Drosophila katanin (Zhang et al., 2007), human katanin actively regulates microtubule dynamics at spindle poles before anaphase onset. While katanin depletion also increased metaphase plate width at anaphase onset (Fig. 5, G and H), these effects were weaker than in WDR62depleted cells and not significant within our sample size. This could be due to the effects of other katanin-pools, as it can also localize to microtubule plus-ends (Zhang et al., 2007), or to even higher suppression of spindle microtubule dynamics, which might limit the amplitude of chromosome movements (Fig. S2 D). During anaphase, katanin depletion led to not only a higher spread of chromosome, but also lower anaphase A and higher anaphase B speeds, an effect not seen after WDR62 depletion. This points to an additional role beyond the pool at spindle poles, consistent with the observation that Drosophila katanin is required for the "Pac-man"-like microtubule plus-end depolymerization during anaphase A (Zhang et al., 2007).

Based on our results, we postulate that WDR62 leads to defective chromosome segregation. Previous work had established that gain or loss of entire chromosomes (aneuploidy) in neural precursor cells can lead to microcephaly via premature differentiation in *D. melanogaster* (Gogendeau et al., 2015) or apoptosis in mice (Marthiens et al., 2013). Here, we speculate that WDR62 loss might lead to microcephaly not via gain or loss of entire chromosomes, but because of a late incorporation into the nucleus. Such events might lead to DNA damage due to incomplete nuclear envelope formation (de Castro et al., 2017) or to incorrect



chromosomal positioning in the future interphasic daughter nuclei (Gerlich et al., 2003). Indeed, chromosome misalignment in metaphase and a high spread in anaphase has been linked to developmental defects in mice, suggesting that lagging chromosomes may similarly disrupt proper development in WDR62 mutants (Fonseca et al., 2019; Orr and Maiato, 2019). Since WDR62 also affects cilia length (Shohayeb et al., 2020; Zhang et al., 2019), this might lead to cumulative defects affecting correct brain development, without necessarily a severe disruption of chromosome segregation.

#### **Materials and methods**

#### Cell culture and drug treatments

HeLa Kyoto, HeLa H2B-GFP (Meraldi et al., 2004), HeLa H2B-GFP WDR62-/-, HeLa WDR62-/- (kind gift of K. Jiang, Wuhan University, China), hTert-RPE1, hTert-RPE1 EB3-GFP/H2BmCherry (kind gift of W. Krek, ETH Zürich, Switzerland), hTert-RPE1 GFP-centrin1/GFP-CENPA (kind gift from A. Khodjakov, State University of New York) cell lines were cultured in DMEM (Thermo Fisher Scientific), supplemented with 10% FCS (Labforce), and 100 U/ml penicillin and 100 mg/ml streptomycin (Thermo Fisher Scientific). hTert-RPE1 PA-GFPα-tubulin cells (Toso et al., 2009) and hTert-RPE1 stably transfected with pIC113-eGFP or pIC113-WDR62-eGFP plasmids encoding for eGFP or WDR62-eGFP were in addition supplemented with 600 µg/ml G418 (InvivoGen). To create HeLa H2B-GFP WDR62<sup>-/-</sup> CRISPR knockout cells, HeLa H2B-GFP cells were transiently transfected with X-tremeGENE 9 (Roche), and a plasmid encoding both the Cas9-mRFP enzyme and a gRNA targeting the first exon of the human WDR62 gene (target sequence: 5'-GCTATGCGCGGAACGATGCAGG-3'; Sigma-Aldrich). Single Cas9-mRFP-positive cells were selected by FACS 24 h after transfection and sorted into a 96-well dish. Growing colonies were tested by PCR for small deletions, sequenced to confirm WDR62 gene frameshift, and validated for loss of WDR62 expression by immunofluorescence. All cells used were female and were cultured at 37°C with 5% CO2 for maximum 6 wk in a humidified incubator. For live-cell imaging, cells were cultured in eight-, four-, or two-well Ibidi chambers (Vitaris) in Leibovitz's L-15 medium (Thermo Fisher Scientific) supplemented with 10% FCS before imaging. The following drugs were added to the culturing or imaging medium: 10 µM MG132 for 30 min, 100 µM monastrol for 12-16 h, 200 ng/ml nocodazole for 15 min, 8 nM taxol (all Sigma-Aldrich) for 12 h, and 50 nM SiR-tubulin (Spirochrome) for 4 h.

#### siRNA and plasmid transfections

For protein depletions, cells were transfected for 48 h (72 h in case of siCAPD2) with 20 nM siRNAs using Opti-MEM and Lipofectamine RNAiMAX (Thermo Fisher Scientific) according to the manufacturer's instructions. The medium was replaced 24 h after transfection. The following sense strands of validated siRNA duplexes were used (all Qiagen unless indicated): siASPM (validation in Fig. S2), 5'-GCUAUAUGUCAGCGUACUATT-3'; si-CAPD2 (Hirota et al., 2004), 5'-CCAUAUGCUCAGUGCUACATT-3'; siKATNB1 (validation in Fig. S2), 5'-GCCUGGAUUUCCACC CGUATT-3'; siWDR62 (Dharmacon; validation in Fig. S1), 5'-AGA

CAAAGGUGACGACAC-3'; and as a negative control, either siCTRL (AllStars Negative Control siRNA; Qiagen), Proprietary or siLaminA (Qiagen), 5'GAAGGAGGGUGACCUGAUA-3'. For transient exogenous gene expression, cells were transfected using X-tremeGENE 9 DNA Transfection Reagent (Roche) with a ratio of 3:1  $\mu$ l/ $\mu$ g plasmid of DNA and analyzed 30 h after transfection. The pIC113-WDR62-eGFP plasmid encoding for an eGFP-tagged WDR62 was synthesized and subcloned by GeneArt (Thermo Fisher Scientific).

#### Monitoring of chromosome segregation by live-cell imaging

To monitor mitotic progression and chromosome segregation, HeLa H2B-eGFP, HeLa H2B-eGFP WDR62<sup>-/-</sup>, or hTert-RPE1 EB3-GFP/H2B-mCherry cells treated with siCTRL or siWDR62 were seeded into Ibidi chambers (Vitaris) supplemented with imaging medium 2-3 h before imaging and recorded on a Nikon Eclipse Ti-E wide-field microscope (Nikon) equipped with a GFP/mCherry filter set (Chroma Technology Corp.), an Orca Flash 4.0 complementary metal-oxide-semiconductor camera (Hamamatsu), and an environmental chamber using NIS software (Nikon). Cells were imaged in the GFP and mCherry channel for 9 h at 37°C, at 1-min intervals, in 9 steps of 2 µm Z-stacks, using a  $60 \times (NA 1.51)$  oil objective and  $2 \times 2$  binning. Alternatively, cells were released from monastrol arrest and imaged under the same conditions for 1 h and 15 min. Time-lapse movies were analyzed manually with NIS Elements software to quantify mitotic timing and segregation errors.

#### Spindle microtubule depolymerization assay

To quantify spindle microtubule stability, live hTert-RPE1 cells were seeded in Ibidi eight-well chamber (Vitaris) and depleted of the indicated protein. Before imaging, 50 nM SiR-tubulin (Spirochrome) was added for 4 h to label microtubules, and 10  $\mu M$  MG132 was added for 30 min to prevent mitotic exit. Imaging medium containing 200 ng/ml nocodazole, 50 nM SiRtubulin, and 10 µM MG132 was added upon starting time-lapse imaging. Cells were imaged every 1 min for 15 min using a 100× (NA 1.4) oil objective on an Olympus DeltaVision wide-field microscope (GE Healthcare) equipped with an environmental chamber maintained at 37°C and with DAPI/FITC/TRITC/Cy5 filter set (Chroma Technology Corp.) and Coolsnap HQ2 chargecoupled device (CCD) camera (Roper Scientific) running Softworx (GE Healthcare). Z-stacks of 15-μm thickness with z-slices separated by 0.5  $\mu m$  were imaged in the Cy5 channel with 2  $\times$ 2 binning to track for microtubule depolymerization. 4D images (XYZT) obtained were deconvolved using Softworx (GE Healthcare) in conservative mode, and the intensity decay of the whole spindle was quantified using an automated ImageJ plugin (coded in NetBeans IDE, Apache Software Foundation; available at https://github.com/AmandaGuerreiro/WDR62\_ 2020). The plugin segments each cell based on Otsu's method and performs a sum intensity projection along the z-axis for all time points. Using RStudio, the values of 4D image pixels were summed, resulting in a fluorescence intensity signal over time. Microtubule loss was expressed as a percentage of the decay of the SiR-tubulin signal normalized to the first time point (100%). Statistical analysis of microtubule



depolymerization was done using repeated paired t test and a 95% CI over time.

#### Kinetochore tracking (KT) assay

hTert-RPE1 GFP-centrin1/GFP-CENPA were treated with the indicated siRNA, and metaphase cells were imaged for 15 min every 15 s using a 100× (NA 1.4) oil objective on an Olympus DeltaVision wide-field microscope (GE Healthcare) equipped with an environmental chamber maintained at 37°C and a GFP/RFP filter set (Chroma Technology Corp.) and Coolsnap HQ2 CCD camera (Roper Scientific) running Softworx (GE Healthcare). Z-stacks of 15- $\mu$ m thickness with z-slices separated by 0.5  $\mu$ m were imaged in the GFP channel with 2 × 2 binning to track for kinetochores from metaphase until anaphase. 4D images (XYZT) obtained were deconvolved in conservative mode and cropped using Softworx (GE Healthcare).

For KT in metaphase, 4D images (XYZT) were analyzed using an automated KT code written in MatLab 2013b (MathWorks; Jaqaman et al., 2010). The latest code is available under https://github.com/cmcb-warwick, and the parameters described in Olziersky et al. (2018). Briefly, the output of this analysis is the frame-to-frame displacement of sister-kinetochores and their relative distance from the center of the metaphase plate. We extracted the interkinetochore distance of sister-kinetochore pairs and used an autocorrelation function to quantify the regularity of the sister-kinetochore oscillations along the spindle axis. Kinetochore velocities were calculated by plotting the distribution of all sister-kinetochore displacements and calculating the SD of this distribution.

For KT in anaphase, 4D acquisitions (XYZT) were processed using Imaris 9.5.1 (Bitplane) to segment kinetochores and centrioles during metaphase and anaphase. All the positions through time were analyzed using a custom-made framework written in Matlab 2019b (available under https://github. com/AmandaGuerreiro/WDR62\_2020). Anaphase onset was automatically detected by finding the abrupt slope change of the pole-to-pole distance during the time course. Accuracy detection was assessed by the user and manually shifted if necessary. Anaphase A speed for each pole was defined as the slope of a linear fit of the kinetochore-to-pole mean distance during 120 s after onset. Anaphase B speed was defined as the slope of the pole-to-pole distance during the same time after onset. Kinetochore spread was quantified by orthogonal projection of all the kinetochores along the pole-to-pole axis and was represented as the maximum distance between the kinetochores over time in metaphase (Fig. 5 G), the average (obtained from the SD) width in the last 30 s before anaphase onset (Fig. 5 H), and the maximum distance between kinetochores during anaphase (Fig. 6 G).

#### Poleward microtubule flux measurement

hTert-RPE1 PA-GFP- $\alpha$ -tubulin cells were incubated with 50 nM SiR-DNA in the last 2 h and 10  $\mu$ M MG132 in the last 30 min. Cells incubated were imaged for  $\leq$ 2 h. Single focal planes of 150-nm pixel size were acquired using a 60× (NA 1.4) CFI Plan Apochromat oil objective on a Nikon A1r point scanning confocal microscope equipped with a 37°C heating chamber and running

NIS elements software. Half-spindles were photoactivated with a 500-ms, 405-nm laser pulse at 30–80% intensity depending on the PA-GFP- $\alpha$ -tubulin expression levels, using a 1-pixel-thick and 100-pixel-long region of interest stretched across the spindle. Single focal planes were imaged every 20 s for 4 min. Photoactivated kinetochore-microtubule bundles were tracked for 80 s. By computing manually the mean distance between the photoactivation mark on kinetochore-microtubule bundles and the corresponding spindle poles at different time points, we calculated the mean displacement of the photoactivation mark over time. Note that since spindle length did not change during the recording period, the rate of progression toward the spindle pole and the rate of displacement away from the metaphase plate is equivalent.

#### **Immunofluorescence**

For the cold-stable assay, hTert-RPE1 and HeLa cells were treated with ice-cold medium for 6 or 20 min. To label microtubules, cells were rinsed with cytoskeleton buffer (10 mM MES, 150 mM NaCl<sub>2</sub>, 5 mM MgCl<sub>2</sub>, and 5 mM glucose; Sigma-Aldrich) before and 2 × 10 min after fixation with a solution composed of 3% formaldehyde, 0.05% glutaraldehyde, and 0.1% Triton X-100 (Sigma-Aldrich) for 15 min at 4°C. The same fixation method was also used to stain astral microtubules. To induce acentrosomal spindles, HeLa cells were treated for 12 h with 8 nM taxol or DMSO. For minus-end quantifications, cells were fixed with -20°C methanol for 7 min and rinsed once for 5 min with 0.15% Triton X-100 in PBS. For MCAK and CAPD2 quantifications, cells were fixed with 10% formaldehyde, 25 M of 8% PIPES, 0.25 M of 4% EGTA, and 2% Triton X-100 (Sigma-Aldrich) in 76% ddH<sub>2</sub>O for 15 min at RT; subsequent extraction was performed in blocking buffer supplemented with 0.5% Triton X-100 for 2 × 10 min followed by PBS with 0.1% Triton X-100 for  $3 \times 5$  min. After fixation, cells were blocked overnight at 4°C in PBS + 3% BSA and 1% N<sub>3</sub>Na (Applichem). Subsequent washings were performed in PBS with 0.05% Tween-20 for 3 × 10 min and in blocking buffer supplemented with 0.1% Triton X-100 for 3 × 10 min for MCAK and CAPD2 quantifications. Labeling steps were performed in blocking solution for 1 h at RT for primary antibodies and 30 min at RT for secondary antibodies. Coverslips were mounted on slides with DAPI Vectashield mounting medium (Vector Laboratories). The following primary antibodies were used: mouse anti-α-tubulin (1:500; Sigma-Aldrich), recombinant human anti-α-tubulin (1 µg/ml; Guerreiro and Meraldi, 2019), rabbit anti-γ-tubulin (1:2,000; Wilhelm et al., 2019), mouse anti-γ-tubulin (1:1,000; Sigma-Aldrich), rabbit anti-ASPM (1:100; Novus Biologicals), guinea pig anti-CENP-C (1:1,000; MBL), mouse anti-centrin-1 (1:2,000; Merck Millipore), rabbit anti-KATNB1 (1:250; Proteintech), rabbit anti-CAPD2 (1:100; Abcam), rabbit anti-NuMA (1:100; Abcam), mouse antipericentrin (1:1,000; Abcam), and rabbit anti-WDR62 (1:1,000; Bethyl). For secondary antibodies, cross-adsorbed Alexa Fluorconjugated antibodies (1:400; Invitrogen) were used. Pictures were acquired using 60× and 100× (NA 1.4) oil objectives on an Olympus DeltaVision wide-field microscope (GE Healthcare) equipped with a DAPI/FITC/TRITC/Cy5 filter set (Chroma Technology Corp.) and Coolsnap HQ2 CCD camera (Roper Scientific) running Softworx (GE Healthcare). Z-stacks of 12.80-µm



thickness were imaged with z-slices separated by 0.2  $\mu$ m. 3D images stacks were deconvolved using Softworx (GE Healthcare) in conservative mode.

#### STED nanoscopy and confocal microscopy

Multicolor 2D-STED imaging was performed with a TCS SP8 STED 3× microscope (Leica) at 21°C using a STED motorized glycerol immersion objective (HC PL Apo 93×/NA 1.30 motCOR). Fluorescence-labeled samples were mounted in Prolong Antifade Gold (Thermo Fisher Scientific) between a coverslip (0.170 ± 0.01 mm thick; Hecht-Assistent) and a microscope slide and sealed with nail polish. Excitation was performed with a white light laser (WLL), and depletion with either a continuous 592nm laser or a 775-nm pulsed laser. Excitation and depletion lasers were calibrated with the STED Expert Alignment Mode and Abberior gold nanoparticles (80 nm in diameter) before starting each imaging session, or with the STED Auto Beam Alignment tool during imaging sessions (Leica LAS X software). Multicolor 2D-STED imaging was made sequentially using excitation at 638 nm (WLL) and a STED 775 depletion laser line for Abberior STAR RED anti-rabbit antibody, followed by excitation at 580 nm (WLL) and a STED 775 depletion laser line for Abberior STAR 580 anti-mouse antibody, and then by excitation at 488 nm (WLL) and a STED 592 depletion laser line for Alexa Fluor 488 anti-human antibody. Detection signals were collected between 647 and 677 nm for STAR RED, between 591 and 612 nm for STAR 580, and between 492 and 562 nm for AF488 using highly sensitive Leica Hybrid Detectors with a fixed gain and offset (100 mV and 0, respectively). Time-gated detection was used for all fluorophores (0.50-6.00 ns). Acquisitions were performed with a line average of 4, a speed of 400 Hz, and an optimized pixel size. 2D-STED images were deconvolved using the Leica Lightning Mode (LAS X software) and analyzed with ImageJ/Fiji (National Institutes of Health). Z-stack confocal acquisitions were obtained in the same conditions, but without depletion and time-gated detection, with an optimized pinhole aperture and by respecting Nyquist criterion.

#### Image processing and analysis

Immunofluorescence images from the cold-stable assay were analyzed blindly: the acquired images were visualized in 3D using Imaris (Bitplane), and cells were categorized into three different classes according to the abundance of kinetochore fibers. For astral microtubules and minus-end immunofluorescence quantifications in metaphase, 3D images were analyzed with ImageJ/Fiji using a plugin developed with NetBeans IDE (v.8.2). Briefly, a mask was created on centrosomes using yen dark thresholding on sum projections. Quantification of fluorescence was performed for each channel using the mask. For kinetochore immunofluorescence quantification in interphase, 3D images were analyzed manually with ImageJ/Fiji using yen dark thresholding on sum projections. For spindle orientation quantification in immunofluorescence, 3D images were analyzed with ImageJ/Fiji. A plugin was used to calculate the angle from two points in regions of interest defined in the Z-stack at centrosome position.

#### **Immunoblotting**

For cell extracts, cells were lysed in radioimmunoprecipitation assay buffer (50 mM Tris-HCl, pH 7.3, 150 mM NaCl, 0.1 mM EDTA, 1% Triton X-100, and 0.5 mM PMSF) supplemented with Protease Inhibitor Cocktail and PhosSTOP phosphatase inhibitor (Sigma-Aldrich). Cell lysates were incubated on ice (30 min) and cleared by centrifugation (16,000 q, 10 min at 4°C). Protein concentrations were determined by Bradford assay (Thermo Fisher Scientific). 2× Laemmli buffer was added before SDS-PAGE and not boiled. Proteins were separated on 4-15% gradient TGX precast gels (Bio-Rad), transferred onto nitrocellulose membrane by wet blotting, and blocked for 1 h at RT with 5% nonfat milk powder in PBS. Subsequent washings were performed in PBS with 0.05% Tween-20 for 3 × 10 min. The following primary antibodies were used: rabbit anti-KATNB1 (1:500; Proteintech), rabbit anti-WDR62 (1:500; Bethyl), and mouse anti-β-actin (1:1,000; Merck Millipore). The following HRP-conjugated secondary antibodies were used: ECL antirabbit IgG and anti-mouse IgG (Thermo Fisher Scientific). Protein bands were detected using the ECL Prime Western Blotting Detection reagent (GE Healthcare) and a PXi/PXi Touch luminescence detector (Syngene). Protein bands were quantified with ImageJ as described in the method outlined at https:// lukemiller.org/index.php/2010/11/analyzing-gels-and-westernblots-with-image-j/. Specific protein signals were normalized to β-actin.

#### Statistical analysis

Data were quantified using ImageJ/Fiji, Imaris software (v7.7 or v9.3), Matlab (versions 2013b, 2018a, or 2019b), and RStudio (v1.2). Statistical analysis was performed in Prism (GraphPad, v8.4), Matlab (KT assay), or RStudio (kinetochore microtubule depolymerization assay and frequency distribution of spindle orientation with pole-to-pole distance). Frequency distributions in RStudio were computed using kernel density estimate function.

#### Online supplemental material

Fig. S1 shows WDR62 deletion and depletion efficiency. Fig. S2 shows that KATNB1 depletion mimics WDR62 depletion. Fig. S3 shows that WDR62<sup>-/-</sup> HeLa cells show no difference in spindle orientation or pole-to-pole distance, and spindle length of MG132-arrested RPE1 cells are constant. Fig. S4 shows validation of CAPD2 depletion in RPE1 cells. Fig. S5 shows that loss of WDR62 in HeLa cells does not affect mitotic timing but increases the percentage of lagging chromosomes. Video 1, Video 2, and Video 3 show microtubule poleward flux after photoactivation of hTert-RPE1 PA-GFP- $\alpha$ -tubulin cells treated with siCTRL, siKATNB1, and siWDR62, respectively. Video 4 shows no error of chromosome segregation in hTert-RPE1 EB3-GFP/ H2B-mCherry cells treated with siCTRL. Video 5 shows lagging chromosomes in anaphase in hTert-RPE1 EB3-GFP/H2BmCherry cells treated with siWDR62. Video 6 shows a DNA bridge in anaphase in hTert-RPE1 EB3-GFP/H2B-mCherry cells treated with siWDR62. Video 7 shows sister-kinetochore oscillations of siCTRL treated hTert-RPE1 GFP-centrin/GFP-CENPA cells, showing tight metaphase plate and synchronous anaphase



onset. Video 8 shows sister-kinetochore oscillations of siWDR62 treated hTert-RPE1 GFP-centrin1/GFP-CENPA cells, showing wide metaphase plate and asynchronous anaphase onset with lagging chromosomes.

#### **Acknowledgments**

We thank A. Khodjakov (State University of New York) and the late W. Krek (ETH Zürich, Switzerland) for cell lines; K. Jiang (Wuhan University, China) for sharing results before publication and the HeLa WDR62<sup>-/-</sup> cells; the Bioimaging Facility at the Medical Faculty, University of Geneva, Switzerland, for microscopy support; M. Hoveyda (University of Geneva) for initiating the investigation of WDR62 and spindle stability; L. Brodier (University of Geneva) for technical discussions and help with R and ImageJ plugins; D. Dudka (University of Pennsylvania), M. Gotta (University of Geneva), and T. Wilhelm (Curie Institute, France) for critical discussions; and members of the Meraldi laboratory for support and technical help.

Work in the Meraldi laboratory of A. Guerreiro, F. De Sousa, D. Ivanova, A. Eskat, and P. Meraldi is supported by a Swiss National Science Foundation project grant (31003A\_179413) and the University of Geneva.

The authors declare no competing financial interests.

Author contributions: The project was initiated by A. Guerreiro and P. Meraldi and directed by P. Meraldi; A. Guerreiro performed all experiments; F. De Sousa contributed to chromosome segregation experiments and immunoblotting; N. Liaudet wrote the anaphase tracking code; A. Eskat generated the HeLa H2B-GFP WDR62<sup>-/-</sup> cell line; D. Ivanova contributed to spindle size and chromosome segregation experiments; A. Guerreiro, F. De Sousa, and P. Meraldi analyzed and interpreted all the results with contribution from N. Liaudet; and A. Guerreiro and P. Meraldi wrote the manuscript.

Submitted: 27 July 2020 Revised: 12 April 2021 Accepted: 18 May 2021

#### References

- Akhmanova, A., and M.O. Steinmetz. 2015. Control of microtubule organization and dynamics: two ends in the limelight. *Nat. Rev. Mol. Cell Biol.* 16:711-726. https://doi.org/10.1038/nrm4084
- Akhmanova, A., and M.O. Steinmetz. 2019. Microtubule minus-end regulation at a glance. J. Cell Sci. 132:jcs227850. https://doi.org/10.1242/jcs...227850
- Amaro, A.C., C.P. Samora, R. Holtackers, E. Wang, I.J. Kingston, M. Alonso, M. Lampson, A.D. McAinsh, and P. Meraldi. 2010. Molecular control of kinetochore-microtubule dynamics and chromosome oscillations. *Nat. Cell Biol.* 12:319–329. https://doi.org/10.1038/ncb2033
- Bakhoum, S.F., G. Genovese, and D.A. Compton. 2009a. Deviant kinetochore microtubule dynamics underlie chromosomal instability. Curr. Biol. 19: 1937–1942. https://doi.org/10.1016/j.cub.2009.09.055
- Bakhoum, S.F., S.L. Thompson, A.L. Manning, and D.A. Compton. 2009b. Genome stability is ensured by temporal control of kinetochore-microtubule dynamics. *Nat. Cell Biol.* 11:27–35. https://doi.org/10.1038/nch1809
- Basto, R., J. Lau, T. Vinogradova, A. Gardiol, C.G. Woods, A. Khodjakov, and J.W. Raff. 2006. Flies without centrioles. Cell. 125:1375–1386. https://doi.org/10.1016/j.cell.2006.05.025

- Bilgüvar, K., A.K. Oztürk, A. Louvi, K.Y. Kwan, M. Choi, B. Tatli, D. Yalnizoğlu, B. Tüysüz, A.O. Cağlayan, S. Gökben, et al. 2010. Whole-exome sequencing identifies recessive WDR62 mutations in severe brain malformations. *Nature*. 467:207-210. https://doi.org/10.1038/nature09327
- Bogoyevitch, M.A., Y.Y.C. Yeap, Z. Qu, K.R. Ngoei, Y.Y. Yip, T.T. Zhao, J.I. Heng, and D.C.H. Ng. 2012. WD40-repeat protein 62 is a JNK-phosphorylated spindle pole protein required for spindle maintenance and timely mitotic progression. J. Cell Sci. 125:5096-5109. https://doi.org/10.1242/jcs.107326
- Bond, J., E. Roberts, G.H. Mochida, D.J. Hampshire, S. Scott, J.M. Askham, K. Springell, M. Mahadevan, Y.J. Crow, A.F. Markham, et al. 2002. ASPM is a major determinant of cerebral cortical size. *Nat. Genet.* 32:316–320. https://doi.org/10.1038/ng995
- Bond, J., E. Roberts, K. Springell, S.B. Lizarraga, S. Scott, J. Higgins, D.J. Hampshire, E.E. Morrison, G.F. Leal, E.O. Silva, et al. 2005. A centrosomal mechanism involving CDK5RAP2 and CENPJ controls brain size. Nat. Genet. 37:353–355. https://doi.org/10.1038/ng1539
- Bond, J., S. Scott, D.J. Hampshire, K. Springell, P. Corry, M.J. Abramowicz, G.H. Mochida, R.C.M. Hennekam, E.R. Maher, J.-P. Fryns, et al. 2003. Protein-truncating mutations in ASPM cause variable reduction in brain size. Am. J. Hum. Genet. 73:1170–1177. https://doi.org/10.1086/379085
- Buster, D.W., D. Zhang, and D.J. Sharp. 2007. Poleward tubulin flux in spindles: regulation and function in mitotic cells. *Mol. Biol. Cell.* 18: 3094–3104. https://doi.org/10.1091/mbc.e06-11-0994
- Chen, J.-F., Y. Zhang, J. Wilde, K.C. Hansen, F. Lai, and L. Niswander. 2014. Microcephaly disease gene Wdr62 regulates mitotic progression of embryonic neural stem cells and brain size. Nat. Commun. 5:3885. https://doi.org/10.1038/ncomms4885
- Conduit, P.T., A. Wainman, and J.W. Raff. 2015. Centrosome function and assembly in animal cells. *Nat. Rev. Mol. Cell Biol.* 16:611–624. https://doi.org/10.1038/nrm4062
- David, A.F., P. Roudot, W.R. Legant, E. Betzig, G. Danuser, and D.W. Gerlich. 2019. Augmin accumulation on long-lived microtubules drives amplification and kinetochore-directed growth. J. Cell Biol. 218:2150–2168. https://doi.org/10.1083/jcb.201805044
- de Castro, I.J., R.S. Gil, L. Ligammari, M.L. Di Giacinto, and P. Vagnarelli. 2017. CDK1 and PLK1 coordinate the disassembly and reassembly of the nuclear envelope in vertebrate mitosis. Oncotarget. 9:7763-7773. https://doi.org/10.18632/oncotarget.23666
- Dudka, D., C. Castrogiovanni, N. Liaudet, H. Vassal, and P. Meraldi. 2019. Spindle-Length-Dependent HURP Localization Allows Centrosomes to Control Kinetochore-Fiber Plus-End Dynamics. Curr. Biol. 29: 3563–3578.e6. https://doi.org/10.1016/j.cub.2019.08.061
- Elting, M.W., C.L. Hueschen, D.B. Udy, and S. Dumont. 2014. Force on spindle microtubule minus ends moves chromosomes. J. Cell Biol. 206:245–256. https://doi.org/10.1083/jcb.201401091
- Fonseca, C.L., H.L.H. Malaby, L.A. Sepaniac, W. Martin, C. Byers, A. Czechanski, D. Messinger, M. Tang, R. Ohi, L.G. Reinholdt, and J. Stumpff. 2019. Mitotic chromosome alignment ensures mitotic fidelity by promoting interchromosomal compaction during anaphase. J. Cell Biol. 218: 1148–1163. https://doi.org/10.1083/jcb.201807228
- Ganem, N.J., S.A. Godinho, and D. Pellman. 2009. A mechanism linking extra centrosomes to chromosomal instability. *Nature*. 460:278–282. https:// doi.org/10.1038/nature08136
- Ganem, N.J., K. Upton, and D.A. Compton. 2005. Efficient mitosis in human cells lacking poleward microtubule flux. Curr. Biol. 15:1827-1832. https://doi.org/10.1016/j.cub.2005.08.065
- Gerlich, D., J. Beaudouin, B. Kalbfuss, N. Daigle, R. Eils, and J. Ellenberg. 2003. Global chromosome positions are transmitted through mitosis in mammalian cells. *Cell.* 112:751–764. https://doi.org/10.1016/S0092-8674(03)00189-2
- Godek, K.M., L. Kabeche, and D.A. Compton. 2015. Regulation of kinetochoremicrotubule attachments through homeostatic control during mitosis. Nat. Rev. Mol. Cell Biol. 16:57-64. https://doi.org/10.1038/nrm3916
- Gogendeau, D., K. Siudeja, D. Gambarotto, C. Pennetier, A.J. Bardin, and R. Basto. 2015. Aneuploidy causes premature differentiation of neural and intestinal stem cells. *Nat. Commun.* 6:8894. https://doi.org/10.1038/ncomms9894
- Gordon, M.B., L. Howard, and D.A. Compton. 2001. Chromosome movement in mitosis requires microtubule anchorage at spindle poles. J. Cell Biol. 152:425-434. https://doi.org/10.1083/jcb.152.3.425
- Gregan, J., S. Polakova, L. Zhang, I.M. Tolić-Nørrelykke, and D. Cimini. 2011. Merotelic kinetochore attachment: causes and effects. *Trends Cell Biol.* 21:374–381. https://doi.org/10.1016/j.tcb.2011.01.003



- Guerreiro, A., and P. Meraldi. 2019. AA344 and AA345 antibodies recognize the microtubule network in human cells by immunofluorescence. *Antibody Rep.* 2:e17. https://doi.org/10.24450/journals/abrep.2019.e17
- Hirota, T., D. Gerlich, B. Koch, J. Ellenberg, and J.-M. Peters. 2004. Distinct functions of condensin I and II in mitotic chromosome assembly. J. Cell Sci. 117:6435–6445. https://doi.org/10.1242/jcs.01604
- Hu, D.J.-K., and H. Jasper. 2019. Control of Intestinal Cell Fate by Dynamic Mitotic Spindle Repositioning Influences Epithelial Homeostasis and Longevity. Cell Rep. 28:2807–2823.e5. https://doi.org/10.1016/j.celrep .2019.08.014
- Hu, W.F., O. Pomp, T. Ben-Omran, A. Kodani, K. Henke, G.H. Mochida, T.W. Yu, M.B. Woodworth, C. Bonnard, G.S. Raj, et al. 2014. Katanin p80 regulates human cortical development by limiting centriole and cilia number. *Neuron.* 84:1240-1257. https://doi.org/10.1016/j.neuron.2014 12.017
- Huang, J., Z. Liang, C. Guan, S. Hua, and K. Jiang. 2021. WDR62 regulates spindle dynamics as an adaptor protein between TPX2/Aurora A and katanin. J. Cell Biol. In press. https://doi.org/10.1083/jcb.202007167
- Hussain, M.S., S.M. Baig, S. Neumann, V.S. Peche, S. Szczepanski, G. Nürnberg, M. Tariq, M. Jameel, T.N. Khan, A. Fatima, et al. 2013. CDK6 associates with the centrosome during mitosis and is mutated in a large Pakistani family with primary microcephaly. Hum. Mol. Genet. 22: 5199–5214. https://doi.org/10.1093/hmg/ddt374
- Insolera, R., H. Bazzi, W. Shao, K.V. Anderson, and S.-H. Shi. 2014. Cortical neurogenesis in the absence of centrioles. *Nat. Neurosci.* 17:1528–1535. https://doi.org/10.1038/nn.3831
- Jaqaman, K., E.M. King, A.C. Amaro, J.R. Winter, J.F. Dorn, H.L. Elliott, N. McHedlishvili, S.E. McClelland, I.M. Porter, M. Posch, et al. 2010. Kinetochore alignment within the metaphase plate is regulated by centromere stiffness and microtubule depolymerases. J. Cell Biol. 188: 665–679. https://doi.org/10.1083/jcb.200909005
- Jayaraman, D., B.-I. Bae, and C.A. Walsh. 2018. The Genetics of Primary Microcephaly. Annu. Rev. Genomics Hum. Genet. 19:177–200. https://doi.org/10.1146/annurev-genom-083117-021441
- Jayaraman, D., A. Kodani, D.M. Gonzalez, J.D. Mancias, G.H. Mochida, C. Vagnoni, J. Johnson, N. Krogan, J.W. Harper, J.F. Reiter, et al. 2016. Microcephaly Proteins Wdr62 and Aspm Define a Mother Centriole Complex Regulating Centriole Biogenesis, Apical Complex, and Cell Fate. Neuron. 92:813–828. https://doi.org/10.1016/j.neuron.2016.09.056
- Jiang, K., S. Hua, R. Mohan, I. Grigoriev, K.W. Yau, Q. Liu, E.A. Katrukha, A.F.M. Altelaar, A.J.R. Heck, C.C. Hoogenraad, and A. Akhmanova. 2014. Microtubule minus-end stabilization by polymerization-driven CAM-SAP deposition. *Dev. Cell.* 28:295–309. https://doi.org/10.1016/j.devcel .2014.01.001
- Jiang, K., L. Rezabkova, S. Hua, Q. Liu, G. Capitani, A.F.M. Altelaar, A.J.R. Heck, R.A. Kammerer, M.O. Steinmetz, and A. Akhmanova. 2017. Microtubule minus-end regulation at spindle poles by an ASPM-katanin complex. Nat. Cell Biol. 19:480–492. https://doi.org/10.1038/ncb3511
- Joglekar, A.P. 2016. A Cell Biological Perspective on Past, Present and Future Investigations of the Spindle Assembly Checkpoint. Biology (Basel). 5:44. https://doi.org/10.3390/biology5040044
- Jordan, M.A., R.J. Toso, D. Thrower, and L. Wilson. 1993. Mechanism of mitotic block and inhibition of cell proliferation by taxol at low concentrations. Proc. Natl. Acad. Sci. USA. 90:9552-9556. https://doi.org/10.1073/pnas.90.20.9552
- Kaseda, K., A.D. McAinsh, and R.A. Cross. 2012. Dual pathway spindle assembly increases both the speed and the fidelity of mitosis. *Biol. Open.* 1: 12–18. https://doi.org/10.1242/bio.2011012
- Kodani, A., T.W. Yu, J.R. Johnson, D. Jayaraman, T.L. Johnson, L. Al-Gazali, L. Sztriha, J.N. Partlow, H. Kim, A.L. Krup, et al. 2015. Centriolar satellites assemble centrosomal microcephaly proteins to recruit CDK2 and promote centriole duplication. *eLife*. 4:e07519. https://doi.org/10.7554/eLife.07519
- Kufer, T.A., H.H.W. Sillje, R. Körner, O.J. Gruss, P. Meraldi, and E.A. Nigg. 2002. Human TPX2 is required for targeting Aurora-A kinase to the spindle. J. Cell Biol. 158:617-623. https://doi.org/10.1083/jcb.200204155
- Lampson, M.A., and E.L. Grishchuk. 2017. Mechanisms to Avoid and Correct Erroneous Kinetochore-Microtubule Attachments. Biology (Basel). 6:1. https://doi.org/10.3390/biology6010001
- Lampson, M.A., K. Renduchitala, A. Khodjakov, and T.M. Kapoor. 2004. Correcting improper chromosome-spindle attachments during cell division. Nat. Cell Biol. 6:232-237. https://doi.org/10.1038/ncb1102
- Lancaster, M.A., and J.A. Knoblich. 2012. Spindle orientation in mammalian cerebral cortical development. Curr. Opin. Neurobiol. 22:737-746. https://doi.org/10.1016/j.conb.2012.04.003

- Levine, M.S., and A.J. Holland. 2018. The impact of mitotic errors on cell proliferation and tumorigenesis. *Genes Dev.* 32:620-638. https://doi.org/ 10.1101/gad.314351.118
- Lim, N.R., Y.Y.C. Yeap, T.T. Zhao, Y.Y. Yip, S.C. Wong, D. Xu, C.-S. Ang, N.A. Williamson, Z. Xu, M.A. Bogoyevitch, and D.C.H. Ng. 2015. Opposing roles for JNK and Aurora A in regulating the association of WDR62 with spindle microtubules. J. Cell Sci. 128:527–540. https://doi.org/10.1242/jcs.157537
- Lim, N.R., Y.Y.C. Yeap, C.-S. Ang, N.A. Williamson, M.A. Bogoyevitch, L.M. Quinn, and D.C.H. Ng. 2016. Aurora A phosphorylation of WD40-repeat protein 62 in mitotic spindle regulation. *Cell Cycle*. 15:413–424. https://doi.org/10.1080/15384101.2015.1127472
- Lukinavičius, G., L. Reymond, E. D'Este, A. Masharina, F. Göttfert, H. Ta, A. Güther, M. Fournier, S. Rizzo, H. Waldmann, et al. 2014. Fluorogenic probes for live-cell imaging of the cytoskeleton. Nat. Methods. 11: 731–733. https://doi.org/10.1038/nmeth.2972
- Marthiens, V., M.A. Rujano, C. Pennetier, S. Tessier, P. Paul-Gilloteaux, and R. Basto. 2013. Centrosome amplification causes microcephaly. *Nat. Cell Biol.* 15:731-740. https://doi.org/10.1038/ncb2746
- Matos, I., A.J. Pereira, M. Lince-Faria, L.A. Cameron, E.D. Salmon, and H. Maiato. 2009. Synchronizing chromosome segregation by flux-dependent force equalization at kinetochores. J. Cell Biol. 186:11–26. https://doi.org/10.1083/jcb.200904153
- McHedlishvili, N., S. Wieser, R. Holtackers, J. Mouysset, M. Belwal, A.C. Amaro, and P. Meraldi. 2012. Kinetochores accelerate centrosome separation to ensure faithful chromosome segregation. J. Cell Sci. 125: 906–918. https://doi.org/10.1242/jcs.091967
- Meraldi, P. 2016. Centrosomes in spindle organization and chromosome segregation: a mechanistic view. Chromosome Res. 24:19-34. https://doi.org/10.1007/s10577-015-9508-2
- Meraldi, P., V.M. Draviam, and P.K. Sorger. 2004. Timing and checkpoints in the regulation of mitotic progression. Dev. Cell. 7:45–60.
- Mishra-Gorur, K., A.O. Çağlayan, A.E. Schaffer, C. Chabu, O. Henegariu, F. Vonhoff, G.T. Akgümüş, S. Nishimura, W. Han, S. Tu, et al. 2014. Mutations in KATNBI cause complex cerebral malformations by disrupting asymmetrically dividing neural progenitors. *Neuron.* 84:1226–1239. https://doi.org/10.1016/j.neuron.2014.12.014
- Mitchison, T.J. 1989. Polewards microtubule flux in the mitotic spindle: evidence from photoactivation of fluorescence. *J. Cell Biol.* 109:637–652.
- Miyamoto, T., S.N. Akutsu, A. Fukumitsu, H. Morino, Y. Masatsuna, K. Hosoba, H. Kawakami, T. Yamamoto, K. Shimizu, H. Ohashi, and S. Matsuura. 2017. PLK1-mediated phosphorylation of WDR62/MCPH2 ensures proper mitotic spindle orientation. Hum. Mol. Genet. 26: 4429-4440. https://doi.org/10.1093/hmg/ddx330
- Nam, H.-J., and J.M. van Deursen. 2014. Cyclin B2 and p53 control proper timing of centrosome separation. Nat. Cell Biol. 16:538–549. https://doi .org/10.1038/ncb2952
- Nano, M., and R. Basto. 2017. Consequences of Centrosome Dysfunction During Brain Development. Adv. Exp. Med. Biol. 1002:19-45. https://doi.org/10.1007/978-3-319-57127-0\_2
- Nicholas, A.K., M. Khurshid, J. Désir, O.P. Carvalho, J.J. Cox, G. Thornton, R. Kausar, M. Ansar, W. Ahmad, A. Verloes, et al. 2010. WDR62 is associated with the spindle pole and is mutated in human microcephaly. Nat. Genet. 42:1010-1014. https://doi.org/10.1038/ng.682
- Nigg, E.A., L. Čajánek, and C. Arquint. 2014. The centrosome duplication cycle in health and disease. FEBS Lett. 588:2366–2372. https://doi.org/10.1016/ j.febslet.2014.06.030
- Noatynska, A., M. Gotta, and P. Meraldi. 2012. Mitotic spindle (DIS)orientation and DISease: cause or consequence? *J. Cell Biol.* 199:1025–1035. https://doi.org/10.1083/jcb.201209015
- O'Neill, R.S., T.A. Schoborg, and N.M. Rusan. 2018. Same but different: pleiotropy in centrosome-related microcephaly. *Mol. Biol. Cell.* 29: 241–246. https://doi.org/10.1091/mbc.E17-03-0192
- Olziersky, A.-M., C.A. Smith, N. Burroughs, A.D. McAinsh, and P. Meraldi. 2018. Mitotic live-cell imaging at different timescales. *Methods Cell Biol.* 145:1–27. https://doi.org/10.1016/bs.mcb.2018.03.009
- Orr, B., and H. Maiato. 2019. No chromosome left behind: The importance of metaphase alignment for mitotic fidelity. J. Cell Biol. 218:1086–1088. https://doi.org/10.1083/jcb.201902041
- Pereira, A.J., and H. Maiato. 2010. Improved kymography tools and its applications to mitosis. Methods. 51:214-219. https://doi.org/10.1016/j .ymeth.2010.01.016
- Prosser, S.L., and L. Pelletier. 2017. Mitotic spindle assembly in animal cells: a fine balancing act. Nat. Rev. Mol. Cell Biol. 18:187–201. https://doi.org/10 .1038/nrm.2016.162

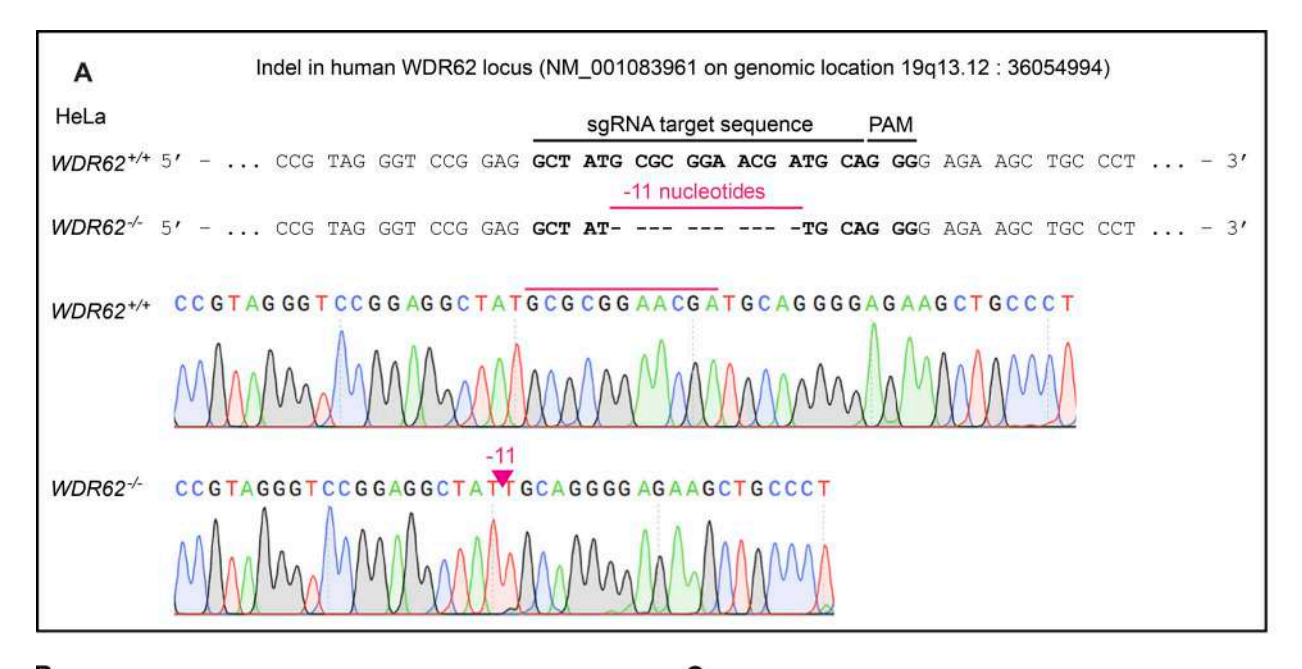


- Ramdas Nair, A., P. Singh, D. Salvador Garcia, D. Rodriguez-Crespo, B. Egger, and C. Cabernard. 2016. The Microcephaly-Associated Protein Wdr62/CG7337 Is Required to Maintain Centrosome Asymmetry in Drosophila Neuroblasts. Cell Rep. 14:1100–1113. https://doi.org/10.1016/j.celrep.2015
- Shohayeb, B., U. Ho, Y.Y. Yeap, R.G. Parton, S.S. Millard, Z. Xu, M. Piper, and D.C.H. Ng. 2020. The association of microcephaly protein WDR62 with CPAP/IFT88 is required for cilia formation and neocortical development. Hum. Mol. Genet. 29:248–263. https://doi.org/10.1093/hmg/ ddz281
- Sikirzhytski, V., V. Magidson, J.B. Steinman, J. He, M. Le Berre, I. Tikhonenko, J.G. Ault, B.F. McEwen, J.K. Chen, H. Sui, et al. 2014. Direct kinetochore-spindle pole connections are not required for chromosome segregation. J. Cell Biol. 206:231–243. https://doi.org/10.1083/jcb.201401090
- Silkworth, W.T., I.K. Nardi, L.M. Scholl, and D. Cimini. 2009. Multipolar spindle pole coalescence is a major source of kinetochore misattachment and chromosome mis-segregation in cancer cells. *PLoS One*. 4:e6564. https://doi.org/10.1371/journal.pone.0006564
- Silkworth, W.T., I.K. Nardi, R. Paul, A. Mogilner, and D. Cimini. 2012. Timing of centrosome separation is important for accurate chromosome segregation. Mol. Biol. Cell. 23:401-411. https://doi.org/10.1091/mbc.e11-02 -0095
- Sir, J.-H., M. Pütz, O. Daly, C.G. Morrison, M. Dunning, J.V. Kilmartin, and F. Gergely. 2013. Loss of centrioles causes chromosomal instability in vertebrate somatic cells. J. Cell Biol. 203:747–756. https://doi.org/10.1083/jcb.201309038
- Skibbens, R.V., V.P. Skeen, and E.D. Salmon. 1993. Directional instability of kinetochore motility during chromosome congression and segregation in mitotic newt lung cells: a push-pull mechanism. *J. Cell Biol.* 122: 859–875.
- Steblyanko, Y., G. Rajendraprasad, M. Osswald, S. Eibes, A. Jacome, S. Geley, A.J. Pereira, H. Maiato, and M. Barisic. 2020. Microtubule poleward flux in human cells is driven by the coordinated action of four kinesins. EMBO J. 39:e105432. https://doi.org/10.15252/embj.2020105432
- Thompson, S.L., and D.A. Compton. 2008. Examining the link between chromosomal instability and aneuploidy in human cells. *J. Cell Biol.* 180: 665–672. https://doi.org/10.1083/jcb.200712029
- Tolić, I.M., M. Novak, and N. Pavin. 2019. Helical Twist and Rotational Forces in the Mitotic Spindle. Biomolecules. 9:132. https://doi.org/10.3390/ biom9040132

- Toso, A., J.R. Winter, A.J. Garrod, A.C. Amaro, P. Meraldi, and A.D. McAinsh. 2009. Kinetochore-generated pushing forces separate centrosomes during bipolar spindle assembly. *J. Cell Biol.* 184:365–372. https://doi.org/10.1083/jcb.200809055
- Toyoshima, F., and E. Nishida. 2007. Integrin-mediated adhesion orients the spindle parallel to the substratum in an EB1- and myosin X-dependent manner. EMBO J. 26:1487–1498. https://doi.org/10.1038/sj.emboj.7601599
- Vargas-Hurtado, D., J.-B. Brault, T. Piolot, L. Leconte, N. Da Silva, C. Pennetier, A. Baffet, V. Marthiens, and R. Basto. 2019. Differences in Mitotic Spindle Architecture in Mammalian Neural Stem Cells Influence Mitotic Accuracy during Brain Development. Curr. Biol. 29: 2993-3005.e9. https://doi.org/10.1016/j.cub.2019.07.061
- Vukušić, K., R. Buđa, and I.M. Tolić. 2019. Force-generating mechanisms of anaphase in human cells. *J. Cell Sci.* 132:jcs231985. https://doi.org/10.1242/jcs.231985
- Walczak, C.E., S. Cai, and A. Khodjakov. 2010. Mechanisms of chromosome behaviour during mitosis. Nat. Rev. Mol. Cell Biol. 11:91–102. https://doi.org/10.1038/nrm2832
- Wilhelm, T., A.-M. Olziersky, D. Harry, F. De Sousa, H. Vassal, A. Eskat, and P. Meraldi. 2019. Mild replication stress causes chromosome missegregation via premature centriole disengagement. Nat. Commun. 10: 3585. https://doi.org/10.1038/s41467-019-11584-0
- Woods, C.G., and R. Basto. 2014. Microcephaly. Curr. Biol. 24:R1109-R1111. https://doi.org/10.1016/j.cub.2014.09.063
- Xu, D., F. Zhang, Y. Wang, Y. Sun, and Z. Xu. 2014. Microcephaly-associated protein WDR62 regulates neurogenesis through JNK1 in the developing neocortex. Cell Rep. 6:104–116. https://doi.org/10.1016/j.celrep.2013.12.016
- Yu, T.W., G.H. Mochida, D.J. Tischfield, S.K. Sgaier, L. Flores-Sarnat, C.M. Sergi, M. Topçu, M.T. McDonald, B.J. Barry, J.M. Felie, et al. 2010. Mutations in WDR62, encoding a centrosome-associated protein, cause microcephaly with simplified gyri and abnormal cortical architecture. Nat. Genet. 42:1015–1020. https://doi.org/10.1038/ng.683
- Zhang, D., G.C. Rogers, D.W. Buster, and D.J. Sharp. 2007. Three microtubule severing enzymes contribute to the "Pacman-flux" machinery that moves chromosomes. J. Cell Biol. 177:231-242. https://doi.org/10.1083/ icb.200612011
- Zhang, W., S.-L. Yang, M. Yang, S. Herrlinger, Q. Shao, J.L. Collar, E. Fierro, Y. Shi, A. Liu, H. Lu, et al. 2019. Modeling microcephaly with cerebral organoids reveals a WDR62-CEP170-KIF2A pathway promoting cilium disassembly in neural progenitors. Nat. Commun. 10:2612–2614. https://doi.org/10.1038/s41467-019-10497-2



#### Supplemental material



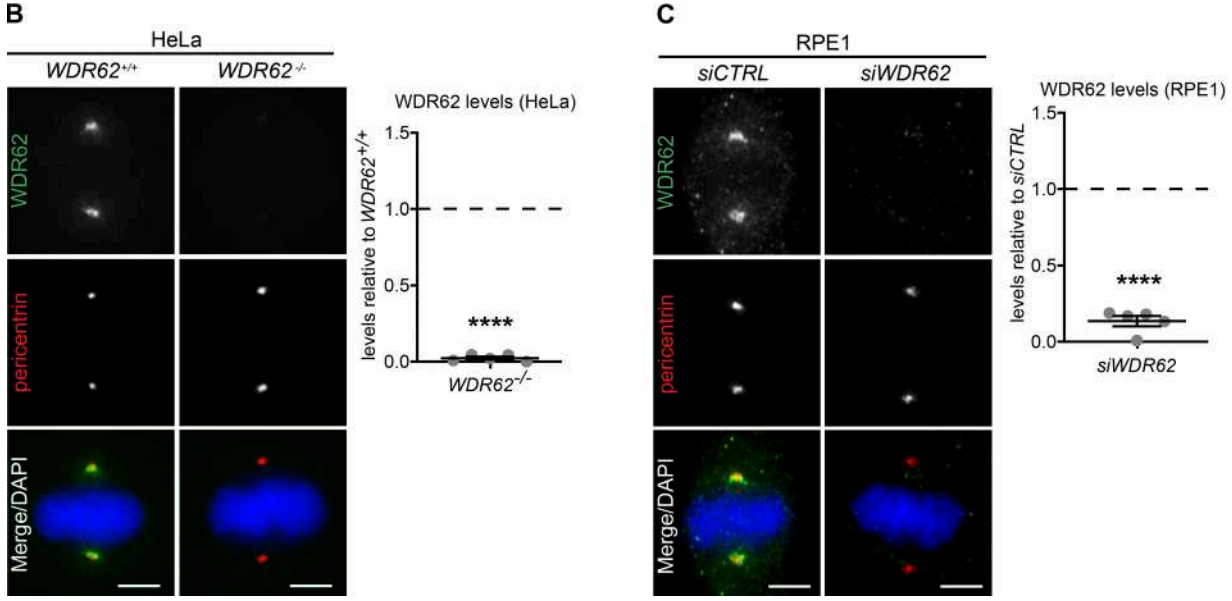


Figure S1. WDR62 deletion and depletion efficiency. Related to Fig. 2. (A) Genomic sequence before and after performing CRISPR-Cas9 WDR62 knockout on HeLa H2B-GFP cells. PAM indicates the protospacer adjacent motif GGG. (B) Immunofluorescence images of metaphase WDR62<sup>+/+</sup> and WDR62<sup>-/-</sup> HeLa H2B-GFP cells. PAM indicates the protospacer adjacent motif GGG. (B) Immunofluorescence images of metaphase WDR62<sup>+/+</sup> and WDR62<sup>-/-</sup> HeLa H2B-GFP cells. GFP cells, stained with WDR62 and pericentrin antibodies and DAPI (left); quantification of WDR62 levels relative to WDR62\*/+ (right): N = 5, n = 310 (WDR62\*/+) and 322 (WDR62<sup>-/-</sup>) cells; dot plot represents median per experiment; bars represent mean  $\pm$  SEM; \*\*\*\*, P < 0.0001, two-tailed unpaired t test. (C) Immunofluorescence images of metaphase RPE1 cells treated with siCTRL and siWDR62, stained with WDR62 and pericentrin antibodies and DAPI (left); quantification of WDR62 levels after siWDR62 treatment relative to siCTRL (right): N = 5, n = 310 cells per conditions; dot plot represents median per experiment; bars represent mean  $\pm$  SEM; \*\*\*\*, P < 0.0001, two-tailed paired t test. All scale bars = 5  $\mu$ m.

Guerreiro et al. Journal of Cell Biology WDR62 recruits katanin at spindle poles



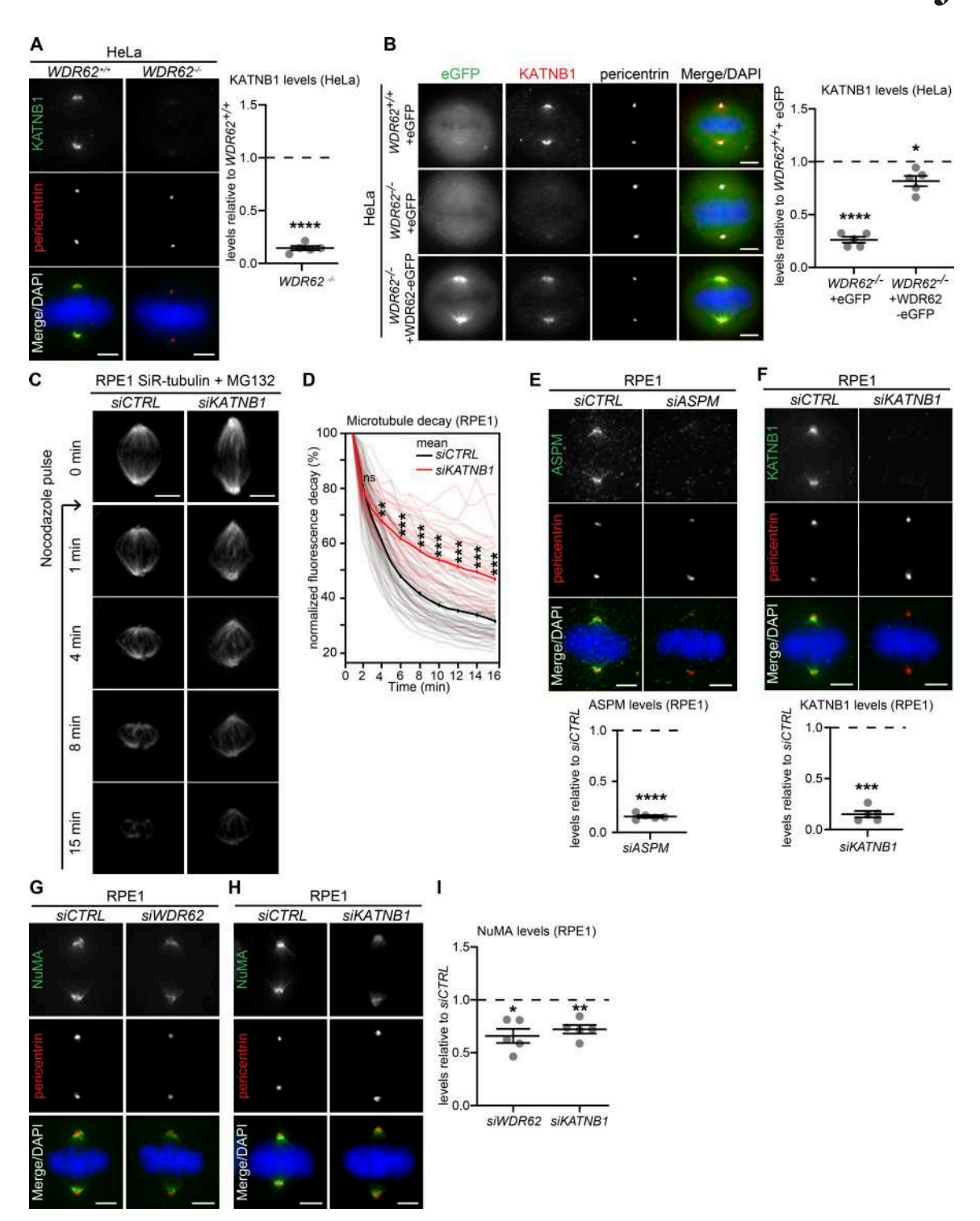


Figure S2. **KATNB1 depletion mimics WDR62 depletion.** Related to Fig. 3. **(A)** Immunofluorescence images of metaphase  $WDR62^{+/+}$  and  $WDR62^{-/-}$  HeLa cells, stained with KATNB1 and pericentrin antibodies and DAPI (left); quantification of KATNB1 levels in  $WDR62^{-/-}$  relative to  $WDR62^{+/+}$  (right): N = 5, n = 308 ( $WDR62^{+/+}$ ) and 292 ( $WDR62^{-/-}$ ) cells; dot plot represents median per experiments; bars represent mean  $\pm$  SEM; \*\*\*\*, P < 0.0001, two-tailed unpaired t test. **(B)** Immunofluorescence images of metaphase  $WDR62^{+/+}$  or  $WDR62^{-/-}$  HeLa cells transfected with indicated constructs and stained with KATNB1 and pericentrin antibodies and DAPI (left). Quantification of KATNB1 levels at spindle poles (right) in N = 5, n = 217-228 cells; dot plot represents median per experiment; bars represent mean  $\pm$  SEM; \*, P < 0.05; \*\*\*\*, P < 0.0001, one-way ANOVA. **(C)** Time-lapse images of MG132-arrested RPE1 cells treated with siCTRL and siKATNB1, labeled with SiR-tubulin, and treated with 200 ng/ml of nocodazole at t = 0. **(D)** Quantification of the spindle microtubule decay over time in siCTRL- and siWDR62-treated RPE1 metaphase cells: N = 4, n = 50 (siCTRL) and 55 (siKATNB1) cells; thick line represents mean; thin line represents single experiments; \*, P < 0.05; \*\*\*, P < 0.01; \*\*\*\*, P < 0.001, repeated two-tailed paired t test. **(E-I)** Immunofluorescence of metaphase RPE1 cells treated with indicated siRNAs, stained with DAPI and antibodies against pericentrin and ASPM (E), KATNB1 (F), or NuMA (G and H); all quantifications (E and F below, and I right) represent the levels in the indicated siRNA vs. siCTRL: N = 5, n = 303-323 cells; dot plots represent median per experiments; bars represent mean  $\pm$  SEM; \*, P < 0.05; \*\*\*, P < 0.001; \*\*\*\*, P < 0.0001; \*\*\*\*, P < 0.0001, in two-tailed paired t test. All scale bars = 5  $\mu$ m.

Guerreiro et al. Journal of Cell Biology

S2

S3



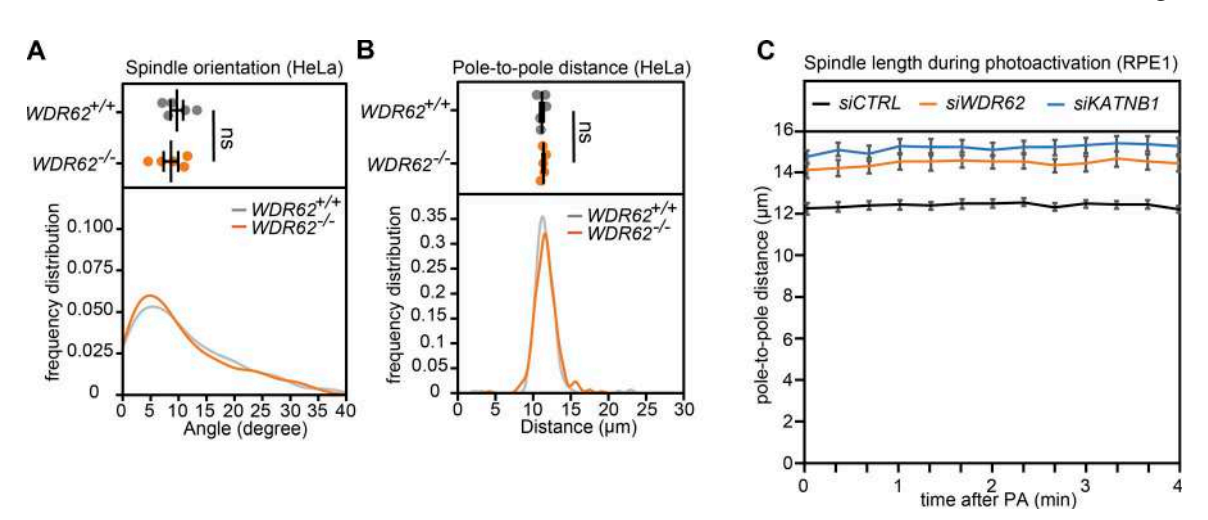


Figure S3.  $WDR62^{-/-}$  HeLa cells show no difference in spindle orientation or pole-to-pole distance, and spindle length of MG132-arrested RPE1 cells are constant. Related to Fig. 4. (A and B) Quantification of spindle orientation (A) and pole-to-pole distances (B) in  $WDR62^{-/-}$  metaphase HeLa H2B-GFP cells; dot plots represent median per experiments with bars displaying mean  $\pm$  SEM (top) and frequency distribution (bottom): N = 5, n = 323 ( $WDR62^{+/+}$ ) and 330 ( $WDR62^{-/-}$ ) cells; two-tailed unpaired t test. (C) Quantification of spindle length during photoactivation (PA) experiments in indicated siRNA treatments; lines represent mean per condition, with bars displaying SEM. n = 15 cells per condition.

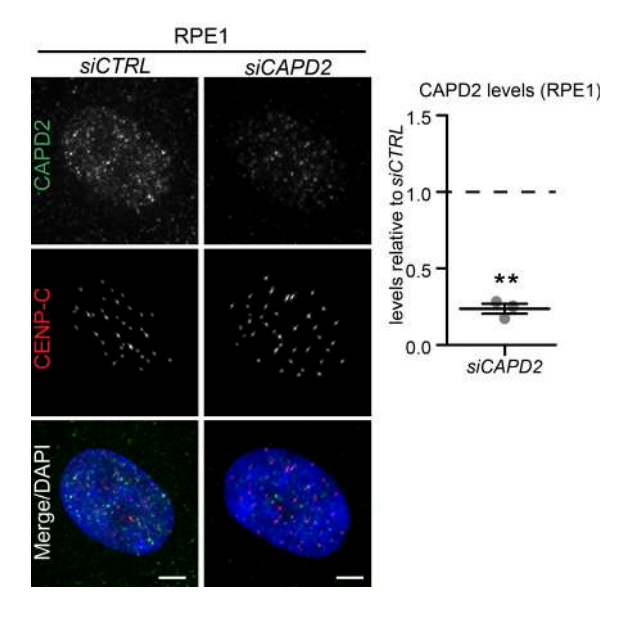


Figure S4. **Validation of CAPD2 depletion in RPE1 cells.** Related to Fig. 5. Immunofluorescence images of interphase RPE1 cells treated with *siCTRL* and *siCAPD2* and stained with CAPD2 and CENP-C antibodies and DAPI (left); quantification of CAPD2 levels in *siCAPD2* relative to *siCTRL* (right): N = 3, n = 125 cells per condition; dot plot represents median per experiment; bars represent mean  $\pm$  SEM; \*\*, P < 0.01, two-tailed paired t test. Scale bars = 5  $\mu$ m.



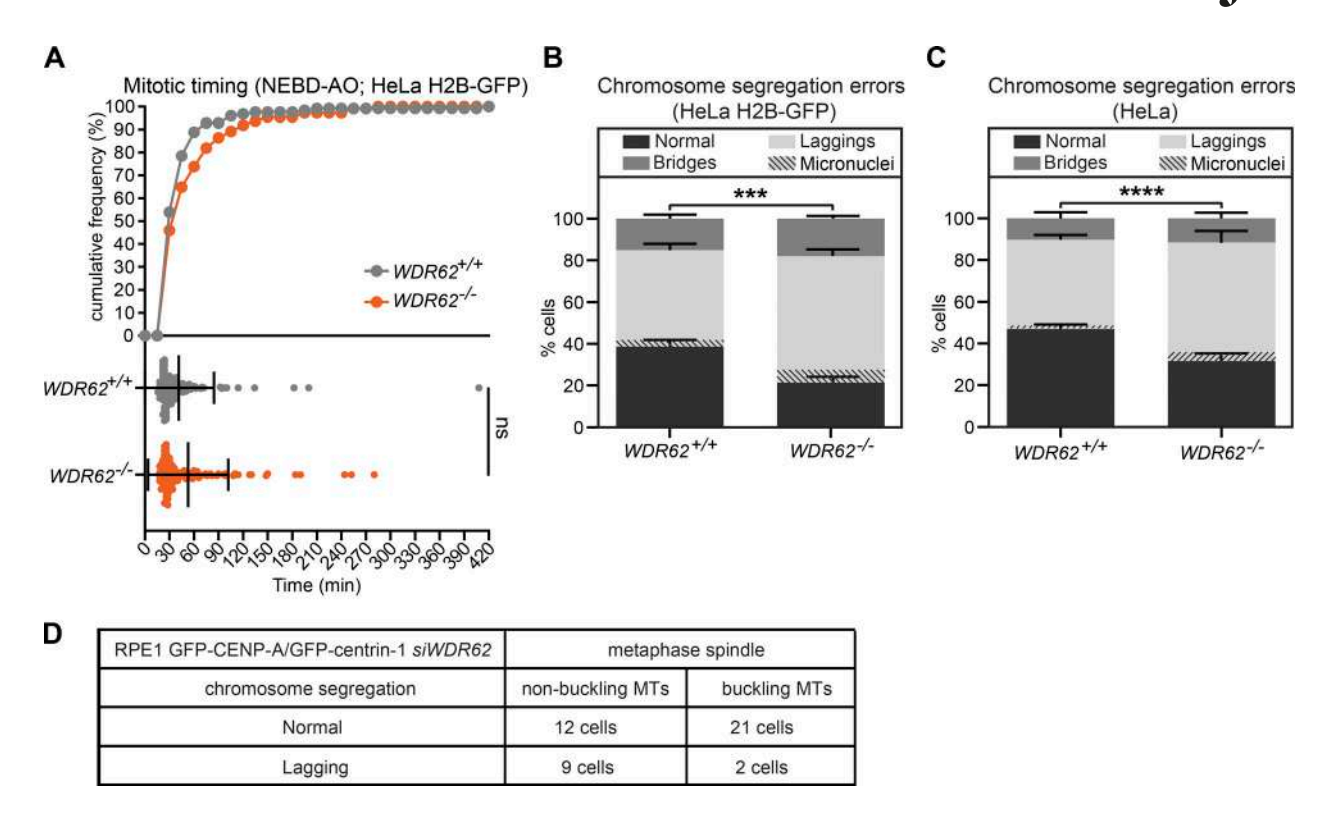


Figure S5. Loss of WDR62 in HeLa cells does not affect mitotic timing but increases the percentage of lagging chromosomes. Related to Fig. 6. (A) Mitotic timing from nuclear breakdown (NEBD) until anaphase onset (AO) of  $WDR62^{-/-}$  and  $WDR62^{-/-}$  HeLa H2B-GFP cells: cumulative frequency (top) with dot plot representing each cell (bottom); bars represent mean  $\pm$  SEM; two-tailed unpaired t test. (B and C) Percentage of chromosome segregation errors from unsynchronized HeLa H2B-GFP (B) or HeLa (C) cells with a  $WDR62^{-/-}$  genotype. Stack bars indicate the number of normal anaphases, anaphases with lagging chromosomes, or anaphases with chromosome bridges; gray stripes represent cells with lagging chromosomes resulting in micronuclei; error bars represent mean  $\pm$  SEM; N = 5, n = 290-367 cells; \*\*\*\*, P = 0.0002; \*\*\*\*\*, P < 0.0001,  $\chi^2$  test. (D) Quantification of lagging chromosomes in SiR-tubulin–stained RPE1 GFP-centrin1/GFP-CENPA cells with buckling or nonbuckling microtubules after siWDR62 treatment.

Video 1. **Photoactivation of** *siCTRL***-treated hTert-RPE1 PA-GFP-α-tubulin cells, showing microtubule poleward flux.** Related to Fig. 4. Sampling rate = 20 s; scale bars = 5 μm. Play rate = 4 frames per second.

Video 2. **Photoactivation of siKATNB1-treated hTert-RPE1 PA-GFP-\alpha-tubulin cells, showing microtubule poleward flux.** Related to Fig. 4. Sampling rate = 20 s; scale bars = 5  $\mu$ m. Play rate = 4 frames per second.

Video 3. Photoactivation of siWDR62-treated hTert-RPE1 PA-GFP- $\alpha$ -tubulin cells, showing microtubule poleward flux. Related to Fig. 4. Sampling rate = 20 s; scale bars = 5  $\mu$ m. Play rate = 4 frames per second.

Video 4. Mitotic progression of siCTRL-treated hTert-RPE1 EB3-GFP/H2B-mCherry cells, showing no error of chromosome segregation. Related to Fig. 6. Sampling rate = 1 min; scale bars = 5  $\mu$ m. Play rate = 3 frames per second.

Video 5. Mitotic progression of siWDR62-treated hTert-RPE1 EB3-GFP/H2B-mCherry cells, showing lagging chromosomes in anaphase. Related to Fig. 6. Sampling rate = 1 min; scale bars =  $5 \mu \text{m}$ . Play rate = 3 frames per second.

Guerreiro et al. Journal of Cell Biology

**S4** 



Video 6. **Mitotic progression of** siWDR62**-treated hTert-RPE1 EB3-GFP/H2B-mCherry cells, showing DNA bridge in anaphase.** Related to Fig. 6. Sampling rate = 1 min; scale bars = 5  $\mu$ m. Play rate = 3 frames per second.

Video 7. Sister-kinetochore oscillations of siCTRL-treated hTert-RPE1 GFP-centrin1/GFP-CENPA cells, showing tight metaphase plate and synchronous anaphase onset. Related to Fig. 6. Sampling rate = 15 s; scale bars = 5 μm. Play rate = 4 frames per second.

Video 8. Sister-kinetochore oscillations of siWDR62-treated hTert-RPE1 GFP-centrin1/GFP-CENPA cells, showing wide metaphase plate and asynchronous anaphase onset with lagging chromosomes. Related to Fig. 6. Sampling rate = 15 s; scale bars = 5 μm. Play rate = 4 frames per second.

S5

### Discussion

Microcephaly is a debilitating neurodevelopmental disorder, leading to a smaller brain and mental retardation. WDR62 and ASPM loss-of-function mutations account for the majority of all primary microcephaly cases (Bolat et al., 2022). However, proposed microcephaly causes such as prolonged mitotic timing (Phan et al., 2021), spindle orientation defects (Lizzaraga et al., 2010), or aneuploidy (Martiens et al., 2013) cannot explain the depletion of the neuronal progenitor pool in these loss-of-function mutations. Instead, our in vivo and in vitro work shows that primary microcephaly is caused by a delay in cell cycle speed (Doria & Ivanova et al., BioRxiv 2024). This effect appears due to an abnormally slow poleward microtubule flux in WDR62-depleted cells causing transient lagging chromosomes, which are recognized by the Aurora B gradient at the central spindle, leading to 53BP1-p21 pathway activation, cell cycle delay, and ultimately a small brain phenotype.

#### Origins of poleward microtubule flux disruption in WDR62 depletion

Many questions about this mechanism still remain unanswered. For example, how does WDR62 depletion lead to a decrease in poleward microtubule flux? In the previous work of the lab, it has been postulated that WDR62 serves as a recruitment platform for the microtubule-severing enzyme Katanin (Guerreiro et al., 2021), which severs microtubules at their minus-ends. We believe that by severing the microtubules, Katanin creates free microtubule minus-ends, which are then depolymerized by microtubule depolymerizers such as MCAK or Kif2A (unpublished data). This process is in competition with microtubule-capping proteins such as Camsap1 which protect microtubule minus-ends. Indeed, some previous results of the lab have demonstrated that MCAK depolymerization activity at spindle poles is regulated by Camsap1 (PhD thesis of Elena Doria, 2024).

WDR62 depletion has also been shown to increase microtubule stability (Guerreiro et al., 2021). But what does one actually understand under microtubule stability? And is microtubule stability coupled with decreased flux rates? Indeed, in my work, I have tried to elucidate the origins of microtubule stability in WDR62-depleted cells. My results indicate that WDR62 depletion does not lead to an increased number of microtubules per k-fiber (Figure 1); however, WDR62 depletion does lead to a higher amount of non-kinetochore microtubules compared to the amount of k-fibers, as has been shown in a ratio between GFP-Tubulin and SiR-Tubulin. This result suggests that Katanin is even more important for the severing of non-kinetochore microtubules. Indeed, the high ratio of GFP-Tubulin to

SiR-Tubulin in WDR62-depleted cells compared to control cells can indicate that Katanin does not sever enough the non-kinetochore microtubules, which are therefore not depolymerized enough, creating a higher GFP Tubulin/SiR Tubulin ratio.

Interestingly, bridging fibers seems to display normal microtubule flux in siWDR62 cells as demonstrated by speckle microscopy and PRC1 overlap length (Thesis of Elena Doria, 2024). This suggests, as previously shown in Guerreiro et al 2021, Katanin has a preference for microtubule minusends, therefore touching only the microtubules having minus-end in the vicinity of spindle poles.

From these results we can hypothesize that while Katanin might be recruited to all the microtubule minus-ends; it maybe has a particular impact on k-fibers and free microtubules emanating from the spindle poles. However, it does not have impact on the bridging fibers, since they are speculated to originate from other microtubules and not the spindle poles (David et al 2019). Indeed, WDR62 depletion seems to lead to normal bridging fibers but abnormal growth of k-fibers (Guerreiro et al., 2021) and increased number of other non-kinetochore microtubules which results in an elevated GFP-Tubulin/SiR-Tubulin ratio. In conclusion, further investigation of kinetochore and non-kinetochore microtubules in siWDR62 is important to shed light on the consequences of Katanin mislocalization on different microtubule subpopulations. An interesting experiment could be to mark k-fibers with fluorescently tagged Kif15 and measure the microtubule stability using nocodazole mediated microtubule decay (Begley et al., 2021).

Current knowledge presents multiple perspectives on microtubule stability, highlighting the diverse ways in which this property can be defined. Different articles have described different types of microtubule stability and their relationships with other dynamic parameters, such as microtubule flux speed and spindle length. Indeed, microtubules can be defined as stable if they are polymerized more or depolymerized less, both of these phenotypes leading to slower microtubule flux. For example, in Almeida et al., the authors have described slower microtubule flux and more stable microtubules due to Augmin depletion. Augmin is a protein which promotes polymerization and its absence leads to shorter spindles and fewer kinetochore microtubules (Almeida et al., 2022). In our study (Guerreiro et al 2021), we have studied the effects of the nocodazole depolymerization assay, which blocks the addition of new tubulin subunits and allows to observe the depolymerization activity only. This allowed us to demonstrate an increase in k-fiber stability, which leads to longer spindles but, as in the case of Augmin depletion, also leads to slower poleward flux (Guerreiro et al., 2021). These findings underscore the complexity of microtubule stability, demonstrating that it manifests in distinct ways depending on the underlying molecular context.

#### Lagging chromosomes in primary microcephaly and their recognition by Aurora B

The central point of the study is the appearance of transient lagging chromosomes due to a microtubule flux defect. Indeed, transient lagging chromosomes, the chromosomes that lag behind the main chromosome mass during anaphase but are eventually correctly incorporated, have never really been considered as an origin of any cellular defects (Guerreiro et al. 2021). These chromosomes usually are not mis-segregated, do not lead to massive DNA damage or micronuclei appearance, or aneuploidy. In WDR62-depleted cells, we have confirmed the absence of structural or numerical aneuploidy (Doria & Ivanova et al. BioRxiv 2024, Figure 2A, B; Supplementary Figure 2A, B, C) and normal mitotic timing (Guerreiro et al. 2021). Interestingly, we have found that other mitotic genes involved in primary microcephaly, such as ASPM (Doria & Ivanova et al., BioRxiv 2024, Figure 2D, E), Sas6 and CDK5RAP2 also lead to transient lagging chromosomes (Figure 2B, C). Therefore, transient lagging chromosomes, which could arise from different abnormalities in microtubule dynamics, might all induce microcephaly via 53BP1-p21 dependent mechanism. Indeed, the majority of genes mutated in primary microcephaly are known to have roles in centriole biogenesis, centrosome functioning, kinetochore, and microtubule dynamics (Jaramayan et al. 2018). While we do not know yet if these depletions lead to prolonged mitotic timing, as for example Sas6 might lead to extended mitotic timing due to its role in centriole biogenesis (Arcquint&Nigg 2016) and centriole absence due to SAS6 depletion in mouse was shown to activate mitotic surveillance pathway (Grzonka&Bazzi 2024), it seems that they display transient lagging chromosomes which might also contribute to microcephaly phenotype as it is the case in ASPM and WDR62 depletion. The mitotic timing, which can also lead to cell proliferation delay in CDK5RAP2 and SAS6 depletions, however, remain to be studied in human cells.

One might say that as long as the chromosomes are correctly incorporated, there is no reason to survey them through the activity of Aurora B. However, recent studies have shown that exposure of DNA to the cytoplasm gradually activates the cGAS pathway, leading to inflammation through the noncanonical NF-kB pathway (Dou et al. 2017). cGAS is mainly known as a pathway with the role of recognizing pathogen DNA in the cytoplasm (Watson et al. 2015). Despite the fact that this pathway was reported by some studies (Zhong et al. 2020) to be inactivated during mitosis, other studies have reported it to be activated due to chromosome bridges (Flynn et al. 2021) or extended mitotic timing. Indeed, recent studies have linked the extended mitotic duration to 53BP1 appearance, which might well be due to the activity of cGAS (Meitinger et al. 2016). The response of the cGAS pathway seems to be gradual and increases with the time the chromosome spends in the cytoplasm (Zierhut et al. 2019). It is therefore possible that phosphorylation of lagging chromosomes by Aurora B could be a

way to protect the chromosomal DNA, which is lagging behind, from even a slight activation of the cGAS-driven inflammatory pathway. On the other hand, it could also be a way to mark the chromosomes which might potentially accumulate cGAS components.

Other reasons for the marking of transient lagging chromosomes could be the potential presence of merotelic attachments (one kinetochore bound by microtubules emanating from two spindle poles), which are not recognized by the spindle assembly checkpoint and do not increase mitotic timing (Gregan et al. 2011). The merotelically attached chromosomes, however, can lead to chromosome mis-segregation and can cause chromosomal instability (Gregan et al. 2011). Indeed, an Aurora Bdependent surveillance mechanism could be a perfect checkpoint to control and correct the merotelic attachments. As Aurora B is already involved in the correction of KT-MT attachments during metaphase (discussed previously), it is conceivable that it can conserve its function in anaphase. While we do not know if WDR62-depleted cells increase the number of merotelic attachments, it can be an interesting hypothesis worth testing. Aurora B on the central spindle during anaphase is known to phosphorylate different kinetochore proteins to stabilize or destabilize their attachment to microtubules (Sen et al. 2021, Papini et al. 2021, Orr et al. 2021). The phosphorylation on the kinetochore was found to be enriched at the lagging chromosomes, which demonstrates that lagging chromosome marking by Aurora B seems to be dependent on the time it spends in the vicinity of Aurora B. Apart from phosphorylating kinetochores, Aurora B has been linked to the phosphorylation of histones on the lagging chromosomes (Fuller et al. 2008, Orr et al. 2021, Papini et al. 2021), such as histone H3.3 Ser10 (Papini et al. 2021).

Additionally, Aurora B gradient at the central spindle monitors chromosome segregation and delays nuclear envelope reformation and chromosome de-condensation (Afonso et al. 2014). This mechanism is hypothesized to have evolved to prevent the exclusion of chromosomes from the nucleus or their damage by the cleavage furrow (Afonso et al. 2014). Additionally, it seems that nuclear envelope reformation around the mis-segregated chromosomes can be detrimental for the cells. Indeed, it has been shown recently that mis-segregated chromosomes lead to misshaped nuclei, which are recognized by a mechanosensitive checkpoint, leading to cell cycle arrest (Hervé et al. 2025). In this publication, the authors have described that misshaped nuclei due to aneuploidy lead to p21 upregulation and cell cycle arrest (Hervé et al. 2025). Also in mice, lagging chromosomes have been described to lead to a defect in chromosome compaction during anaphase, which results in abnormal nuclear shapes and chromosome organization (Fonseca et al. 2019). In our work, we have also tested the nuclear shapes in siCTRL and siWDR62-depleted cells. We have found a difference only in the circularity of the nuclei, but not in eccentricity or solidity. Hervé et al. (2025) have found differences in all those parameters, which allowed them to conclude the presence of abnormal nuclear shapes

(Hervé et al. 2025). Other papers, which have relied on the circularity parameter only, have shown a much larger difference (0.8 in Control vs 0.6 in depletion, Tataki et al. 2017) in the circularity compared to our measurements (0.85 to 0.83). Therefore, we have concluded that despite some differences in circularity, the nuclei in WDR62-depleted cells have a largly normal shape.

Taken together, we concluded that Aurora B is important for the lagging chromosome recognition mechanism, allowing the cell to keep these chromosomes under surveillance.

#### 53BP1 appearance and its consequences

In our work (Doria & Ivanova et al., 2024, BioRxiv), we have demonstrated that Aurora B is involved in 53BP1 foci formation. Indeed, partial depletion of Aurora B led to the rescue of the number of cells positive for 53BP1 foci. In contrast, the depletion of NPL4 and UBASH3B, adaptor proteins of the p97 complex, led to partial retention of Aurora B on the chromosomes, resulting in an increased number of 53BP1-positive cells. Moreover, we were able to demonstrate that Aurora B inhibition in the depletion background of NPL4 or UBASH3B leads to the rescue of the NPL4 or UBASH3B-induced 53BP1 phenotype. We have also demonstrated that 53BP1 is upregulated in response to any lagging chromosome, persistent or transient. Indeed, our experiments using the MPS-1 inhibitor Reversine to create persistent lagging chromosomes have shown that almost all persistent lagging chromosomes lead to 53BP1 accumulation in the nucleus. Also, we have demonstrated that this 53BP1 upregulation following the presence of persistent lagging chromosomes is dependent on Aurora B. Indeed, we have demonstrated that partial inhibition of Aurora B using Baracertib in MPS-1-deficient cells leads to a decrease in the number of cells displaying 53BP1 following a persistent lagging chromosome. It seems, therefore, that Aurora B is responsible for 53BP1 upregulation on the persistent or transient lagging chromosomes. A very interesting experiment would be to have Aurora B induced degradation specifically in anaphase, for example by using an AID tag. Another interesting experiment could involve the creation of a kinase-dead mutant Aurora B or non-phosphorylatable substrates of H3.3 Ser10 and Ser31 (two top candidates for lagging chromosome marking) and observe the 53BP1 in the following G1. Finally, direct visualization of H3.3 Ser10 or Ser31 would be great, however, it was technically impossible in the lab.

Despite the absence of proof for phosphorylation of the H3.3 histone by Aurora B, we managed to directly correlate the presence or absence of transient lagging chromosomes to 53BP1 appearance using the hTERT-RPE 53BP1 GFP cell line (see Doria & Ivanova et al., BioRxiv 2024, Figure 2C). As mentioned previously, this is not surprising, as 53BP1 has already been shown previously to be

implicated in mitotic surveillance mechanisms in cases of prolonged mitotic timing (Lambrus et al., 2016, Meitinger et al., 2016, 2021) or merotelic microtubule attachments (Wang et al., 2017). However, what remains unclear is what exactly 53BP1 marks. Some preliminary results of our lab, costaining Cenp-A and 53BP1 have indicated that 53BP1 in WDR62 depletion could colocalize with pericentromeric regions. Indeed, previous studies have reported that 53BP1 preferentially binds to kinetochores during mitosis (Julien et al., 2002). In this study, authors suggest the role of 53BP1 as a kinetochore signaling unit in the event of spindle assembly checkpoint activation. However, if 53BP1 can localize to the centromere regions of lagging chromosomes still remains unclear. An interesting experiment could be a co-immunoprecipitation of 53BP1 with DNA, which could allow to identify the precise location of 53BP1 binding on the chromosome.

However, is there even a precise genomic site where 53BP1 is binding? This remains debatable. Some studies have shown that mis-segregated chromosomes are labeled at H3.3 Ser31 side all over the chromosome, which leads to p53-dependent cell cycle arrest (Hinchcliffe et al., 2016). Indeed, in this paper, authors demonstrate a very homogenous phosphorylation of histone H3 on the lagging chromosomes, which would suggest that if 53BP1 recognizes this histone phosphorylation, it should lead to 53BP1 localization all along the chromosome.

Additionally, in our experiments with MPS-1 inhibited RPE-1 cells, we have shown that cells with persistent lagging chromosomes lead to micronucleus, which is likely to be the chromosome which was persistently lagging (Ford et al 1988). However, in these cells the 53BP1 was almost never found in the micronucleus (Figure 4).

Taken together, the 53BP1 response seems therefore to be more systemic as it is not linked to DNA damage or other type of damage. This result lets us hypothesize that likely 53BP1 is not specific to the lagging chromosome.

In our visualization of 53BP1, we could demonstrate that most of the time, WDR62 depletion leads to the accumulation of so-called "53BP1 nuclear bodies." The nuclear body pattern of 53BP1 is distinct from its usual focal appearance in cases of DNA damage, as it is, for example, the case in Doxorubicin treatment (see Doria & Ivanova et al., BioRxiv 2024, Figure 1C, Lukas et al., 2011) and was reported in previous studies to accumulate at a low level even in cells which do not experience any stress (Bekker-Jensen et al., 2005). These bodies have also been shown to form around DNA lesions generated by replication stress (Lukas et al., 2011). Not much is known about the composition of these nuclear bodies during mitotic surveillance, however in DNA damage repair, these bodies usually contain DSB repair signaling proteins such as ATM, γH2AX, and MDC1 (reviewed in Kilgas et al., 2024). It would be interesting to analyze if 53BP1 nuclear bodies in WDR62-depleted cells colocalize with ATM, as ATM

has also been known to be an important mitotic regulator. Some studies have shown that ATM monitors the integrity of the mitotic spindle (Oricchio et al., 2006) and is activated by Aurora B (Yang et al., 2011). Activated ATM seems to phosphorylate Bub1 and ensure the correct functioning of the spindle assembly checkpoint (Yang et al., 2011). Another co-localizing factor could be USP28 (Meitinger et al., 2016). Indeed, in our studies, we have some preliminary evidence that 53BP1 activation necessitates USP28, as reported previously (Meitinger et al., 2016, 2021), and in the absence of USP28, the number of 53BP1-positive cells goes down in siWDR62 cells (see Figure 3). It is possible that the absence of USP28 leads to mislocalization of 53BP1 from the yet unknown 53BP1 sites on the lagging chromosomes or elsewhere. It would be really interesting to study if these two proteins colocalize at the same site. Taken together, the involvement of USP28 in the 53BP1 regulation mechanism remains to be studied further.

Interestingly, USP28 KO cells seem to be bigger compared to the parental cell line and have more 53BP1 background compared to the parental cell line, where the signal is more concentrated in the nuclear bodies. As USP28 is important for p53 stabilization in the event of centrosome loss or extensive mitotic timing (Lambrus et al., 2016), the USP28 KO cells could accumulate DNA damage related to centrosome loss, but these cells are not eliminated and continue cycling, leading to higher levels of 53BP1. It is therefore possible that they could become more error-prone in the absence of centrosomes, which could lead to polyploidy and consequentially to nuclear size increase.

Overall, I believe that it would be important to understand if WDR62 depletion leads to lagging of some specific chromosomes and if this is different from Camsap1 depletion-induced lagging. Indeed, in our study (Doria & Ivanova et al., 2024, BioRxiv), we show the transient lagging after WDR62 and Camsap1 depletion, however Camsap1 depletion-induced laggings do not lead to cell proliferation defects compared to WDR62 depletion-induced laggings. We have found that the time of 53BP1 appearance directly correlates to the time spent lagging during anaphase. WDR62-depleted cells on average have longer lasting lagging compared to Camsap1, which leads to earlier appearance of 53BP1 (Doria&Ivanova et al 2024, Biorxiv, Figure 4). This missegregation can be random; however, some previous studies have found that nuclear localization of chromosomes prior to mitosis dictates their missegregation rates (Klaasen et al., 2022). Indeed, the error frequencies in RPE cells are directly correlated to lamina-associated chromosome domains, meaning that peripheral chromosomes, which are often larger chromosomes, have a higher chance for missegregation (Klaasen et al., 2022). Other studies have reported that chromosomes 1 and 2 are more susceptible to missegregation after Nocodazole washout due to chromosome cohesion fatigue (Worrall et al., 2018). Also, the centromere size has been linked to the frequency of missegregation, with bigger chromosomes having smaller centromeres being at the peak of missegregation (Dumont et al., 2019). However, it is unclear if such

bias exists for transient lagging chromosomes. According to some studies, chromosomes with large kinetochores have an easier time to congress and bi-orient. Indeed, this allows chromosomes to interact more with microtubules and not only depend on CenpE for alignment (Drpic et al., 2018). Since WDR62 depletion leads to microtubule stabilization, one can imagine that the more stable and less dynamic microtubules interact less with big peripheral chromosomes with small centromeres, resulting in their missegregation. In anaphase, those bigger chromosomes could demonstrate more resistance by moving through the cytoplasm, leading to longer permanence in the Aurora B gradient. It could be really exciting to perform a FISH experiment on WDR62-depleted cells to determine the presence of a transient lagging bias for one of the chromosomes.

# Rescue of downstream transient lagging chromosomes consequences by siCamsap1

A strong point of this work is the rescue of downstream consequences of poleward microtubule flux defects in siWDR62 cells by co-depletion of Camsap1/Patronin. As discussed previously, Camsap1 is a microtubule capping protein, playing a role in the protection of microtubule minus-ends from the action of microtubule depolymerizers (Thesis of Elena Doria, 2024). Depletion of Camsap1 leads to faster microtubule flux, as we hypothesize, by exposing the microtubule minus-ends to the action of depolymerizers. Camsap1 co-depletion leads to the rescue of all downstream consequences of the microtubule flux defect: transient lagging chromosomes, an increase in 53BP1 and p21-positive cells, as well as cell cycle defects. Interestingly, Ki-67 signal in CAMSAP1/WDR62 co-depletion did not show a complete rescue compared to the CFSE assay (Figure 6A,B; Doria & Ivanova et al., 2024, BioRxiv, Figure 4D). Indeed, Ki-67 is a proliferation marker that is expressed only in the active phases of the cell cycle and is downregulated in deeply quiescent or senescent cells (Sun & Kaufman, 2018). It seems that WDR62 depletion leads to two different cell populations: the majority of cells proliferate slower; however, some cells seem to undergo senescence or quiescence. The co-depletion of WDR62 with Camsap1 seems to bring back to normal or even slightly accelerate the cell cycle speed of the slower proliferating cells, however, the G0 arrested population seems to remain stable. In accordance with this result, the levels of pRB phosphorylation in the co-depletion of WDR62 and Camsap1 seem to be slightly increased, which is known to promote proliferation (Figure 6C, Engeland, 2022). Finally, the cell cycle profile shows that all the cell cycle stages are the same length between different conditions (Figure 6E). Taken together, we can hypothesize that WDR62 depletion leads to prolonged whole cell cycle duration but does not change the distribution of cell cycle stages. Our data suggests that most of the cells after WDR62 depletion have prolonged G1, then prolonged S and G2 phases, with a small number of cells being stuck in G0. It seems that the co-depletion of WDR62 with Camsap1 rescues the speed of the majority of slow-cycling cells but does not rescue the number of G0 senescent or quiescent cells in WDR62 depletion. Indeed, p21 is known to bind to cyclins D/E/A and B and cyclin-dependent kinases CDK4/6, CDK2, and CDK1 (Lin et al 1996). Therefore, the activation of p21 is known to cause a delay in every cell cycle phase (Bates et al 1998) and also known to lead to overall cell cycle delay (Gartel et al 1996). This seems to agree with our model, as we see no difference in the cell cycle profile (Figure 6).

In the Drosophila melanogaster brain, co-depletion of WDR62 and Camsap1 ortholog Patronin leads to an increase in brain size. As we have found in our study (Doria & Ivanova et al., 2024, BioRxiv), the double depletion of WDR62 and Patronin leads to shorter cell cycle compared to single depletions. This could explain the bigger brain phenotype as the neuroblasts would divide more often in double-depleted larvae compared to control larvae, generating more proliferative tissue. This could be verified by staining the brains with proliferative tissue markers, such as Prospero (Gogendeau et al., 2015). However, what is interesting is that co-depletion of WDR62 with Camsap1 in human cells does not lead to faster cell cycle speed. There can be several explanations for this. One possibility is that, as it was shown in Drosophila, Patronin interacts with the Hippo pathway (Yang et al., 2021), an important organ size regulator (Poon et al., 2016). WDR62, on the other hand, was shown to interact with JNK, a known regulator of the Hippo pathway (Zeke et al., 2016; Lim et al., 2015; Tomlinson et al., 2010). Can the co-depletion of both proteins hyper-activate the Hippo pathway in Drosophila? This is unknown, but it would be interesting to investigate by determining the levels of different Hippo pathway proteins.

Another possibility is that Drosophila is just more sensitive to a slight decrease in cell cycle duration, as the total duration of a fruit fly cell cycle is just 1 hour compared to 24 hours in humans. Additionally, according to our data, Patronin RNAi slightly decreases the cell cycle duration compared to control, which demonstrates that even a single Patronin depletion cannot fully recapitulate the Camsap1 phenotype in human cells. Indeed, Patronin is a Camsap1, 2, and 3 ortholog in Drosophila (Khanal et al., 2016). Camsap2 and 3 might have independent roles in cell cycle regulation.

#### Current primary microcephaly hypotheses

In our study, we have tested the most common hypotheses for primary microcephaly in our system. Indeed, it has been previously shown that microcephaly can arise from abnormal mitotic timing, abnormal spindle orientation, or aneuploidy of neuronal progenitor cells. In our study, we have

investigated these three hypotheses in human RPE cells. First of all, in Guerreiro et al., we have shown that WDR62 depletion does not lead to an increase in mitotic timing (Guerreiro et al., 2021), in contrast to a study by Chen et al 2014. Indeed, Chen et al. reported a mitotic arrest following WDR62 depletion in murine cells. This difference can be explained by the use of mice as a model organism or the fact that the results in mice arose from a 3D embryonic culture compared to our 2D human tissue culture in our case.

Other studies have indicated that premature neuronal differentiation in Drosophila (Gogendeau et al., 2015) and apoptosis in mice (Martiens et al., 2013) due to gain or loss of entire chromosomes (aneuploidy) in neuronal progenitor cells can lead to primary microcephaly. We could not confirm the presence of aneuploidy in our cells. Indeed, karyotyping of the control and WDR62-depleted cells, as well as single-cell sequencing of the cells, demonstrated an absence of structural or numerical aneuploidy in our cells. Indeed, in both of these studies, the authors used PLK4/SAK overexpression (OE), which leads to centrosome overduplication and multipolar spindles, which is not the case in WDR62 depletion. Interestingly, despite the fact that aneuploidy is a common cause of tumorigenesis (Weaver & Cleveland, 2007), the downregulation of MCPH proteins does not lead to a significant increase in cancer incidence (Xu et al., 2020). This strengthens even more the point that aneuploidy, while it can lead to aneuploidy in some cases, cannot be the cause of ASPM or WDR62-dependent microcephaly.

Finally, several studies have reported spindle orientation defects in WDR62-depleted cells and have hypothesized that these spindle orientation defects could be at the origin of primary microcephaly. Indeed, the reasoning behind this hypothesis is the premature switch to asymmetric division mode in neuronal progenitor cells. It has been reported previously that the premature switch from symmetric cell division mode to asymmetric cell division mode causes neuronal progenitor pool exhaustion (Daynac et al., 2017). Several studies have previously reported spindle orientation defects in WDR62-mutated cells (Bogoyevitch et al., 2012; Miyamoto et al., 2017). Other studies (Chen et al., 2014; Jayaraman et al., 2016; Guerreiro et al., 2021; Doria & Ivanova et al., 2024, BioRxiv) have found no significant spindle orientation defects. In Guerreiro et al. (2021), we found no major spindle orientation phenotype in human tissue culture, reporting a spindle orientation more parallel to the surface in WDR62 depletion compared to control. Moreover, in another one of our studies (Doria & Ivanova et al., 2024, BioRxiv), we found that both Patronin and WDR62 RNAi in Drosophila led to an insignificant spindle orientation change in the Drosophila brain (Doria & Ivanova et al., 2024, BioRxiv, Figure 5). However, Patronin RNAi did not lead to a decrease in brain size, which is a strong argument against a spindle orientation defect in WDR62-dependent microcephaly.

We therefore hypothesize that in WDR62- and ASPM-dependent microcephaly, the presence of transient lagging chromosomes leads to 53BP1-p21-dependent cell cycle delay and microcephaly.

#### Why does the WDR62 depletion only affects brain size?

As the brain grows and expands, neuronal progenitor cells start to switch from expansion mode, in which they expand the progenitor pool, to differentiation mode, in which they begin to divide asymmetrically to produce one progenitor cell and one differentiated cell. According to various publications, different cell cycle proteins are crucial for neural fate determination (Bally-Cuif et al., 2003; Ohnuma et al., 2003). Indeed, the length of the G1 phase seems to be correlated with the switch to differentiation mode, where neuronal progenitor cells start to divide asymmetrically (Salomoni & Calegari, 2010). Some papers propose that the longer the G1 phase, the more time cell differentiation factors have to induce cell differentiation (Calegari & Huttner, 2003). Additionally, the cell cycle phase seems to be intrinsically linked to migration through the different layers during neurodevelopment, which might enhance cell fate determination (reviewed in Salomoni & Calegari, 2010).

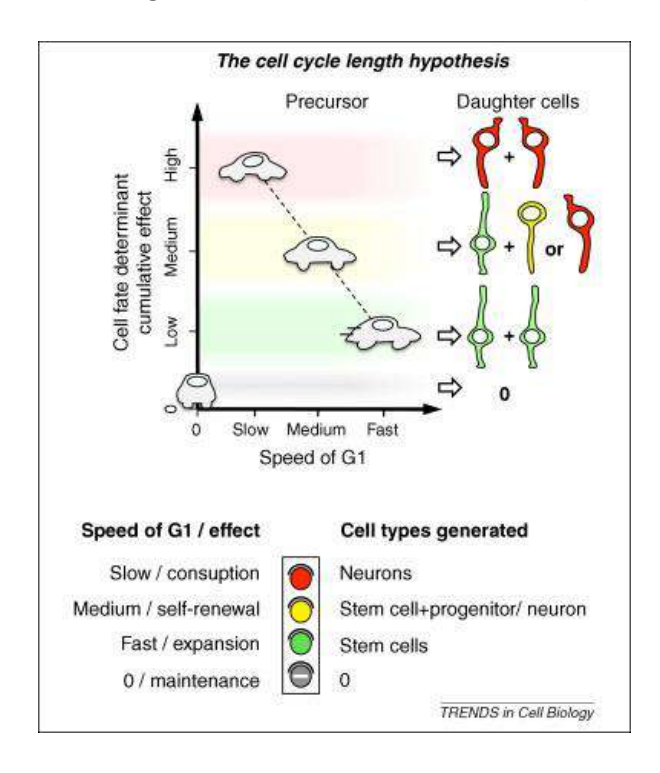


Figure 1: Cell cycle length hypothesis.

Cell fate depends on the speed of G1. Slower a cell progresses through G1, more cell fate determinant factors it accumulates and more it is prone to cell fate change from expansion to consumption.

Adopted from Salomoni&Calegari 2010.

But why is cell fate determined by the duration of the G1 phase and not other cell cycle phases? Some authors have speculated that transcriptional programs linked to the determination of cell fate reset at mitosis, and once the cell proceeds to G1, epigenetic programs—often dependent on chromatin repositioning—need to be set in place to change cellular fate (Dalton et al., 2015). However, other studies have not found a causality relationship between the duration of the cell cycle and cell fate decision (Lobjois et al., 2008).

While the correlation between G1 duration and cell fate determination remains unclear, another possibility for why WDR62 depletion leads to a decrease only in brain size is the dynamicity and speed of cell divisions in neuronal progenitor cells. Indeed, neuronal progenitor cells are among the fastest-dividing cells during embryonic and fetal development (Sensenbrenner et al., 1994) as they need to reach a certain population size in a limited time during progenitor pool expansion (Belmonte-Mateos et al., 2022). During just a few weeks, they need to increase the pool size from a few thousand cells to several million. To achieve this, neuronal progenitor cells need to divide very fast, and any delay in cell division could lead to a decrease in the neuronal progenitor pool size, neuronal number, and, consequently, brain size.

#### Microcephaly and brain evolution

Primary microcephaly genes are hypothesized to have been selected for during evolution due to the atavistic nature of the microcephaly disease—a unique reduction in brain size in the absence of other physical defects. Indeed, the size of a microcephalic patient's brain resembles the size of the brain of hominids *Sahelanthropus tchadensis* and *Australopithecus afarensis* (Pervaiz et al., 2021). Different MCPH genes have been reported previously in various evolutionary investigations, which have demonstrated the involvement of positive selection for these genes during evolution. For example, MCPH1 (Microcephalin) appears to be one of the most rapidly evolving genes, accumulating more amino acid-changing nucleotide substitutions for each silent substitution than most other genes (Ponting & Jackson, 2005). Similarly, ASPM seems to have accumulated a high number of changes since the last common ancestor of chimpanzees and humans. Interestingly, most of the substitutions have occurred in microtubule-binding and calmodulin-binding regions, demonstrating the unique importance of ASPM microtubule binding on the evolutionary scale (Ponting & Jackson, 2005). Additionally, other microcephaly-mutated genes, such as CDK5RAP2, demonstrate positive selection for brain size (Xu et al., 2017).

Interestingly, from a pathological point of view, primary microcephaly disease often shows a reduction in the more superficial layers of the brain cortex—the layers that developed latest during evolution.

For example, the Wdr62 <sup>-/-</sup> brain in one study has a reduced ratio of superficial to deep-layered neurons, as does the ASPM <sup>-/-</sup> brain. The authors have shown a preferential decrease in the size of the superficial cortical layer (Jaramayan et al., 2016).

During human evolution, the massive expansion in cortex size has been linked to an extraordinary increase in neuron number through the increased rate of neural progenitor cell division (Kalebic et al., 2019). Indeed, this hypothesis proposes a dramatic increase in cortex size through the prolonged symmetric division period. Also, recently discovered basal radial glia have been hypothesized to lead to evolutionary neocortex expansion due to their increased capacity for proliferation (Pinson & Huttner, 2021). Therefore, the evolutionary selection for MCPH genes, combined with the decrease in superficial layers in the brain cortex and the evolutionary increase in neuron number, seems to be intricately linked to cell division and the cell cycle process. This allows us to hypothesize the importance of neuronal progenitor division and cycling in human brain evolution.

#### Cytoskeleton in context of physiology and disease

The cytoskeleton plays an important role in many different cellular processes during interphase and mitosis by ensuring intracellular transport and allowing for precise chromosome segregation. In my study, I have investigated the involvement of microtubules in physiological and pathological contexts, learning how their dynamic nature allows cells to respond to different intrinsic and extrinsic cues and how their perturbation can have profound physiological consequences on human health.

In our work, we have uncovered the importance of microtubule severing during mitosis through Katanin, which promotes microtubule flux by creating microtubule minus-ends. This flux leads to precise chromosome segregation in anaphase. In pathological conditions, in the absence of Katanin, microtubules cannot flux correctly, which leads to the neurodevelopmental disorder of primary microcephaly. Similarly, our work on mitochondrial dynamics has led us to an understanding of the importance of cytoskeletal dynamics in maintaining organelle integrity and allowed us to postulate that the cytoskeleton is truly the "skeleton" of the cell, without which many different dynamic processes would be impossible.

Taken together, these findings underscore the dual role of the cytoskeleton in both physiological homeostasis and disease pathology. It is important to further study and understand the exact mechanisms of cytoskeletal regulation to allow for future therapeutic advances.

## Materials and Methods

#### Cell culture and drug treatments

hTert-RPE1 (ATCC: CRL-4000), hTert-RPE1-53BP1-GFP (kind gift of Réné Medema, Princess Maxima Center, Utrecht (Janssen et al 2011) hTert-RPE1 GFP-Centrin1/GFP-CENPA (kind gift from A. Khodjakov, State University of New York), hTert-RPE1 eGFP-aTubulin (kind gift of Daniel Gerlich), hTert-RPE1 USP28Δ (kind gift of Franz Meitinger, Meitinger et al 2024) and hTert-RPE1 PAGFP-atubulin cell lines (Toso et al 2009) were cultured in Dulbecco's Modified Eagle's Medium (DMEM; Thermo Fisher Scientific: 61965-026), supplemented with 10% FCS (Labforce, S181T), 100 U/ml penicillin and 100 mg/ml streptomycin (Life, 15140122). All cells were cultured at 37°C with 5% CO2 in a humidified incubator. For live-cell imaging, cells were cultured in eight-, four-, or two-well Ibidi chambers (Vitaris) in Leibovitz's L-15 medium (Thermo Fisher Scientific, 21083027) supplemented with 10% FCS before imaging for maximum 12 h in the absence of CO<sub>2</sub>. The following drugs were added to the culture or imaging medium: 10 µM MG132 (Sigma Aldrich, C2211-5MG) for 30 min, 100 nM Doxorubicin (Sigma, D1515) for 12 h, 50 nM Aurora B inhibitor Barasertib (AZD1152, S1147, Selleckchem), 50 nM SiR-Tubulin (Spirochrome, SC002) for 2 h, 500nM Reversin (Sigma-Aldrich, R3904-1MG) for 12h, 100 uM Monastrol (GLP BIO, GC14929) for 12h, 400nM Aphidicolin (Sigma-Aldrich, A0781) for 12h, 100 nM SiR DNA (Spirochrome, SC007) for 2 h, 100 nM SiR Tubulin (Spirochrome, SC002) for 2 h, 100 nM SpY DNA (Spirochrome, SC101) for 5 h.

#### siRNA and plasmid transfections

For protein depletions, cells were transfected for 48 h in case of single depletions and 72 h in case of the double depletions with 20 nM siRNAs using Opti-MEM (Invitrogen, 31985-047) and Lipofectamine RNAiMAX (Invitrogen, 13778075) according to the manufacturer's instructions. For the double depletions, a double amount of Lipofectamine RNAiMAX was used. The medium was replaced 24 h after transfection. The following sense strands of validated siRNA duplexes were used (all Qiagen unless indicated): siASPM (16), 5'-GCU AUA UGU CAG CGU ACU ATT-3'; siCamsap1 (validated in Supplementary Figure 3, Doria&Ivanova 2024, Biorxiv) 5'-CAUCGAGAAGCUUAACGAATT-3'; siWDR62 5'-AGA CAA AGG (39), (Dharmacon; (14)), UGA CGA GCA C-3'; siNPL4 CAGCCUCCUCCAACAAUCdTdT-3'; siUBASH3B - 1 (40), 5'-CCGCTTAAGGATGCTAACATT-3', siUBASH3B - 2 (40), ), 5'-AAGAGAGTTGTTCTTAGGTTA-3' mixed 1:1, siKIF4a (Wandke et al 2012), 5'-GCAGAUUGAAAGCCUAGAGTT-3', siCDK5RAP2 (Thomas et al 2024), 5'- UGGAAGAUCUCCUAACUAATT

-3', siSAS6 (Tan et al 2015), 5'-GCACGUUAAUCAGCUACAATT-3', and as a negative control siCTRL (AllStars Negative Control siRNA; Qiagen, 1027281, Proprietary).

#### *Immunofluorescence*

To stain for WDR62, 53BP1, p21, yH2AX, Aurora B, NPL4, UBASH3B, RB, Ki-67 and Nup62 hTert-RPE1 cells were fixed at -20°C for 7 min with ice-cold methanol stored at -20°C. To stain for CAMSAP1, MCAK, hTert-RPE1 cells were fixed at room temperature for 15 minutes with a solution containing 4% Formaldehyde (Applichem, A3592), 2mM of PIPES (Applichem, A1079.0500), pH 6.8, 1mM of EGTA (Applichem, A0878.0100), and 0.2% -Triton X-100 (Applichem, A4975.0100). To stain for 2-tubulin cells were washed 30 seconds in a 37°C warm buffer containing 80mM M KOH-PIPES, 10mM MgCl2 (Applichem, 131396.1211), 5mM EGTA, 0.5% Triton-X and fixed at room temperature for 10 minutes in a 12.5% Glutaraldehyde (Sigma Aldrich, G5882), 80mM KOH-PIPES, 10mM MgCl2, 5mM EGTA and 0.5% Triton-X solution. Cells were washed for 7 minutes in a freshly prepared 0.1% NaBH4 (Sigma Aldrich, 16940-66-2) in PBS quenching solution. The samples were washed twice for 2 minutes in PBS. After all fixations cells were rinsed with PBS and blocked 1 hour in blocking buffer (PBS + 3% BSA (LabForce, S181T) and 1% N₃Na (Applichem, A1430). After blocking, cells were washed thrice for 5 minutes with PBS and incubated 1 hour with the primary antibody diluted in blocking buffer. Next, cells were washed twice in PBS and incubated 1 hour with the secondary antibody diluted in blocking buffer. Coverslips were mounted on microscopes slides with DAPI Vectashield mounting medium (Vector Laboratories, H1200).

The following primary antibodies were used: recombinant human anti-α-tubulin (1:500; Guerreiro&Meraldi 2019), rabbit anti-CAMSAP1(1:1500; Novus Biologicals NBP1-26645), rabbit anti-WDR62 (1:1000; Bethyl A301-560A), rabbit anti-MCAK (1:1000; Amaro et al 2010), rabbit anti-53BP1 (1:1000; Cell Signalling Technology 4937), mouse anti-p21 (1:1000; Cell Signalling Technology 2947), mouse anti-yH2Ax (1:2000; EMD Millipore, 05-636), mouse anti-AuroraB (1:2000; BD Biosciences 611083), rabbit anti-NPL4(1:500; Novus Biologicals NBP1-82166), rabbit anti-UBASH3B (1:500; Proteintech 19563-1-AP), rabbit anti-RB (1:1000; Abcam, ab181616), rabbit anti-Nup62 (1:1000, kind gift of Ulrike Kutay), mouse anti-Ki-67(1:1000, BD Biosciences, 550609). For secondary antibodies, Alexa Fluor—conjugated antibodies (1:400; Invitrogen) were used. The pictures used for the analysis were acquired using 60× and 100× (NA 1.4) oil objectives on Olympus DeltaVision wide-field microscope (GE Healthcare) equipped with a DAPI/FITC/TRITC/Cy5 filter set (Chroma Technology Corp.) and Coolsnap HQ2 CCD camera (Roper Scientific) running Softworx (GE Healthcare). Alternatively, they were also acquired using a HC PL APO CS2 63x/1.40 Oil objective on a Leica Stellaris

5 confocal microscope equipped with 405 nm, 488nm, 561nm and 638 nm lasers and two Hybrid S detectors (HyD S1 and HyD S2) running LAS X software (version: 4.5.0.25531).

#### Live-cell imaging

To monitor mitotic progression and chromosome segregation, hTert-RPE1 and hTert-RPE1-53BP1 GFP cells were seeded into Ibidi chambers (Vitaris) and treated with siRNAs as described above. Prior to imaging, cells were supplemented with L15 medium containing SiR DNA (Spirochrome #SC007) according to manufacturer protocol and recorded on a Nikon Eclipse Ti-E wide-field microscope (Nikon) equipped with a GFP/mCherry/Cy5 filter set (Chroma Technology Corp.), an Orca Flash 4.0 complementary metal-oxide-semiconductor camera (Hamamatsu), and an environmental chamber using NIS software (Nikon). For normal movies cells were imaged in the GFP and Cy5 channels for 12 h at 37°C, at 1-min, 1-min 30 sec or 2 min intervals, in 17 steps of 1 μm Z-stacks, using a 60× (NA 1.51) oil objective and 2 × 2 binning. To correlate the persistence of lagging chromosomes (SiR-DNA) and the timing of appearance of GFP-53BP1 foci, a first movie was recorded in the Cy5 channel for 1 h at 37°C at 30 sec intervals, in 17 steps of 1  $\mu$ m Z-stacks, using a 60× (NA 1.51) oil objective and 2 × 2 binning. The movie was stopped and restarted at the same positions using both the GFP and Cy5 channels for 12 h at 37°C at 3 min intervals, in 17 steps of 1 μm Z-stacks, using a 60× (NA 1.51) oil objective and 2 × 2 binning. For cell cycle duration measurement, hTert-RPE1 cells were seeded into Ibidi chambers and treated with siRNAs as described above. Prior to imaging, cells were supplemented with Leibovitz's L-15 Medium and recorded on the same Nikon Eclipse Ti-E wide-field microscope using brightfield illumination for 30h at 37°C, at 3 min interval, in single plane, using a 10× objective and 2× 2 binning. For imaging of non-kinetochore microtubules, Nipkow spinning disk microscope was used equiped with EC Plan-Neofluar 10x / 0.3 Ph1 M27 WD=5.2mm and LCI Plan-Neoflur 63x / 1.3 Imm Korr DIC for Water Silicone Glycerole immersion WD=0.15-0.17 objectives and 405 nm, 488nm, 561nm and 638 nm lasers. For this experiment, a 63x glycerol objective was used; metaphase cells were selected and recorded every 6 sec using 488nm and 647nm lasers for 100 timepoints. For the measurement of spindle length in MG132-arrested RPE PA-GFP cells were cultured in 4 well IBIDI chambers, blocked in metaphase with 10 μM MG132 for 30 min and imaged using Olympus DeltaVision wide-field microscope (GE Healthcare) equipped with an environmental chamber maintained at 37°C and a GFP/RFP filter set (Chroma Technology Corp.). Cells were after incubated with 100 nM SiR Tubulin (Spirochrome, SC002) for 2 h prior imaging. The metaphase cells were imaged in Z-stacks of 12.8-um thickness with z-slices separated by 0.28 um in GFP channel and the spindle length was analysed using signal Imaris (Bitplane) 10.

#### Anaphase kinetochore tracking assay

hTert-RPE1 GFP-centrin1/GFP-CENPA were treated with the reported siRNAs, and metaphase cells imaged for 15 min every 15 s using a  $100 \times (NA~1.4)$  oil objective on an Olympus DeltaVision wide-field microscope (GE Healthcare) equipped with an environmental chamber maintained at  $37^{\circ}$ C and a GFP/RFP filter set (Chroma Technology Corp.). Z-stacks of 15- $\mu$ m thickness with z-slices separated by 0.5  $\mu$ m were imaged in the GFP channel with 2 × 2 binning to track kinetochores from metaphase until late anaphase. 4D images (XYZT) obtained were deconvolved in conservative mode and cropped using Softworx (GE Healthcare). The kinetochores and the poles were segmented using Imaris (Bitplane) during metaphase and anaphase. The kinetochores positions over time were analysed using a Matlab code ((14), https://github.com/AmandaGuerreiro/WDR62\_2020).

#### Poleward microtubule flux measurement

hTert-RPE1 PA-GFP- $\alpha$ -tubulin cells were incubated with 10  $\mu$ M MG132 for 30 minutes and imaged for 1 hour. Single focal planes of 150-nm pixel size were acquired using a 60× (NA 1.4) CFI Plan Apochromat oil objective on a Nikon A1r point scanning confocal microscope equipped with a 37°C heating chamber and running NIS elements software. A 3-pixel-thick and 100-pixel-long ROI parallel to the DNA and close to spindle centre was photoactivated with a 500-ms, 405-nm laser pulse at 50–100% intensity depending on the PA-GFP- $\alpha$ -tubulin expression levels and imaged every 20 seconds for 4 min in a single focal plane. The photoactivated mark was tracked manually for 120 s with Fiji (ImageJ). Distance between the photoactivated mark and the corresponding spindle pole was tracked in time and the displacement of the photoactivated mark over time was calculated.

#### Single cell sequencing

Cells were arrested in G1 phase using the CDK4/6 inhibitor Palbociclib (Cayman Chemical Company: 16273) at 100 nM for 12 hours. Cells were next sorted as single cells into a 384-well plate by FACS using the MoFlo Astrios cell sorter at the FACS facility of the Medical Faculty of the University of Geneva. At the single cell core facility of the ONCODE institute facility, nuclei in each well were digested with Nlalli, after which the genomic fragments (following end processing) were ligated to barcoded adapters containing a unique molecular identifier (UMI), cell-specific barcode, and T7 promoter allowing linear amplification by in vitro transcription (IVT). Libraries were sequenced on an Illumina Nextseq 500 at 16M reads. At the University of Geneva Bioinformatics facility, the raw fastq files were mapped to GRCH38 using the Burrows–Wheeler aligner. The mapped data were analyzed

using custom scripts in R (available at GitHub: https://github.com/DIvanova-EDoria/master.git), which parsed for library barcodes, removed reads without a NIaIII sequence and removed PCR-duplicated reads. To perform quality control of the sequences, the following gates were set: minimum count: 10000 reads, maximum count: 75000 reads. The data which did not fail the QC were normalized to simulate the same amount of reads in every cell as following: 10000 \* value / sum(value).

#### Metaphase spreads

Cells were incubated with 1mM Nocodazole (Sigma Aldrich, M1404-2MG) for 1h at 37C. Mitotic cells were shaken off, centrifuged and resuspended in 0.56% KCl (Applichem, A3582.0500) at room temperature for 6 min, before resuspending them dropwise in a 5 ml 3:1 MeOH/ CH3COOH (AppliChem, A2369) solution. The excess of supernatant was removed and 20ul of cells suspension was added dropwise on cooled microscopy slides (Epredia, 1.0mm) and left to dry in humid air chamber for 1h. The metaphase spreads were mounted using DAPI Vectashield and Epredia cover slips 22x22 mm.

#### CFSE labelling for cell proliferation assay

To measure cell proliferation over 5 days, hTert-RPE1, hTert-RPE1-PCNA-mRuby and hTert-RPE1-PCNA-mRuby p21 KO 2a (both kind gifts of Prof A. Barr, Imperial College London) cells were trypsinized, centrifuged, washed once with PBS, and resuspended in PBS at a concentration of  $1 \times 10^6$  cells/ml in the presence of 1  $\mu$ M CFSE (BioLegend, 423801) for 20 min at 37 °C. The CFSE was quenched by adding 5 times the original staining volume of cell culture medium for 10 min. After a final washing step, a fraction of the cells was resuspended in PBS with 20mM Tris (Applichem, A1379.5000) and 0.1% FCS and quantified by flow cytometry for reference (see below). The remaining cells was seeded and treated with siRNAs for 5 days. After 5 days of incubation, CFSE signal intensity was measured using 488 nm laser on Beckman Coulter Cytoflex.

#### Cell cycle measurements using Propidium Iodide

Prior to cell cycle measurements, hTert-RPE1 cells were treated for 48h with siCTRL and siWDR62 (described above). Cells were then harvested and counted prior to being centrifuged at 300 x g for 5 minutes. The pellet was washed twice using phosphate-buffered saline at RT. Then cells were resuspended in 100 ul of phosphate-buffered saline. 900 ul of 80% EtOH (Sigma-Aldrich, 02878-1) was added dropwise to the cells while constant vortexing for a final EtOH concentration of 72%. The fixed cells are placed in the -20C freezer for 12h. Cells were washed with phosphate-buffered saline twice

and propidium iodide (Sigma-Aldrich, 81845-25MG) was added in concentration 40 ul per 1000000 cells. Propidium Iodide signal intensity was measured using 568 nm laser on Beckman Coulter Cytoflex.

#### Electron microscopy

hTert-RPE1 cells were treated for 48h with siCTRL and siWDR62 (described above). On the day, cells were incubated with 10uM MG132 for 2h to enrich metaphase cells. The mitotic cells were collected using a mitotic shake-off procedure (Dudka et al 2018), centrifuged at 100xg for 5 min in a Megafuge 1.0 centrifuge (Heraeus Instrument, Switzerland). The cells were then fixed for 30 min at RT with cell culture medium (DMEM) supplemented with 2% EM-grade glutaraldehyde (Sigma Aldrich). Next, cells were centrifuged as described above and collected into 1.5ml Eppendorf tubes and fixed the pellet (without resuspending) with 2% glutaraldehyde EM grade in 0.1M Sodium Phosphate buffer for 30 min at RT. Pellet was then centrifuged at 100xg for 5 min in Eppendorff mini-centrifuge (Eppendorff, Switzerland) and washed with phosphate-buffered saline. At the electron microscopy facility, pellets were treated with 2% osmium tetraoxyde in buffer and immersed in a solution of uranyl acetate 0.25% overnight (Tandler et al 2020). Pellets were dehydrated in increasing concentrations of ethanol followed by pure propylene oxide. Then pellets were embedded in Epon resin. The pellet was sliced into thin sections which were stained with uranyl acetate and lead citrate. The sections were observed in a Tecnai 20 electron microscope (FEI Company, USA). MT numbers in each k-fiber were calculated as reported in (Booth et al 2011, Dudka et al 2018). Bundles of microtubules were only counted as kfibers if they were within a 1 um of a chromosome, if the bundle contained at least 7 microtubules and if the microtubules were not separated by more than 80 nm.

#### Mitochondrial laser stimulation

hTERT-RPE 1 cells were cultured as described above in a 2,4 or 8 well IBIDI dishes (). Dye staining was performed on the cells as follows; PKmito Orange was applied at 500 nM for 1 hour at 37°C standard incubation, MitoTracker Green (Thermo #M36005) was applied at at 500 nM for 1 hour at 37°C standard incubation. At Marine Biology Laboratory, Nikon CSU-W1 spinning-disk confocal system was used for imaging and stimulation paired with Andor Zyla sCMOS camera (5.5 megapixels), Nikon Perfect Focus system, Oko stage top incubator, and Vortran 405 nm photoactivation and photobleaching laser. Imaging was performed with 488 nm and 561 excitation lasers using a Plan Apo VC 100x/1.4 oil objective and a zET405/488/561/635m quad filter. FRAP laser was calibrated before each experiment using a 0.1mg/ml fluorescein-coated coverslip (Thermo #L13251.36).At the University of Geneva, cells were stimulated by FRAP using Nipkow spinning disk microscope equiped with EC Plan-Neofluar 10x / 0.3 Ph1 M27 WD=5.2mm and LCI Plan-Neoflur 63x / 1.3 Imm Korr DIC for

Water Silicone Glycerole immersion WD=0.15-0.17 objectives and 488nm, 561nm and 638 nm lasers and 405 nm photoactivation and photobleaching laser. Imaging was performed using 63x glycerol objective. For cytoskeleton disruption, following drugs were used for 1h incubation at 37°C: 100nM Taxol (Sigma #PHL89806), 100nM Nocodazole (Sigma #M1404- 2MG), 1uM Latrunculin B (Sigma #L5288). The images were taken in a single z-plane every 5 seconds for a total duration of 5 min.

Image processing, nuclear shape and 53BP1, p21 and yH2AX quantifications

Immunofluorescence images were first converted to z-stack (sum slices) using ImageJ/Fiji and opened in QuPath 0.4.3 (Bankhead et al 2017). To quantify 53BP1, p21 or yH2AX, nuclei were segmented using the DAPI channel. To detect 53BP1 foci, a code was used to determine foci with a minimal area of 0.2 μm<sup>2</sup> and an intensity higher than the mean nuclear intensity plus 2 standard deviations. For p21 or γH2AX intensities, an automatized QuPath analysis was used to analyse p21 or γH2AX levels in segmented nuclei. The background was subtracted, and cells were counted as positive if their intensity was higher than the mean plus one standard deviation of the intensity in siCTRL-treated cells. For nuclear shape quantification, nuclei were segmented using the DAPI channel. Circularity was characterized directly using automatized QuPath analysis parameter. Eccentricity was calculated as left foci of the ellipse divided by right foci of the ellipse, both foci were characterized using automatized QuPath analysis. Solidity was calculated as area of the nucleus (calculated using automatized QuPath analysis) divided by convex hull area (calculated using automatized QuPath analysis) (Bankhead et al 2017). Time-lapse movies were analysed manually with NIS Elements software to quantify mitotic timing and presence of 53BP1 foci, taking into account cells 4h after mitosis. Time-lapse movies were also analysed manually with NIS Elements software to quantify the presence or absence of transient lagging chromosomes. These were quantified as present when DNA clouds in anaphase were > 6um apart and the lagging was > 2um long. For siRNA immunofluorescence quantification and pRB quantifications, 3D images were analysed manually with ImageJ/Fiji. Aurora B intensity in anaphase was quantified using surface tool on DNA signal Imaris (Bitplane) 10.

All the data were plotted using GraphPad Prism 8.2.1.

#### D. melanogaster strains

The following sources of different D. melanogaster lines were used in this study:

| Source         | Strain                      | ID                                  |  |
|----------------|-----------------------------|-------------------------------------|--|
| Régis Giet lab | w; InscuteableGal4/Cyo (II) | Bloomington <i>Drosophila</i> Stock |  |
|                |                             | centre: 8751                        |  |

| Régis Giet lab  | w; Jupiter-GFP, His2Av-mRFP | (47, 48) |
|-----------------|-----------------------------|----------|
|                 | (III)                       |          |
| NIG-Fly         | w; UAS-Wdr62-RNAi (III)     | 7337-R1  |
| VDRC            | w; UAS-PatroninRNAi (II)    | 108927   |
| Emi Nagoshi lab | w <sup>1118</sup> +         |          |

D. melanogaster fruit flies were raised at 25 °C in standard medium.

#### Immunofluorescence of D. melanogaster brain larvae

3rd instar larvae were collected 120h after an egg laying of 5h. Larval brains were dissected in testis buffer (TB, 183 mM KCl, 47 mM NaCl, 10 mM Tris, and 1 mM EDTA, pH 6.8 MT) and brains were fixed at room temperature for 20 min in TB + 10% FA and 0.01% Triton-X. Brains were washed 2 times x 15 minutes in PBS and then 2 times x 15 minutes in PBS + 0.1% Triton-X. Brains were blocked for 1 hour in PBSTB (1% BSA, 0.1% Triton-X in PBS). Brains were incubated with the primary antibodies in PBSTB for 1 hour at room temperature. After 1 wash with PBS, brains were incubated with secondary antibodies in PBSTB for 1 hour at room temperature. After washes, samples were mounted on microscope slides with DAPI Vectashield mounting medium (to avoid brain deformation, for brain size measurements, spacer were used while mounting microscope slides).

The following primary antibody was used: rat anti-Miranda (1:500, Abcam, ab197788). For secondary antibodies, Alexa Fluor—conjugated antibodies (1:400; Invitrogen) were used. For neuroblast counting and spindle orientation experiments, images were acquired using a HC PL APO CS2 40x/1.40 air objective on a Leica stellaris 5 confocal microscope equipped with 405 nm, 488nm, 561nm and 638 nm lasers and two Hybrid S detectors (HyD S1 and HyD S2) running LAS X software (version: 4.5.0.25531). For brain size image acquisitions, a Nikon Eclipse Ti-E wide-field microscope (Nikon) equipped with a GFP/mCherry filter set (Chroma Technology Corp.), an Orca Flash 4.0 complementary metal-oxide-semiconductor camera (Hamamatsu), and an environmental chamber using NIS software was used.

To measure brain lobe sizes, the average diameter of one brain lobe was calculated as the mean of two measurements in orthogonal orientation (length + width / 2) using Fiji. The brain lobe shape was approximated to a circle shape and the area was calculated with the formula:  $Area = (\pi \times diameter^2)/4$ . The number of neuroblasts in the central brain was calculated as the number of Miranda positive cells, manually using FIJI, and the average of the two lobes was reported. For spindle orientation, Fiji from

ImageJ software was used to calculate the angle between the spindle poles axis and a line perpendicular to Miranda signal.

Live cell imaging of D. melanogaster brain larvae

3rd instar larvae were collected 120h after an egg laying of 5h. Larval brains were dissected in Schneider's Drosophila Medium (Gibco, 21720024) and transferred in testis buffer into Ibidi chambers (Vitaris). Brains were then imaged on Nipkow spinning disk microscope equiped with EC Plan-Neofluar 10x / 0.3 Ph1 M27 WD=5.2mm and LCI Plan-Neoflur 63x / 1.3 Imm Korr DIC for Water Silicone Glycerole immersion WD=0.15-0.17 objectives and 405 nm, 488nm, 561nm and 638 nm lasers. For transient lagging chromosome and mitotic timing experiment, a 63x glycerol objective was used; metaphase cells were selected and recorded every 6 sec using 488nm and 561nm lasers until they were in late anaphase. QC gate of  $1\mu$ m was used to differentiate a transient lagging chromosome. For cell cycle duration, a 10x objective was used and brains were acquired using 488nm and 561nm lasers every 2 min with a z-step of  $1\mu$ m for a total of 31 steps.

#### Cognitive tests

For the running assay, all 3<sup>rd</sup> instar larvae were recorded directly after collection on a 0.8% agar 10 cm (500 ml water, 4 g agar (Roth, Karlsruhe)) surface. Prior to recording, larvae were briefly washed with PBS. Turning frequency is indicated as the number of peristaltic movements a larva needs to make before turning. Movies of 5 min were made and analysed by hand selecting a 1 min interval. For fructose assay, all 3<sup>rd</sup> instar larvae were recorded directly after collection on a 0.8% agar 10 cm (500 ml water, 4 g agar (Roth, Karlsruhe)) surface, containing in one half 0.2M Fructose (Sigma Aldrich, F0127, 3.6g in 100 ml 0.8% agar) and no fructose in the other half. Prior to recording, larvae were briefly washed with PBS. Fructose preference was evaluated by setting the larvae in the middle of the dish and allowing them to choose a side. The movements were recorded, and the final choice was analysed by the end of 5 min.

## Annex of other published articles

### The biophysical mechanism of mitochondrial pearling

This work was initiated during the advanced summer course "Physiology: Modern Cell Biology Using Microscopic, Biochemical, and Computational Approaches" at the Marine Biology Laboratory, Woods Hole, MA, USA, under the supervision of Professor Wallace Marshall's lab at UCSF. I participated in this course during the summer of 2023.

The project was originally developed by Gav Sturm, a PhD student in the lab. During my training in Woods Hole, we observed that mitochondria undergo pearling in response to laser-induced stimulation. Given the critical role of the cytoskeleton in mitochondrial transport and structural support, we tested the effects of microtubule disruption using various drugs. Interestingly, we found that microtubule disruption altered the pearling behavior of mitochondria.

I assisted Gav during my training at Woods Hole and continued contributing to the project afterward by conducting laser stimulation experiments and analyzing mitochondrial pearling following cytoskeletal disruptions (Figure 3K).

#### The biophysical mechanism of mitochondrial pearling

Authors: Gabriel Sturm<sup>1,2</sup>, Kayley Hake<sup>2</sup>, Austin E.Y.T. Lefebvre<sup>2</sup>, Caleb J. Rux<sup>1</sup>, Daria Ivanova<sup>3</sup>, Alfred Millett-Sikking<sup>2</sup>, Kevin M. Tharp<sup>4</sup>, Beiduo Rao<sup>2</sup>, Michael Closser<sup>2</sup>, Adam Waite<sup>2</sup>, Magdalena Precido-Lopez<sup>2</sup>, Sophie Dumont<sup>1</sup>, Wen Lu<sup>2</sup>, Suliana Manley<sup>5</sup>, Juan C. Landoni<sup>5</sup>, Wallace F. Marshall<sup>1</sup>

#### **Abstract**

Mitochondrial networks exhibit remarkable dynamics that are driven in part by fission and fusion events. However, there are other reorganizations of the network that do not involve fission and fusion. One such exception is the elusive, "beads-on-a-string" morphological transition of mitochondria. During such transitions, the cylindrical tubes of the mitochondrial membrane transiently undergo shape changes to a string of "pearls" connected along thin tubes. These dynamics have been anecdotally observed in many contexts and given disparate explanations. Here we unify these observations by proposing a common underlying mechanism based on the biophysical properties of tubular fluid membranes for which it is known that, under particular regimes of tension and pressure, membranes reach an instability and undergo a shape transition to a string of connected pearls. First, we use high-speed light-sheet microscopy to show that transient, short-lived pearling events occur spontaneously in the mitochondrial network in every cell type we have examined, including primary fibroblasts, T-cells, neurons, and budding yeast. We present evidence that transient mitochondrial pearling occurs during important biological events, particularly during T cell activation and neuronal firing. Using our high-temporal resolution data, we identify two distinct categories of spontaneous pearling, i) internal pressure-driven pearling regulated by ionic flux, and ii) external tension-driven pearling regulated by molecular motors. By applying live-cell STED microscopy we document the structural reorganization of inner cristae membranes during mitochondrial pearling. We then compare numerous methods for inducing pearling, including the ability to induce these dynamics with single mitochondrion precision. These methods include ionophores, channel activators, osmotic shock, detergents, laser stimulation, membrane intercalating molecules, chemical fixation, and micro-needle force. These disparate inducers establish three main physical causes of pearling, i) ionic flux amplifying internal osmotic pressure, ii) membrane packing lowering bending elasticity, and iii) external mechanical force increasing membrane tension. Pearling dynamics thereby reveal a fundamental biophysical facet of mitochondrial biology. We suggest that pearling should take its place beside fission and fusion as a key process of mitochondrial dynamics, with implications for physiology, disease, and aging.

<sup>&</sup>lt;sup>1</sup> University of California, San Francisco, San Francisco, CA, USA.

<sup>&</sup>lt;sup>2</sup> Calico Life Sciences LLC, South San Francisco, CA, USA.

<sup>&</sup>lt;sup>3</sup> Université de Genève, Geneva, Switzerland.

<sup>&</sup>lt;sup>4</sup> Sanford Burnham Prebys Medical Discovery Institute, San Diego, CA, USA.

<sup>&</sup>lt;sup>5</sup> Swiss Federal Institute of Technology Lausanne, Lausanne, Switzerland.

#### Introduction

Inside the cell, mitochondrial units are arranged in complex networks that continually reorganize via dynamic processes including fission and fusion events <sup>1,2</sup>. A less appreciated dynamical behavior of mitochondria involves a transient shape transition from a cylindrical tubule to a "beads-on-a-string" morphology (**Figure 1A**), first observed in 1915 by Margeret and Warren Lewis <sup>3</sup>. This morphology has since been observed in numerous biological contexts and has been referred to as "beads-on-a-string" <sup>4</sup>, "COMIC" <sup>5</sup>, "MOAS" <sup>6</sup>, "nodules", "condensation", "beading", "fragmentation sites" <sup>4,7</sup>, and "thread-grain transitions" <sup>8</sup>. These sightings include the muscle cells of *C. elegans* <sup>9</sup>, the hypocotyl cells of Arabidopsis plants <sup>10</sup>, and during the growth phase and meiosis of budding yeast <sup>11,12</sup>. Additionally, beads-on-a-string mitochondria have been observed *in vivo* including in postmortem brains of healthy, aged, Alzheimer's, and hypoxic-treated mice and humans <sup>6,13,14</sup>.

One proposed explanation of this pearled morphology is that the mitochondrial fission machinery, largely through GTP hydrolysis by the dynamin-like protein, Drp1, could provide a force to constrict the mitochondrial membrane, forming the pinched regions between pearls. But such a model is not consistent with experiments in DRP1 knock-out cells, which have increased rather than decreased pearling rates that propagate across their highly fused mitochondrial networks <sup>5,15</sup>. Other hypothesized explanations for this phenomenon include reactive oxygen species (ROS) generation <sup>16</sup>, ER constrictions around the mitochondrial tube, cytoskeleton remodeling, and non-conventional permeability transition pores (mPTP, <sup>17</sup>), but each fails to fully explain the experimental observations. More recently, the beads-on-a-string morphology was explained by contact-sites with the ER <sup>18</sup>. At these junctions, calcium release by the ER is followed by calcium influx into the mitochondria. However, axonal mitochondria undergo pearling spontaneously, as well as by laser axotomy <sup>14</sup>, coinciding with matrix alkalization, depolarization, and increased oxidation, but without an influx in calcium. Similarly, during mitochondrial transplantation, pearl formation is independent of calcium influx <sup>19</sup>. Thus, the mechanism by which pearls form is unclear.

A radically different mechanism for these dynamics comes from the physics of the Rayleigh-Plateau instability governed by the Helfrich model of elastic membranes (eq. 1) <sup>20–22</sup>. The basis of this model is the fact that a cylinder is not actually the minimal surface area shape for an elongated membrane tube. If the surface is folded into sinusoidal curves, the same internal volume can be enclosed with a smaller surface area. The normally smooth cylindrical shape of membrane tubes results from the fact that the energy of bending a membrane is substantially larger than the energy of stretching them, thus the lowest energy state is one in which the surface is minimally curved (cylinder) at the expense of having to stretch to accommodate the internal volume. If membrane tension is increased, either by inflating the internal volume or else by

applying mechanical pulling forces, the energy balance shifts such that the stretching term becomes larger than the bending term, resulting in a lower energy state in which the membrane curves into pearls <sup>22–25</sup>.

$$E = E_b + E_s + E_p$$
 (eq. 1)

Equation (1) consists of a simplified version of the Helfrich model which determines the total energy of the membrane surface. This model consists of three energies; i) bending energy (Eb) derived from membrane's curvatures and bending modulus, ii) surface tension energy (Es) capturing stretching or compressing of the membrane surface, and iii) pressure energy (Ep) representing the work done by the pressure difference across the membrane, proportional to the enclosed volume.

The Rayleigh-Plateau mechanism should further dictate the transitions of cellular structures. Any cylindrical tube of membranes, including double membranes such as cellular membranes, and reticulated organelle networks like mitochondria will undergo a spontaneous shape transition when the energy stored by membrane stretching exceeds the elastic energy stored by membrane bending. These energies are determined by the organelle's physical properties; in particular, membrane tension and elastic modulus. The membrane can reach this threshold from i) increased internal osmotic pressure, ii) increased external mechanical tension, or iii) reduced bending elasticity (i.e. stiffness) <sup>22,26</sup>. In accordance with this mechanism, we refer to this dynamical phenomenon as mitochondrial pearling.

Such pearling-like forms have also been described in other cellular structures such as plasma membranes <sup>27,28</sup>, axons <sup>29,30</sup>, microtubule-associated proteins <sup>31</sup>, contractile vacuoles <sup>32</sup> and the endoplasmic reticulum (ER) <sup>33–35</sup>. However, because the mitochondrion has an inner membrane that is electrochemically coupled and highly structured into helicoid cristae <sup>36</sup>, it has an elastic modulus an order of magnitude greater than typical double membranes of its size <sup>20</sup>. These properties make it particularly resistant to deformation and thereby physically unique among cellular organelles.

Here we propose that the Rayleigh-Plateau mechanism may provide a unified model of mitochondrial pearling that can account for the many circumstances in which it has been observed. Using a combination of live-cell imaging, high-resolution structural information, and perturbation experiments, we find that biological events that either apply osmotic pressure or mechanical tension, or alter the mitochondrial membrane, can induce a similar pearling instability. The ability of such disparate causes to drive mitochondrial pearling can most parsimoniously be explained if they all work by altering the balance of tension and bending energies in the membrane, thus avoiding the need to invoke a collection of distinct molecular processes.

#### Results

#### Spontaneous mitochondrial pearling encompasses two physically distinct events

Mitochondrial tubules generally take on cylindrical shapes interwoven into larger networks through fission and fusion processes. However, live-cell time lapse imaging of individual mitochondria tubules has revealed that mitochondria will occasionally transition into pearled units connected by thin membrane tubules, a shape that is held transiently before transitioning back to a uniform shape (Figure 1B and Movie 1). These events have previously been observed in standard imaging conditions in mammalian cells such as U2OS, HEK293, HepG2, MEFs, and cortical neurons <sup>5,14,15,19</sup>. These reports have documented events lasting 5 seconds to 2 minutes, with each mitochondrion having a 10%-50% chance of pearling every 10 minutes, depending on cell type. Here, we refine these reports with a single-objective light-sheet (SOLS) microscope (a.k.a. "Snouty", 37) by imaging whole-cell mitochondrial networks in 3D at 2 Hz (i.e. 2 volumes/second) with minimal phototoxicity compared to standard 3D imaging. We found transient pearling events in every cell type we studied, which included U2OS, HEK293, COS7 (monkey), RPE1, Jurkat cells, primary human CD8 T cells, primary human fibroblasts, iPSCderived neurons, and budding yeast (Figure 1B, Methods Table 1 Supplementary Figure 1A-H). Using the SOLS microscope, pearling events underwent a full transition (cylinder-pearlcylinder) in as little as 2 seconds (0.5 Hz) (Figure 1C & Movie 2). Based on these dynamics, imaging these events with a typical confocal microscope (<0.2 Hz) would miss up to 27% of pearling events, depending on cell type. Additionally, imaging with SOLS microscopy at 1 Hz revealed the probability of a pearling event can vary widely between cell types: In a ten minute interval, it can be as low as 1.4% of mitochondria in iPSC-derived neurons or as high as 22.3% in U2OS cells (Figure 1D & Supplementary Figure 1I). Measuring the curvature of the mitochondrial profile throughout these videos revealed differential dynamics between cell types, with mitochondria that pearl tending to undergo 2nd and 3rd events within regular time intervals of 10-14 seconds (Figure 1E). Remarkably, the shape of these pearls across cell types was highly conserved with an average width (i.e cross-diameter) of 320-480 nm and peak-to-peak distance between pearls of 0.8-1.3 µm (Figure 1F-G).

In support of the physiological relevance of these dynamics, we have observed pearling events during reconstituted biological events. First, we culture iPSC-derived neurons and observed spontaneous pearling of individual mitochondrial tubules under baseline action potentials, and cell-wide pearling during chemically-induced (50 mM KCl) action potentials (Supplementary Figure 1E, Supplementary Figure 2A-B, Movie 3). Second, frequent transient pearls formed at the immune synapses of both primary human CD8 T cells and Jurkat cells when conjugated with Raji cells pulsed with Staphylococcus enterotoxin E (SEE) (Supplementary

**Figure 2C-D, Movie 4-5**). These vastly different biological contexts support the ubiquitous and physiological nature of mitochondrial pearling.

Further resolving this temporal transition revealed a wide range of intermediate pearl shapes shared across many cell types (**Supplementary Figure 1A-H, Movie 6**), in some cases with different temporal dynamics. For example, in a U2OS cell treated with the complex III inhibitor rotenone (5µM for 30min), a spontaneous pearling event was observed across a 25 µm long tubule (**Supplementary Figure 1J and Movie 7**). One minute later, the same tubule underwent a second transition to the pearled state. However, in this second event an additional fused 20 µm long tubule synchronously pearled with the original tubule. This second tubule had remained cylindrical during the first observed pearling event. This suggests that pearling can propagate across physically coupled units of mitochondria.

Co-labeling the mitochondrial inner membrane and mitochondrial calcium (Mito-R-GECO1, 38) revealed that these spontaneous pearling events fall into two distinct classes of pearling events which occurred at similar frequencies. Class I included those preceded by a rise in calcium accompanied by shrinking of the tubule length (Figure 1H). Class II included those not preceded by a detectable increase in calcium uptake, but instead underwent elongation of the tubule (Figure 11). Close examination of Class II elongation events revealed the tips of the mitochondria appeared to be pulled into thin protrusions, 180-300 nm in width, projected outwards 1-6 µm (Movie 8), and tended to be followed by fission events, consistent with the literature 5. On the other hand, class I calcium-associated pearling events tended to shrink the mitochondria. such that all peripheral branches were rapidly compacted into a smaller area (Movie 9). These two classes can further be distinguished by tracking their structure and movement over time (Figure 1J), with class II elongation-associated pearling events recovering faster and maintaining a straight path throughout the event. It is worth noting there is a small subset of events that displayed both elongation and calcium uptake, but there were no observed events of shrinking without calcium uptake (Figure 1K-L). Additionally, the ratio of elongation-associated to calciumassociated event frequencies differed by cell type with the highest ratio in primary fibroblasts (8:2), followed by U2OS (7:4), and HEK (1:5) cells. Considering these observations in the context of the Rayleigh-Plateau instability, we hypothesized that these two classes of spontaneous events may reflect two different physical forces. We further hypothesize that class I involved changes to internal ionic pressure and class II involved external mechanical pulling. Each class is capable of increasing the energetic contribution of membrane tension until it exceeded the energetic contribution of bending elasticity, at which point the membrane transitions to the pearled shape to minimize its surface area.

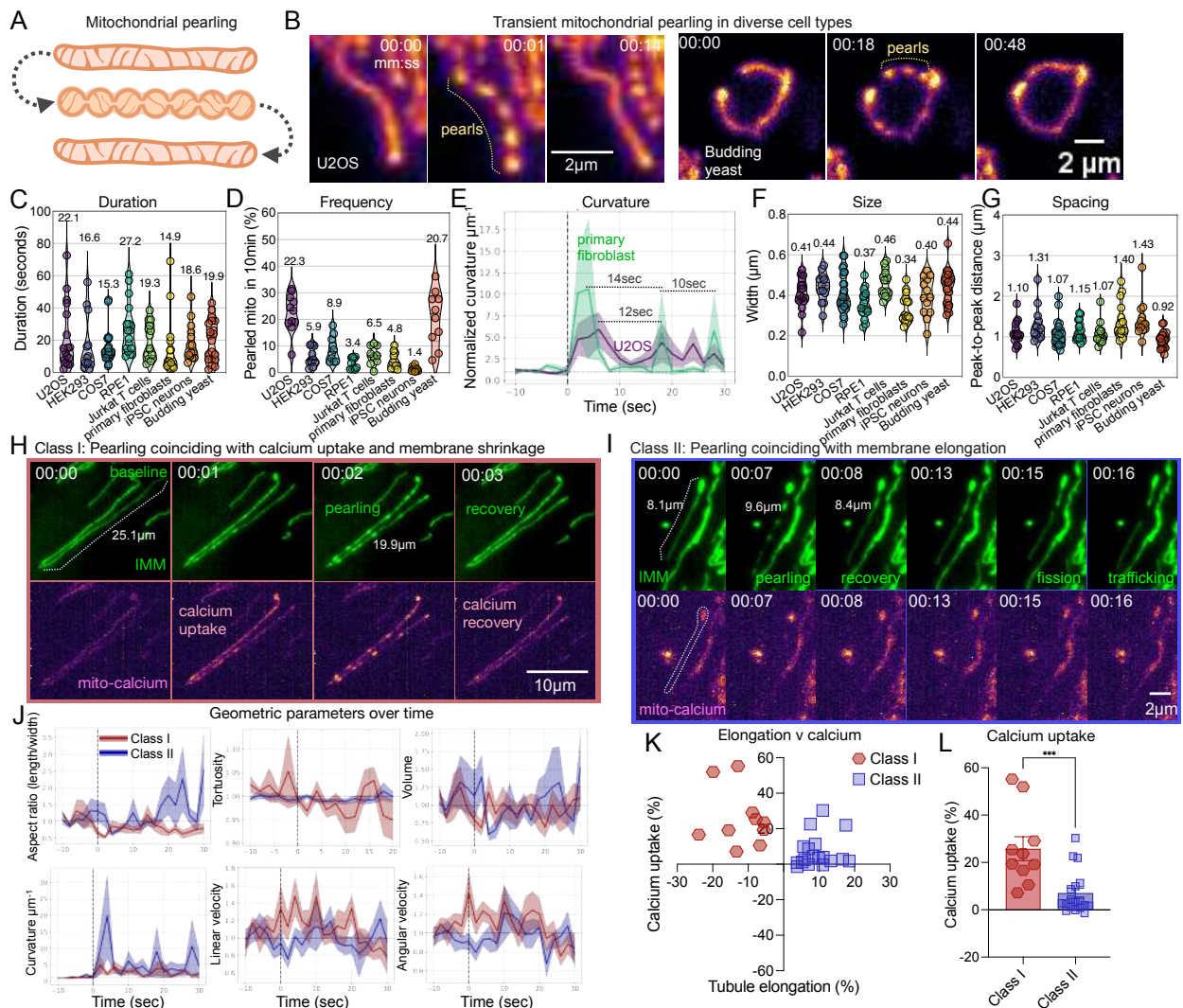


Figure 1. Spontaneous pearling is conserved and encompasses two distinct biophysical events. (A) Schematic of a transient mitochondrial pearling event. (B) Representative examples of transient pearling along the inner mitochondrial membrane of U2OS (COX8a-mEmerald), Jurkat T cells (COX8a-StayGold) and budding yeast (pre-COX4-mNeonGreen) (C) Duration of pearling transitions from uniform to pearl back to uniform transition amongst 8 different cell types (n= 13-25 events per cell type). (D) Rate of pearling events measured as the probability any mitochondria will pearl over a 10 minute period (n=10-11 videos per group). (E) Normalized curvature per µm across the length of mitochondrial tubule over time for primary fibroblasts (n=19 events) and U2OS cells (n=18 events). Each event is normalized to the average of the 3 initial timepoints. Dotted vertical line indicates the onset of pearling. (F-G) Mean cross-diameter width (F) and distance between the center of each neighboring pearl (G) for listed cell types (n=13-25 events per cell type). (H-I) Representative time series of tubule (G) shrinking and (H) elongation during a spontaneous pearling event in primary human fibroblasts co-labeled with the mitochondrial inner-membrane (COX8a-mStayGold) and mitochondrial calcium (genetically-encoded mito-R-GECO1). Dotted line indicates length of adjacent mitochondrial tubule. (J) Structural and dynamical metrics comparing pearls that undergo stretching (red) and shrinking (blue). All values normalized the average of the first three timepoints. Dotted line indicates the onset of pearling. Error bars = S.E.M. (K) Calcium uptake vs tubule elongation amongst spontaneous pearling events. Blue circles and red dots mark events under which elongation or shrinking occurred, respectively. (L) Comparison of calcium uptake between elongated and shrunk mitochondria during pearling. \*\* = p < 0.01 performed by non-parametric Mann-Whitney test. n = 10-20 events per group.

Osmotic pressure drives chemically-induced mitochondrial pearling

We next investigated the mechanism of class I pearling events characterized by ionic flux. The most likely source of internal pressure resulting from uptake of ions into the mitochondrial interior is osmotic pressure, whereby water molecules surge into the mitochondrial matrix. Osmotic shock is known to result in pressure-driven pearling instability in membrane tubes <sup>32</sup>. To confirm that internal pressure is capable of pearling mitochondria, we replicated the 1915 osmotic shock experiment of Margaret Lewis using repetitive media changes between hyper and hypoosmotic media. By replacing the cell medium (280 mOsm) with a hypotonic solution of 0.1x PBS (28 mOsm i.e. low-salt water) pearling was induced across the entire mitochondrial network (Movie 10). This was subsequently reversed by swapping media back to the original medium or a balanced salt solution of 1x PBS (280 mOsm) (Figure 2A-B, Supplementary Figure 3A). Additionally, swapping media with hypertonic solution of 10x PBS (2800 mOsm) resulted in the mitochondrial network becoming flaccid spaghetti-like cylinders with minimal movement (presumably from Brownian motion) (Movie 11). When the hyper-osmotic media was replaced with hypo-osmotic media, pearls appeared. Remarkably, repetition between these two conditions could convert the mitochondrial network between flaccid (hypertonic) to pearled (hypotonic) states up to five times until the cells detached from the cover glass (Supplementary Figure 3B, Movie 12). Surprisingly, a 20 second burst of hyperosmotic shock, followed by a return to normal media did not return mitochondria to baseline morphology, but instead resulted in cell wide pearling that took 10 minutes to recover back to a uniform state (Movie 13). Additionally, hypotonic induced pearling occurred even if the mitochondria were depolarized with the proton ionophore FCCP. though depolarized mitochondria did not recover baseline curvature after isotonic rescue (Supplementary Figure 3C, Movie 14). Under hypotonic shock, pearled mitochondria were accompanied by shrinking of the tubule length and an influx of calcium, which were reversed by a return to an isotonic environment (Supplementary Figure 3D-F). Class I spontaneous pearling events may therefore share a common mechanism with hypotonic shock induced by osmotic pressure.

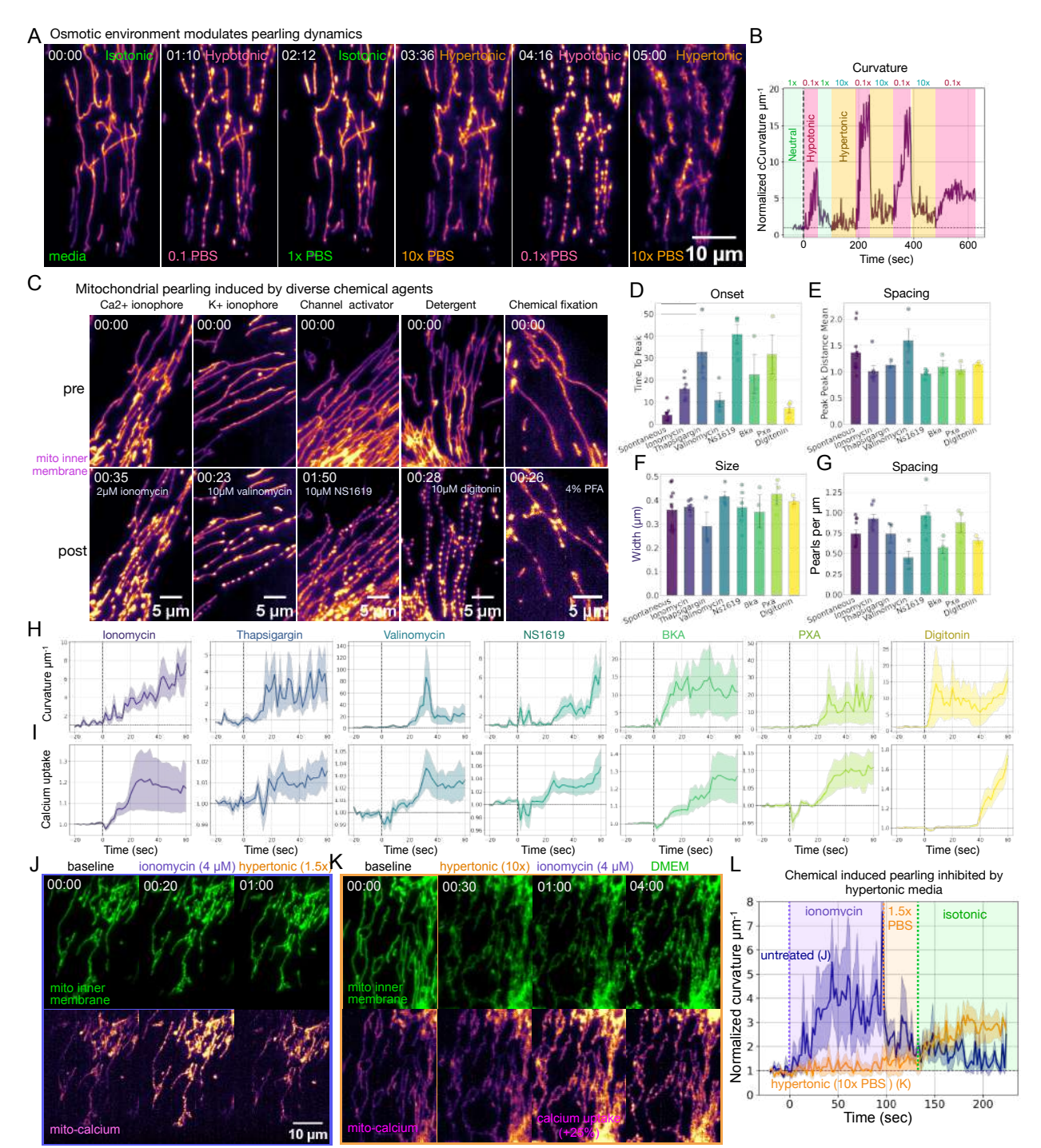


Figure 2. Osmotic pressure underpins chemically induced mitochondrial pearling (A) Osmotic shock of primary human fibroblasts. Media is repeatedly swapped between isotonic (DMEM), hypotonic (0.1x PBS) and hypertonic (10x PBS) conditions. (B) Quantifying pearling based on normalized curvature per  $\mu$ m over time during different osmotic shock regiments corresponding to (A). (C) Classes of chemical inducers of mitochondria pearling encompassing calcium and potassium ionophores, potassium channel activator (BKCa), membrane permeabilization, and chemical fixation. (D-G) Comparison of chemical agents along with spontaneous pearling of primary human fibroblasts for the (D) time to the peak of pearling curvature (E) the distance between the centers of neighboring pearls at the peak of pearling, (F) the cross-diameter width of pearls, and (G) the number of pearls per micron of tubule length before the onset of pearling. (H) Panel of mitochondrial curvature per  $\mu$ m normalized to first time points over time. Dotted line indicates the point of injection of the chemical agent. (J) Rescue of tubular morphology induced by ionomycin (2  $\mu$ m) by addition of 1.5x hyper-

osmotic PBS to the media. (**K**) Inhibition of ionomycin-induced pearling (2  $\mu$ M) by preconditioning the cell with hypertonic media (10x PBS). Three minutes after ionomycin addition, media is swapped back to untreated isotonic DMEM. (**L**) Intensity-based curvature per  $\mu$ m normalized to first time points over time for primary human fibroblasts without pre-treatment (blue) or placed in hypertonic 10x PBS (orange). Cells then underwent chemical-induction by  $4\mu$ M ionomycin and recovery by either 1.5x hypertonic solution or isotonic media. Vertical dotted lines indicate injection of  $4\mu$ M ionomycin (purple), injection of hypertonic 1.5x PBS (orange), or media swap to isotonic media (green). n=7 cells per group.

To determine whether there is a specific ion or channel regulating mitochondrial osmotic pressure, we performed perturbation experiments using several chemical agents capable of inducing mitochondrial pearling (Table 1, Supplementary Figure 4). Both calcium and potassium ionophores and channel activators induced cell-wide mitochondrial pearling within a minute of treatment (Figure 2C, Movie 15). To confirm that these agents were acting through their respective ionic species, we co-labeled cells with mitochondrial calcium marker Mito-R-Geco1. As expected, the calcium ionophore ionomycin, as well as thapsigargin, induced an uptake in mitochondrial calcium that preceded the onset of pearling. The potassium ionophore, valinomycin, and the BKCa channel activator, NS1619, caused cell-wide pearling that did not always accompany calcium uptake (Supplementary Figure 3H), suggesting multiple ion species can induce mitochondrial pearling.

Compounds with less direct ionic flux targets such as bonkeric acid (BKA), and phomoxanthone A (PXA) also caused cell-wide pearling. Interestingly, close examination of the intermediate time points of NS1619, BKA, PXA and valinomycin immediately before the formation of pearls, revealed that mitochondria tubules entered a flaccid shape identical to hyperosmotic shock (**Supplementary Figure 3G, Movie 16**). These compounds may have caused hyperosmotic pressure on mitochondria which later pearled when recovering back to isotonic balance.

In mammalian cells, the plasma membrane maintains a negative ionic differential of -50 to -70mV between the inside and outside of the cell by pumping out and sequestering positively charged ions like calcium and sodium. The membrane permeabilization agent, digitonin, resulted in the fastest onset of global pearling (**Figure 2D**, **right-most graph**, **Movie 17**) which can be explained as an increase in osmotic pressure as water followed the ionic gradient into the cell. Further, the widely used fixative paraformaldehyde (PFA, 4%), caused cell-wide pearling, consistent with earlier reports of it being osmotically active <sup>39</sup> (**Supplementary Figure 3I**, **Movie 18**). Pearl formation was inhibited by fixation with a combination of 3% PFA and >0.5% glutaraldehyde (GA), but this was cell type dependent. (**Supplementary Figure 3J**, **Movie 19**). This inhibition is likely due to the faster fixation rate of GA (see discussion). Other reported inducers of mitochondrial pearling not tested here include histamine, tunicamycin, A23187, and glutamate <sup>18,40–42</sup>. Direct comparison of pearl properties of these diverse chemical inducers with

spontaneous pearling events revealed similar width, peak-to-peak distances, and pearls per µm within the initial onset of pearl formation (**Figure 2D-G**). Further, all of these chemical agents led to a shrinking of tubule length (**Supplementary Figure 4C**), again reminiscent of Class I spontaneous events.

Confirming that all of these compounds were acting via osmotic pressure, the addition of 1.5x PBS (420 mOsm/L) into the media containing the chemical agent rescued pearled morphology (Figure 2J, Movie 20). Finally, and most importantly, when cells were placed in a hyperosmotic solution of 10x PBS (2800 mOsm/L) the calcium ionophore, ionomycin, still caused calcium uptake in mitochondria but tubules remained flaccid, without any visible pearling or rise in membrane curvature (Figure 2K-L, Movie 21). Only after removal of the hypertonic media did the mitochondria display pearling. This is direct evidence that osmotic pressure mediated the effect of ionic flux. This shared property amongst diverse chemical inducers of pearling indicated that it is unlikely that a single molecular ligand-binding mechanism can explain the shared dynamics of such experiments. Instead, osmotic pressure itself, being the common feature in all cases, is likely to be the driving force of these pearl events.

| Pearling inducer | Concentr<br>ation<br>(µM) | Time of onset (sec) | Known target                             | FCCP<br>dependent | Hyperosmotic recovery |
|------------------|---------------------------|---------------------|--|-------------------|-----------------------|
| ionomycin        | 2-20                      | 15-45               | calcium ionophore                        | no                | yes                   |
| thapsigargin     | 0.2-10                    | 20-50               | inhibitor of calcium ATPase (SERCA) pump | no                | yes                   |
| valinomycin      | 10                        | 20-50               | potassium ionophore                      | no                | yes                   |
| NS1619           | 10-30                     | 60-90               | BKCa channel activator                   | yes               | yes                   |
| PXA              | 10                        | 30-60               | fungal toxin                             | no                | yes                   |
| ВКА              | 10                        | 15-45               | ATP/ADP translocase and mPTP inhibitor   | no                | yes                   |
| digitonin        | 10                        | 5-35                | membrane permeabilization                | no                | yes                   |
| PFA              | 4%                        | 30-60               | fixative                                 | NA                | yes                   |

**Table 1: List of chemical agents that induce cell-wide mitochondrial pearling transitions.**NA indicates the combination was not tested or is not experimentally plausible.

Mitochondrial pearling can be induced with single-mitochondrion precision.

To experimentally manipulate pearling dynamics of individual mitochondria, we exposed cells to focused laser light (0.3 mW for 200 milliseconds) pinpointed to individual mitochondrial tubules (Figure 3A. This stimulation photobleached fluorophores within a <1 µm diameter (Supplementary Figure 5A), while inducing pearled morphology in all mitochondrial tubules connected to the tubule targeted by the laser, but not in unconnected tubules. In primary fibroblasts, with long and fused mitochondrial tubules, laser stimulation induced pearls as far as 140 µm away from the point of stimulation, again highlighting that connected components of mitochondrial network are biophysically coupled (Figure 3B, Movie 22). Stimulating a random selection of mitochondria tubules revealed that a subset of mitochondria would not respond to the stimulation at all, including in some cases all mitochondria of some cells. In the reverse case, cells with fully fused mitochondrial networks would pearl simultaneously across the entire cell, despite stimulation of a small fraction of an individual mitochondrial branch in the cell (Figure 3C, Movie 23). Reminiscent of spontaneous pearling events, laser-induced pearls recovered a cylindrical morphology on average 15 seconds post laser stimulation (Figure 3D). However, stimulated tubules that recovered back to baseline did on occasion revert back to a pearl morphology within 60 seconds post-stimulation (Supplementary Figure 5B, Movie 24). Additionally, pearls induced by laser stimulation tended to have farther peak-to-peak distances than spontaneous events, but otherwise maintained similar pearl structure and dynamics to spontaneous events (Figure 3E). Colabeling with Mito-R-GECO1 revealed a rise in mitochondrial calcium uptake that sometimes preceded the onset of pearls (Supplementary Figure 5D, Movie 25). Further, these pearling events were all marked by retraction of branching tubules that were stimulated, suggesting a shared mechanism to class I spontaneous pearling events that underwent calcium uptake and shrinkage (Figure 3F). Like chemical inducers of pearling, laser stimulation did not pearl mitochondria when cells were placed in hypertonic media (Figure 3D), suggesting osmotic pressure is also the downstream driver of pearling resulting from laserstimulation.

Next, we sought to confirm that pearls maintained matrix connection during pearl formation by using a FRAP laser to deplete the fluorophores of individual pearls and track fluorophore recovery (**Figure 3G**). Recovery time of fluorescence within depleted pearls of spontaneous and laser-induced pearls took 9.6 seconds and 7.1 seconds, respectively (p = 0.98), (**Figure 3H-I**). The majority (>70%) of pearls recovered from depletion, indicating that most pearled mitochondria maintain matrix flow between connected inner membranes. The few events that did not recover were all located at the tips of mitochondrial tubules, had independent movements from the adjacent tubule, and therefore likely underwent complete fragmentation during the pearling event.

To uncover what properties regulate mitochondrial pearling, we applied a series of functional markers and chemical inhibitors and then induced pearling with laser stimulation (**Methods Tables 4-5**). Like other inducers of pearling, depolarizing mitochondria with FCCP reduced pearl formation after laser stimulation by 94% (**Figure 3J, Movie 26**). Similarly, inhibiting electron transport chain (ETC) complex I, III, and V with rotenone, antimycin A, or oligomycin, mitigated pearl curvature by 76%, 79%, and 59% respectively. Note, that these ETC inhibitors independently raised baseline curvature by 2-fold before laser stimulation (i.e. caused partial pearl formation) (**Supplementary Figure 5C**). Overall, depolarization with FCCP had the most dramatic reduction in formation of pearls by laser stimulation. Interestingly, while untreated cells took on average 10 seconds to recover back to a uniform morphology, oligomycin-treated cells delayed recovery to 35 seconds (p<0.01). This may be because inhibiting the ATP synthase causes mild hyperpolarization on the inner membrane <sup>43</sup>, or due to off-target effects on actin polymerization

Similar to oligomycin, laser stimulation of mitochondrial tubules following depolymerization of the actin cytoskeleton with latrunculin B, resulted in a permanent transition to pearl morphology that could not recover back to the cylindrical shape (**Figure 3K, Movie 27**). These pearls often would progressively accumulate into larger pearls as was seen in the downstream chemically-induced pearls. In contrast, with microtubule polymerization inhibited, pearls had reduced curvature by ~10% and recovered back to the baseline state 10 seconds faster than controls. Further, the microtubule stabilizing agent, taxol, mimicked the behavior of latrunculin B, whereby pearled mitochondria did not recover back to a uniform morphology. Taken together, these inhibitors reveal that both electron transport chain activity as well as cytoskeleton structure influence pearling dynamics.

Colabeling with the membrane potential marker, TMRE, revealed that the IMM depolarized after the onset of pearling and recovered back to baseline after 70% of laser-induced pearling events (**Figure 3L-M**, **Movie 28**). This recovery often occurred on only specific portions of the original tubule that had separated during pearl formation. As previously reported, pearl shapes recovered back to a cylindrical shape faster than the recovery of membrane potential (**Figure 3N**) <sup>15</sup>. Interestingly, membrane potential recovery was necessary for a second induction of pearling on the same tubule by laser stimulation. Overall, laser-induced pearling matched the behavior of DRP1-KO pearls <sup>15</sup>, in that both were supported by electron transport chain activity and resulted in transient depolarization of the inner membrane.

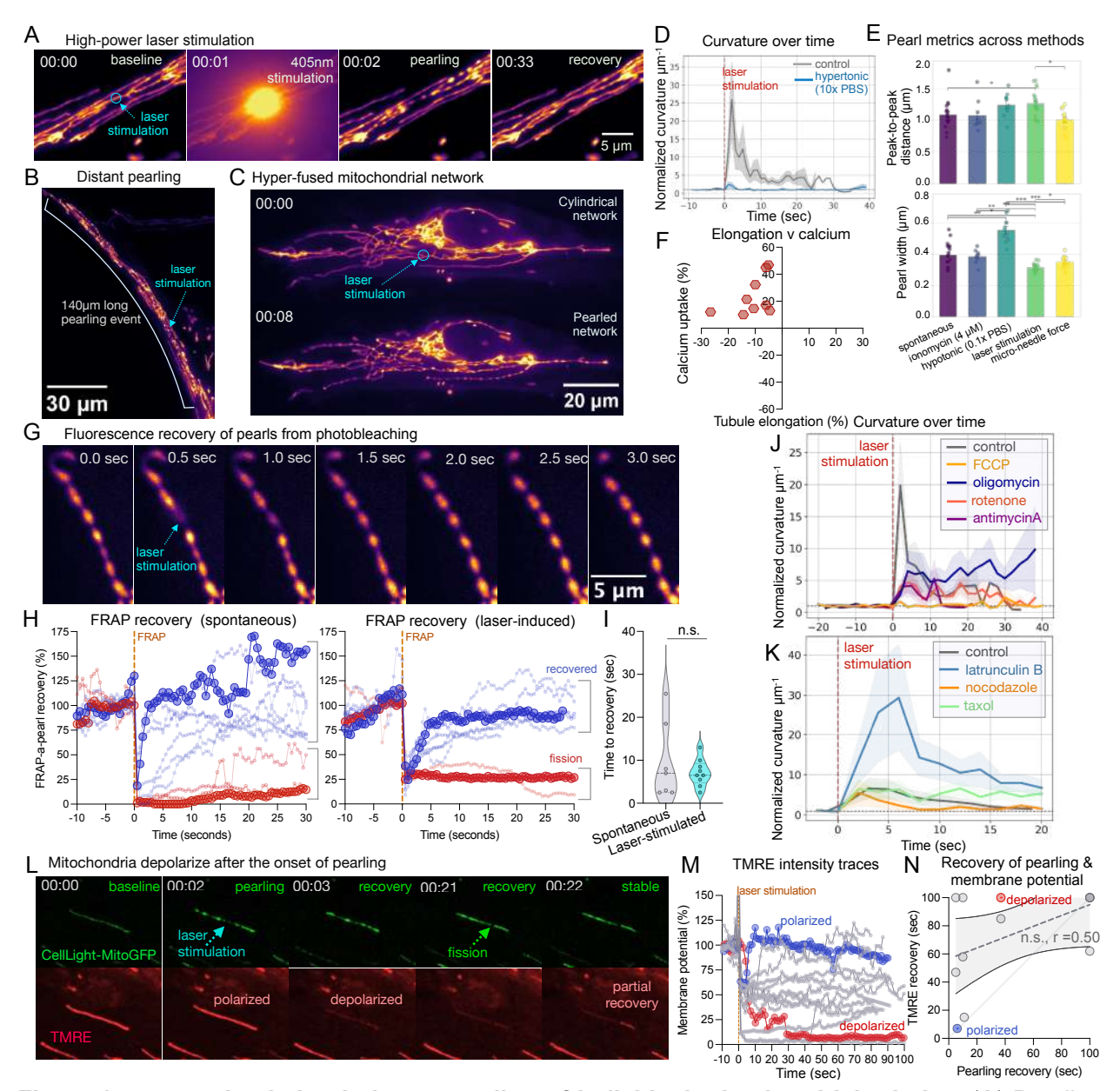


Figure 3. Laser stimulation induces pearling of individual mitochondrial tubules. (A) Pearling induced on primary fibroblast by a pinpointed 405nm stimulation laser. The 405 nm laser was fired at 20mW (0.3mW reaching sample) for 200 milliseconds pointed directly on the mitochondrial tubule (blue arrow). (B) Primary fibroblast with elongated mitochondria tubule pearled by laser stimulation. (C) Hyper-fused mitochondrial network of a primary fibroblasts before and after laser stimulation to a region marked by a blue circle. (D) Curvature per µm over time for laser stimulated untreated cells (n=22, gray) and cells placed in 10X PBS (n=15, blue). (E) Comparison of peak-to-peak distance between pearls and pearl width (minor-axis) amongst different methods to induce mitochondrial pearling. One-way anova model used. \* = p < 0.05, \*\* = p < 0.01, \*\*\* = p < 0.001. (F) Scatter plot of calcium uptake vs tubule elongation amongst laser-stimulated pearling events. Red dots mark events under which shrinking occurred. n = 10 events. (G) Spontaneous mitochondrial pearls depleted with laser and fluorescence recovery tracked over time. (H) Fluorescence recovery after photobleaching of individual pearls of spontaneous and laser stimulated pearling events (n = 10 events/group). Each line indicates an individual event. Blue indicates recovery, while red indicates minimal recovery. (I) Comparison of FRAP recovery times between different methods of induction, Mann-Whitney nonparametric t-test. (J) Curvature per unit µm comparing electron transport chain inhibitors, n=21 oligomycin (1 uM) events, n=18 FCCP (4 µM) events, n=18 rotenone (5 uM) events, n=18 antimycin

A (5 uM) events. Red dotted line indicates the point of laser stimulation. All data normalized to the average of the first five timepoints for each treatment group. (**K**) Curvature per  $\mu$ m over time for laser stimulated untreated cells, latrunculin B (1  $\mu$ M), nocodazole (200 nM), and taxol (100 nM) (n=8-10 events per treatment). Data normalized to the first three timepoints of each treatment group. (**L**) Representative time series of membrane potential collapse and recovery after laser-stimulated pearling. CellLight MitoGFP labels the IMM and mitochondrial matrix. TMRE labels mitochondrial membrane potential. (**M**) Normalized TMRE intensity over time. Each line indicates an individual event. Blue indicates an event that recovered back to baseline intensity. Red indicates an event which does not recovery within the duration of imaging. (**N**) Spearman correlation between time for pearls to recovery back to cylindrical shape and time of TMRE signal to return to stable signal. Red and blue dots match individual events highlighted in (M). Faded gray line indicates an ideal correlation of 1.0. Dotted line indicates linear regression with 95% confidence lines.

#### Endogenous fluorescence predicts pearling response to laser stimulation

Dim-emission detection of the 488-525 nm channel revealed an endogenous fluorescent signal coming from mitochondrial inner matrix that accumulated after the onset of both spontaneous and laser-stimulated pearling events (**Supplementary Figure 6A-B, Movies 29-30**). This endogenous molecule that fluoresces in the green channel accumulates in the mitochondrial matrix after pearling occurs and sometimes recovers. This autofluorescent signal was amplified by depolarization with FCCP (4 μM) or cholesterol depletion by atorvastatin (50 μM) (**Supplementary Figure 6C**). The identity of the endogenous fluorophore could be the endogenous metabolite FAD and NAD/H, whose autofluorescent properties have been widely reported <sup>45–47</sup>. Whatever its identity, this fluorescence predicted whether an individual mitochondrial tubule would pearl from laser stimulation (**Supplementary Figure 6D**).

#### STED reveals swollen cristae ultrastructure in mitochondrial pearls

Using super-resolution STED imaging, we then characterized mitochondrial cristae ultrastructure of pearls. The cristae of laser-induced pearls (class I) under STED had a similar structure to the helicoidal ramp structures to the Mic60 complex maintaining crista junctions <sup>48,49</sup> (**Figure 4A, Movie 31**). Comparison of mitochondrial size before and after laser stimulation under STED confirmed an 20.4% increase in cross-sectional area and 70.7% increase in inter-cristae distance at the onset of laser-induced pearling (**Figure 4B-C**). Optical sectioning at STED resolution revealed 3D pearled mitochondria with swollen regions containing nucleoids at the center of most pearls and continuous inner membrane between pearls (**Figure 4D-E**).

To investigate a potential functional role of cristae organization in pearling we targeted the cristae junction complex, MICOS, and generated Mic60 knockout cells in budding yeast with the inner mitochondrial membrane protein TIM50 labeled with the fluorophore mNeonGreen. Pearling was induced with laser stimulation (**Figure 4F, Movie 32**). The resulting pearling events showed more homogeneously spaced pearls with 21% reduction of inter-pearl distance (p<0.001) and a 50% reduction in pearl volume (p<0.01) (**Figure 4G-H**). This suggested that the MICOS complex

influenced the shapes of pearls through its architectural support to the mitochondrial tubule, but is not itself required for pearl formation <sup>5</sup>.

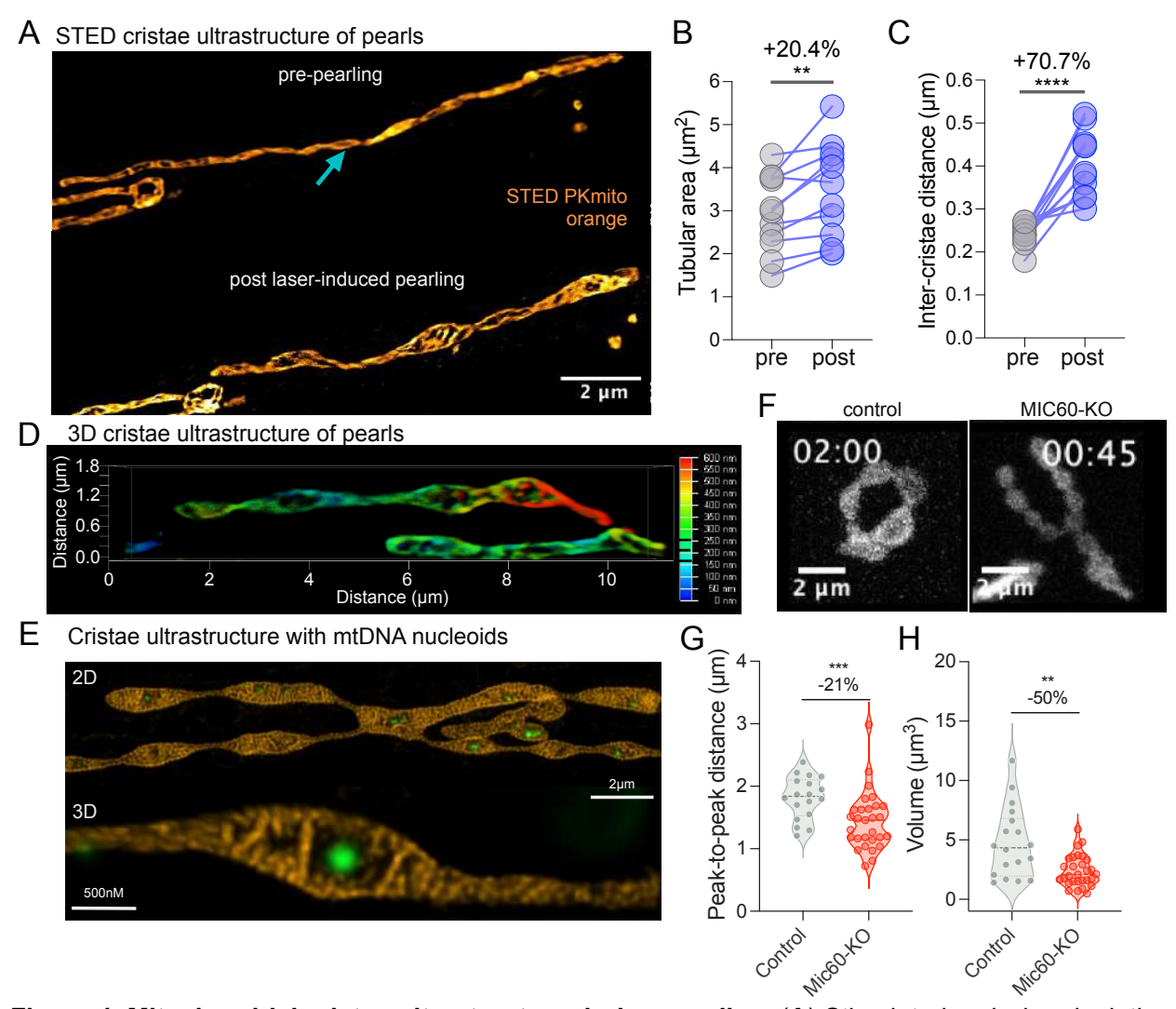


**Figure 4. Mitochondrial cristae ultrastructure during pearling.** (**A**) Stimulated emission depletion (STED) microscopy of mitochondrial cristae labelled with PKmito Orange dye, before and after laser stimulation of mitochondrial tubule. Two-way anova, \*\* = p < 0.01. (**B**) Comparison of tubular area before and after laser-induced pearling. n=11 mitochondria. (**C**) Inter-cristae distance before and after laser-induced pearling. n=11 mitochondria. Two-way anova, \*\*\*\* = p < 0.0001. (**D**) Cristae architecture in 3-dimensions using tauSTED. Depth-encoded color mapping. (**E**) Deconvolved STED imaging of mitochondrial inner membrane (orange, MitoOrange) along with mitochondrial DNA (green, Sybr Gold) during laser-induced pearling event. An example 2D image is shown in the top panel and a separate 3D image in the bottom panel. (**F**) Laser-induced pearling of budding yeast labelled with TIM50 mNeon-green (inner membrane) in wild-type and MIC60-knockout cells. Pearling induced by a 405nm stimulation laser at 0.3mW for 200 ms. (**G**) Distance between centers of neighboring pearls, and (**G**) the pearl volume amongst laser-induced pearling of mitochondria in wildtype (n=20 events) and MIC60-KO yeast (n=25 events).

Mitochondrial membrane elasticity regulates pearling dynamics

The molecules that compose the mitochondrial membrane influence the elastic properties of the tubule (**Figure 5A**), and thus we sought to investigate the consequences of their modulation

to laser-induced pearling. These molecules include cholesterol, cardiolipin, and the MICOS complex. Depleting cholesterol with the statin atorvastatin (24hr of 50uM) resulted in mitochondria that did not pearl in response to laser-stimulation (Figure 5B-C). Without sufficient cholesterol content the mitochondrial membrane may have been too elastic to hold tension and undergo a pearling transition. On the other hand, knockout of the MICOS complex genes, MIC10, MIC12, MIC60 all increased the frequency of spontaneous pearling events by 6.9 to 8.4% (p<0.01) (Figure 5D). We suspect that disruption of cristae lamella folding decreases the membrane's exceptionally high bending modulus, and thereby basal levels of tension more easily exceed its elasticity and cross the pearling instability. We further tested the removal of the cardiolipin synthesis gene, TAZ1, or CRD1. Cardiolipin is a unique lipid of the IMM and supports cristae invaginations in the inner membrane <sup>50</sup>. However, knockout of TAZ1 and CRD1 did not show a statistically significant increase in the frequency of spontaneous pearling events with a +2.813% and -1.5% change compared to wildtype, respectively. We attempted to measure mitochondrial membrane tension with the membrane intercalating dye, Mito Flipper-TR (1 µM), a reporter of mitochondrial membrane tension (Goujon et al. 2019). Although we were unable to capture a consistent fluorescence lifetime shift in membrane tension during pearling, we were surprised to see that even mild exposure to confocal laser light to cells labelled with Mito-Flipper-TR caused cell-wide mitochondrial pearling (Figure 5E-F, Movie 33). We speculate that similar to the presence of cholesterol, membrane intercalating dyes stiffened the IMM, resulting in an increased rate of pearling. We next ruled out other potential mechanistic explanations of spontaneous pearling including fission proteins, ER constrictions, actin or microtubule polymerization, ROS generation, and mtDNA presence.

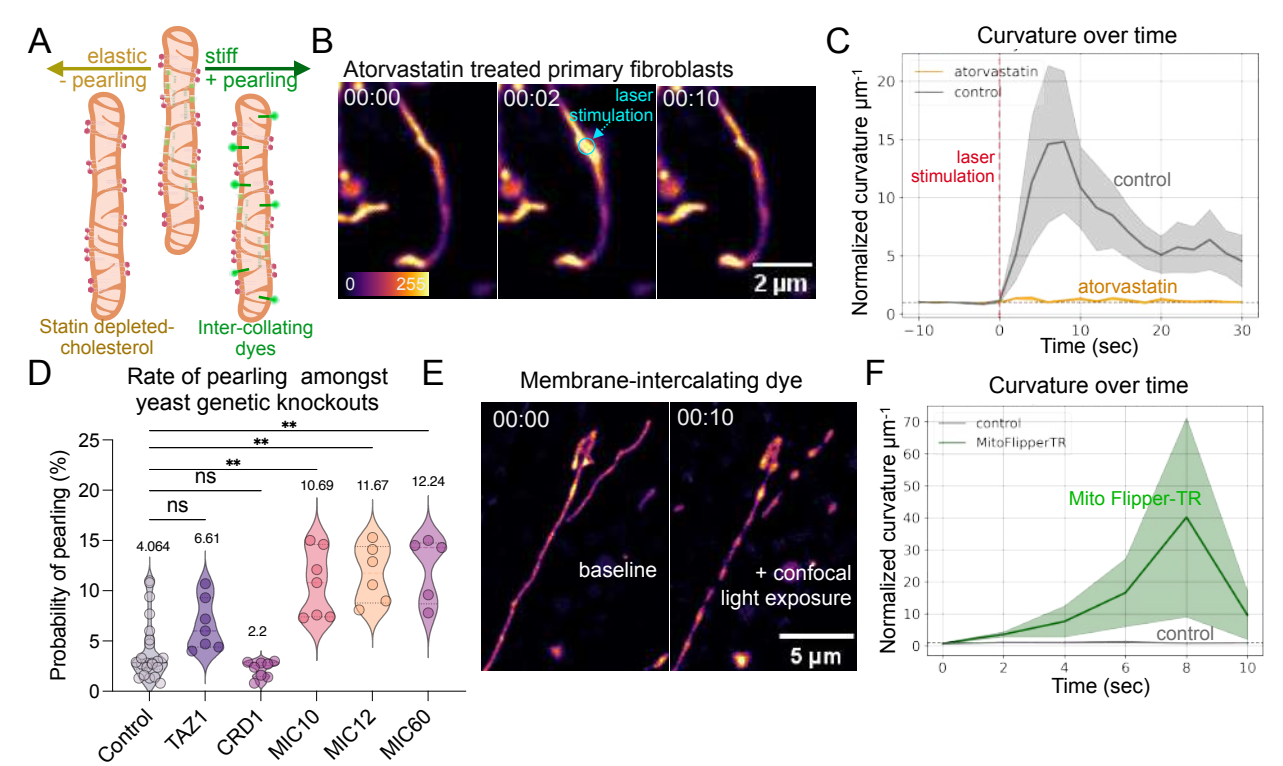


Figure 5. Altering mitochondrial membrane elasticity regulates pearling dynamics. (A) Schematic of how membrane content affects the biophysical properties of the mitochondria and influence its likelihood to pearl. (B) Mitochondria of a primary fibroblast treated overnight with 50  $\mu$ M atorvastatin before and after 405nm laser stimulation (blue circle). Cells are labelled with PKmito Orange. (C) Time series of the membrane curvature along the mitochondrial tubule of control (n=11) and overnight atorvastatin-treated (24hr of 50 $\mu$ M, n=13) primary human fibroblasts. (D) Probability of a pearling occurring in a yeast cell over 100 volumes of imaging for wild-type, and genetic knockouts of TAZ1 & CRD1 (cardiolipin synthesis), and MIC10, MIC12, MIC19, MIC26, MIC27, and MIC60 (MICOS complex). Non-parametric Kruskal-Wallis test performed. \*\* = p < 0.01. (E) Images of mitochondria labelled with the intercalating membrane dye, Mito Flipper-TR (1  $\mu$ M), before and after exposure to confocal laser light. Note: no stimulation laser was fired, rather just the field of view was illuminated to image the cell. (F) Time series of the membrane curvature along the mitochondrial tubule of control (n=9) and cells dyed with Mito-Flipper-TR (15-60 minutes 1  $\mu$ M, n=10) primary human fibroblasts.

#### Alternative mechanisms of mitochondrial pearling

Other potential mechanisms of mitochondrial pearling include dynamin-like fission machinery, ER constriction events, ROS oxidative stress, actin waves, and mtDNA nucleoid colocalization. In regard to the idea that DRP1 constrictions create the pearls, several studies reported increased pearling when DRP1 and related fission machinery was removed <sup>5,15,16</sup>, clearly showing that DRP1 mediated fission is not required. Regarding the idea that ER rings squeeze the mitochondrion into pearls, we colabelled ER and mitochondrial networks and saw ER network structures often did not form ring shapes around pearl constriction points (**Figure 6A-C, Movies 34-37**), with 25% of mitochondrial pearl constriction points forming without any nearby ER signal labeled with KDEL and calreticulin probes (**Figure 6D**).

To rule out the possibility of phototoxic initiation of pearling events we examined the distribution of pearling events across all cell types (**Figure 6E**). We did not see any increase of pearling events with time, and additionally observed 9 events at the first volume of imaging showing that pearls were already formed in the absence of illumination (**Figure 6G**). Regarding the idea that ROS-related oxidative stress drives pearling, treatments of cells with antioxidants mitoTEMPO (20 nM) and N-acetyl cysteine (NAC, 5 µM) failed to inhibit the induction of pearling by laser stimulation (**Figure 6F**). Additionally, co-labeling with the mitochondrial-specific ROS markers, MitoSOX green and MitoSOX, red did not increase at the onset of laser-stimulated pearling, with a change in +0.4% and -1.2%, respectively (**Supplementary Figure 5E**). Mitochondrial intermembrane ROS sensor, Hyper7 did increase by 18.3% directly after laser-stimulation but this increase occurred across the all mitochondria of the cell, and was not specific to tubules that underwent pearling (**Supplementary Figure 5F-H, Movie 38**).

Colabeling with a microtubule marker, Sir-Tubulin, revealed that microtubule structure remains intact during laser induced pearling (**Figure 6H**). Further, treatment with microtubule depolymerization with 10  $\mu$ M nocodazole did not stop the induction of pearling by laser-stimulation (Figure 3K) or by chemical-induction with 4  $\mu$ M ionomycin (**Supplementary Figure 5I**). Regarding the idea that actin mediated forces drive pearling, actin depolymerization did not stop spontaneous pearling events (**Figure 6I**) or pearling induced by 4  $\mu$ M ionomycin (**Supplementary Figure 5J**). Instead, the lack of actin inhibits pearls from recovering back to the tubule form (Figure 3K).

Another explanation of pearls could be a reorganization of mtDNA nucleoids to discrete spheres marking membrane pearls. In U2OS cells, 77% of pearls marked by the mitochondrial inner membrane colocalized with mtDNA nucleoids, while in primary fibroblasts only 20% of pearls colocalized with nucleoids (**Figure 6J-L**). Further depletion of mtDNA with ethidium bromide did not stop the induction of pearling by laser-stimulation (**Figure 6K-L**). This ruled out the possibility that pearl shapes on the membrane were downstream of nucleoid structures.

Given the inability of these molecular mechanisms to account for the pearling that we observed, we instead turned to a biophysical mechanism, whereby ionic flux and tension forces within the cell can explain the onset spontaneous pearling that coincides with either class I calcium waves passing across cells and amplified by many different experimental contexts <sup>40,51–53</sup> or class II molecular motors pulling on the mitochondrial membrane <sup>54,55</sup>. These forces could be the source of osmotic pressure and mechanical tension on the mitochondrial tubule that cause spontaneous pearling events.

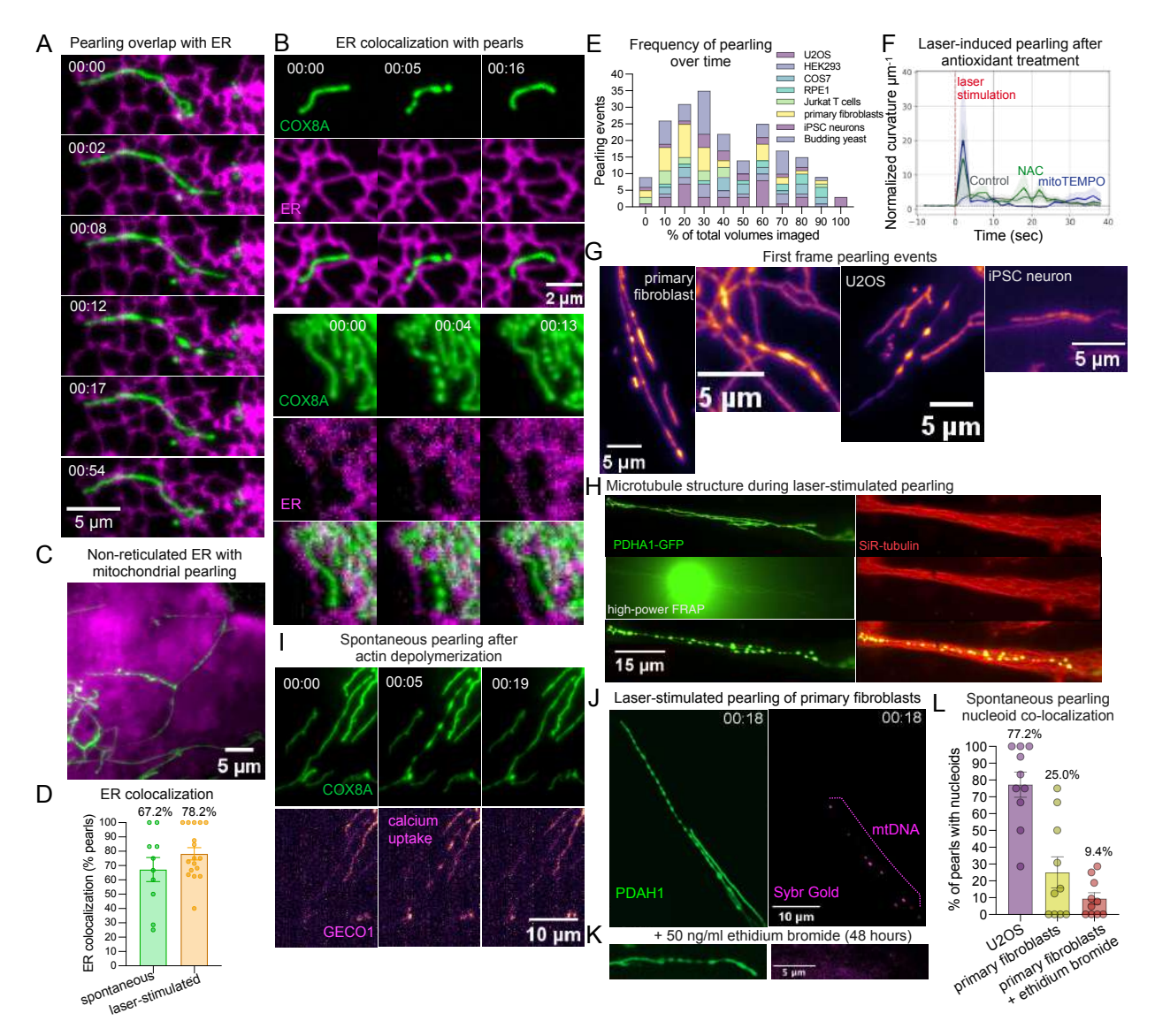


Figure 6. ER constrictions, oxidative stress, microtubule organization, actin polymerization, and nucleoid localization fail to regulate mitochondrial pearling dynamics (A-B) Spontaneous pearling events with both mitochondria (COX8A-mEmerald) and ER (KDEL, CellLight-ER-RFP) labelled in U2OS cells. (C) A cloudy ER network surrounding mitochondrial pearls in a U2OS cell. Mitochondria (COX8A-mEmerald) and ER (KDEL, CellLight-ER-RFP) labelled. (D) Percentage of pearl constriction points with or without overlapping ER fluorescence signal from both U2OS and primary fibroblasts either from spontaneous events (green, n=10 events) or laser-induction (orange, n=17 events). (E) Frequency distribution of the frame at which a pearling event was first observed normalized to the total number of frames (i.e. 3D volumes) taken in a video. (F) Mean curvature per µm over time for primary fibroblasts treated with antioxidants 5 µM NAC and 20 nM mitoTEMPO (n=10-14 events per treatment group). Red line indicates point of laser stimulation. (G) Mitochondrial pearls imaged in the first frame of a timelapse video. (H) Laser-induced pearling with both the mitochondrial inner membrane (green, CellLight MitoGFP) and microtubules (red, Sir-tubulin) labelled. (I) A spontaneous pearling event observed in U2OS cells treated with 1 µM latrunculin B for 1 hr. Top panel contains the mitochondrial inner membrane (COX8A-mStayGold) and the bottom panel contains mitochondrial calcium (Mito-R-GECO1). (J) Mitochondrial pearls overlapping with mtDNA (Sybr Gold) induced by laser-stimulation of a primary fibroblast mitochondria in (I) untreated, and (K) DNA intercalating ethidium bromide (50 ng/mL) for 48 hours. IMM = CellLight MitoGFP, mtDNA = Sybr Gold. (L) Quantification of the number of pearls with overlapping mtDNA signal for U2OS cells (purple),

primary fibroblasts (yellow) and primary fibroblasts treated with 50 ng/ml ethidium bromide for 48 hours. n=10 events per group.

Micro-needle manipulation induces mechanical force-based pearling on individual mitochondria tubules.

The chemical and laser induction of pearling described above can all be explained by the influx of ions resulting in mitochondrial shrinkage, swelling, and osmotic pressure. An alternative mechanism for pearling via the Rayleigh-Plateau instability could involve mechanical forces pulling on the membrane such as class II stretching-associated spontaneous pearling events observed above. To test this idea, mechanical forces were applied to individual mitochondrial tubules within the cell using a fluorescently-labeled glass microneedle with a triple axis (X,Y,Z) 56 nm step-motor (Figure 7A)<sup>56</sup>. Bringing the micro-needle within a micron of the mitochondrial tubule induced a rapid and transient pearling transition on the specific mitochondria of choice (Figure 7B, Movie 39). Like laser-induced pearling, depolarizing the mitochondria with the proton ionophore FCCP inhibited the ability of needle force to convert tubules to pearls (Figure 7E. Movie 40). Attempting to further manipulate the tubule by pulling the depolarized tubule largely resulted in cutting (i.e. mechanical fission) at the point of needle manipulation. Regardless of whether the mitochondria were polarized or not, the insertion of the needle into the cell often induced a rise in cell-wide mitochondrial calcium uptake, which was quickly followed by mitochondrial pearling across the entire cell (Figure 7C-D, Movie 41). These global pearling events may be a result of actin waves caused by the introduction of the needle in the cell. Previous work has shown the calcium ionophore, ionomycin, induces actin waves followed by calcium uptake into the mitochondria and an increase the rate of pearling events <sup>18</sup>.

To overcome the needle's tendency to cause global pearling, the actin polymerization inhibitor, Latrunculin B, was applied (1 µM for 30-60 minutes). In actin inhibited cells, manipulated mitochondria tubules were more likely to undergo localized pearling at the targeted mitochondria, while non-manipulated remained stably cylindrical (**Figure 7C-D**) and calcium uptake remained low in non-manipulated mitochondria (**Figure 7G**). This further dispels the idea that actin is itself the constrictive actor that forms mitochondrial pearls. Remarkably, with actin inhibited, the needle could pull on the mitochondrial strand resulting in a transition to a pearled morphology specifically on the portion of the tubule undergoing deformation (**Figure 7H, Movie 42**). Further, in some cases this same force-induced pearling preceded a rise in calcium uptake by the mitochondria (**Supplementary Figure 7, Movie 43**). These experiments highlight a scenario in which calcium on its own was not sufficient to induce pearling. Rather, only with an added mechanical force on the membrane was a pearling instability reached. Thus, both the internal osmotic pressure of ionic flux as well as external mechanical tension of the membrane can result in a pearling instability across the mitochondrial tubule.

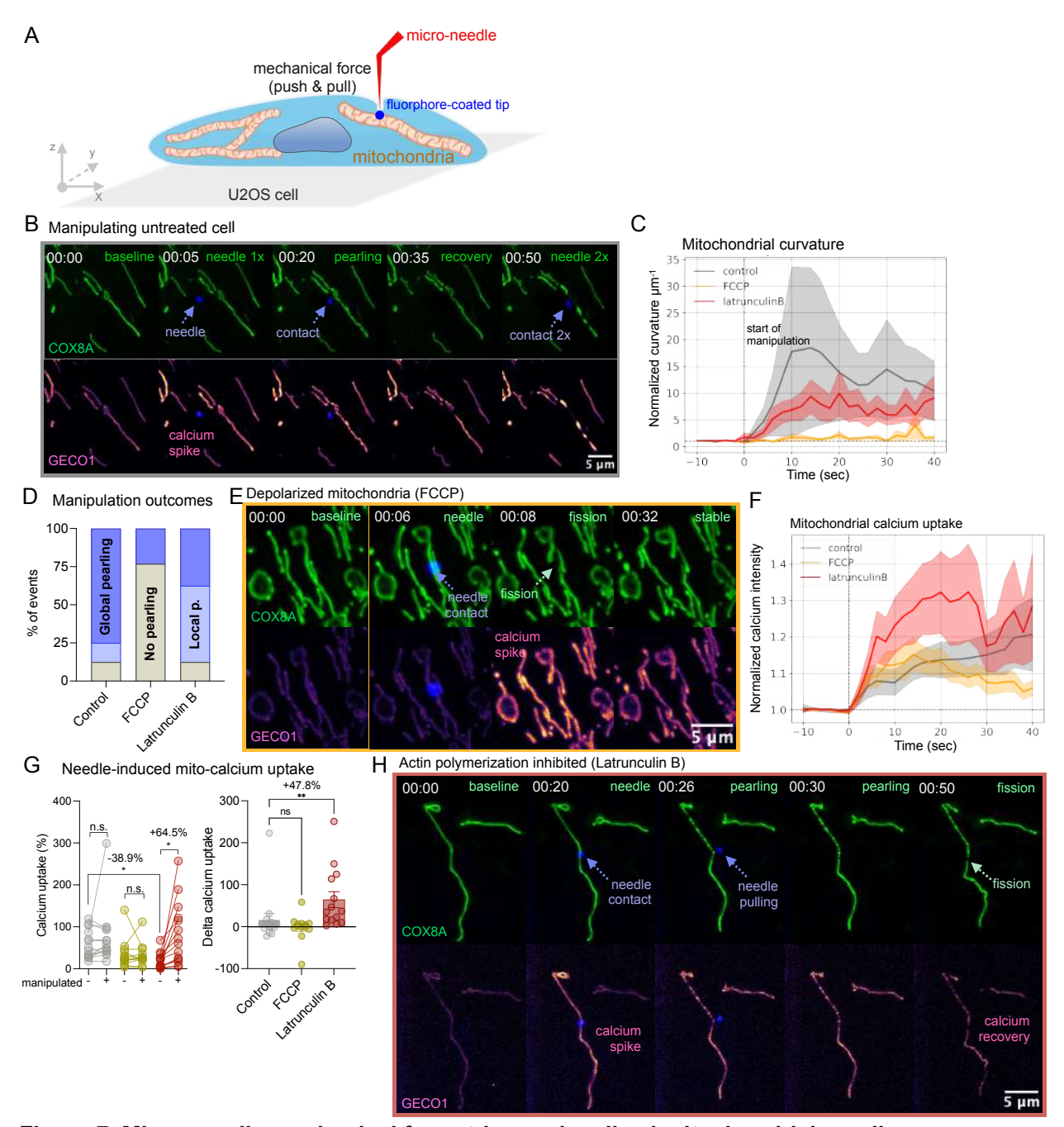


Figure 7. Micro-needle mechanical force triggers localized mitochondrial pearling.

(A) Schematic of micro-needle experimental design. Red needle is manipulated in x, y, z dimensions with a 56 nm step-size control. The tip is coated with fluorescent pigment (far-red channel, labeled dark-blue in figure). Pico-nano newton forces are then applied to individual mitochondrial tubules with push and pull forces. (B) Representative time series of untreated U2OS cell mitochondria manipulated with micro-needle. Mitochondrial inner membrane labeled with COX8A-mStayGold (green). Mitochondrial calcium flux labeled with Mito-R-GECO1 (red). Needle was pushed against tubule before being removed from the cell and then reapplied for a repeated manipulation of the same tubule. (C) Curvature over time for single mitochondria tubules manipulated with micro-needle in untreated controls (n=14 cells), FCCP (10μM, 10-60 minutes, n=13 cells) and Latrunculin B (10μM, 30-60 minutes, n=16 cells). Thick lines represent mean weighted curvature per μm normalized to the first 3 timepoints before manipulation. Error bars indicate standard error of the mean. Dotted vertical line indicates the beginning of needle manipulation on the tubule. Curvature values are weighed per μm of distance and normalized to the mean of the first three pre-pearl timepoints. (D) Categorical outcome

from attempted micro-needle manipulation of mitochondria. No pearling (gray) indicates that curvature of all mitochondria tubules remained stable throughout the experiment. Local pearling (light-blue) indicates pearling was uniquely induced on the tubule targeted by the needle. Global pearling (dark-blue) indicates that all other tubules in the cell underwent pearling whether or not it was targeted by the micro-needle. 13-16 cells per treatment group. (**E**) Representative time series of U2OS cell mitochondria depolarized with  $10\mu M$  FCCP for 30 minutes and manipulated with micro-needle. (**G**) Calcium uptake derived from Mito-R-GECO1 maximum intensity values after the needle is present in the cell for non-manipulated (-) and manipulated (+) mitochondria. Right-panel shows delta calcium uptake between the mitochondria manipulated by the needle and those untouched. (**H**) Representative time series of manipulated mitochondria from a U2OS cell with actin polymerization inhibited by  $10\mu M$  Latrunculin B for 45 minutes.

## Discussion

#### Mechanism of pearling induction

Our biophysical model of mitochondrial pearling describes the organelle as a network with electrically coupled membranes under tension that exists near a critical threshold of instability. Under sufficient tension these tubules collapse and reorganize into thinly connected spherical units. This instability is regularly crossed due to changes in three physical forces. First, the internal osmotic pressure resulting from the ionic flux of cations entering the mitochondrial matrix. Second, from changes to elasticity of the membrane such as addition of cholesterol or removal of cristae junctions. Third, from external forces pulling on the membrane. Ultimately, all three forces can result in the membrane tension surpassing its bending energy (**Figure 8**). This biophysical mechanism unifies mitochondrial pearling events observed in diverse chemical, physical, and genetic, and physiological scenarios (**Supplementary Figure 8**). In physiological scenarios such as neuronal action potentials, and T cell synapse formation, pearling is likely a result of ionic flux, which results in an influx of water molecules, matrix swelling, and osmotic pressure on the inner membrane thereby collapsing the mitochondrial tubule into pearls.

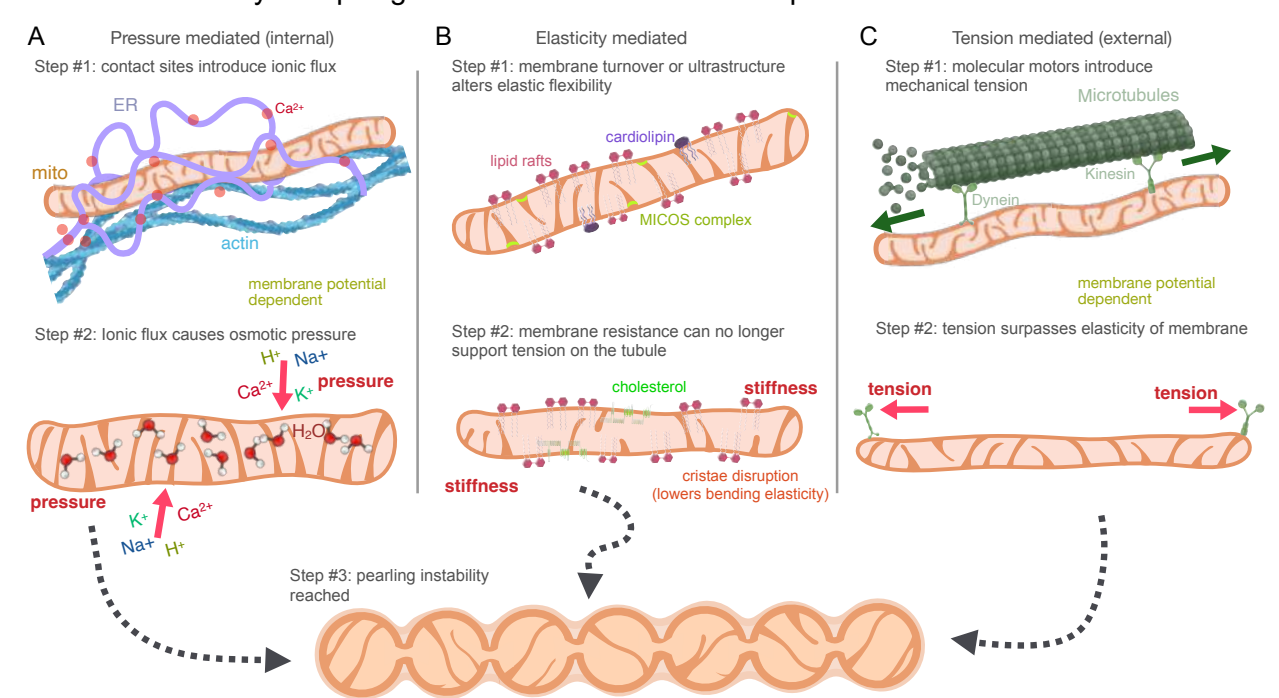


Figure 8. Biophysical mechanism of mitochondrial pearling dynamics. (A-C) Pressure, tension, and elasticity are the three main physical properties that influence the pearling instability of the mitochondria membrane. (A) Contact sites with other organelle systems introduce ionic flux on the mitochondrial membrane. Ionic flow into the mitochondria causes an osmolarity difference between the inside of the mitochondria causing an influx in water. Osmotic pressure increases tension on the membrane which exceeds its bending elasticity and collapses the mitochondrial tubule into pearls. (B) Alteration to components of the mitochondrial membrane such as cholesterol, cardiolipin, and cristae organization change the elasticity of the membrane and can collapse the tubular mitochondria into pearls. (C) Molecular motors traffic mitochondria and introduce external mechanical tension through

pulling forces on the membrane. Mechanical tension exceeds the bending elasticity of the membrane and collapses the mitochondria tubule into pearls, following a Rayleigh-plateau 'pearling' instability.

Spontaneous pearling triggered by multiple physical forces

With this biophysical framework, the two different types of spontaneous pearling we have uncovered, stretching and calcium associated pearling, respectively, can be driven by two distinct biophysical causes. On one hand, stretching can be sourced from motor proteins on the cytoskeleton network tethered to mitochondria and pulling the membrane <sup>57</sup>. This is directly validated by activation of these motors with optogenetically-activated motors, which results in force-dependent elongation of mitochondrial tubules followed by network wide mitochondrial pearling events within the stimulated cell <sup>58</sup>. On the other hand, spontaneous events that coincide with calcium uptake and membrane shrinkage may be explained by calcium waves propagating through the cell that are soaked up by mitochondria's buffering capacity <sup>59</sup> leading to internal osmotic pressure. We further identified genetic and metabolic perturbations that validate the importance of the mitochondrial inner membrane's high elastic modulus supported by cristae ultrastructure. Removal of lipid packing components, cholesterol or cardiolipin, as well as essential junction proteins of the MICOS complex alters the mitochondria's capacity for crossing a pearling instability. Therefore, only by characterizing the state of individual mitochondrial tubules in terms of the osmotic pressure, mechanical tension, and its membrane's elastic and electrochemical state can one properly predict a pearling transition.

# Electrochemical coupling supports mitochondrial pearling

Our findings indicate that the membrane polarization maintained by the IMM is a primary regulator of pearling transitions. This suggests that the flux of ions and water that build tension on the IMM are supported by the electrical coupling of the IMM. A future direction of this work would refine our biophysical model of mitochondrial pearling to explain how the inner membrane's electrochemical coupling is capable of regulating pearling events. There remains open questions, such as why depolarized mitochondria are unable to undergo a pearling transition spontaneously or by laser stimulation and micro-needle force? Yet, depolarized mitochondria still pearl from osmotic pressure, such as 0.1x PBS or ionomycin. We postulate that membrane polarization reinforces lipid organization of the mitochondrial inner membrane. Polarized inner membranes may induce a conformation of lipids that supports increased tension on the membrane. Without the electrochemical gradient, mitochondrial membranes become "soft" with disorganized lipids and thereby unable to maintain higher tension states. Further, like a neuronal action potential, the electrical pulse resulting from membrane depolarization should be accompanied by a mechanical wave that propagates across the membrane <sup>60</sup>. This electrically-driven mechanical wave may drive the structural reorganization necessary for pearl formation.

lonic flux, not oxidative stress, explains the onset and frequency of pearling transitions

We report that the frequency of spontaneous pearling events is dependent on the amount of light exposure on a given sample. A common explanation of this phototoxic effect <sup>16</sup> is an increase in ROS which causes oxidative damage on macromolecules. Downstream it is speculated that the mitochondria induce mitophagy to recycle these damaged materials. With this logic, pearling may therefore represent a damage-response to isolate dysfunctional materials for autophagy. We attempted to inhibit pearling by addition of antioxidants NAC and MitoTEMPO. However, none of them were capable of altering the pearling induced by laser stimulation (Figure 6K). Additionally, using the mitochondrial ROS sensor, mitoSOX green and red, no detectable increase of the fluorophore was observed. The intermembrane ROS sensor, Hyper7-IMS, revealed increased H2O2 directly following laser-stimulation but was not specific to tubules that underwent a pearling transition. Regardless of the role of ROS, we contend that this hypothesis does not adequately explain the structure and dynamics of the observed pearling event. Why do the constriction sites appear at regular intervals? Why is it a modular event affecting connected tubules? Why does the tubule transiently recover back to a cylindrical morphology? Without an understanding of the biophysical properties of the mitochondrial membranes themselves these questions remain unanswered. That being said, our work does corroborate the link between increased light exposure and increased pearling transitions. We report that the frequency of pearling events is increased on higher-power imaging systems. We are confident that these pearling events, although amplified by exposure to laser power, occur spontaneously for several reasons, i) we observe these spontaneous events at the beginning of imaging an individual cell. without previous exposure to light (Figure 6F). ii) the distribution of spontaneous pearling events does not increase the longer the sample is imaged (Figure 6E). iii) The events are transient and rapidly revert back to tubular shapes unlike direct exposure to high power-laser or LED light which results in a permanent pearled state that aggregate into larger spherical shapes. iv) phasecontrast imaging of cells still reveals pearling events (Landoni et al., 2024).

# Chemical fixation induces pearling artifacts

Paraformaldehyde has previously been reported to be osmotically active <sup>39</sup>. Others have found that the addition of glutaraldehyde can mitigate this artifact through its faster fixation rate <sup>61–63</sup>. It is worth noting that in addition to a pearling artifact, the reverse 'hyper-osmotic' artifact of flaccid tubules of mitochondria is also visible at higher levels of glutaraldehyde (**Supplementary Figure 3D-E**). It is for this reason that a titration of PFA:GA should be performed under the microscope to maintain ideal ultrastructure. Alternatively, switching to high-pressure freezing or cryo-fixation should achieve the same aim <sup>30</sup>. With this in mind, it is possible that earlier reports

of mitochondrial pearling in tissue samples <sup>6,13</sup> may be an artifact of the osmotic pressure exerted by 4% PFA during perfusion of the animal.

## Functional utility of mitochondrial pearling

Beyond generating ATP, one of the core functions of mitochondria is to buffer ions undergoing flux within cells. Mitochondrial membranes contain many species of ionic pumps regulating the flux of H+ (ATP synthase), Ca2+ (calcium uniporter, MCU), K+ (mitoKATP, , mitoBKCa, mitoKv, mitoTASK, mitoIKCa), Na+ (mitoSLO2), Mq2+ (MRS2), and Cl- (CLIC4&5, Ano-1). The fact that the presence of each channel varies from tissue to tissue and we have observed pearling in diverse cell types across evolutionary distinct species, hints that it is unlikely for a specific ion channel to regulate the entirety of pearling events. However, it is still possible that many of these pores evolved in order to mitigate or potentiate pearling events for cellular homeostasis. We have yet to establish how pearling affects mitochondrial function, particularly energy production. This is largely because current readouts of bioenergetic output, namely Seahorse extracellular flux analyzer, measures oxygen consumption on the order of minutes and pearling occurs on the order of seconds. Future bioenergetic instrumentation may enable access to energy production on the same timescale as a pearling event. We hypothesize that energy production will follow a biphasic effect with increased OXPHOS as the IMM increases in tension and approaches instability followed by OXPHOS precipitously declines upon crossing the instability. Supporting evidence is the fact that membrane potential collapses after the onset of pearling (Figure 3H-I). This leads us to believe that in energetically demanding cells, such as muscle cells, mitochondria are driven to the threshold of membrane tension to maximize energy production. Pearling, in this context, represents a physical barrier or breakpoint that these cells strive to avoid. However, in other cell types such as neurons or cardiomyocytes, mitochondria's primary function is to buffer ions to help potentiate action potentials periodically moving across the cell <sup>59,64</sup>. In this context, pearling dynamics may be a necessary event to support ionic buffering and ionic channels are tuned to ensure rapid pearl recovery for periodic neuronal activity.

# Fission machinery reduces network tension

We hypothesize that the reason why mitochondria of Drp1 knock-out cells have an increased rate of pearling event <sup>5,15</sup> is because with a hyperfused network pearling events will spread along all physically coupled segments of material, as we have shown with laser-stimulated induced pearling. With fission blocked, the spontaneous pearling events, whether triggered by calcium microwaves or motor protein pulling, will spread through the interconnected tubules, instead of the typical event occurring along a relatively isolated segment of mitochondria. We further argue that without fission, hyperfused mitochondria will enter a higher tension regime,

similar to senescent fibroblasts, and thereby more readily cross a pearling instability from exposure to normal imaging light. Molecular fission machinery may thereby serve to mitigate the physical coupling of pearling, isolating these transitions to smaller regions of the cell.

In conclusion, our experimental results indicate that mitochondrial pearling is governed by the biophysical forces of elasticity, pressure, and tension. The ubiquitous presence of mitochondrial pearling in diverse biological contexts across evolutionary scales, places pearling as a core dynamic event of mitochondria alongside fission and fusion processes. Our unified biophysical mechanism bridges mitochondria dynamics with ionic flux, molecular motors, and cellular energetics. Pearling is thereby a prime example justifying mitochondria's role as the central processor of the cell <sup>65</sup> simultaneously integrating both biochemical and biophysical signals. Other mitochondrial dynamics such as fission and fusion were previously implicated in aging and age-related disease <sup>66</sup>. Mitochondrial pearling may similarly advance our understanding of key health transitions. With that in mind, this paper establishes a unified biophysical model to understand the driving forces of mitochondrial pearling.

## Methods

#### Mammalian cell culture

Cell lines include U2O2, HEK293, COS7, RPE1, human primary fibroblasts (hFB12, hFB13), Jurkat cells, Raji cell, primary human CD8 T cells, and iPSC-derived neurons (**Methods Table 1**). All cells were maintained in normal 37°C incubator conditions. Immortalized cells were grown in DMEM (GlutaMax, 25mM glucose) supplemented with 10% FBS, passaged weekly, and maintained for less than 20 passages. Primary human fibroblasts were grown in DMEM (GlutaMax, 5.5mM glucose).

Non-adherent Jurkat cells were grown in RPMI media supplemented with 10% FBS. Cells were transduced with lentivirus labeled with COX8A-mitoStayGold using a spin-transduction protocol for 1.5 hours at 2400 rpm. Plating was performed in an 8-well chamber slide coated with 10  $\mu$ g/ml fibronectin and 5  $\mu$ g/ml ICAM-1 for 3 hours at 37°C. Jurkat cells were then co-cultured with SEE-pulsed Raji cells labeled with Sybr Gold (1:10,000x) in the chamber for 30 min at 37°C before imaging.

Primary human CD8 T cells were grown in X-VIVO 15 media (Lonza #04-418Q) with gentamicin and phenol red, supplemented with 5% FBS, 4 mM n-cysteine, 55 mM 2-mercaptoethanol (Thermo #21985023). Primary cells were activated by three day incubation with DynaBeads Human T-Activator CD3/CD28 (Thermo #11131D). Beads were magnetically removed and cells imaged with 8 hours of activation. For synapse formation, Raji cells labeled with Sybr Gold (1:10,000x for 30 min) were co-cultured with primary T cells labeled with PKmito Orange (500 µM for 1hr). Synapse formation between T cells and Raji cells were found by scanning imaging plates for adjacent cells with distinct fluorescent labels.

iPSCs were cultured in mTESR Plus media (Stem Cell Technologies #100-0276) on hESC qualified matrigel (Corning #354277) coated tissue culture dishes. Differentiation to ventral midbrain identity was adapted from a previously described method <sup>67</sup> with modifications for 3D embryoid body based differentiation instead of 2D differentiation. On Day 0, iPSCs were dissociated into single cells with accutase and seeded into ultra low attachment 96 well plates at 5K cells per well to form embryoid bodies in Neural Differentiation Media (1:1 Neurobasal (Thermo #A3582901)/Advanced DMEM F12 (Thermo #12634010), N2 (Thermo #17502048), B27 -vitA (Thermo #12587-010), Glutamax (Thermo #35050-061), Sodium Pyruvate (Thermo #11360070), NEAA (Thermo #11140050), Pen/Strep (Thermo #15140-122) and 55 μM b-ME (Thermo #21985-023) supplemented with 10μM SB431542 (Selleck Chemicals #S1067), 100 nM LDN193189 (Selleck Chemicals #S2618), 0.75 μM CHIR99021 (Thermo #S1263), 500nM SAG (Thermo #S6384), 100 μM Ascorbic Acid (Sigma #A4034-100G) and 10 μM Y-27632 (BioTechne #1254). After 2 days media was exchanged to remove Y-27632. On day four of differentiation media was exchanged and CHIR99021 concentration was increased to 7.5 μM. On Day 7 of differentiation

embryoid bodies were collected and transferred to 10 cm low attachment plates using wide bore pipet tips and incubated for the remainder of differentiation on an orbital shaker at 40 rpm. Media was changed to Neural Differentiation Media supplemented with 7.5 µM CHIR99021, 500 nM SAG, and 100 µM AA until Day 10. On Day10 CHIR99021 and SAG were removed and 0.5 ng/mL TGF-b (Bio-Techne #243-B3-002/CF) and 200 µM dbcAMP (Sigma #D0627- 1G) was added. On Day 12 media was exchanged and supplemented with 10 µM DAPT (BioTechne #2634/50). On Day 15 media was exchanged to the same conditions with an additional supplement of 10 ng/ml BDNF (Bio-Techne 11166-BD-01M) and GDNF (Bio-Techne #212-GD-01M/CF). Media was maintained the same changing every 3-4 days until dissociation. On Day 20-22 of differentiation EBs were collected and dissociated at 37°C in Accumax(~15 EBs/ml of Accumax). EBs were incubated at 37°C with agitation. Following 15 mins EBs were pipetted with p1000 narrow bore tips to check state of dissociation. If still intact then EBs were returned to the shaker. Following 30 mins of enzymatic digestion 25 µg/ml DNase1 was added and EBs were manually triturated 5-10 times to begin manual dissociation. If EBs begin to dissociate then they are manually triturated ~10-20 times, if not they are returned to the shaker for an additional 10 mins. EBs were dissociated by manual trituration into single cells with one volume of media. After dissociation neurons were pelleted by centrifugation and then filtered through a 30 µm cell strainer before plating to remove clumps. Neurons were plated in Neuronal Maintenance Media (Neurobasal Plus, B27 plus, Glutamax, Pen/Strep and 55 μM b-ME) supplemented with 10 ng/ml BDNF, 10 ng/ml GDNF, 100 µM Ascorbic Acid, 200 µM dbcAMP, 10 µM DAPT and 20 mM each of Uridine (Sigma #U3750) and Fluorodeoxyuridine (Sigma #F0503) for 1.5 weeks. Neurons were plated on 8-well chamber slides pre-coated with poly-ornithine, laminin and fibronectin. For imaging experiments, neuronal cultures were labelled with PKmito Orange (500 µM for 1 hr) and CalBryte (1 µM for 1hr) followed by a 3x media wash and a final addition of probenecid (1 mM).

| Cell line      | Cell type                | Species    | Media  | Source                                   |
|----------------|--------------------------|------------|--|--|
| U2OS           | epithelial               | human      | DMEM (25mM<br>glucose)                         | ATCC HTB-96                              |
| HEK293         | kidney                   | human      | DMEM (25mM<br>glucose)                         | ATCC CRL-1573                            |
| RPE1           | fibroblast               | epithelial | DMEM (25mM<br>glucose)                         | ATCC CRL-4000                            |
| COS7           | fibroblasts              | monkey     | DMEM (25mM<br>glucose)                         | ATCC CRL-1651                            |
| hFB12          | fibroblasts              | human      | DMEM (5.5mM glucose)                           | Lifeline CellTech FC-0024<br>Lot # 03099 |
| hFB13          | fibroblasts              | human      | DMEM (5.5mM glucose)                           | Lifeline CellTech FC-0024<br>Lot # 00967 |
| Jurkat         | T cells                  | human      | RPMI   | ATCC TIB-152                             |
| Raji           | B cells                  | human      | RPMI   | ATCC CCL-86                              |
| CD8 T<br>cells | primary T<br>cell        | human      | X-VIVO 15                                      | in-house                                 |
| iPSC           | dopaminerg<br>ic neurons | human      | Neurobasal/Adva<br>nced DMEM F12<br>mTESR Plus | in-house                                 |

Methods Table 1. List of mammalian cell types images for mitochondrial pearling dynamics

#### Yeast culture

Budding yeast were grown in synthetic complete medium supplemented with 2% glucose and 2% methyl-alpha-D-mannopyranoside (MMP, Sigma #M6882) to the stationary phase. Cells were plated in pre-coated overnight with 1:100 concanavalin A 8-well glass-bottom chamber slides (CellVis #C8-1.5H-N). Yeast knockout strains are listed in **Methods Table 2**.

| Knockout        | Yeast strain                    | Target                   | Label               |
|-----------------|---------------------------------|--------------------------|---------------------|
| HO<br>(Control) | CGY14.31xYKO<br><ho></ho>       | НО                       | preCox4 mNeon-green |
| CRD1            | CGY14.31xYKO<br><crd1></crd1>   | cardiolipin synthesis    | preCox4 mNeon-green |
| TAZ1            | CGY14.31xYKO<br><taz1></taz1>   | cardiolipin synthesis    | preCox4 mNeon-green |
| MIC10           | CGY14.31xYKO<br><mic10></mic10> | MICOS complex subunit    | preCox4 mNeon-green |
| MIC19           | CGY14.31xYKO<br><mic19></mic19> | MICOS complex subunit    | preCox4 mNeon-green |
| MIC60           | CGY14.31xYKO<br><mic60></mic60> | MICOS complex subunit 60 | preCox4 mNeon-green |
| Control         | CGY49.77                        | wildtype                 | TIM50-mNeon-green   |
| MIC60           | CGY57.57                        | MICOS complex subunit 60 | TIM50-mNeon-green   |

Methods Table 2. Yeast knockout strains screened for pearling

#### Fluorescent Labeling

All fluorescent labels used in the current study are listed in **Methods Table 3**. Transiently transfection of cells for Mito-R-GECO1 plasmid (Addgene #46021) was performed overnight using 0.2 µl lipofectamineTM 3000 (Thermo #L3000008) with 250 ng of plasmid DNA and 0.2 µl P3000™ reagent following the manufacturer's protocol. Stable cell line of COX8a-mEmerald was made by transfection with 1 µg of DNA using the SE Cell Line Nucleofector Kit (Lonza #V4XC-1032) following the manufacturer's protocols. Transfected cells were cultured on collagen-coated plates to facilitate the recovery process. After two days, cells were selected with 1mg/ml Geneticin Selective Antibiotic (G418 Sulfate, ThermoFisher #10131035) for a week. Fluorescence signals were continuously monitored during the selection process. Upon recovery, G418 at a concentration of 0.5 mg/ml was used for stable cell line maintenance. FACS-sorting for moderate-expression cells was performed to enhance the homogeneity of cells containing labeled mitochondria.

Lentivirus construction of COX8A-mStayGold and Mito-R-GECO1 was constructed with an RSV promoter, EF-1a promoter, and puromycin resistant gene using VectorBuilder custom pipeline. Virus was added at 20 particles per cell (ppc) with 10 µg/ml polybrene (PL200) and incubated overnight. Cells then recovered in normal media for 4-7 days. Selection was performed with 1 µg/ml Puromycin Dihydrochloride (Thermo #A1113803). FACs-sorting was used to filter for high-expression cells (top 10%) to enhance homogeneity and maximize fluorescent intensity signals. Cells infected with both constructs were engineered in sequential transductions.

Dye staining was performed to cells as follows; PKmito Orange was applied at 500 nM for 1 hour at 37°C standard incubation, followed by 2x media wash, two hour incubation, and another 2x media wash. Sybr Gold staining was performed 10,000x dilution for 30 minutes at 37°C standard incubation, followed by a 3x wash. Fluo4 was added 2 μM for 30 minutes at 37°C and then addition of 0.02% Pluronic<sup>TM</sup> F-127 (Thermo #P3000MP). Calbryte<sup>TM</sup> 520 AM was added at 1 μM for 1 hour at 37°C followed by a 3x media wash and addition of the anion transporter inhibitor, probenecid (1mM). Fluo4 was added for 30 min at 1 μM followed by a 1x media swap and addition of 0.02% Pluronic<sup>TM</sup> F-127 (Thermo #P3000MP).

| Label                        | Category                             | Target  | Properties   | Source   |
|------------------------------|--------------------------------------|---|--|--|
| PKmito Orange                | dye                                  | IMM   | membrane potential<br>dependent  | Cytoskeleton<br>Inc #CY-<br>SC053                  |
| Sybr Gold                    | dye                                  | mtDNA intercalation                                     | membrane potential<br>dependent (partial)                              | Thermo<br>#S11494                                  |
| TMRE                         | dye                                  | mitochondrial inner<br>matrix                           | Mitochondrial membrane potential dependent                             | Thermo # T669                                      |
| CellLight Mito-<br>GFP       | transient<br>plasmid                 | PDHA1 IMM and matrix                                    | Marker of mitochondrial structure                                      | Thermo<br>#C10600                                  |
| CellLight Mito-<br>RFP       | transient<br>plasmid                 | PDHA1 IMM and matrix                                    | Marker of mitochondrial structure                                      | Thermo<br>#C10601                                  |
| CellLight ER-RFP             | transient<br>plasmid<br>transfection | ER  | Marker of ER structure   | Thermo<br>#C10591                                  |
| COX8A-<br>mEmerald           | genetically<br>encoded<br>sequence   | COX8A protein on the IMM and mitochondrial matrix       | geneticin selection,<br>FACS-sorted                                    | Addgene<br>#54160                                  |
| COX8A-<br>mStayGold          | lenti-<br>transduction               | COX8A protein on<br>the IMM and<br>mitochondrial matrix | lentivirus package,<br>puromycin selection,<br>FACS-sorted             | https://doi.org/<br>10.1038/s4159<br>2-023-02085-6 |
| Mito-R-GECO1                 | lenti-<br>transduction               | mitochondrial<br>calcium                                | ratiometric intensity<br>mitochondrial calcium<br>flux                 | Addgene<br>#46021                                  |
| MitoSOX red                  | dye                                  | mitochondrial ROS                                       | mitochondrial<br>superoxide indicator                                  | Thermo<br>#M36008                                  |
| MitoSOX green                | dye                                  | mitochondrial ROS                                       | Superoxide indicator   | Thermo<br>#M36005                                  |
| Hyper7-IMS                   | dye                                  | mitochondrial H <sub>2</sub> O <sub>2</sub><br>ROS      | mitochondrial<br>intermembrane space<br>hydrogen peroxide<br>indicator | Addgene<br>#136469                                 |
| Calbryte <sup>™</sup> 520 AM | dye                                  | intracellular calcium                                   | cytoplasmic calcium flux   | AAT Bioquest<br>#20651                             |
| Mito Flipper-TR              | dye                                  | mitochondrial<br>membrane tension                       | mitochondrial membrane<br>tension                                      | Cytoskeleton<br>#CY-SC023                          |

**Methods Table 3**: IMM = inner mitochondrial membrane

| Inhibitor     | []<br>(µM) | Duration<br>(min) | Known target                          | Pearling effect       | Source                             |
|---------------|------------|-------------------|---------------------------------------|-----------------------|------------------------------------|
| FCCP          | 10         | 10-60             | mitochondrial membrane potential      | full inhibition       | Sigma<br>#C2920                    |
| Oligomycin    | 1          | 10-60             | ATP synthase inhibitor                | inhibits<br>recovery  | Sigma<br>#75351                    |
| Rotenone      | 4          | 10-60             | complex II inhibitor                  | partial<br>inhibition | Sigma<br>#R8875                    |
| Antimycin A   | 2          | 10-60             | complex II inhibitor                  | partial<br>inhibition | Sigma<br>#A8674                    |
| Latrunculin B | 10         | 30-60             | actin polymerization                  | inhibits<br>recovery  | Sigma<br>#L5288                    |
| Nocodazole    | 10         | 30-60             | microtubule polymerization            | partial<br>inhibition | Sigma<br>#M1404-<br>2MG            |
| Taxol         | 10         | 30-60             | microtubule stabilization             | inhibits<br>recovery  | Sigma<br>#PHL89806                 |
| Cyclosporin A | 10         | 10-60             | mPTP inhibitor                        | increased             | Sigma<br>#30024                    |
| Atorvastatin  | 50         | 240               | cholesterol depletion                 | full inhibition       | Selleck<br>Chemical #<br>S207750MG |
| NAC           | 5          | 24 hour           | cytoplasmic antioxidant               | n.s.                  | Thermo<br>#A15409.36               |
| MitoTEMPO     | 0.02       | 24 hour           | mitochondrial-specific<br>antioxidant | n.s.                  | Sigma<br>#SML0737                  |

Methods Table 4. Chemical inhibitors of mitochondria

## Live cell imaging

Live cell imaging was performed on several systems including an in-house single-objective light-sheet (SOLS) microscope, a Nikon CSU-W1 spinning disk microscope with laser stimulation, and a Leica Stellaris TauSTED microscope. For all microscopes, cells were plated on fibronectin coated (Sigma #F1141-1mg) 8-well glass-bottom chamber slides (CellVis #C8-1.5H-N) and incubated overnight prior to imaging.

#### **SNOUTY Light Sheet**

The in-house single-objective light-sheet (SOLS) microscope <sup>37</sup> was equipped with a 100x NA 1.35 Silicone primary objective, a fast optical scanner (galvo) for quickly taking 3D data (up to ~100x100x30µm XYZ field of view), a Gaussian light-sheet (~12µm Rayleigh range) and a stage-

top incubator for maintaining a temperature of 37°C with 5% CO<sub>2</sub> throughout. The majority of the imaging was acquired at a frequency of 1 volume/second (1 ms exposures per image) using 5% 488 nm and 12% 561 nm laser powers (20.67 uJ and 70.47 uJ per volume on the sample, respectively) and a quad emission filter (zET405/488/561/635m). Max projected 2D image previews were generated from the 3D data. Deskewing of the 3D light-sheet data was computed using Snouty Viewer (v0.2.5).

#### CSU-W1 Spinning Disk and FRAP Laser-stimulation

Laser stimulation was performed on Nikon CSU-W1 spinning-disk confocal system paired with Andor Zyla sCMOS camera (5.5 megapixels), Nikon Perfect Focus system, Oko stage top incubator, and Vortran 405 nm photoactivation and photobleaching laser. Imaging was performed with 488 nm and 561 excitation lasers using a Plan Apo VC 100x/1.4 oil objective and a zET405/488/561/635m quad filter. FRAP laser was calibrated before each experiment using a 0.1mg/ml fluorescein-coated coverslip (Thermo #L13251.36). Laser power was recorded with a Microscope Power Slide Meter Sensor (ThorLabs #S175C). Full 3D z-stacks were acquired with 250 nm slices for a total of 5.25 μm depth across the cell. Imaging 2D time series videos were collected at 0.33 frames sec-1. For autofluorescence detection the camera was swapped to Andor DU-888 EMCCD camera ideal for amplifying low-emission signals.

#### Stimulated Emission Depletion Microscopy (STED)

For cristae labeling, cells were incubated with 500nM PKmito orange (PKMO, #CYSC053, Cytoskeleton Inc. <sup>68</sup> for 1 hour at 37°C, followed by 4 successive washes over a two hour period. Additionally, mtDNA nucleoid staining was performed with 1:10,000x SybrGold (#S11494, ThermoFisher) for 30 min incubation at 37°C followed by a 3x wash. Images were acquired using an 86x water objective, taken at 7x zoom, 16x line averaging, and 1024x524 resolution with PKMO acquired with a 5% 591 nm white light laser excitation line, a 70% 775 nm STED laser depletion line, and SybrGold at 4% 488 nm excitation. Tau-Sted lifetime enhancement was applied at 100%.

#### Micro-needle manipulation

Microneedle manipulation was adapted for interphase U2OS cells based on previous techniques detailed in Suresh et al. Microneedles were made from glass capillaries with an inner and outer diameter of 0.58 mm and 1 mm respectively (1B100-4 or 1B100F-4, World Precision Instruments). Glass capillaries were pulled via micropipette puller (P-87, Sutter Instruments, Novato, CA), bent and polished using a microforge (Narishige International, Amityville, NY) according to the same specifications, parameters, and geometries described in detail in Suresh et al. These parameters allowed for the needle to approach cells orthogonal to the imaging plane and conduct manipulations without rupturing the cell (Suresh et al.) Prior to imaging microneedles

were coated with BSA Alexa Fluor 647 (A34785, Invitrogen) by soaking them in solution for 60s. The solution was created via dissolving BSA-Alexa dye and Sodium Azide (Nacalai Tesque, Kyoto, Japan) in 0.1 M phosphate-buffered saline (PBS) at a final concentration of 0.02% and 3 mM, respectively (Sasaki et al., 2012). The solution allows needles to be visualized via fluorescence imaging, aiding in positioning of the needle along a single mitochondrion. It should be noted, that due to technical constraints involved with manipulation experiments, the imaging chamber lid had to be removed. As such, the sample dish was only able to achieve a stable temperature of 30 C.

Cells for microneedle manipulation were chosen based on the following criteria: chosen cell was in interphase and cell possessed one or more mitochondria that are well separated from the surrounding mitochondria network. These criteria were important for perturbing single mitochondrion without affecting the entire network.

The micromanipulator was mounted to the scope body and positioned above samples as described in Suresh et al. Manipulations were performed in 3D using an x-y-z stepper-motor micromanipulator (MP-225, Sutter Instruments, Novato, CA). A 3-axis-knob (ROE-200) connected to the manipulator via a controller box (MPC-200, Sutter Instruments). Prior to manipulation, the needle was positioned via phase imaging at the approximate x-y position of the intended manipulation site ~ 10 µm above the cell in z. While imaging every 2 seconds at 3 z-planes (0.0 +/- 0.5 µm) the needle was manually lowered into place near a single mitochondrion. If necessary, the needle's position in x-y was changed by first raising the needle above the cell and repositioning in x-y before approaching the intended mitochondrion. Once properly positioned, the needle was manually moved to tap the mitochondrion to apply a brief mechanical load. After, the needle was slowly removed from the cell.

To be analyzed, the manipulated cells had to demonstrate all listed attributes: cell health was not significantly impacted via manipulation (ie cell rupture), mechanically challenged mitochondrion was clearly visible throughout the entirety of manipulation, the mitochondrion demonstrated slight deformation due to the applied mechanical load, a single mitochondrion was contacted by the needle.

#### Image Analysis

Image analysis was performed in fiji software as well as an updated version of MitoMeter called Nellie and available at <a href="https://github.com/aelefebv/nellie">https://github.com/aelefebv/nellie</a>. This pipeline enables automated segmentation, tracking, and feature extraction of individual organelles over time. Metrics derived from Nellie include mitochondrial counts, tubule length, tubule width, aspect ratio, linear velocity, linear acceleration, angular velocity, angular acceleration. A separate pearl

detection script was added on the end of Nellie specifically to identify pearls and measure pearl shape. First a polygon mask was drawn over the pearled region. Pearls were then detected by applying Frangi filtering to enhance tubular structure within each image. The filtered images were thresholded to binary masks, followed by KDtree-based distance transformation and maximum filtering to identify local maxima for potential pearls. Candidate peaks were labeled and refined using a proximity-based region growing algorithm, followed by removal of small objects, and those touching image edges to eliminate false positives.

#### Frequency of pearling events

The frequency of pearling events was calculated with two approaches. The first method counted the number of pearling events in each video and normalized to the duration of imaging. The total number of mitochondria was measured using the Nellie software object detection, yielding the number of events per mitochondria per second. The event probability over 10 minutes was then calculated. The second method measured the total length of pearled mitochondria across a minute of time, and divided by the sum of lengths across all mitochondria in the cell outputted by Nellie software. To distinguish pearling from other dynamics such as fission events, inclusion criteria for pearling included, i) the mitochondria underwent a full transition from cylinder to pearls to cylinder. ii) the pearl formation contained at least three pearls, and iii) the pearls remained tethered to one another during the transition.

#### Intensity-based curvature

Curvature metrics were calculated on tracked skeleton line profiles of individual mitochondrial tubules over time outputted by Nellie software. Curvature was calculated using a 2D parametric curve formula to a spline fitted line across the skeleton. Smoothing factors were optimized for each time series to maximize the difference in curvature between a pearled morphology and the frame before the onset of pearling. Curvature was weighed by the length of the skeleton and normalized to the first 3 timepoints before the onset of pearling. Other extracted metrics include peak-to-peak distance, volume, length, width, height, duration of event, pre/post tortuosity, the duration of the full transition, time to peak of event, time of recovery, number of pearls, length of pearled segment, pearls per micron, width/length of tubule before and after pearling, number of pearling events per tubule.

# Acknowledgements

This work was funded by NSF GRFP, HFSP grant RGP0038/2021 (SM and WFM), NIH grant R35 GM130327 (WFM), the Center for Cellular Construction supported by NSF grant DBI1548297 (SM and WFM). We further thank the Calico Life Sciences internship program for the initiation of this project.

## **Author Contributions**

G.S. conceptualized the study, designed and ran the experiments, analyzed the data, and wrote the initial draft of the manuscript

K.H. assisted in project conceptualization and experimental design

A.Y.T.L developed image analysis software and assisted in analysis

C.R. and S.D. developed and assisted in microneedle experiments

D.I. assisted in running laser stimulation experiments

M.C. generated iPSC neurons

K.M.T. assisted in experimental design

W.L. designed and assisted in T cell activation experiments

B.R. and A.W. generated yeast knockout strains

J.C.L assisted in project conceptualization and protocol development

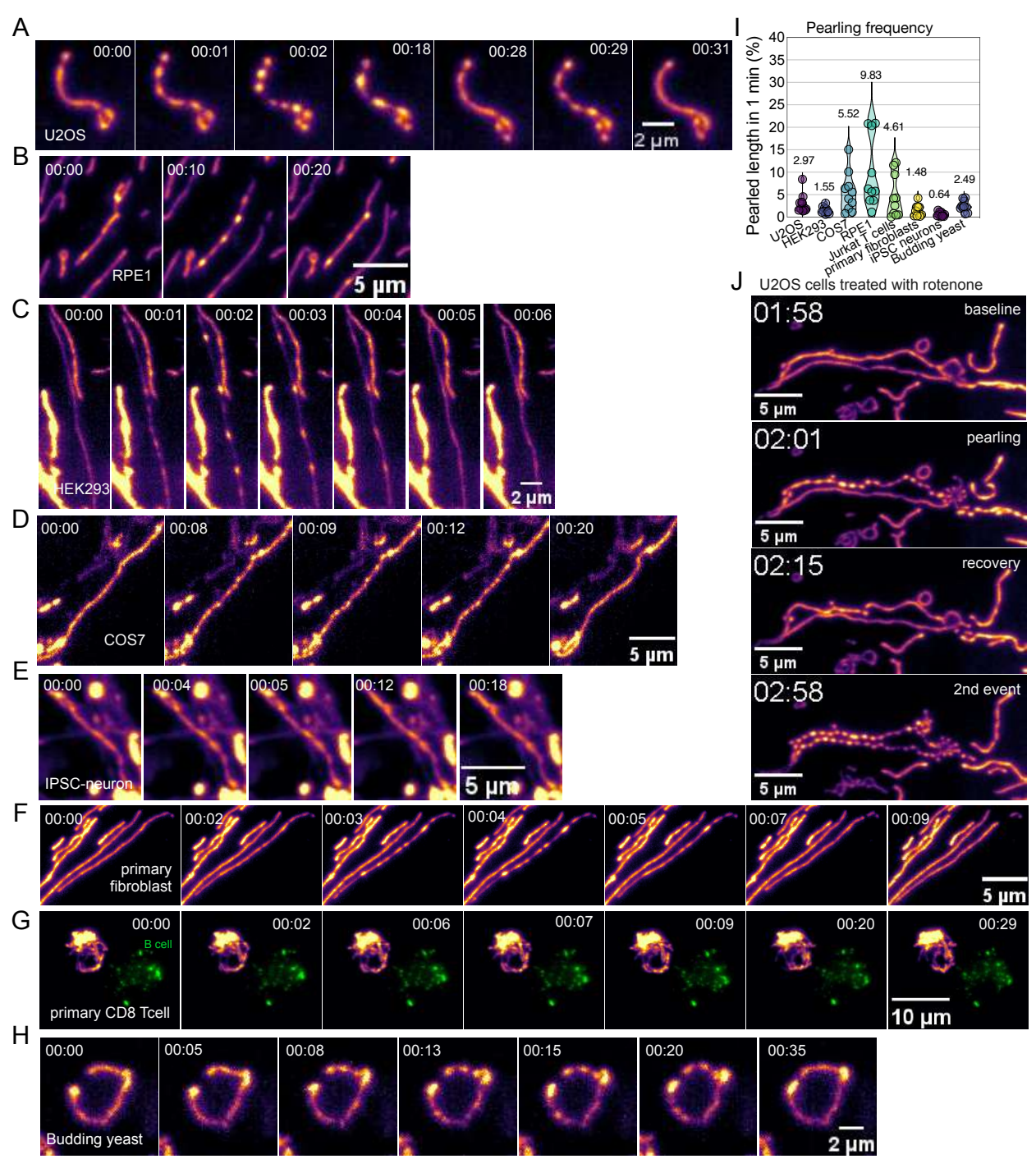
W.M. and S.M. secured funding and assisted in project conceptualization

All authors reviewed and edited the manuscript

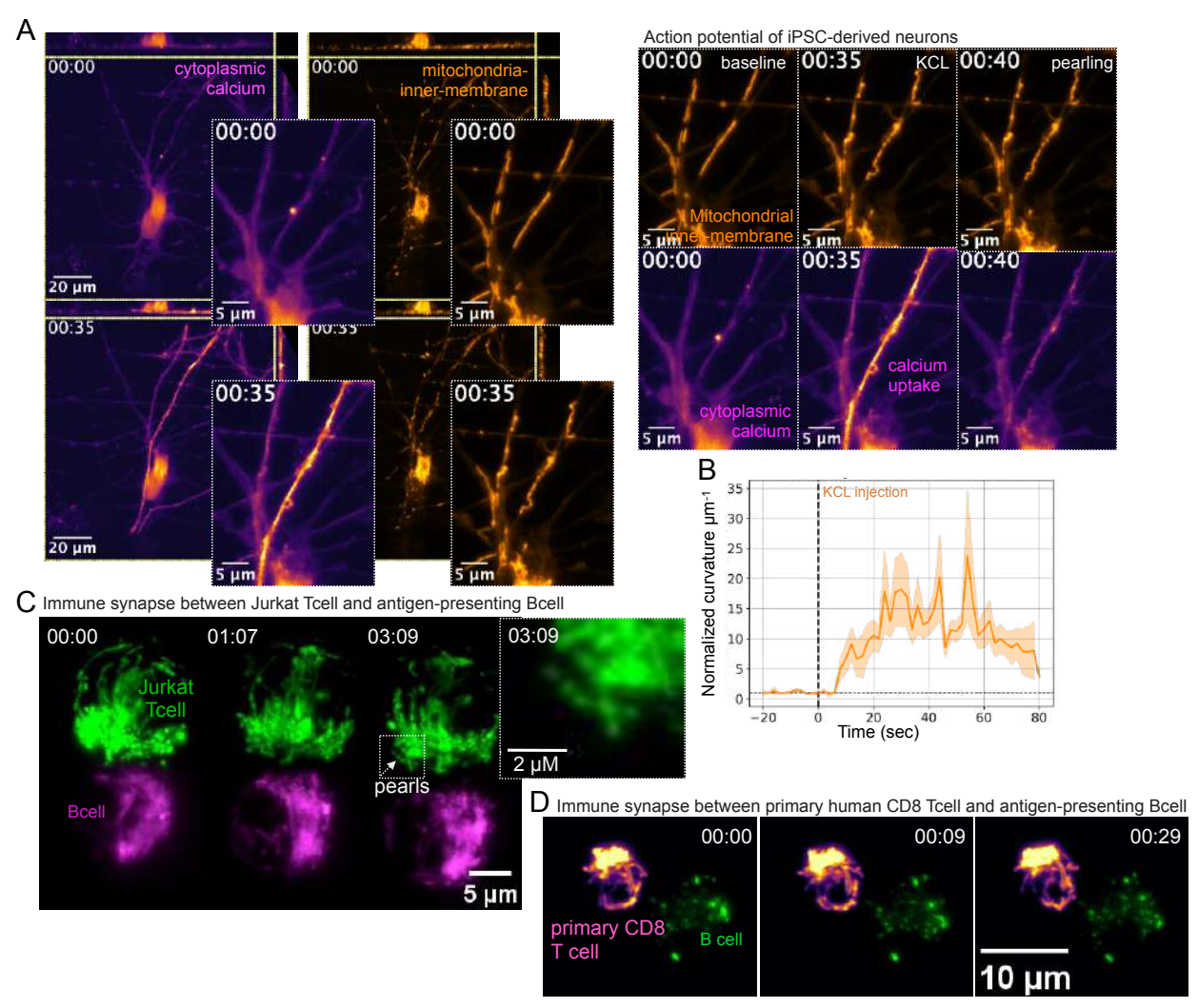
# Supplemental Movies

Movies 1-43 along with supporting metadata are available on our public repository at <a href="https://github.com/gav-sturm/Mitochondrial\_Pearling">https://github.com/gav-sturm/Mitochondrial\_Pearling</a>.

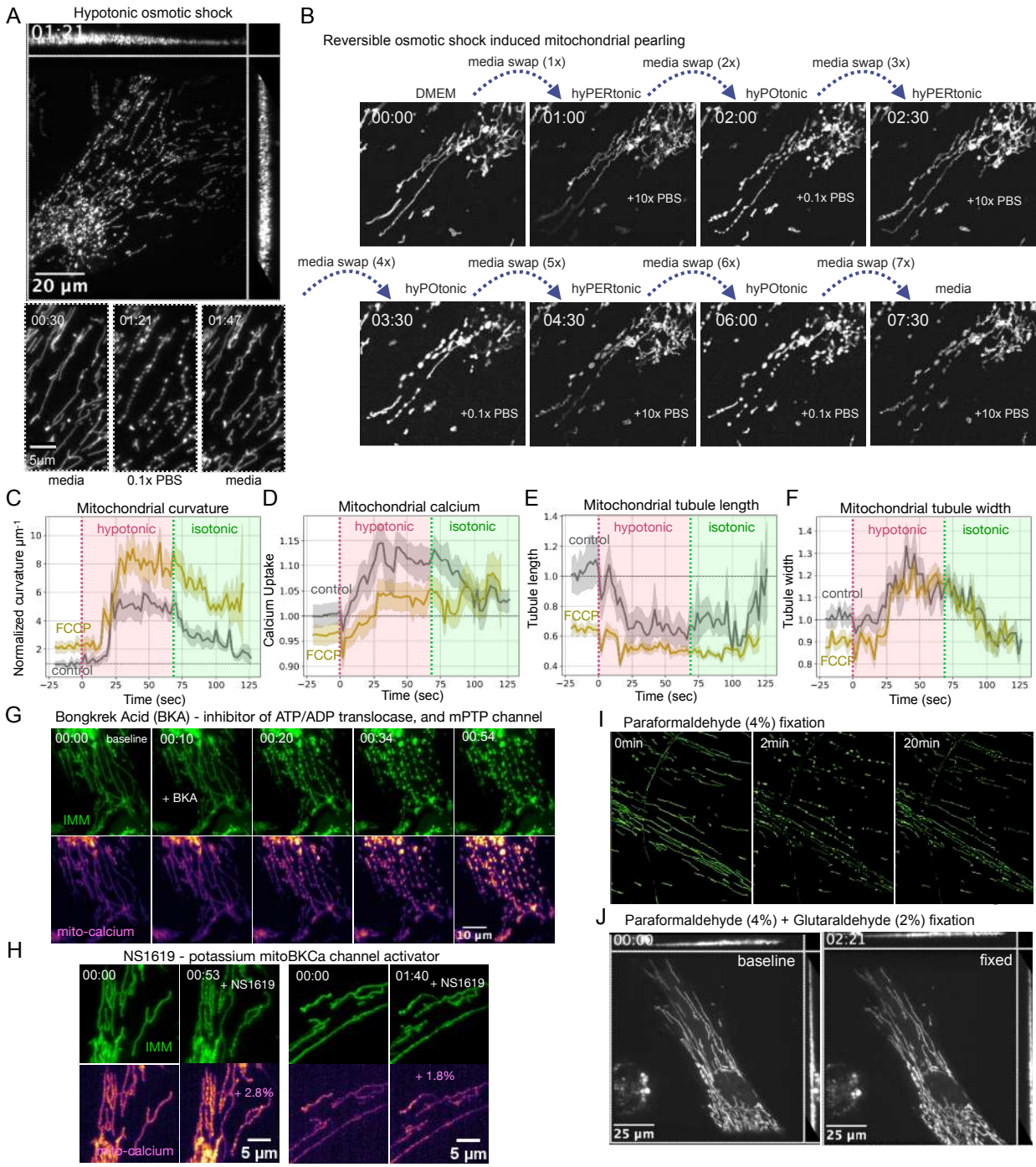
# Supplementary Figures



Supplementary Figure 1. Panel of pearling by cell type (A-H) Transient mitochondrial pearling occurring spontaneously under light sheet microscopy (SNOUTY), imaging at 1 3D volume per second. (I) Rate of pearling per  $\mu$ m of length measured as the percent of mitochondrial length that has pearl within one minute period (n=10-11 videos per group). (J) Spontaneous pearling of mitochondria tubule of a U2OS cell. U2OS cells treated with rotenone (5  $\mu$ M for 30min) undergo a pearling transition twice. Mitochondrial inner membrane (inferno LUT) labelled with genetically-encoded COX8A-mEmerald.

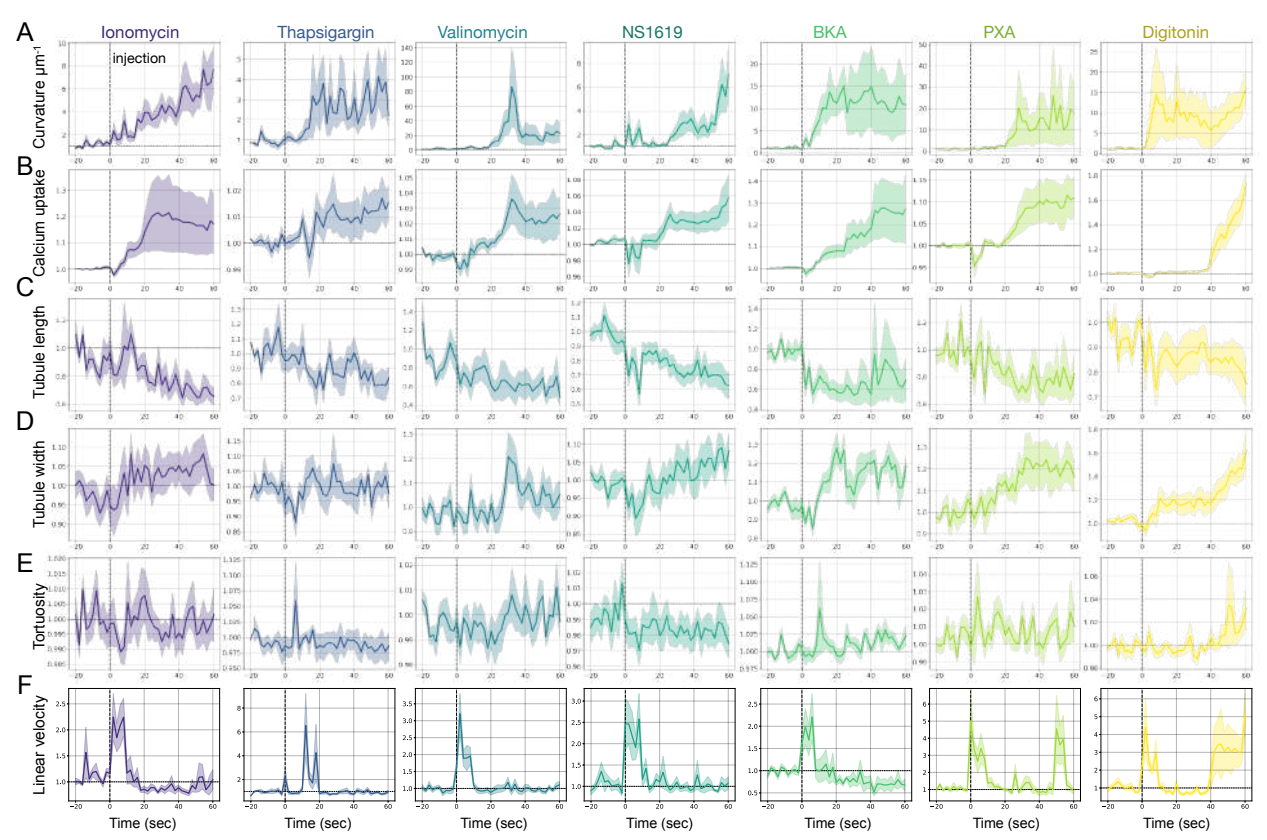


Supplementary Figure 2. Mitochondrial pearling observed across physiological events marked by ionic flux (A) Pearling observed during a KCL (50 mM) triggered action potential of iPSC-derived dopaminergic neurons. Top panel tracks the mitochondrial inner membrane using the dye PKmito Orange. Bottom-panel tracks global calcium levels using Calbryte<sup>™</sup> 520 AM dye. (B) Curvature per μm over time normalized to the first three time points. Dotted line indicates the point of 50mM KCl injection (n=5 cells). (C) Mitochondrial pearling observed at the synapse between a Jurkat cell labelled with Mito-mStayGold targeting an SEE-pulsed Raji cell labelled with PKmito Orange. Both labels mark the mitochondrial inner membrane. (D) Mitochondrial pearling observed at the synapse between a primary human CD8+ T cell labelled with PKmito orange (IMM) targeting an SEE-pulsed Raji cell labelled with Sybr Gold (mtDNA).

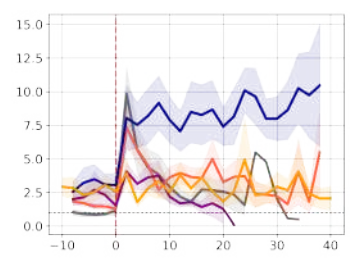


Supplementary Figure 3. Osmotic shock and chemical induction of mitochondrial pearling. (A) Mitochondrial pearling induced by replacing DMEM with hypotonic medium, 0.1x PBS and then recovered by replacing medium back to DMEM. (B) Reproduction of the 1915 experiment (Lewis & Lewis, AJA, 1915) showing reversible pearling morphology via altering from hypo-osmotic (0.1x PBS) to hyper-osmotic (10x PBS) media conditions. The mitochondria of human epithelial U2OS cells are marked with genetically encoded COX8A-mEmerald. (C-F) Time series of untreated (gray) and cells pre-treated with 10  $\mu$ M FCCP for 15min (yellow) with (F) Normalized curvature per  $\mu$ m (COX8a-mStayGold), (G) mitochondrial calcium uptake (Mito-R-GECO1) and (H) mitochondrial tubule length (COX8a-mStayGold). n = 12 cells per group. Data normalized the mean of the first 5 control timepoints. Red vertical dotted line indicates media swap to hypotonic shock (0.1x PBS). Green line indicates media swap to isotonic DMEM. (G) Time series of 10  $\mu$ M BKA induced pearling with a transient 'hypertonic' signature visible at 10 seconds, which precedes the rise in calcium. Top panel is labelled

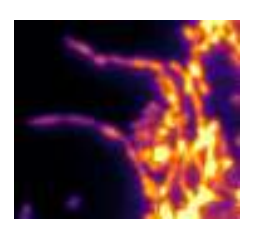
with IMM (COX8A-mStayGold), bottom-panel is labelled with mitochondrial calcium (Mito-R-GECO1). (H) Time series of the potassium BKCa channel activator NS1619 (10  $\mu$ M) induced pearling with or without calcium uptake. Top panel is labelled with IMM (COX8A-mStayGold), bottom-panel is labelled with mitochondrial calcium (Mito-R-GECO1). (I) Pearling induced by fixation with 4% paraformaldehyde (PFA) and remains pearled indefinitely. (J) Stable mitochondrial network maintained after fixation by combining 4% PFA with 2% glutaraldehyde (GA).



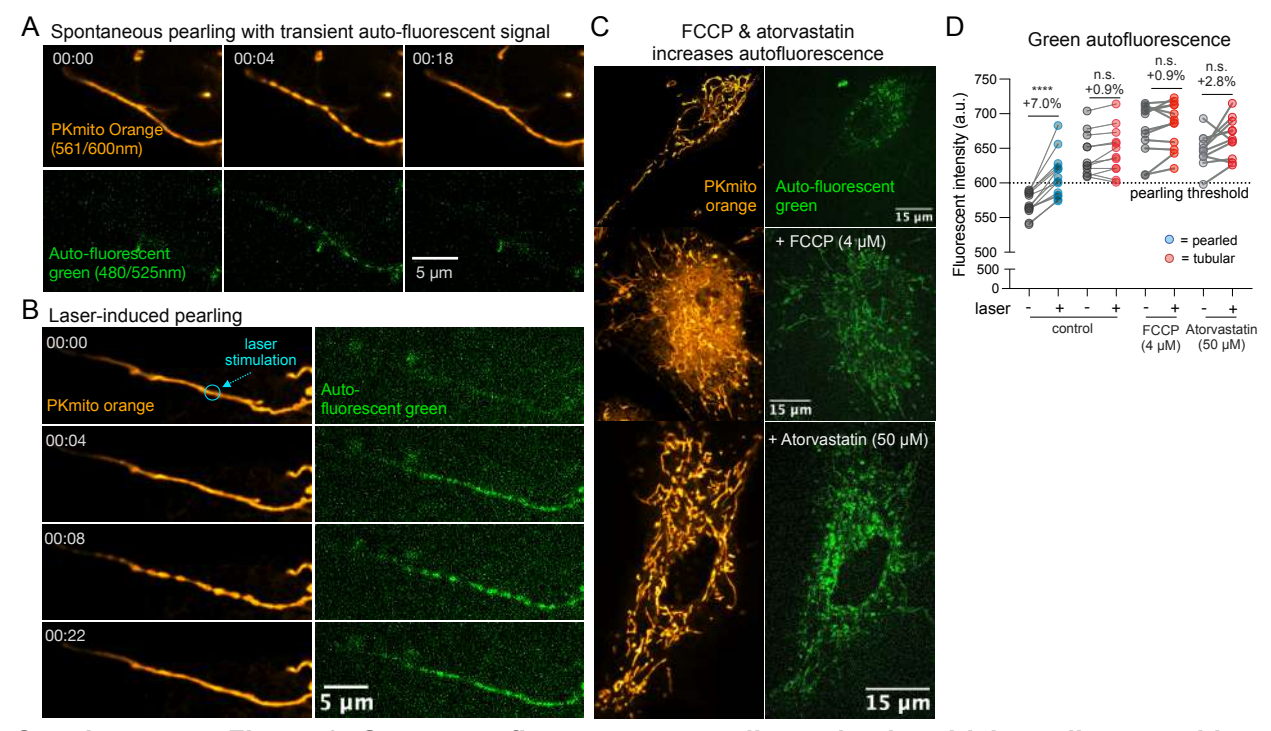
Supplementary Figure 4. Dynamical metrics tracked after chemically induced pearling. (A-F) Tracked feature of mitochondrial pearling induced, from left to right, by ionomycin (4  $\mu$ M), thapsigargin (10  $\mu$ M), valinomycin (10  $\mu$ M), NS1619 (10  $\mu$ M), BKA (10  $\mu$ M), PXA (10  $\mu$ M), and digitonin (10  $\mu$ M). All data is normalized to the average of the first 5 timepoints of that treatment. Tracked metrics include; (A) normalized curvature per  $\mu$ m measured on IMM marker COX8A-MitoStayGold, (B) calcium uptake as measured by the change in mean fluorescence intensity of Mito-R-GECO1, (C) mean tubule length, (D) mean tubule width, (E) tortuosity (F) linear velocity ( $\mu$ m²). Black dotted line indicates the time at which the chemical was added.





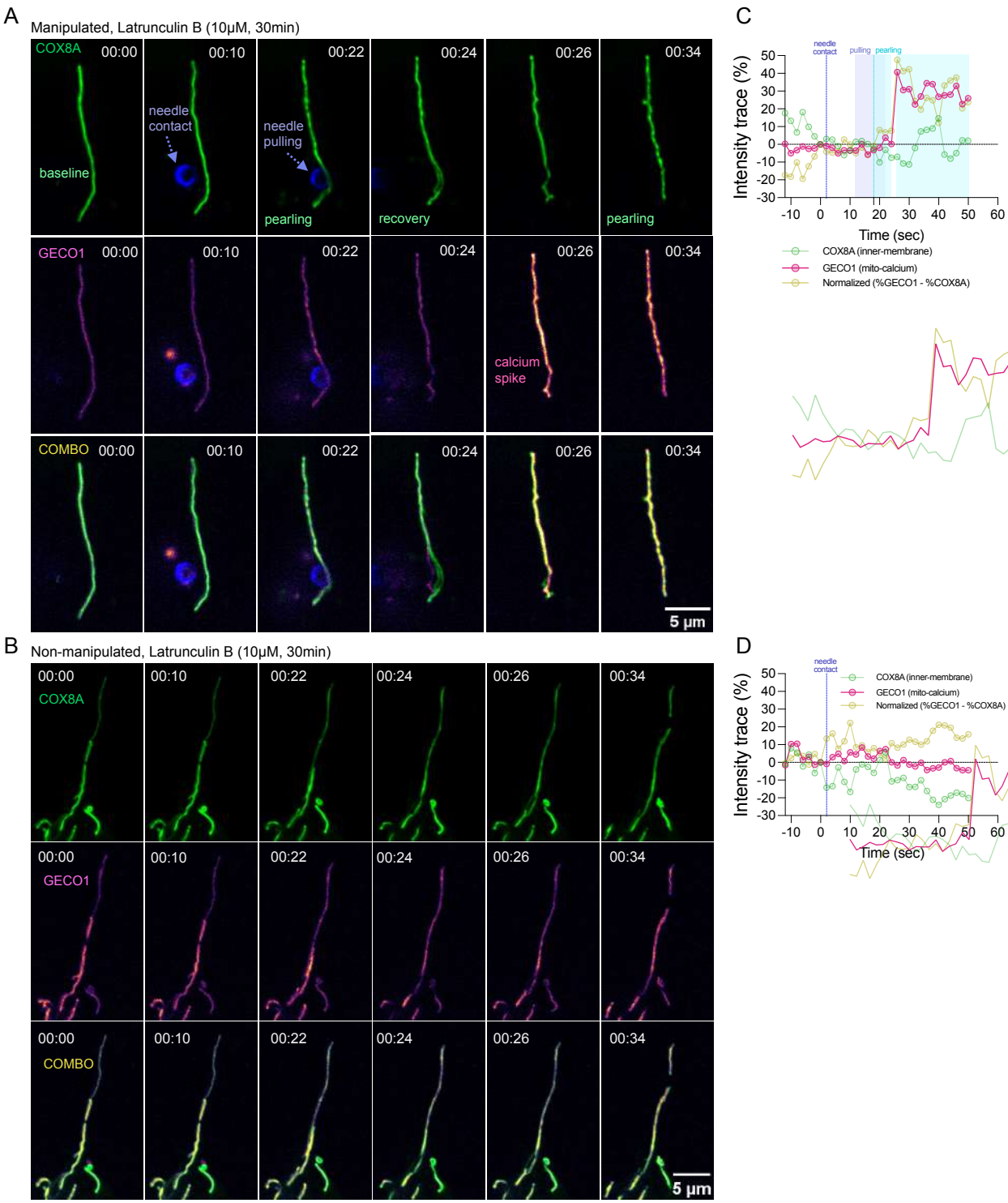


Supplementary Figure 5. Characterizing laser-induced pearling events. (A) Precision of 405nm stimulation laser, Crest-C2, with 100x oil immersion objective, 20mW (0.3mW reaching sample) for 200 milliseconds. (B) Laser-induced pearling recovers back to cylindrical shape but then spontaneously returns back to the pearled shaped. (C) Curvature per unit µm comparing electron transport chain inhibitors, n=21 oligomycin (1 uM) events, n=18 FCCP (4 µM) events, n=18 rotenone (5 uM) events, n=18 antimycin A (5 uM) events. Red dotted line indicates point of laser stimulation. All data normalized to the average of the first five timepoints of the control group. (D) High-temporal tracking of calcium rise that precedes the onset of laser-induced pearling. COX8A = IMM and GECO1 = mitochondrial calcium. (E) ROS fluorescent sensors tracked over time after laser-induced pearling event (n=10 events per sensor). Data normalized to the average of the 5 timepoints before stimulation. (F) ROS sensors percent change in fluorescent intensity after laser-stimulation that induced pearling events. (G) Representative example of Hyper7-IMS ROS sensor increasing across mitochondrial network after laser stimulation, regardless of pearling event occurring. (H) Hyper7-IMS percent change in fluorescent intensity after laser-stimulation for tubules that remained uniform (left bar) and those that underwent a pearling event (right bar). Mann-Whitney non-parametric t-test performed. (I-J) U2OS cell treated with 10 µM of nocodazole (I) or 1 µM latrunculin B (J) for 1 hour and mitochondria labeled with COX8A-mStayGold (IMM). Pearling is then induced by injection of 4 μM ionomycin.



# Supplementary Figure 6. Green autofluorescence predicts mitochondrial pearling transition.

(A) Spontaneous pearling event is followed by a rise in green-shifted autofluorescence that recovers back to background as the tubule reforms. (B) Laser-induced pearling similarly results in a rise in green-shifted autofluorescence within the mitochondrial tubule. (C) Cells treated with FCCP (4  $\mu$ M) and atorvastatin (50  $\mu$ M) increase green-shifted autofluorescence and do not respond to the laser but rather remain in the tubular state. (D) Level of green-shifted autofluorescence within the mitochondrial tubule before and after firing the laser. Mitochondria are split left to right by those that pearl (blue-dots) and those that remain in the tubular state (red-dots). Dotted-line indicates fluorescent threshold at which mitochondria will pearl after firing a 405nm stimulation laser. Mixed-effects anova performed with multiple comparison. \*\*\*\* = 0.00001, n.s. = 0.10 p value.



Supplementary Figure 7. Micro-needle induced pearling precedes calcium uptake. (A) Glass micro-needle manipulation of mitochondria in a U2OS cell treated with 1  $\mu$ m latrunculin B for 30 minutes. (B) A tubule from the same cell that was not manipulated by the needle. Cells are labelled with COX8A-mStayGold (inner-membrane) and Mito-R-GECO1 (C-D) Intensity trace (R1/R0) over time normalized to the point prior to the presence of the needle in the cell for the (C) manipulated tubule of A and (D) a non-manipulated tubule of B.

#### **Instant induction** Increased frequency **Pharmacological** calcium ionophores potassium ionophore channel activator Genetic **Dyes** (ionomycin, thapsigargin, (valinomycin) (NS1619) histamine) DRP1-ko flipper-TR & MIC10,12,19,60-ko TMRE dye hypotonic shock ER protein unfolding TAZ1-ko (0.1x PBS, paraformaldehyde) (Tunicamycin) **Inhibitors Physiological** membrane permeabilization PXA fungal toxin (digitonin/saponin) BKA toxin rotenone & antimycin A aging, Alzheimer's, **Physical force** cyclosporinA and hypoxia (Zhang et al., 2016) FRAP & ablation micro-needle bacterial collisions force-controlled nanopipette (Gäbelein et al., 2022) (Stavru et al., PNAS, 2013) mitochondrial fluid force optical tweezers pearling Inhibition

Hypertonic shock (10x PBS, complete inhibition)

Depolarization (FCCP, complete inhibition), Cholesterol depletion (atorvastatin),

Microtubule depolymerization (nocodazole, partial inhibition), Actin inhibitors (latrunculin B, taxol, pearl recovery)

Oligomycin (pearl recovery)

#### Supplementary Figure 8. Experimental perturbations that influence mitochondrial pearling.

Perturbations are characterized by those that induce pearling across the entire mitochondrial network in the cell (light-green box), those that increase the frequency of spontaneous pearling events (light-blue box), and those that inhibit either the induction or recovery of pearling events (light-red box).

#### References

- Giacomello, M., Pyakurel, A., Glytsou, C. & Scorrano, L. The cell biology of mitochondrial membrane dynamics. *Nat. Rev. Mol. Cell Biol.* 21, 204–224 (2020).
- Tábara, L.-C., Segawa, M. & Prudent, J. Molecular mechanisms of mitochondrial dynamics.
   Nature Reviews Molecular Cell Biology 1–24 (2024).
- 3. Lewis, M. R. & Lewis, W. H. Mitochondria (and other cytoplasmic structures) in tissue cultures. *Am. J. Anat.* **17**, 339–401 (1915).
- Griparic, L., van der Wel, N. N., Orozco, I. J., Peters, P. J. & van der Bliek, A. M. Loss of the Intermembrane Space Protein Mgm1/OPA1 Induces Swelling and Localized Constrictions along the Lengths of Mitochondria \*. J. Biol. Chem. 279, 18792–18798 (2004).
- 5. Cho, B. *et al.* Constriction of the mitochondrial inner compartment is a priming event for mitochondrial division. *Nat. Commun.* **8**, 15754 (2017).
- Zhang, L. et al. Altered brain energetics induces mitochondrial fission arrest in Alzheimer's Disease. Sci. Rep. 6, 18725 (2016).
- 7. Stavru, F., Palmer, A. E., Wang, C., Youle, R. J. & Cossart, P. Atypical mitochondrial fission upon bacterial infection. *Proceedings of the National Academy of Sciences* **110**, 16003–16008 (2013).
- Skulachev, V. P. et al. Thread-grain transition of mitochondrial reticulum as a step of mitoptosis and apoptosis. Mol. Cell. Biochem. 256, 341–358 (2004).
- Labrousse, A. M., Zappaterra, M. D., Rube, D. A. & van der Bliek, A. M. C. elegans dynamin-related protein DRP-1 controls severing of the mitochondrial outer membrane.
   Mol. Cell 4, 815–826 (1999).
- 10. Jaipargas, E.-A., Barton, K. A., Mathur, N. & Mathur, J. Mitochondrial pleomorphy in plant cells is driven by contiguous ER dynamics. *Front. Plant Sci.* **6**, 783 (2015).
- Sawyer, E. M. et al. Developmental regulation of an organelle tether coordinates mitochondrial remodeling in meiosis. J. Cell Biol. 218, 559–579 (2019).

- 12. Legesse-Miller, A., Massol, R. H. & Kirchhausen, T. Constriction and Dnm1p recruitment are distinct processes in mitochondrial fission. *Mol. Biol. Cell* **14**, 1953–1963 (2003).
- Wei, D. et al. MitoEM Dataset: Large-scale 3D Mitochondria Instance Segmentation from EM Images. Med. Image Comput. Comput. Assist. Interv. 12265, 66–76 (2020).
- 14. Breckwoldt, M. O. *et al.* Multiparametric optical analysis of mitochondrial redox signals during neuronal physiology and pathology in vivo. *Nat. Med.* **20**, 555–560 (2014).
- 15. Lee, H. & Yoon, Y. Transient contraction of mitochondria induces depolarization through the inner membrane dynamin OPA1 protein. *J. Biol. Chem.* **289**, 11862–11872 (2014).
- Hemel, I. M., Knoops, K., López-Iglesias, C. & Gerards, M. The curse of the red pearl: a fibroblast specific pearl-necklace mitochondrial phenotype caused by phototoxicity. *bioRxiv* 2024.09.05.611420 (2024) doi:10.1101/2024.09.05.611420.
- 17. Yoon, Y., Lee, H., Federico, M. & Sheu, S.-S. Non-conventional mitochondrial permeability transition: Its regulation by mitochondrial dynamics. *Biochim. Biophys. Acta Bioenerg.* **1864**, 148914 (2023).
- Chakrabarti, R. et al. INF2-mediated actin polymerization at the ER stimulates mitochondrial calcium uptake, inner membrane constriction, and division. J. Cell Biol. 217, 251–268 (2018).
- Gäbelein, C. G. et al. Mitochondria transplantation between living cells. PLoS Biol. 20, e3001576 (2022).
- 20. Gonzalez-Rodriguez, D. *et al.* Elastocapillary Instability in Mitochondrial Fission. *Phys. Rev. Lett.* **115**, 088102 (2015).
- 21. Helfrich, W. Elastic properties of lipid bilayers: theory and possible experiments. *Z. Naturforsch. C* **28**, 693–703 (1973).
- 22. Bar-Ziv, R. & Moses, E. Instability and 'pearling' states produced in tubular membranes by competition of curvature and tension. *Phys. Rev. Lett.* **73**, 1392–1395 (1994).
- 23. Markin, V. S., Tanelian, D. L., Jersild, R. A., Jr & Ochs, S. Biomechanics of stretch-induced beading. *Biophys. J.* **76**, 2852–2860 (1999).

- 24. Seifert, U. Configurations of Fluid Membranes and Vesicles. (1997).
- 25. Goldstein, R. E., Nelson, P., Powers, T. & Seifert, U. Front Progagation in the Pearling Instability of Tubular Vesicles. *J. Phys. II* **6**, 767–796 (1996).
- Sanborn, J., Oglecka, K., Kraut, R. S. & Parikh, A. N. Transient pearling and vesiculation of membrane tubes under osmotic gradients. *Faraday Discuss.* 161, 167–76; discussion 273– 303 (2013).
- 27. Heinrich, D., Ecke, M., Jasnin, M., Engel, U. & Gerisch, G. Reversible Membrane Pearling in Live Cells upon Destruction of the Actin Cortex. *Biophys. J.* **106**, 1079 (2014).
- Bar-Ziv, R., Tlusty, T., Moses, E., Safran, S. A. & Bershadsky, A. Pearling in cells: A clue to understanding cell shape. *Proceedings of the National Academy of Sciences* 96, 10140– 10145 (1999).
- 29. Pan, X. et al. Actomyosin-II protects axons from degeneration induced by mild mechanical stress. *J. Cell Biol.* **223**, (2024).
- 30. Griswold, J. M. *et al.* Membrane mechanics dictate axonal pearls-on-a-string morphology and function. *Nat Neurosci* (2024) doi:10.1038/s41593-024-01813-1.
- Setru, S. U. et al. A hydrodynamic instability drives protein droplet formation on microtubules to nucleate branches. *Nat. Phys.* 17, 493–498 (2021).
- 32. Al-Izzi, S. C., Rowlands, G., Sens, P. & Turner, M. S. Hydro-osmotic Instabilities in Active Membrane Tubes. *Phys. Rev. Lett.* **120**, 138102 (2018).
- 33. Dabora, S. L. & Sheetz, M. P. The microtubule-dependent formation of a tubulovesicular network with characteristics of the ER from cultured cell extracts. *Cell* **54**, 27–35 (1988).
- 34. Obara, C. J. *et al.* Motion of VAPB molecules reveals ER–mitochondria contact site subdomains. *Nature* **626**, 169 (2024).
- 35. Espadas, J. *et al.* Dynamic constriction and fission of endoplasmic reticulum membranes by reticulon. *Nat Commun* **10**, 5327 (2019).
- 36. Mendelsohn, R. *et al.* Morphological principles of neuronal mitochondria. *J. Comp. Neurol.* **530**, 886–902 (2022).

- 37. Millett-Sikking, A. & York, A. G. High NA single-objective lightsheet. Github.io (2019).
- 38. Wu, J. et al. Red fluorescent genetically encoded Ca2+ indicators for use in mitochondria and endoplasmic reticulum. *Biochem. J* **464**, 13 (2014).
- 39. Gao, Y., Spahn, C., Heilemann, M. & Kenney, L. J. The Pearling Transition Provides Evidence of Force-Driven Endosomal Tubulation during Salmonella Infection. *MBio* **9**, (2018).
- Brustovetsky, T., Li, V. & Brustovetsky, N. Stimulation of glutamate receptors in cultured hippocampal neurons causes Ca2+-dependent mitochondrial contraction. *Cell Calcium* 46, 18–29 (2009).
- 41. Lee, J.-S. *et al.* Aquaporin-assisted and ER-mediated mitochondrial fission: A hypothesis. *Micron (Oxford, England : 1993)* **47**, 50 (2013).
- 42. Abramov, A. Y. & Duchen, M. R. Actions of ionomycin, 4-BrA23187 and a novel electrogenic Ca2+ ionophore on mitochondria in intact cells. *Cell calcium* **33**, (2003).
- 43. Nicholls, D. G. & Budd, S. L. Mitochondria and Neuronal Survival. *Physiological Reviews* (2000) doi:10.1152/physrev.2000.80.1.315.
- 44. Chakrabarti, R. *et al.* Mitochondrial dysfunction triggers actin polymerization necessary for rapid glycolytic activation. *The Journal of Cell Biology* **221**, e202201160 (2022).
- 45. Kolenc, O. I. & Quinn, K. P. Evaluating Cell Metabolism Through Autofluorescence Imaging of NAD(P)H and FAD. *Antioxid Redox Signal* **30**, 875–889 (2019).
- Lemire, S. et al. Natural NADH and FAD Autofluorescence as Label-Free Biomarkers for Discriminating Subtypes and Functional States of Immune Cells. *International Journal of Molecular Sciences* 23, 2338 (2022).
- 47. Eng, J., Lynch, R. M. & Balaban, R. S. Nicotinamide adenine dinucleotide fluorescence spectroscopy and imaging of isolated cardiac myocytes. *Biophys J* **55**, 621–630 (1989).
- 48. Stoldt, S. *et al.* Mic60 exhibits a coordinated clustered distribution along and across yeast and mammalian mitochondria. *Proc. Natl. Acad. Sci. U. S. A.* **116**, 9853–9858 (2019).
- 49. Chabanon, M. & Rangamani, P. Geometric coupling of helicoidal ramps and curvature-

- inducing proteins in organelle membranes. J. R. Soc. Interface 16, 20190354 (2019).
- 50. Jiang, Z. *et al.* Cardiolipin Regulates Mitochondrial Ultrastructure and Function in Mammalian Cells. *Genes* **13**, 1889 (2022).
- 51. Masala, N. *et al.* Aberrant hippocampal Ca2+ microwaves following synapsin-dependent adeno-associated viral expression of Ca2+ indicators. (2024) doi:10.7554/eLife.93804.
- 52. Lock, J. T. & Parker, I. IP mediated global Ca signals arise through two temporally and spatially distinct modes of Ca release. *Elife* **9**, (2020).
- 53. Melamed-Book, N., Kachalsky, S. G., Kaiserman, I. & Rahamimoff, R. Neuronal calcium sparks and intracellular calcium 'noise'. *Proc Natl Acad Sci U S A* **96**, 15217–15221 (1999).
- 54. Santel, A. & Fuller, M. T. Control of mitochondrial morphology by a human mitofusin. *J Cell Sci* **114**, 867–874 (2001).
- 55. Nangaku, M. *et al.* KIF1B, a novel microtubule plus end-directed monomeric motor protein for transport of mitochondria. *Cell* **79**, 1209–1220 (1994).
- Suresh, P., Galstyan, V., Phillips, R. & Dumont, S. Modeling and mechanical perturbations reveal how spatially regulated anchorage gives rise to spatially distinct mechanics across the mammalian spindle. (2022) doi:10.7554/eLife.79558.
- 57. Kruppa, A. J. & Buss, F. Motor proteins at the mitochondria–cytoskeleton interface. *J. Cell Sci.* **134**, jcs226084 (2021).
- 58. Liu, X. et al. Force-induced tail-autotomy mitochondrial fission and biogenesis of matrix-excluded mitochondrial-derived vesicles for quality control. *Proceedings of the National Academy of Sciences* **121**, e2217019121 (2024).
- Drago, I., De Stefani, D., Rizzuto, R. & Pozzan, T. Mitochondrial Ca2+ uptake contributes to buffering cytoplasmic Ca2+ peaks in cardiomyocytes. *Proceedings of the National Academy of Sciences* 109, 12986–12991 (2012).
- 60. El Hady, A. & Machta, B. B. Mechanical surface waves accompany action potential propagation. *Nature Communications* **6**, 1–7 (2015).
- 61. Huebinger, J., Spindler, J., Holl, K. J. & Koos, B. Quantification of protein mobility and

- associated reshuffling of cytoplasm during chemical fixation. Sci. Rep. 8, 17756 (2018).
- 62. Kim, S. Y. *et al.* Neuronal mitochondrial morphology is significantly affected by both fixative and oxygen level during perfusion. *Front. Mol. Neurosci.* **15**, 1042616 (2022).
- Hinton, A. et al. A Comprehensive Approach to Sample Preparation for Electron
   Microscopy and the Assessment of Mitochondrial Morphology in Tissue and Cultured Cells.

   Advanced Biology 7, 2200202 (2023).
- 64. Walters, G. C. & Usachev, Y. M. Mitochondrial calcium cycling in neuronal function and neurodegeneration. *Front Cell Dev Biol* **11**, 1094356 (2023).
- 65. Picard, M. & Shirihai, O. S. Mitochondrial signal transduction. Cell metabolism 34, (2022).
- 66. Sharma, A., Smith, H. J., Yao, P. & Mair, W. B. Causal roles of mitochondrial dynamics in longevity and healthy aging. *EMBO Rep.* **20**, e48395 (2019).
- 67. Kim, T. W. *et al.* Biphasic Activation of WNT Signaling Facilitates the Derivation of Midbrain Dopamine Neurons from hESCs for Translational Use. *Cell stem cell* **28**, (2021).
- Liu, T. et al. Multi-color live-cell STED nanoscopy of mitochondria with a gentle inner membrane stain. Proceedings of the National Academy of Sciences 119, e2215799119 (2022).
- 69. Lefebvre, A. E. Y. T., Ma, D., Kessenbrock, K., Lawson, D. A. & Digman, M. A. Automated segmentation and tracking of mitochondria in live-cell time-lapse images. *Nat. Methods* **18**, 1091–1102 (2021).
- 70. Lefebvre, A. E. Y. T. *et al.* Nellie: Automated organelle segmentation, tracking, and hierarchical feature extraction in 2D/3D live-cell microscopy. (2024).

## Acknowledgements

First and foremost, I express my deepest gratitude to my supervisor, Prof. Patrick Meraldi, for giving me the incredible opportunity to pursue my PhD in his lab. His unwavering belief in me, continuous support, and invaluable guidance over the past years have shaped not only my research but also my growth as a scientist. I am truly grateful for his mentorship.

I extend my heartfelt thanks to my dearest colleague and friend, Elena Doria (now already PhD), with whom I had the privilege of sharing both a project and a wonderful friendship. Elena, my PhD journey would have been infinitely lonelier without you. From scientific discussions to shared moments of joy and challenge, your presence made this experience immeasurably richer.

To Kristjana Skendo, thank you for your friendship and support. Though you joined the lab in the middle of my PhD, it feels as if you have been here forever. Your kindness, encouragement, and ability to be there in both happy and difficult times have meant the world to me.

A special thank you goes to our incredible lab manager, Dan Harry, whose immense help, both scientifically and personally, has been indispensable. Your generosity, patience, and dedication have made a lasting impact, and my PhD experience would not have been the same without you.

I also wish to thank Amanda Guerreiro, the former PhD student whose project I had the honor of continuing. Amanda, your help at the start of my PhD was invaluable, and I deeply appreciate the knowledge and support you shared. My gratitude extends to Ennio Silvestri and Cedric Castrogiovanni, two former members of our lab who played an important role in my journey. Your insights, collaboration, and camaraderie have left a meaningful imprint on my experience.

A very special thanks goes to Alexandre Thomas for his boundless scientific enthusiasm, encouragement during the publication process, and the ever-present positive energy that made every discussion and challenge a little lighter.

I also extend my sincere appreciation to all the members of the Meraldi lab, Devashish, Batuhan, Sheba and Crissalida, Mireia and George for their thought-provoking discussions and support.

I am deeply grateful to the Gotta lab, especially to Sofia Barbieri. Sofia, your friendship, your support—both scientific and personal—and all the unforgettable moments we shared have meant so much to me. Thank you for making these years so much more joyful! A heartfelt thank you to Prof. Monica Gotta for her valuable insights and engaging discussions during lab meetings, which enriched my project in many ways. Also, I would like to extend my gratitude to all the present and past members

of Gotta lab: Ece, Merve, Francoise, William, Victoria, Adriano and Yi. Thank you all for all the fun time we had, all the games and outings!

I would also like to extend my sincere thanks to Prof. Vladimir Katanaev for his support with the HumanaFly facility. A special acknowledgment goes to Mikhail Savitsky, whose help with our Drosophila experiments was not only scientifically invaluable but always accompanied by kindness.

I am especially grateful to my thesis committee: Prof. Ivana Gasic, Prof. Miriam Ströber and Prof. Alexis Barr for their willingness to be a part of my committee. I thank you for this! I would like to acknowledge the Bioimaging Facility and in particular Nicolas Liaudet who helped me a lot for data analysis. I also would like to thank FACS Facility and Bioinformatic facility of the Faculty of Medicine at the University of Geneva whose expertise greatly contributed to my work. My thanks also go to the Department of Physiology and Metabolism for the stimulating discussions. Also, the support of assistant staff, Tamara, Carole and Veronique has been invaluable. Finally, I thank the University of Geneva and the Swiss National Foundation for their generous support throughout my PhD.

A very special place in my heart is reserved for the Marine Biology Laboratory and the past Physiology course directors, Prof. Nicole King and Prof. Daniel Fletcher, for accepting me into the course and giving me the opportunity to spend two of the most scientifically enriching and inspiring months of my life. This experience was truly exceptional, and I will always cherish the lessons I learned and the incredible people I met. My gratitude extends to the Physiology Course 2023 cohort, the course assistants, and the companies that continue to support this remarkable program. I sincerely hope it continues for years to come. I also wish to thank my collaborators from UCSF, Prof. Wallace Marshall and Gav Sturm, for allowing me to be part of the mitochondria project and for their insightful guidance. I am also profoundly grateful to the grant agencies that supported my participation in this course and the many conferences I attended throughout these years.

Finally, my deepest, most heartfelt thanks go to my partner and best friend, Felicien Gautier. Your unwavering love, patience, and tireless support have been my rock throughout this journey. I could not have done this without you.

To my family, though far away, your constant belief in me has been a source of strength and motivation. A special thank you to Janna and Christoph Lingenfelder for their enduring friendship and emotional support. To all my dear friends, Monica, Jeanne, Jan, and Nikita, thank you for your love, your encouragement, and for always being there for me. Your support has meant more than words can express. To everyone who has been part of my PhD journey in ways big and small, thank you. This thesis is as much yours as it is mine.

## References

A. Guerreiro, P. Meraldi, AA344 and AA345 antibodies recognize the microtubule network in human cells by immunofluorescence. Antib Reports 2, e17 (2019).

A. Janssen, M. van der Burg, K. Szuhai, G. J. P. L. Kops, R. H. Medema, Chromosome Segregation Errors as a Cause of DNA Damage and Structural Chromosome Aberrations. Science 333, 1895–1898 (2011)

Abraham, R. T. (2001). Cell cycle checkpoint signaling through the ATM and ATR kinases. *Genes & development*, 15(17), 2177-2196.

Abuelo, D. (2007, September). Microcephaly syndromes. In *Seminars in pediatric neurology* (Vol. 14, No. 3, pp. 118-127). WB Saunders.

Acuna-Hidalgo, R., Schanze, D., Kariminejad, A., Nordgren, A., Kariminejad, M. H., Conner, P., ... & Zenker, M. (2014). Neu-Laxova syndrome is a heterogeneous metabolic disorder caused by defects in enzymes of the L-serine biosynthesis pathway. *The American Journal of Human Genetics*, 95(3), 285-293.

Adams, M. M., & Carpenter, P. B. (2006). Tying the loose ends together in DNA double strand break repair with 53BP1. *Cell division*, 1, 1-13.

Addi, C., Presle, A., Frémont, S., Cuvelier, F., Rocancourt, M., Milin, F., ... & Echard, A. (2020). The Flemmingsome reveals an ESCRT-to-membrane coupling via ALIX/syntenin/syndecan-4 required for completion of cytokinesis. *Nature communications*, *11*(1), 1941.

Afonso, O., Matos, I., Pereira, A. J., Aguiar, P., Lampson, M. A., & Maiato, H. (2014). Feedback control of chromosome separation by a midzone Aurora B gradient. Science, 345(6194), 332-336.

Afza, F., Singh, N., Shriya, S., Bisoyi, P., Kashyap, A. K., & Jain, B. P. (2022). Genome wide identification and analysis of WD40 domain containing proteins in Danio rerio. *Gene Reports*, *26*, 101426.

Alfaro-Aco, R., Thawani, A., & Petry, S. (2017). Structural analysis of the role of TPX2 in branching microtubule nucleation. *Journal of Cell Biology*, *216*(4), 983-997.

Alfaro-Aco, R., Thawani, A., & Petry, S. (2020). Biochemical reconstitution of branching microtubule nucleation. *Elife*, *9*, e49797.

Almeida, A. C., & Maiato, H. (2018). Chromokinesins. Current Biology, 28(19), R1131-R1135.

Álvarez-Fernández, M., & Malumbres, M. (2014). Preparing a cell for nuclear envelope breakdown: spatio-temporal control of phosphorylation during mitotic entry. Bioessays, 36(8), 757-765.

Amaro, A. C., Samora, C. P., Holtackers, R., Wang, E., Kingston, I. J., Alonso, M., ... & Meraldi, P. (2010). Molecular control of kinetochore-microtubule dynamics and chromosome oscillations. Nature cell biology, 12(4), 319-329.

Amin, M. A., McKenney, R. J., & Varma, D. (2018). Antagonism between the dynein and Ndc80 complexes at kinetochores controls the stability of kinetochore–microtubule attachments during mitosis. Journal of Biological Chemistry, 293(16), 5755-5765.

Arquint, C., & Nigg, E. A. (2016). The PLK4–STIL–SAS-6 module at the core of centriole duplication. Biochemical Society Transactions, 44(5), 1253-1263.

Ashraf, M., & Godward, M. B. E. (1980). The nucleolus in telophase, interphase and prophase. *Journal of Cell Science*, *41*(1), 321-329.

Atwood, S. X., & Prehoda, K. E. (2009). Phosphorylation-mediated cortical displacement of fate determinants by aPKC during neuroblast asymmetric cell division. Current biology: CB, 19(9), 723.

Baines, A. J., Bignone, P. A., King, M. D., Maggs, A. M., Bennett, P. M., Pinder, J. C., & Phillips, G. W. (2009). The CKK domain (DUF1781) binds microtubules and defines the CAMSAP/ssp4 family of animal proteins. *Molecular biology and evolution*, 26(9), 2005-2014.

Baldin, V., Lukas, J., Marcote, M. J., Pagano, M., & Draetta, G. (1993). Cyclin D1 is a nuclear protein required for cell cycle progression in G1. Genes & development, 7(5), 812-821.

Bally-Cuif, L., & Hammerschmidt, M. (2003). Induction and patterning of neuronal development, and its connection to cell cycle control. *Current opinion in neurobiology*, 13(1), 16-25.

Bankhead, M. B. Loughrey, J. A. Fernández, Y. Dombrowski, D. G. McArt, P. D. Dunne, S. McQuaid, R. T. Gray, L. J. Murray, H. G. Coleman, J. A. James, M. Salto-Tellez, P. W. Hamilton, QuPath: Open source software for digital pathology image analysis. Sci. Rep. 7, 16878 (2017)

Barbosa, J., Sunkel, C. E., & Conde, C. (2022). The role of mitotic kinases and the RZZ complex in kinetochore-microtubule attachments: doing the right link. Frontiers in Cell and Developmental Biology, 10, 787294.

Barisic, M., & Rajendraprasad, G. (2021). Mitotic poleward flux: Finding balance between microtubule dynamics and sliding. *Bioessays*, 43(8), 2100079.

Barisic, M., Rajendraprasad, G., & Steblyanko, Y. (2021, September). The metaphase spindle at steady state—Mechanism and functions of microtubule poleward flux. In *Seminars in cell & developmental biology* (Vol. 117, pp. 99-117). Academic Press.

Barr, A. R., & Gergely, F. (2008). MCAK-independent functions of ch-Tog/XMAP215 in microtubule plus-end dynamics. *Molecular and cellular biology*, *28*(23), 7199-7211.

Bastaki, F., Mohamed, M., Nair, P., Saif, F., Tawfiq, N., Aithala, G., ... & Hamzeh, A. R. (2016). Novel splice-site mutation in WDR 62 revealed by whole-exome sequencing in a S udanese family with primary microcephaly. *Congenital Anomalies*, *56*(3), 135-137.

Basto, R. et al. Centrosome amplification can initiate tumorigenesis in flies. Cell 133, 1032–1042 (2008).

Basto, R., Lau, J., Vinogradova, T., Gardiol, A., Woods, C. G., Khodjakov, A., & Raff, J. W. (2006). Flies without centrioles. *Cell*, 125(7), 1375-1386.

Bates, S., Ryan, K. M., Phillips, A. C., & Vousden, K. H. (1998). Cell cycle arrest and DNA endoreduplication following p21Waf1/Cip1 expression. Oncogene, 17(13), 1691-1703.

Begley, M. A., Solon, A. L., Davis, E. M., Sherrill, M. G., Ohi, R., & Elting, M. W. (2021). K-fiber bundles in the mitotic spindle are mechanically reinforced by Kif15. Molecular Biology of the Cell, 32(22), br11.

Bekker-Jensen, S., Lukas, C., Melander, F., Bartek, J., & Lukas, J. (2005). Dynamic assembly and sustained retention of 53BP1 at the sites of DNA damage are controlled by Mdc1/NFBD1. The Journal of cell biology, 170(2), 201-211.

Belmonte-Mateos, C., & Pujades, C. (2022). From cell states to cell fates: how cell proliferation and neuronal differentiation are coordinated during embryonic development. Frontiers in Neuroscience, 15, 781160.

Bertran, M. T., Sdelci, S., Regué, L., Avruch, J., Caelles, C., & Roig, J. (2011). Nek9 is a Plk1-activated kinase that controls early centrosome separation through Nek6/7 and Eg5. *The EMBO journal*, 30(13), 2634-2647.

Besson, A., Dowdy, S. F., & Roberts, J. M. (2008). CDK inhibitors: cell cycle regulators and beyond. Developmental cell, 14(2), 159-169.

Bhat, V., Girimaji, S. C., Mohan, G., Arvinda, H. R., Singhmar, P., Duvvari, M. R., & Kumar, A. (2011). Mutations in WDR62, encoding a centrosomal and nuclear protein, in Indian primary microcephaly families with cortical malformations. *Clinical genetics*, 80(6), 532-540.

Bilgüvar, K., Öztürk, A. K., Louvi, A., Kwan, K. Y., Choi, M., Tatlı, B., ... & Günel, M. (2010). Whole-exome sequencing identifies recessive WDR62 mutations in severe brain malformations. *Nature*, *467*(7312), 207-210.

Bishop, K. M., Goudreau, G., & O'Leary, D. D. (2000). Regulation of area identity in the mammalian neocortex by Emx2 and Pax6. *Science*, *288*(5464), 344-349.

Bishop, K. M., Rubenstein, J. L., & O'Leary, D. D. (2002). Distinct actions of Emx1, Emx2, andPax6 in regulating the specification of areas in the developing neocortex. *Journal of Neuroscience*, 22(17), 7627-7638.

Bizard, A. H., & Hickson, I. D. (2018). Anaphase: a fortune-teller of genomic instability. *Current opinion in cell biology*, *52*, 112-119.

Blanco-Ameijeiras, J., Lozano-Fernández, P., & Martí, E. (2022). Centrosome maturation—in tune with the cell cycle. *Journal of Cell Science*, 135(2), jcs259395.

Bleiler, M., Cyr, A., Wright, D. L., & Giardina, C. (2023). Incorporation of 53BP1 into phase-separated bodies in cancer cells during aberrant mitosis. *Journal of Cell Science*, 136(1), jcs260027.

Bogoyevitch, M. A., Yeap, Y. Y., Qu, Z., Ngoei, K. R., Yip, Y. Y., Zhao, T. T., ... & Ng, D. C. (2012). WD40-repeat protein 62 is a JNK-phosphorylated spindle pole protein required for spindle maintenance and timely mitotic progression. Journal of cell science, 125(21), 5096-5109.

Bolat, H., Sağer, S. G., Türkyılmaz, A., Çebi, A. H., Akın, Y., Onay, H., ... & Ünsel-Bolat, G. (2022). Autosomal recessive primary microcephaly (MCPH) and novel pathogenic variants in ASPM and WDR62 genes. Molecular Syndromology, 13(5), 363-369.

Bond, J., Roberts, E., Mochida, G. H., Hampshire, D. J., Scott, S., Askham, J. M., ... & Woods, C. G. (2002). ASPM is a major determinant of cerebral cortical size. *Nature genetics*, *32*(2), 316-320.

Booth, D. G., Hood, F. E., Prior, I. A., & Royle, S. J. A TACC3/ch-TOG/clathrin complex stabilises kinetochore fibres by inter-microtubule bridging. *EMBO J.* 30, 906–919 (2011).

Brito, C., Serna, M., Guerra, P., Llorca, O., & Surrey, T. (2024). Transition of human γ-tubulin ring complex into a closed conformation during microtubule nucleation. *Science*, *383*(6685), 870-876.

Brito, D. A., & Rieder, C. L. (2006). Mitotic checkpoint slippage in humans occurs via cyclin B destruction in the presence of an active checkpoint. *Current Biology*, *16*(12), 1194-1200.

Bromley, B., & Benacerraf, B. R. (1995). Difficulties in the prenatal diagnosis of microcephaly. *Journal of ultrasound in medicine*, *14*(4), 303-306.

Brouhard, G. J. (2004). *Polar ejection forces in mitosis*. University of Michigan.

Brouhard, G. J., & Rice, L. M. (2018). Microtubule dynamics: an interplay of biochemistry and mechanics. *Nature reviews Molecular cell biology*, 19(7), 451-463.

Brust-Mascher, I., & Scholey, J. M. (2011). Mitotic motors and chromosome segregation: the mechanism of anaphase B. Biochemical Society Transactions, 39(5), 1149-1153.

Burigotto, M., Vigorito, V., Gliech, C., Mattivi, A., Ghetti, S., Bisio, A., ... & Fava, L. L. (2023). PLK1 promotes the mitotic surveillance pathway by controlling cytosolic 53BP1 availability. *EMBO reports*, *24*(12), e57234.

Cabral, G., Laos, T., Dumont, J., & Dammermann, A. (2019). Differential requirements for centrioles in mitotic centrosome growth and maintenance. Developmental Cell, 50(3), 355-366.

Caillat, C., & Perrakis, A. (2012). Cdt1 and geminin in DNA replication initiation. The Eukaryotic Replisome: a Guide to Protein Structure and Function, 71-87.

Caldecott, K. W. (2008). Single-strand break repair and genetic disease. *Nature Reviews Genetics*, 9(8), 619-631.

Calegari, F., & Huttner, W. B. (2003). An inhibition of cyclin-dependent kinases that lengthens, but does not arrest, neuroepithelial cell cycle induces premature neurogenesis. *Journal of cell science*, *116*(24), 4947-4955.

Carazo-Salas, R. E., Gruss, O. J., Mattaj, I. W., & Karsenti, E. (2001). Ran–GTP coordinates regulation of microtubule nucleation and dynamics during mitotic-spindle assembly. *Nature cell biology*, *3*(3), 228-234.

Carmena, M., Wheelock, M., Funabiki, H., & Earnshaw, W. C. (2012). The chromosomal passenger complex (CPC): from easy rider to the godfather of mitosis. Nature reviews Molecular cell biology, 13(12), 789-803.

Cassimeris, L. U., Walker, R. A., Pryer, N. K., & Salmon, E. D. (1987). Dynamic instability of microtubules. *Bioessays*, 7(4), 149-154.

Chan, G. K., Liu, S. T., & Yen, T. J. (2005). Kinetochore structure and function. *Trends in cell biology*, 15(11), 589-598

Cheerambathur, D. K., Prevo, B., Hattersley, N., Lewellyn, L., Corbett, K. D., Oegema, K., & Desai, A. (2017). Dephosphorylation of the Ndc80 tail stabilizes kinetochore-microtubule attachments via the Ska complex. Developmental Cell, 41(4), 424-437.

Cheeseman, I. M., Chappie, J. S., Wilson-Kubalek, E. M., & Desai, A. (2006). The conserved KMN network constitutes the core microtubule-binding site of the kinetochore. Cell, 127(5), 983-997.

Chen, J. F., Zhang, Y., Wilde, J., Hansen, K. C., Lai, F., & Niswander, L. (2014). Microcephaly disease gene Wdr62 regulates mitotic progression of embryonic neural stem cells and brain size. *Nature communications*, *5*(1), 3885.

Chuang, M., Goncharov, A., Wang, S., Oegema, K., Jin, Y., & Chisholm, A. D. (2014). The microtubule minus-end-binding protein patronin/PTRN-1 is required for axon regeneration in C. elegans. *Cell reports*, *9*(3), 874-883.

Chumová, J., Kourová, H., Trögelová, L., Daniel, G., & Binarová, P. (2021). γ-tubulin complexes and fibrillar arrays: Two conserved high molecular forms with many cellular functions. *Cells*, 10(4), 776.

Cimini, D. (2023). Twenty years of merotelic kinetochore attachments: a historical perspective. *Chromosome Research*, 31(3), 18.

Cimini, D., Wan, X., Hirel, C. B., & Salmon, E. D. (2006). Aurora kinase promotes turnover of kinetochore microtubules to reduce chromosome segregation errors. Current Biology, 16(17), 1711-1718.

Clarke, P. R., & Zhang, C. (2008). Spatial and temporal coordination of mitosis by Ran GTPase. *Nature reviews Molecular cell biology*, *9*(6), 464-477.

Cooke, C. A., Schaar, B., Yen, T. J., & Earnshaw, W. C. (1997). Localization of CENP-E in the fibrous corona and outer plate of mammalian kinetochores from prometaphase through anaphase. *Chromosoma*, 106(7), 446-455.

Craske, B., & Welburn, J. P. (2020). Leaving no-one behind: how CENP-E facilitates chromosome alignment. Essays in biochemistry, 64(2), 313-324.

Crasta, K., Ganem, N. J., Dagher, R., Lantermann, A. B., Ivanova, E. V., Pan, Y., ... & Pellman, D. (2012). DNA breaks and chromosome pulverization from errors in mitosis. *Nature*, *482*(7383), 53-58.

Crews, S. T. (2019). Drosophila embryonic CNS development: neurogenesis, gliogenesis, cell fate, and differentiation. *Genetics*, 213(4), 1111-1144.

Dalton, S. (2015). Linking the cell cycle to cell fate decisions. Trends in cell biology, 25(10), 592-600.

Dasika, G. K., Lin, S. C. J., Zhao, S., Sung, P., Tomkinson, A., & Lee, E. Y. (1999). DNA damage-induced cell cycle checkpoints and DNA strand break repair in development and tumorigenesis. *Oncogene*, *18*(55), 7883-7899.

David, A. F., Roudot, P., Legant, W. R., Betzig, E., Danuser, G., & Gerlich, D. W. (2019). Augmin accumulation on long-lived microtubules drives amplification and kinetochore-directed growth. *Journal of Cell Biology*, *218*(7), 2150-2168.

Daynac, M., & Petritsch, C. K. (2017). Regulation of asymmetric cell division in mammalian neural stem and cancer precursor cells. Asymmetric cell division in development, differentiation and cancer, 375-399.

De Miguel, M. P., Montiel, F. A., Iglesias, P. L., Martinez, A. B., & Nistal, M. (2009). Epiblast-derived stem cells in embryonic and adult tissues. *International Journal of Developmental Biology*, *53*(8-9-10), 1529-1540.

De Wulf, P., McAinsh, A. D., & Sorger, P. K. (2003). Hierarchical assembly of the budding yeast kinetochore from multiple subcomplexes. Genes & development, 17(23), 2902-2921.

Dehaene, M. (2019). Heterotopia. The Wiley Blackwell encyclopedia of urban and regional studies, 1-4.

del Mar Mora-Santos, M., Hervas-Aguilar, A., Sewart, K., Lancaster, T. C., Meadows, J. C., & Millar, J. B. (2016). Bub3-Bub1 binding to Spc7/KNL1 toggles the spindle checkpoint switch by licensing the interaction of Bub1 with Mad1-Mad2. Current Biology, 26(19), 2642-2650.

DeLuca, K. F., Meppelink, A., Broad, A. J., Mick, J. E., Peersen, O. B., Pektas, S., ... & DeLuca, J. G. (2018). Aurora A kinase phosphorylates Hec1 to regulate metaphase kinetochore–microtubule dynamics. Journal of Cell Biology, 217(1), 163-177.

Dicke, U., & Roth, G. (2016). Neuronal factors determining high intelligence. Philosophical Transactions of the Royal Society B: Biological Sciences, 371(1685), 20150180.

Dionne, L. K., Wang, X. J., & Prekeris, R. (2015). Midbody: from cellular junk to regulator of cell polarity and cell fate. *Current opinion in cell biology*, *35*, 51-58.

Dobrynin, G., Popp, O., Romer, T., Bremer, S., Schmitz, M. H., Gerlich, D. W., & Meyer, H. (2011). Cdc48/p97–Ufd1–Npl4 antagonizes Aurora B during chromosome segregation in HeLa cells. Journal of cell science, 124(9), 1571-1580.

Doria, E., Ivanova, D., Thomas, A., & Meraldi, P. (2024). Transient lagging chromosomes cause primary microcephaly. bioRxiv, 2024-05.

Dou, Z., Ghosh, K., Vizioli, M. G., Zhu, J., Sen, P., Wangensteen, K. J., ... & Berger, S. L. (2017). Cytoplasmic chromatin triggers inflammation in senescence and cancer. Nature, 550(7676), 402-406.

Driscoll, M.K.; Albanese, J.L.; Xiong, Z.-M.; Mailman, M.; Losert, W.; Cao, K. Automated image analysis of nuclear shape: What can we learn from a prematurely aged cell? Aging 2012, 4, 119–132. [CrossRef] [PubMed]

Drpic, D., Almeida, A. C., Aguiar, P., Renda, F., Damas, J., Lewin, H. A., ... & Maiato, H. (2018). Chromosome segregation is biased by kinetochore size. *Current Biology*, 28(9), 1344-1356.

Dudka, D., Noatynska, A., Smith, C. A., Liaudet, N., McAinsh, A. D., & Meraldi, P. (2018). Complete microtubule–kinetochore occupancy favours the segregation of merotelic attachments. *Nature communications*, *9*(1), 2042.

Duffy, J. B. (2002). GAL4 system in Drosophila: a fly geneticist's Swiss army knife. genesis, 34(1-2), 1-15.

Dumont, S., & Mitchison, T. J. (2009). Force and length in the mitotic spindle. *Current Biology*, 19(17), R749-R761.

Egger, B., Gold, K. S., & Brand, A. H. (2011). Regulating the balance between symmetric and asymmetric stem cell division in the developing brain. *Fly*, *5*(3), 237-241.

Elia, N., Sougrat, R., Spurlin, T. A., Hurley, J. H., & Lippincott-Schwartz, J. (2011). Dynamics of endosomal sorting complex required for transport (ESCRT) machinery during cytokinesis and its role in abscission. *Proceedings of the National Academy of Sciences*, 108(12), 4846-4851.

Ems-McClung, S. C., & Walczak, C. E. (2010, May). Kinesin-13s in mitosis: Key players in the spatial and temporal organization of spindle microtubules. In *Seminars in cell & developmental biology* (Vol. 21, No. 3, pp. 276-282). Academic Press.

Eytan, E., Moshe, Y., Braunstein, I., & Hershko, A. (2006). Roles of the anaphase-promoting complex/cyclosome and of its activator Cdc20 in functional substrate binding. Proceedings of the National Academy of Sciences, 103(7), 2081-2086.

Fame, R. M., Cortés-Campos, C., & Sive, H. L. (2020). Brain ventricular system and cerebrospinal fluid development and function: light at the end of the tube: a primer with latest insights. *BioEssays*, *42*(3), 1900186.

Feng, Y., & Walsh, C. A. (2004). Mitotic spindle regulation by Nde1 controls cerebral cortical size. *Neuron*, *44*(2), 279-293.

Fernandez-Capetillo, O., Chen, H. T., Celeste, A., Ward, I., Romanienko, P. J., Morales, J. C., ... & Nussenzweig, A. (2002). DNA damage-induced G2–M checkpoint activation by histone H2AX and 53BP1. *Nature cell biology*, *4*(12), 993-997.

Ferrari, S. (2006). Protein kinases controlling the onset of mitosis. *Cellular and Molecular Life Sciences CMLS*, 63, 781-795.

Ferrer, I., & Catalá, I. (1991). Unlayered polymicrogyria: structural and developmental aspects. *Anatomy and embryology*, 184, 517-528.

Fietz, S. A., & Huttner, W. B. (2011). Cortical progenitor expansion, self-renewal and neurogenesis—a polarized perspective. *Current opinion in neurobiology*, *21*(1), 23-35.

Fish, J. L., Kosodo, Y., Enard, W., Pääbo, S., & Huttner, W. B. (2006). Aspm specifically maintains symmetric proliferative divisions of neuroepithelial cells. *Proceedings of the National Academy of Sciences*, 103(27), 10438-10443.

FitzHarris, G. (2012). Anaphase B precedes anaphase A in the mouse egg. Current Biology, 22(5), 437-444.

Flores-Sarnat, L. (2002). Hemimegalencephaly: part 1. Genetic, clinical, and imaging aspects. *Journal of child neurology*, 17(5), 373-384.

Florio, M., & Huttner, W. B. (2014). Neural progenitors, neurogenesis and the evolution of the neocortex. *Development*, 141(11), 2182-2194.

Flynn, P. J., Koch, P. D., & Mitchison, T. J. (2021). Chromatin bridges, not micronuclei, activate cGAS after drug-induced mitotic errors in human cells. *Proceedings of the National Academy of Sciences*, 118(48), e2103585118.

Fong K.W., Choi Y.K., Rattner J.B., Qi R.Z.. 2008. CDK5RAP2 is a pericentriolar protein that functions in centrosomal attachment of the y-tubulin ring complex. Mol. Biol. Cell. 19:115–125.

Fong, C. S., Mazo, G., Das, T., Goodman, J., Kim, M., O'Rourke, B. P., ... & Tsou, M. F. B. (2016). 53BP1 and USP28 mediate p53-dependent cell cycle arrest in response to centrosome loss and prolonged mitosis. *Elife*, *5*, e16270.

Fonseca, C. L., Malaby, H. L., Sepaniac, L. A., Martin, W., Byers, C., Czechanski, A., ... & Stumpff, J. (2019). Mitotic chromosome alignment ensures mitotic fidelity by promoting interchromosomal compaction during anaphase. *Journal of Cell Biology*, *218*(4), 1148-1163.

Fonseca, C. L., Malaby, H. L., Sepaniac, L. A., Martin, W., Byers, C., Czechanski, A., ... & Stumpff, J. (2019). Mitotic chromosome alignment ensures mitotic fidelity by promoting interchromosomal compaction during anaphase. *Journal of Cell Biology*, *218*(4), 1148-1163.

Ford JH, Schultz CJ, Correll AT . Chromosome elimination in micronuclei: a common cause of hypoploidy. Am J Hum Genet 1988; 43:733–740.

Fujimori, A., Itoh, K., Goto, S., Hirakawa, H., Wang, B., Kokubo, T., ... & Fushiki, S. (2014). Disruption of Aspm causes microcephaly with abnormal neuronal differentiation. *Brain and Development*, *36*(8), 661-669.

Gai, M., Bianchi, F. T., Vagnoni, C., Vernì, F., Bonaccorsi, S., Pasquero, S., ... & Di Cunto, F. (2016). ASPM and CITK regulate spindle orientation by affecting the dynamics of astral microtubules. *EMBO reports*, *17*(10), 1396-1409.

Galjart, N. (2005). CLIPs and CLASPs and cellular dynamics. Nature reviews Molecular cell biology, 6(6), 487-498.

Ganem, N. J., Upton, K., & Compton, D. A. (2005). Efficient mitosis in human cells lacking poleward microtubule flux. *Current biology*, *15*(20), 1827-1832.

Gardner, M. K., Zanic, M., Gell, C., Bormuth, V., & Howard, J. (2011). Depolymerizing kinesins Kip3 and MCAK shape cellular microtubule architecture by differential control of catastrophe. Cell, 147(5), 1092-1103.

Gartel, A. L., Serfas, M. S., & Tyner, A. L. (1996). p21—negative regulator of the cell cycle. *Proceedings of the Society for Experimental Biology and Medicine*, 213(2), 138-149.

Ge, S., Skaar, J. R., & Pagano, M. (2009). APC/C-and Mad2-mediated degradation of Cdc20 during spindle checkpoint activation. Cell cycle, 8(1), 167-171.

Giacinti, C., & Giordano, A. (2006). RB and cell cycle progression. Oncogene, 25(38), 5220-5227.

Gil-Sanz, C., Franco, S. J., Martinez-Garay, I., Espinosa, A., Harkins-Perry, S., & Müller, U. (2013). Cajal-Retzius cells instruct neuronal migration by coincidence signaling between secreted and contact-dependent guidance cues. *Neuron*, *79*(3), 461-477.

Gimona, M., & Winder, S. J. (2005). The calponin homology (CH) domain. *Wiley-VCH Verlag GmbH & Co. KGaA, Weinheim*.

Glickstein, S. B., Monaghan, J. A., Koeller, H. B., Jones, T. K., & Ross, M. E. (2009). Cyclin D2 is critical for intermediate progenitor cell proliferation in the embryonic cortex. *Journal of Neuroscience*, *29*(30), 9614-9624.

Glotzer, M. (1997). Cytokinesis. Current Biology, 7(5), R274-R276.

Goffinet, A. M., Bar, I., Bernier, B., Trujillo, C., Raynaud, A., & Meyer, G. (1999). Reelin expression during embryonic brain development in lacertilian lizards. *Journal of Comparative Neurology*, 414(4), 533-550.

Gogendeau, D., K. Siudeja, D. Gambarotto, C. Pennetier, A.J. Bardin, and R. Basto. 2015. Aneuploidy causes premature differentiation of neural and intestinal stem cells. Nat. Commun. 6:8894.

Gomez-Ferreria, M. A., Bashkurov, M., Helbig, A. O., Larsen, B., Pawson, T., Gingras, A. C., & Pelletier, L. (2012). Novel NEDD1 phosphorylation sites regulate  $\gamma$ -tubulin binding and mitotic spindle assembly. Journal of cell science, 125(16), 3745-3751.

Goodwin, S. S., & Vale, R. D. (2010). Patronin regulates the microtubule network by protecting microtubule minus ends. *Cell*, *143*(2), 263-274.

Gorbsky, G. J., & Borisy, G. G. (1989). Microtubules of the kinetochore fiber turn over in metaphase but not in anaphase. *Journal of Cell Biology*, *109*(2), 653-662.

Gorbsky, G. J., Simerly, C., Schatten, G., & Borisy, G. G. (1990). Microtubules in the metaphase-arrested mouse oocyte turn over rapidly. Proceedings of the National Academy of Sciences, 87(16), 6049-6053.

Goshima, G., Mayer, M., Zhang, N., Stuurman, N., & Vale, R. D. (2008). Augmin: a protein complex required for centrosome-independent microtubule generation within the spindle. *The Journal of cell biology*, *181*(3), 421-429.

Goto, H., Yasui, Y., Kawajiri, A., Nigg, E. A., Terada, Y., Tatsuka, M., ... & Inagaki, M. (2003). Aurora-B regulates the cleavage furrow-specific vimentin phosphorylation in the cytokinetic process. Journal of Biological Chemistry, 278(10), 8526-8530.

Green, R. A., Paluch, E., & Oegema, K. (2012). Cytokinesis in animal cells. *Annual review of cell and developmental biology*, *28*(1), 29-58.

Gregan, J., Polakova, S., Zhang, L., Tolić-Nørrelykke, I. M., & Cimini, D. (2011). Merotelic kinetochore attachment: causes and effects. *Trends in cell biology*, *21*(6), 374-381.

Gruss, O. J., & Vernos, I. (2004). The mechanism of spindle assembly: functions of Ran and its target TPX2. *The Journal of cell biology*, *166*(7), 949-955.

Guan, C., Hua, S., & Jiang, K. (2023). The CEP170B-KIF2A complex destabilizes microtubule minus ends to generate polarized microtubule network. *The EMBO Journal*, 42(11), e112953.

Guerreiro, A., De Sousa, F., Liaudet, N., Ivanova, D., Eskat, A., & Meraldi, P. (2021). WDR62 localizes katanin at spindle poles to ensure synchronous chromosome segregation. *Journal of Cell Biology*, 220(8), e202007171.

Güller, M., Toualbi-Abed, K., Legrand, A., Michel, L., Mauviel, A., Bernuau, D., & Daniel, F. (2008). c-Fos overexpression increases the proliferation of human hepatocytes by stabilizing nuclear Cyclin D1. World journal of gastroenterology: WJG, 14(41), 6339.

Gutierrez, C. (2022). A journey to the core of the plant cell cycle. International Journal of Molecular Sciences, 23(15), 8154.

Hannan, A. J., Servotte, S., Katsnelson, A., Sisodiya, S., Blakemore, C., Squier, M., & Molnár, Z. (1999). Characterization of nodular neuronal heterotopia in children. *Brain*, *122*(2), 219-238.

Haubst, N., Georges-Labouesse, E., De Arcangelis, A., Mayer, U., & Götz, M. (2006). Basement membrane attachment is dispensable for radial glial cell fate and for proliferation, but affects positioning of neuronal subtypes.

Heald, R., & Khodjakov, A. (2015). Thirty years of search and capture: The complex simplicity of mitotic spindle assembly. *Journal of Cell Biology*, 211(6), 1103-1111.

Hendershott, M. C., & Vale, R. D. (2014). Regulation of microtubule minus-end dynamics by CAMSAPs and Patronin. *Proceedings of the National Academy of Sciences*, 111(16), 5860-5865.

Henkin, G., Chew, W. X., Nédélec, F., & Surrey, T. (2022). Cross-linker design determines microtubule network organization by opposing motors. *Proceedings of the National Academy of Sciences*, 119(33), e2206398119.

Henne, W. M., Buchkovich, N. J., & Emr, S. D. (2011). The ESCRT pathway. Developmental cell, 21(1), 77-91.

Herculano-Houzel, S. (2009). The human brain in numbers: a linearly scaled-up primate brain. *Frontiers in human neuroscience*, *3*, 857.https://doi.org/10.1073/pnas.0611396104

Higgins, J., Midgley, C., Bergh, A. M., Bell, S. M., Askham, J. M., Roberts, E., ... & Bond, J. (2010). Human ASPM participates in spindle organisation, spindle orientation and cytokinesis. *BMC cell biology*, *11*, 1-17.

Hinchcliffe, E. H., Day, C. A., Karanjeet, K. B., Fadness, S., Langfald, A., Vaughan, K. T., & Dong, Z. (2016). Chromosome missegregation during anaphase triggers p53 cell cycle arrest through histone H3. 3 Ser31 phosphorylation. *Nature cell biology*, *18*(6), 668-675.

Hindriksen, S., Lens, S. M., & Hadders, M. A. (2017). The ins and outs of Aurora B inner centromere localization. *Frontiers in cell and developmental biology*, *5*, 112.

Hirano, T. (2006). At the heart of the chromosome: SMC proteins in action. *Nature reviews Molecular cell biology*, *7*(5), 311-322.

Hirota, Y., & Nakajima, K. (2017). Control of neuronal migration and aggregation by reelin signaling in the developing cerebral cortex. *Frontiers in cell and developmental biology*, *5*, 40.

Hiruma, Y., Sacristan, C., Pachis, S. T., Adamopoulos, A., Kuijt, T., Ubbink, M., ... & Kops, G. J. (2015). Competition between MPS1 and microtubules at kinetochores regulates spindle checkpoint signaling. Science, 348(6240), 1264-1267.

Homem, C. C., & Knoblich, J. A. (2012). Drosophila neuroblasts: a model for stem cell biology. *Development*, 139(23), 4297-4310.

Hu, C. K., Coughlin, M., Field, C. M., & Mitchison, T. J. (2011). KIF4 regulates midzone length during cytokinesis. *Current Biology*, *21*(10), 815-824.

Huang, J., Liang, Z., Guan, C., Hua, S., & Jiang, K. (2021). WDR62 regulates spindle dynamics as an adaptor protein between TPX2/Aurora A and katanin. *Journal of Cell Biology*, 220(8), e202007167.

Hueschen, C. L., Kenny, S. J., Xu, K., & Dumont, S. (2017). NuMA recruits dynein activity to microtubule minusends at mitosis. Elife, 6, e29328.

Huitorel, P., & Kirschner, M. W. (1988). The polarity and stability of microtubule capture by the kinetochore. Journal of Cell Biology, 106(1), 151-159.

lemura, K., & Tanaka, K. (2015). Chromokinesin Kid and kinetochore kinesin CENP-E differentially support chromosome congression without end-on attachment to microtubules. Nature communications, 6(1), 6447.

Ip, B. K., Wappler, I., Peters, H., Lindsay, S., Clowry, G. J., & Bayatti, N. (2010). Investigating gradients of gene expression involved in early human cortical development. *Journal of anatomy*, 217(4), 300-311.

Isler, K., & Van Schaik, C. P. (2014). How humans evolved large brains: comparative evidence. Evolutionary Anthropology: Issues, News, and Reviews, 23(2), 65-75.

Ito, K. K., Watanabe, K., & Kitagawa, D. (2020). The emerging role of ncRNAs and RNA-binding proteins in mitotic apparatus formation. *Non-coding RNA*, *6*(1), 13.

Itoh, Y., Moriyama, Y., Hasegawa, T., Endo, T. A., Toyoda, T., & Gotoh, Y. (2013). Scratch regulates neuronal migration onset via an epithelial-mesenchymal transition—like mechanism. *Nature neuroscience*, *16*(4), 416-425.

Jagrić, M., Risteski, P., Martinčić, J., Milas, A., & Tolić, I. M. (2021). Optogenetic control of PRC1 reveals its role in chromosome alignment on the spindle by overlap length-dependent forces. *Elife*, 10, e61170.

Jansen, A., & Andermann, E. (2005). Genetics of the polymicrogyria syndromes. Journal of medical genetics, 42(5), 369-378.

Janssen, A. F., Breusegem, S. Y., & Larrieu, D. (2022). Current methods and pipelines for image-based quantitation of nuclear shape and nuclear envelope abnormalities. *Cells*, 11(3), 347.

Jasin, M., & Rothstein, R. (2013). Repair of strand breaks by homologous recombination. *Cold Spring Harbor perspectives in biology*, *5*(11), a012740.

Jayaraman, D., Bae, B. I., & Walsh, C. A. (2018). The genetics of primary microcephaly. Annual review of genomics and human genetics, 19(1), 177-200.

Jayaraman, D., Kodani, A., Gonzalez, D. M., Mancias, J. D., Mochida, G. H., Vagnoni, C., ... & Walsh, C. A. (2016). Microcephaly proteins Wdr62 and Aspm define a mother centriole complex regulating centriole biogenesis, apical complex, and cell fate. *Neuron*, *92*(4), 813-828.

Jiang, H., & Chan, Y. W. (2024). Chromatin bridges: stochastic breakage or regulated resolution?. *Trends in Genetics*, 40(1), 69-82.

Jiang, K., Hua, S., Mohan, R., Grigoriev, I., Yau, K. W., Liu, Q., ... & Akhmanova, A. (2014). Microtubule minus-end stabilization by polymerization-driven CAMSAP deposition. *Developmental cell*, 28(3), 295-309.

Jiang, K., Rezabkova, L., Hua, S., Liu, Q., Capitani, G., Altelaar, A. M., ... & Akhmanova, A. (2017). Microtubule minus-end regulation at spindle poles by an ASPM–katanin complex. *Nature cell biology*, *19*(5), 480-492.

Jones, M. J., & Jallepalli, P. V. (2012). Chromothripsis: chromosomes in crisis. Developmental cell, 23(5), 908-917.

Joshi, H. C. (1994). Microtubule organizing centers and γ-tubulin. Current opinion in cell biology, 6(1), 55-62.

Jullien, D., Vagnarelli, P., Earnshaw, W. C., & Adachi, Y. (2002). Kinetochore localisation of the DNA damage response component 53BP1 during mitosis. *Journal of cell science*, *115*(1), 71-79.

Kajtez, J., Solomatina, A., Novak, M., Polak, B., Vukušić, K., Rüdiger, J., ... & Tolić, I. M. (2016). Overlap microtubules link sister k-fibres and balance the forces on bi-oriented kinetochores. *Nature communications*, 7(1), 10298.

Kakita, A., Hayashi, S., Moro, F., Guerrini, R., Ozawa, T., Ono, K., ... & Takahashi, H. (2002). Bilateral periventricular nodular heterotopia due to filamin 1 gene mutation: widespread glomeruloid microvascular anomaly and dysplastic cytoarchitecture in the cerebral cortex. *Acta neuropathologica*, 104, 649-657.

Kalebic, N., Gilardi, C., Stepien, B., Wilsch-Bräuninger, M., Long, K. R., Namba, T., ... & Huttner, W. B. (2019). Neocortical expansion due to increased proliferation of basal progenitors is linked to changes in their morphology. Cell stem cell, 24(4), 535-550.

Kapoor, T. M. (2017). Metaphase spindle assembly. Biology, 6(1), 8.

Keating, P., Rachidi, N., Tanaka, T. U., & Stark, M. J. (2009). Ipl1-dependent phosphorylation of Dam1 is reduced by tension applied on kinetochores. Journal of cell science, 122(23), 4375-4382.

Khan, M. A., Rupp, V. M., Orpinell, M., Hussain, M. S., Altmuller, J., Steinmetz, M. O., Enzinger, C., Thiele, H., Hohne, W., Nurnberg, G., Baig, S. M., Ansar, M., Nurnberg, P., Vincent, J. B., Speicher, M. R., Gonczy, P., Windpassinger, C. A missense mutation in the PISA domain of HsSAS-6 causes autosomal recessive primary microcephaly in a large consanguineous Pakistani family. Hum. Molec. Genet. 23: 5940-5949, 2014.

Khanal, I., Elbediwy, A., Diaz de la Loza, M. D. C., Fletcher, G. C., & Thompson, B. J. (2016). Shot and Patronin polarise microtubules to direct membrane traffic and biogenesis of microvilli in epithelia. *Journal of cell science*, 129(13), 2651-2659.

Kilb, W., & Frotscher, M. (2016). Cajal-Retzius cells: organizers of cortical development. *e-Neuroforum*, 22(4), 82-88.

Kilgas, S., Swift, M. L., & Chowdhury, D. (2024). 53BP1-the 'Pandora's box' of genome integrity. *DNA repair*, 103779.

Kim, S., & Yu, H. (2011, August). Mutual regulation between the spindle checkpoint and APC/C. In Seminars in cell & developmental biology (Vol. 22, No. 6, pp. 551-558). Academic Press.

King, M. R., & Petry, S. (2020). Phase separation of TPX2 enhances and spatially coordinates microtubule nucleation. *Nature communications*, *11*(1), 270.

Kirschner, M., & Mitchison, T. (1986). Beyond self-assembly: from microtubules to morphogenesis. *Cell*, 45(3), 329-342.

Klaasen, S. J., Truong, M. A., van Jaarsveld, R. H., Koprivec, I., Štimac, V., de Vries, S. G., ... & Kops, G. J. (2022). Nuclear chromosome locations dictate segregation error frequencies. *Nature*, *607*(7919), 604-609.

Kollu, S., Bakhoum, S. F., & Compton, D. A. (2009). Interplay of microtubule dynamics and sliding during bipolar spindle formation in mammalian cells. Current Biology, 19(24), 2108-2113.

Kon, E., Cossard, A., & Jossin, Y. (2017). Neuronal polarity in the embryonic mammalian cerebral cortex. Frontiers in cellular neuroscience, 11, 163.

Koprivec, I., Štimac, V., Mikec, P., & Tolić, I. M. (2024). Microtubule pivoting driven by spindle elongation rescues polar chromosomes to ensure faithful mitosis. bioRxiv, 2024-06.

Kops, G. J., & Gassmann, R. (2020). Crowning the kinetochore: the fibrous corona in chromosome segregation. Trends in cell biology, 30(8), 653-667.

Kraus, J., Travis, S. M., King, M. R., & Petry, S. (2023). Augmin is a Ran-regulated spindle assembly factor. *Journal of Biological Chemistry*, 299(6).

Kraut, R., Chia, W., Jan, L. Y., Jan, Y. N., & Knoblich, J. A. (1996). Role of inscuteable in orienting asymmetric cell divisions in Drosophila. *Nature*, *383*(6595), 50-55.

Krenn, V., & Musacchio, A. (2015). The Aurora B kinase in chromosome bi-orientation and spindle checkpoint signaling. *Frontiers in oncology*, *5*, 225.

Krupina, K., Kleiss, C., Metzger, T., Fournane, S., Schmucker, S., Hofmann, K., ... & Sumara, I. (2016). Ubiquitin receptor protein UBASH3B drives Aurora B recruitment to mitotic microtubules. Developmental cell, 36(1), 63-78.

Kuijpers, M., & Hoogenraad, C. C. (2011). Centrosomes, microtubules and neuronal development. *Molecular and Cellular Neuroscience*, 48(4), 349-358.

Kuseyri, F., Bilge, I., Bilgiç, L., & Apak, M. Y. (1993). Neu-Laxova syndrome: report of a case from Turkey. *Clinical genetics*, 43(5), 267-269.

Lakomá, J., Garcia-Alonso, L., & Luque, J. M. (2011). Reelin sets the pace of neocortical neurogenesis. *Development*, *138*(23), 5223-5234.

Lambrus, B. G., Daggubati, V., Uetake, Y., Scott, P. M., Clutario, K. M., Sluder, G., & Holland, A. J. (2016). A USP28–53BP1–p53–p21 signaling axis arrests growth after centrosome loss or prolonged mitosis. *Journal of Cell Biology*, *214*(2), 143-153.

Lampson, M. A., & Grishchuk, E. L. (2017). Mechanisms to avoid and correct erroneous kinetochore-microtubule attachments. *Biology*, *6*(1), 1.

Lara-Gonzalez, P., Pines, J., & Desai, A. (2021, September). Spindle assembly checkpoint activation and silencing at kinetochores. In Seminars in cell & developmental biology (Vol. 117, pp. 86-98). Academic Press.

Lee CY, Robinson KJ, Doe CQ. 2006c. Lgl, Pins and aPKC regulate neuroblast self-renewal versus differentiation. Nature 439: 594–598

Leonardi, R., Licciardello, L., Zanghì, A., La Cognata, D., Maniaci, A., Vecchio, M., ... & Praticò, A. D. (2024). Megalencephaly: Classification, Genetic Causes, and Related Syndromes. *Journal of Pediatric Neurology*, *22*(02), 149-157.

Li, M., York, J. P., & Zhang, P. (2007). Loss of Cdc20 causes a securin-dependent metaphase arrest in two-cell mouse embryos. Molecular and cellular biology, 27(9), 3481-3488.

Li, Y., Yu, W., Liang, Y., & Zhu, X. (2007). Kinetochore dynein generates a poleward pulling force to facilitate congression and full chromosome alignment. Cell research, 17(8), 701-712.

Lim, N. R., Shohayeb, B., Zaytseva, O., Mitchell, N., Millard, S. S., Ng, D. C., & Quinn, L. M. (2017). Glial-specific functions of microcephaly protein WDR62 and interaction with the mitotic kinase AURKA are essential for Drosophila brain growth. *Stem cell reports*, *9*(1), 32-41.

Lim, N. R., Shohayeb, B., Zaytseva, O., Mitchell, N., Millard, S. S., Ng, D. C., & Quinn, L. M. (2017). Glial-specific functions of microcephaly protein WDR62 and interaction with the mitotic kinase AURKA are essential for Drosophila brain growth. *Stem cell reports*, *9*(1), 32-41.

Lim, Y., & Golden, J. A. (2020). Congenital and postnatal microcephalies. In *Neurodevelopmental Disorders* (pp. 377-408). Academic Press.

Lin, J., Reichner, C., Wu, X., & J. Levine, A. (1996). Analysis of wild-type and mutant p21 WAF-1 gene activities. Molecular and cellular biology, 16(4), 1786-1793.

Lin, Y., Wei, Y. L., & She, Z. Y. (2020). Kinesin-8 motors: regulation of microtubule dynamics and chromosome movements. *Chromosoma*, 129(2), 99-110.

Linderkamp, O., Janus, L., Linder, R., & Skoruppa, D. B. (2009). Time table of normal foetal brain development. *International Journal of Prenatal and Perinatal Psychology and Medicine*, *21*(1/2), 4-16.

Liu, D., Vleugel, M., Backer, C. B., Hori, T., Fukagawa, T., Cheeseman, I. M., & Lampson, M. A. (2010). Regulated targeting of protein phosphatase 1 to the outer kinetochore by KNL1 opposes Aurora B kinase. *Journal of Cell Biology*, 188(6), 809-820.

Lizarraga, S. B., Margossian, S. P., Harris, M. H., Campagna, D. R., Han, A. P., Blevins, S., ... & Fleming, M. D. (2010). Cdk5rap2 regulates centrosome function and chromosome segregation in neuronal progenitors. *Development*, 137(11), 1907-1917.

Lobjois, V., Bel-Vialar, S., Trousse, F., & Pituello, F. (2008). Forcing neural progenitor cells to cycle is insufficient to alter cell-fate decision and timing of neuronal differentiation in the spinal cord. *Neural development*, *3*, 1-16.

Lüders, J. (2021). Nucleating microtubules in neurons: Challenges and solutions. *Developmental neurobiology*, *8*1(3), 273-283.

Lukas, C., Savic, V., Bekker-Jensen, S., Doil, C., Neumann, B., Sølvhøj Pedersen, R., ... & Lukas, J. (2011). 53BP1 nuclear bodies form around DNA lesions generated by mitotic transmission of chromosomes under replication stress. Nature cell biology, 13(3), 243-253.

Lukas, C., Savic, V., Bekker-Jensen, S., Doil, C., Neumann, B., Sølvhøj Pedersen, R., ... & Lukas, J. (2011). 53BP1 nuclear bodies form around DNA lesions generated by mitotic transmission of chromosomes under replication stress. *Nature cell biology*, *13*(3), 243-253.

Ma, D., Wang, F., Teng, J., Huang, N., & Chen, J. (2023). Structure and function of distal and subdistal appendages of the mother centriole. Journal of Cell Science, 136(3), jcs260560.

Maiato, H., DeLuca, J., Salmon, E. D., & Earnshaw, W. C. (2004). The dynamic kinetochore-microtubule interface. *Journal of cell science*, *117*(23), 5461-5477.

Malik, S., Vinukonda, G., Vose, L. R., Diamond, D., Bhimavarapu, B. B., Hu, F., ... & Ballabh, P. (2013). Neurogenesis continues in the third trimester of pregnancy and is suppressed by premature birth. *Journal of neuroscience*, 33(2), 411-423.

Malumbres, M. (2014). Cyclin-dependent kinases. Genome biology, 15, 1-10.

Marelli, M., Lusk, C. P., Chan, H., Aitchison, J. D., & Wozniak, R. W. (2001). A link between the synthesis of nucleoporins and the biogenesis of the nuclear envelope. Journal of cell biology, 153(4), 709-724.

Maresca, T. J., Groen, A. C., Gatlin, J. C., Ohi, R., Mitchison, T. J., & Salmon, E. D. (2009). Spindle assembly in the absence of a RanGTP gradient requires localized CPC activity. *Current Biology*, 19(14), 1210-1215.

Marín Parra, Ó., Valdeolmillos, M., & Moya, F. (2006). Neurons in motion: same principles for different shapes.

Marston, A. L. (2015). Shugoshins: tension-sensitive pericentromeric adaptors safeguarding chromosome segregation. *Molecular and cellular biology*, *35*(4), 634-648.

Marthiens, V., Rujano, M. A., Pennetier, C., Tessier, S., Paul-Gilloteaux, P., & Basto, R. (2013). Centrosome amplification causes microcephaly. *Nature cell biology*, *15*(7), 731-740.

McAinsh, A. D., & Marston, A. L. (2022). The four causes: the functional architecture of centromeres and kinetochores. *Annual review of genetics*, *56*(1), 279-314.

Mchedlishvili, N., Matthews, H. K., Corrigan, A., & Baum, B. (2018). Two-step interphase microtubule disassembly aids spindle morphogenesis. BMC biology, 16, 1-16.

McIntosh, J. R. (2016). Mitosis. Cold Spring Harbor perspectives in biology, 8(9), a023218.

McIntosh, J. R., Hepler, P. K., & Wie, D. V. (1969). Model for mitosis. Nature, 224(5220), 659-663.

McNEILL, P. A., & Berns, M. W. (1981). Chromosome behavior after laser microirradiation of a single kinetochore in mitotic PtK2 cells. Journal of Cell Biology, 88(3), 543-553.

McNEILL, P. A., & Berns, M. W. (1981). Chromosome behavior after laser microirradiation of a single kinetochore in mitotic PtK2 cells. *Journal of Cell Biology*, 88(3), 543-553.

Meadows, J. C. (2013). Interplay between mitotic kinesins and the Aurora kinase–PP1 (protein phosphatase 1) axis. Biochemical Society Transactions, 41(6), 1761-1765.

Medina, L., Abellán, A., & Desfilis, E. (2021). Evolving views on the pallium. *Brain Behavior and Evolution*, *96*(4-6), 181-199.

Meitinger, F., Anzola, J. V., Kaulich, M., Richardson, A., Stender, J. D., Benner, C., ... & Oegema, K. (2016). 53BP1 and USP28 mediate p53 activation and G1 arrest after centrosome loss or extended mitotic duration. *Journal of Cell Biology*, 214(2), 155-166.

Meitinger, F., Belal, H., Davis, R. L., Martinez, M. B., Shiau, A. K., Oegema, K., & Desai, A. (2024). Control of cell proliferation by memories of mitosis. *Science*, *383*(6690), 1441-1448.

Meng, W., Mushika, Y., Ichii, T., & Takeichi, M. (2008). Anchorage of microtubule minus ends to adherens junctions regulates epithelial cell-cell contacts. *Cell*, *135*(5), 948-959.

Meraldi, P., Draviam, V. M. & Sorger, P. K. Timing and checkpoints in the regulation of mitotic progression. Dev. Cell 7, 45–60 (2004)

Meyer, H., & Popp, O. (2008). Role (s) of Cdc48/p97 in mitosis. Biochemical Society Transactions, 36(1), 126-130.

Mitchison, T. J. (1989). Polewards microtubule flux in the mitotic spindle: evidence from photoactivation of fluorescence. *The Journal of cell biology*, 109(2), 637-652.

Mitchison, T., Evans, L., Schulze, E., & Kirschner, M. (1986). Sites of microtubule assembly and disassembly in the mitotic spindle. Cell, 45(4), 515-527.

Miyamoto, T., Akutsu, S. N., Fukumitsu, A., Morino, H., Masatsuna, Y., Hosoba, K., ... & Matsuura, S. (2017). PLK1-mediated phosphorylation of WDR62/MCPH2 ensures proper mitotic spindle orientation. *Human molecular genetics*, 26(22), 4429-4440.

Miyamoto, T., Hosoba, K., Ochiai, H., Royba, E., Izumi, H., Sakuma, T., ... & Matsuura, S. (2015). The microtubule-depolymerizing activity of a mitotic kinesin protein KIF2A drives primary cilia disassembly coupled with cell proliferation. *Cell reports*, *10*(5), 664-673.

Moore, S. A., & Iulianella, A. (2021). Development of the mammalian cortical hem and its derivatives: the choroid plexus, Cajal–Retzius cells and hippocampus. *Open biology*, *11*(5), 210042.

Moores, C. A., Perderiset, M., Kappeler, C., Kain, S., Drummond, D., Perkins, S. J., ... & Francis, F. (2006). Distinct roles of doublecortin modulating the microtubule cytoskeleton. The EMBO journal, 25(19), 4448-4457.

Moynihan, L., Jackson, A. P., Roberts, E., Karbani, G., Lewis, I., Corry, P., ... & Woods, C. G. (2000). A third novel locus for primary autosomal recessive microcephaly maps to chromosome 9q34. *The American Journal of Human Genetics*, 66(2), 724-727.

Mukherjee, A., & Conduit, P. T. (2019). γ-TuRCs. Current Biology, 29(11), R398-R400.

Mukherjee, S., Kong, J., & Brat, D. J. (2015). Cancer stem cell division: when the rules of asymmetry are broken. Stem cells and development, 24(4), 405-416.

Mullard, A. (2008). Achieving entry. Nature Reviews Molecular Cell Biology, 9(8), 587-587.

Müller-Reichert, T., CHREtien, D. E. N. I. S., Severin, F., & Hyman, A. A. (1998). Structural changes at microtubule ends accompanying GTP hydrolysis: Information from a slowly hydrolyzable analogue of GTP, guanylyl ( $\alpha$ ,  $\beta$ ) methylenediphosphonate. *Proceedings of the National Academy of Sciences*, *95*(7), 3661-3666.

Mullins, J., & Biesele, J. J. (1977). Terminal phase of cytokinesis in D-98s cells. *Journal of Cell Biology*, 73(3), 672-684.

Musacchio, A. (2015). The molecular biology of spindle assembly checkpoint signaling dynamics. *Current biology*, *25*(20), R1002-R1018.

Musacchio, A., & Salmon, E. D. (2007). The spindle-assembly checkpoint in space and time. *Nature reviews Molecular cell biology*, 8(5), 379-393.

Musgrove, E. A. (2006). Cyclins: roles in mitogenic signaling and oncogenic transformation: mini review. Growth factors, 24(1), 13-19.

Mustyatsa, V. V., Boyakhchyan, A. V., Ataullakhanov, F. I., & Gudimchuk, N. B. (2017). EB-family proteins: Functions and microtubule interaction mechanisms. *Biochemistry (Moscow)*, *82*, 791-802.

Muzio, L., & Mallamaci, A. (2003). Emx1, emx2 and pax6 in specification, regionalization and arealization of the cerebral cortex. *Cerebral cortex*, *13*(6), 641-647.

Nadarajah, B., Brunstrom, J. E., Grutzendler, J., Wong, R. O., & Pearlman, A. L. (2001). Two modes of radial migration in early development of the cerebral cortex. *Nature neuroscience*, *4*(2), 143-150.

Nair, A. R., Singh, P., Garcia, D. S., Rodriguez-Crespo, D., Egger, B., & Cabernard, C. (2016). The microcephaly-associated protein Wdr62/CG7337 is required to maintain centrosome asymmetry in Drosophila neuroblasts. *Cell reports*, *14*(5), 1100-1113.

Nakayama, K. I., & Nakayama, K. (1998). Cip/Kip cyclin-dependent kinase inhibitors: brakes of the cell cycle engine during development. Bioessays, 20(12), 1020-1029.

Newville, J., Ortega, M., & Maxwell, J. (2018). Babies born early can have brain injury. *Front. Young Minds*, 6(10.3389).

Nezi, L., & Musacchio, A. (2009). Sister chromatid tension and the spindle assembly checkpoint. *Current opinion in cell biology*, *21*(6), 785-795.

Nicklas, R. B., & Koch, C. A. (1969). Chromosome micromanipulation: Iii. spindle fiber tension and the reorientation of mal-oriented chromosomes. *The Journal of cell biology*, *43*(1), 40-50.

Nigg, E. A., & Stearns, T. (2011). The centrosome cycle: Centriole biogenesis, duplication and inherent asymmetries. *Nature cell biology*, *13*(10), 1154-1160.

Nilsson, J. (2012). Looping in on Ndc80–How does a protein loop at the kinetochore control chromosome segregation?. Bioessays, 34(12), 1070-1077.

Nishikuni, K., & Ribas, G. C. (2013). Study of fetal and postnatal morphological development of the brain sulci. *Journal of Neurosurgery: Pediatrics*, 11(1), 1-11.

Nishimura, T., & Kaibuchi, K. (2007). Numb controls integrin endocytosis for directional cell migration with aPKC and PAR-3. *Developmental cell*, 13(1), 15-28.

Nishitani, H., & Lygerou, Z. (2004). DNA replication licensing. Front Biosci, 9(2115), 10-2741.

Noatynska, A., Gotta, M., & Meraldi, P. (2012). Mitotic spindle (DIS) orientation and DISease: cause or consequence? Journal of Cell Biology, 199(7), 1025-1035.

Nogales, E. (2001). Structural insights into microtubule function. *Annual review of biophysics and biomolecular structure*, *30*(1), 397-420.

O'Rahilly, R., & Müller, F. (2008). Significant features in the early prenatal development of the human brain. *Annals of Anatomy-Anatomischer Anzeiger*, 190(2), 105-118.

O'Shea, K. S. (2004). Self-renewal vs. differentiation of mouse embryonic stem cells. *Biology of reproduction*, 71(6), 1755-1765.

Oguchi, Y., Uchimura, S., Ohki, T., Mikhailenko, S. V., & Ishiwata, S. I. (2011). The bidirectional depolymerizer MCAK generates force by disassembling both microtubule ends. *Nature cell biology*, *13*(7), 846-852.

Ohnuma, S. I., & Harris, W. A. (2003). Neurogenesis and the cell cycle. *Neuron*, 40(2), 199-208.

Oliveira, S. L., Pillat, M. M., Cheffer, A., Lameu, C., Schwindt, T. T., & Ulrich, H. (2013). Functions of neurotrophins and growth factors in neurogenesis and brain repair. *Cytometry Part A*, 83(1), 76-89.

Oricchio, E., Saladino, C., Iacovelli, S., Soddu, S., & Cundari, E. (2006). ATM is activated by default in mitosis, localizes at centrosomes and monitors mitotic spindle integrity. *Cell cycle*, *5*(1), 88-92.

Orr, B., De Sousa, F., Gomes, A. M., Afonso, O., Ferreira, L. T., Figueiredo, A. C., & Maiato, H. (2021). An anaphase surveillance mechanism prevents micronuclei formation from frequent chromosome segregation errors. *Cell Reports*, *37*(6).

Palmer, R. E., Sullivan, D. S., Huffaker, T., & Koshland, D. (1992). Role of astral microtubules and actin in spindle orientation and migration in the budding yeast, Saccharomyces cerevisiae. *The Journal of cell biology*, *119*(3), 583-593.

Panier, S., & Boulton, S. J. (2014). Double-strand break repair: 53BP1 comes into focus. *Nature reviews Molecular cell biology*, *15*(1), 7-18.

Pannunzio, N. R., Watanabe, G., & Lieber, M. R. (2018). Nonhomologous DNA end-joining for repair of DNA double-strand breaks. Journal of Biological Chemistry, 293(27), 10512-10523.

Panzade, S., & Matis, M. (2021). The microtubule minus-end binding protein patronin is required for the epithelial remodeling in the Drosophila abdomen. *Frontiers in Cell and Developmental Biology*, *9*, 682083.

Papalopulu, N., & Kintner, C. R. (2007, September). Molecular genetics of neurulation. In *Ciba Foundation Symposium 181-Neural Tube Defects: Ciba Foundation Symposium 181* (pp. 90-102). Chichester, UK: John Wiley & Sons, Ltd..

Papini, D., Levasseur, M. D., & Higgins, J. M. (2021). The Aurora B gradient sustains kinetochore stability in anaphase. *Cell Reports*, *37*(6).

Paridaen, J. T., & Huttner, W. B. (2014). Neurogenesis during development of the vertebrate central nervous system. *EMBO reports*, *15*(4), 351-364.

Paschal, C. R., Maciejowski, J., & Jallepalli, P. V. (2012). A stringent requirement for Plk1 T210 phosphorylation during K-fiber assembly and chromosome congression. Chromosoma, 121, 565-572.

Passemard, Sandrine, Angela M. Kaindl, and Alain Verloes. "Microcephaly." *Handbook of clinical neurology* 111 (2013): 129-141.

Passerini, V., & Storchová, Z. (2016). Too much to handle—how gaining chromosomes destabilizes the genome. Cell Cycle, 15(21), 2867-2874.

Patthey, Cédric, Lena Gunhaga, and Thomas Edlund. "Early development of the central and peripheral nervous systems is coordinated by Wnt and BMP signals." *PLoS One* 3.2 (2008): e1625.

Pavin, N., & Tolić-Nørrelykke, I. M. (2013). Dynein, microtubule and cargo: a menage a trois. *Biochemical Society Transactions*, *41*(6), 1731-1735.

Pearson, C. G., Maddox, P. S., Salmon, E. D., & Bloom, K. (2001). Budding yeast chromosome structure and dynamics during mitosis. The Journal of cell biology, 152(6), 1255-1266.

Pei, S. P., Guan, H. L., & Jin, F. (2023). Prenatal diagnosis of microcephaly through combined MRI and ultrasonography: Analysis of a case series. *Medicine*, *102*(50), e36623.

Pennings, C. (2014). Molecular composition and function of the kinetochore-microtubule interface in chromosome segregation.

Pervaiz, N., Kang, H., Bao, Y., & Abbasi, A. A. (2021). Molecular evolutionary analysis of human primary microcephaly genes. BMC Ecology and Evolution, 21(1), 76.

Peterson, F. C., Penkert, R. R., Volkman, B. F., & Prehoda, K. E. (2004). Cdc42 regulates the Par-6 PDZ domain through an allosteric CRIB-PDZ transition. *Molecular cell*, 13(5), 665-676.

Petry, S., Groen, A. C., Ishihara, K., Mitchison, T. J. & Vale, R. D. Branching microtubule nucleation in Xenopus egg extracts mediated by augmin and TPX2. Cell 152, 768–777 (2013).

Phan, T. P., Maryniak, A. L., Boatwright, C. A., Lee, J., Atkins, A., Tijhuis, A., ... & Holland, A. J. (2021). Centrosome defects cause microcephaly by activating the 53BP1-USP28-TP53 mitotic surveillance pathway. *The EMBO journal*, 40(1), e106118.

Piekny, A., Werner, M., & Glotzer, M. (2005). Cytokinesis: welcome to the Rho zone. *Trends in cell biology*, *15*(12), 651-658.

Pierce, A. J., Stark, J. M., Araujo, F. D., Moynahan, M. E., Berwick, M., & Jasin, M. (2001). Double-strand breaks and tumorigenesis. *Trends in cell biology*, *11*(11), S52-S59.

Pinson, A., & Huttner, W. B. (2021). Neocortex expansion in development and evolution—from genes to progenitor cell biology. Current opinion in cell biology, 73, 9-18.

Piskadlo, E., & Oliveira, R. A. (2017). A topology-centric view on mitotic chromosome architecture. *International journal of molecular sciences*, *18*(12), 2751.

Ponting, C., & Jackson, A. P. (2005). Evolution of primary microcephaly genes and the enlargement of primate brains. Current opinion in genetics & development, 15(3), 241-248.

Prehoda, K. E. (2009). Polarization of Drosophila neuroblasts during asymmetric division. *Cold Spring Harbor perspectives in biology*, *1*(2), a001388.

Qian, J., Lesage, B., Beullens, M., Van Eynde, A., & Bollen, M. (2011). PP1/Repo-man dephosphorylates mitotic histone H3 at T3 and regulates chromosomal aurora B targeting. *Current Biology*, *21*(9), 766-773.

Qie, S., & Diehl, J. A. (2016). Cyclin D1, cancer progression, and opportunities in cancer treatment. Journal of molecular medicine, 94, 1313-1326.

Rallu, M., Corbin, J. G., & Fishell, G. (2002). Parsing the prosencephalon. *Nature Reviews Neuroscience*, 3(12), 943-951.

Rass, E., Willaume, S., & Bertrand, P. (2022). 53BP1: keeping it under control, even at a distance from DNA damage. Genes, 13(12), 2390.

Reinemann, D. N., Sturgill, E. G., Das, D. K., Degen, M. S., Vörös, Z., Hwang, W., ... & Lang, M. J. (2017). Collective force regulation in anti-parallel microtubule gliding by dimeric Kif15 kinesin motors. *Current Biology*, *27*(18), 2810-2820.

Reiter, L. T., Potocki, L., Chien, S., Gribskov, M., & Bier, E. (2001). A systematic analysis of human disease-associated gene sequences in Drosophila melanogaster. *Genome research*, 11(6), 1114-1125.

Remus, D., Beuron, F., Tolun, G., Griffith, J. D., Morris, E. P., & Diffley, J. F. (2009). Concerted loading of Mcm2–7 double hexamers around DNA during DNA replication origin licensing. Cell, 139(4), 719-730.

Rew, D. A. (2001). The drosophila genome and its oncological implications. *European journal of surgical oncology*, *27*(1), 105-108.

Rezabkova, L., Jiang, K., Capitani, G., Prota, A. E., Akhmanova, A., Steinmetz, M. O., & Kammerer, R. A. (2017). Structural basis of katanin p60: p80 complex formation. *Scientific reports*, 7(1), 14893.

Rhodes, J. D., Haarhuis, J. H., Grimm, J. B., Rowland, B. D., Lavis, L. D., & Nasmyth, K. A. (2017). Cohesin can remain associated with chromosomes during DNA replication. Cell reports, 20(12), 2749-2755.

Rickmyre, J. L., DasGupta, S., Ooi, D. L. Y., Keel, J., Lee, E., Kirschner, M. W., ... & Lee, L. A. (2007). The Drosophila homolog of MCPH1, a human microcephaly gene, is required for genomic stability in the early embryo. *Journal of cell science*, 120(20), 3565-3577.

Risteski, P., Božan, D., Jagrić, M., Bosilj, A., Pavin, N., & Tolić, I. M. (2022). Length-dependent poleward flux of sister kinetochore fibers promotes chromosome alignment. *Cell reports*, *40*(5).

Risteski, P., Jagrić, M., Pavin, N., & Tolić, I. M. (2021). Biomechanics of chromosome alignment at the spindle midplane. Current Biology, 31(10), R574-R585.

Risteski, P., Martinčić, J., Jagrić, M., Tintor, E., Petelinec, A., & Tolić, I. M. (2024). Microtubule poleward flux as a target for modifying chromosome segregation errors. *Proceedings of the National Academy of Sciences*, *121*(47), e2405015121.

Rogers, G. C., Rogers, S. L., Schwimmer, T. A., Ems-McClung, S. C., Walczak, C. E., Vale, R. D., ... & Sharp, D. J. (2004). Two mitotic kinesins cooperate to drive sister chromatid separation during anaphase. *Nature*, *427*(6972), 364-370.

Roll-Mecak, A., & McNally, F. J. (2010). Microtubule-severing enzymes. *Current opinion in cell biology*, 22(1), 96-103.

Rolls, M. M. (2022). Principles of microtubule polarity in linear cells. Developmental biology, 483, 112-117.

Roostalu, J., Cade, N. I., & Surrey, T. (2015). Complementary activities of TPX2 and chTOG constitute an efficient importin-regulated microtubule nucleation module. *Nature cell biology*, *17*(11), 1422-1434.

Rousso, D. L., Pearson, C. A., Gaber, Z. B., Miquelajauregui, A., Li, S., Portera-Cailliau, C., ... & Novitch, B. G. (2012). Foxp-mediated suppression of N-cadherin regulates neuroepithelial character and progenitor maintenance in the CNS. *Neuron*, *74*(2), 314-330.

Salaun, P., Rannou, Y., & Claude, P. (2008). Cdk1, Plks, Auroras, and Neks: the mitotic bodyguards. *Hormonal Carcinogenesis V*, 41-56.

Salomoni, P., & Calegari, F. (2010). Cell cycle control of mammalian neural stem cells: putting a speed limit on G1. Trends in cell biology, 20(5), 233-243.

Samora, C. P., & McAinsh, A. D. (2011). Photoactivatable-GFP- $\alpha$ -tubulin as a tool to study microtubule plus-end turnover in living human cells. In *Microtubule Dynamics: Methods and Protocols* (pp. 223-233). Totowa, NJ: Humana Press.

Santaguida, S., & Amon, A. (2015). Short-and long-term effects of chromosome mis-segregation and aneuploidy. *Nature reviews Molecular cell biology*, *16*(8), 473-485.

Saxton, W. M., & McIntosh, J. R. (1987). Interzone microtubule behavior in late anaphase and telophase spindles. *The Journal of cell biology*, *105*(2), 875-886.

Schaar, B. T., Chan, G. K. T., Maddox, P., Salmon, E. D., & Yen, T. J. (1997). CENP-E function at kinetochores is essential for chromosome alignment. Journal of Cell Biology, 139(6), 1373-1382.

Schleicher, K., Porter, M., Ten Have, S., Sundaramoorthy, R., Porter, I. M., & Swedlow, J. R. (2017). The Ndc80 complex targets Bod1 to human mitotic kinetochores. *Open Biology*, 7(11), 170099.

Schmidt, M., Rohe, A., Platzer, C., Najjar, A., Erdmann, F., & Sippl, W. (2017). Regulation of G2/M transition by inhibition of WEE1 and PKMYT1 kinases. Molecules, 22(12), 2045.

Schmitz, M. H., Held, M., Janssens, V., Hutchins, J. R., Hudecz, O., Ivanova, E., ... & Gerlich, D. W. (2010). Live-cell imaging RNAi screen identifies PP2A–B55 $\alpha$  and importin- $\beta$ 1 as key mitotic exit regulators in human cells. *Nature cell biology*, *12*(9), 886-893.

Schoenwolf, G. C., & Smith, J. L. (2000). Gastrulation and early mesodermal patterning in vertebrates. *Developmental Biology Protocols: Volume I*, 113-125.

Seki, A., Coppinger, J. A., Jang, C. Y., Yates III, J. R., & Fang, G. (2008). Bora and Aurora A cooperatively activate Plk1 and control the entry into mitosis. Science (New York, NY), 320(5883), 1655.

Sen, O., Harrison, J. U., Burroughs, N. J., & McAinsh, A. D. (2021). Kinetochore life histories reveal an Aurora-B-dependent error correction mechanism in anaphase. *Developmental cell*, *56*(22), 3082-3099.

Sensenbrenner, M., Deloulme, J. C., & Gensburger, C. (1994). Proliferation of neuronal precursor cells from the central nervous system in culture. Reviews in the neurosciences, 5(1), 43-54.

Sgourdou, P., Mishra-Gorur, K., Saotome, I., Henagariu, O., Tuysuz, B., Campos, C., ... & Louvi, A. (2017). Disruptions in asymmetric centrosome inheritance and WDR62-Aurora kinase B interactions in primary microcephaly. *Scientific reports*, 7(1), 43708.

Shan, Z., Tu, Y., Yang, Y., Liu, Z., Zeng, M., Xu, H., ... & Wen, W. (2018). Basal condensation of Numb and Pon complex via phase transition during Drosophila neuroblast asymmetric division. Nature communications, 9(1), 737.

Sheng, G. (2015). Epiblast morphogenesis before gastrulation. Developmental biology, 401(1), 17-24.

Shimamoto, Y., Forth, S., & Kapoor, T. M. (2015). Measuring pushing and braking forces generated by ensembles of kinesin-5 crosslinking two microtubules. *Developmental cell*, 34(6), 669-681.

Shohayeb, B., Ho, U., Yeap, Y. Y., Parton, R. G., Millard, S. S., Xu, Z., ... & Ng, D. C. (2020). The association of microcephaly protein WDR62 with CPAP/IFT88 is required for cilia formation and neocortical development. *Human molecular genetics*, *29*(2), 248-263.

Shrestha, R. L., & Draviam, V. M. (2013). Lateral to end-on conversion of chromosome-microtubule attachment requires kinesins CENP-E and MCAK. Current biology, 23(16), 1514-1526.

Shrestha, R. L., & Draviam, V. M. (2013). Lateral to end-on conversion of chromosome-microtubule attachment requires kinesins CENP-E and MCAK. *Current biology*, *23*(16), 1514-1526.

Sigrist, S., Jacobs, H., Stratmann, R., & Lehner, C. F. (1995). Exit from mitosis is regulated by Drosophila fizzy and the sequential destruction of cyclins A, B and B3. *The EMBO journal*, *14*(19), 4827-4838.

Sild, M., & Ruthazer, E. S. (2011). Radial glia: progenitor, pathway, and partner. *The Neuroscientist*, 17(3), 288-302.

Siller, K. H., & Doe, C. Q. (2008). Lis1/dynactin regulates metaphase spindle orientation in Drosophila neuroblasts. *Developmental biology*, 319(1), 1-9.

Silva, P. M., Reis, R. M., Bolanos-Garcia, V. M., Florindo, C., Tavares, Á. A., & Bousbaa, H. (2014). Dynein-dependent transport of spindle assembly checkpoint proteins off kinetochores toward spindle poles. FEBS letters, 588(17), 3265-3273.

Simunić, J., & Tolić, I. M. (2016). Mitotic spindle assembly: building the bridge between sister K-fibers. *Trends in biochemical sciences*, *41*(10), 824-833.

Singh, U., & Westermark, B. (2011). CGGBP1 is a nuclear and midbody protein regulating abscission. *Experimental cell research*, 317(2), 143-150.

Sirbu, B. M., & Cortez, D. (2013). DNA damage response: three levels of DNA repair regulation. *Cold Spring Harbor perspectives in biology*, *5*(8), a012724.

Slack, C., Overton, P. M., Tuxworth, R. I., & Chia, W. (2007). Asymmetric localisation of Miranda and its cargo proteins during neuroblast division requires the anaphase-promoting complex/cyclosome.

Smith, D. S., Niethammer, M., Ayala, R., Zhou, Y., Gambello, M. J., Wynshaw-Boris, A., & Tsai, L. H. (2000). Regulation of cytoplasmic dynein behaviour and microtubule organization by mammalian Lis1. Nature cell biology, 2(11), 767-775.

Srayko, M., O'Toole, E. T., Hyman, A. A., & Müller-Reichert, T. (2006). Katanin disrupts the microtubule lattice and increases polymer number in C. elegans meiosis. Current biology, 16(19), 1944-1949.

Stach, L., & Freemont, P. S. (2017). The AAA+ ATPase p97, a cellular multitool. Biochemical Journal, 474(17), 2953-2976.

Stark, G. R., & Taylor, W. R. (2004). Analyzing the G2/M checkpoint. *Checkpoint Controls and Cancer: Volume 1:* Reviews and Model Systems, 51-82.

Steblyanko, Y., Rajendraprasad, G., Osswald, M., Eibes, S., Jacome, A., Geley, S., ... & Barisic, M. (2020). Microtubule poleward flux in human cells is driven by the coordinated action of four kinesins. *The EMBO journal*, *39*(23), e105432.

Stiles, J., & Jernigan, T. L. (2010). The basics of brain development. Neuropsychology review, 20(4), 327-348.

Stirnimann, C. U., Petsalaki, E., Russell, R. B., & Müller, C. W. (2010). WD40 proteins propel cellular networks. *Trends in biochemical sciences*, *35*(10), 565-574.

Sturm, G., Hake, K., Lefebvre, A. E., Rux, C. J., Ivanova, D., Millett-Sikking, A., ... & Marshall, W. F. (2024). The biophysical mechanism of mitochondrial pearling. bioRxiv, 2024-12.

Stutterd, C. A., & Leventer, R. J. (2014, June). Polymicrogyria: a common and heterogeneous malformation of cortical development. In *American Journal of Medical Genetics Part C: Seminars in Medical Genetics* (Vol. 166, No. 2, pp. 227-239).

Sudakin, V., Chan, G. K., & Yen, T. J. (2001). Checkpoint inhibition of the APC/C in HeLa cells is mediated by a complex of BUBR1, BUB3, CDC20, and MAD2. Journal of Cell Biology, 154(5), 925-936.

Sumara, I., & Peter, M. (2007). A Cul3-based E3 ligase regulates mitosis and is required to maintain the spindle assembly checkpoint in human cells. Cell Cycle, 6(24), 3004-3010.

Sun, X., & Kaufman, P. D. (2018). Ki-67: more than a proliferation marker. Chromosoma, 127, 175-186.

Syrovatkina, V., Fu, C., & Tran, P. T. (2013). Antagonistic spindle motors and MAPs regulate metaphase spindle length and chromosome segregation. Current Biology, 23(23), 2423-2429.

Takaki, T., Montagner, M., Serres, M. P., Le Berre, M., Russell, M., Collinson, L., ... & Petronczki, M. (2017). Actomyosin drives cancer cell nuclear dysmorphia and threatens genome stability. Nature communications, 8(1), 16013.

Talbert, P. B., & Henikoff, S. (2022). The genetics and epigenetics of satellite centromeres. *Genome Research*, 32(4), 608-615.

Tanaka, N., Meng, W., Nagae, S., & Takeichi, M. (2012). Nezha/CAMSAP3 and CAMSAP2 cooperate in epithelial-specific organization of noncentrosomal microtubules. *Proceedings of the National Academy of Sciences*, 109(49), 20029-20034.

Tandler, B. Improved uranyl acetate staining for electron microscopy. J. Electron Microsc. Tech. 16, 81–82 (1990).

Tanenbaum, M. E., & Medema, R. H. (2010). Mechanisms of centrosome separation and bipolar spindle assembly. *Developmental cell*, 19(6), 797-806.

Tanenbaum, M. E., Macůrek, L., Janssen, A., Geers, E. F., Alvarez-Fernández, M., & Medema, R. H. (2009). Kif15 cooperates with eg5 to promote bipolar spindle assembly. *Current biology*, 19(20), 1703-1711.

Thomas, A., & Meraldi, P. (2024). Centrosome age breaks spindle size symmetry even in cells thought to divide symmetrically. *Journal of Cell Biology*, 223(8), e202311153.

Thompson, S. L., & Compton, D. A. (2011). Chromosome missegregation in human cells arises through specific types of kinetochore–microtubule attachment errors. Proceedings of the National Academy of Sciences, 108(44), 17974-17978.

Tilney, L. G., Bryan, J., Bush, D. J., Fujiwara, K., Mooseker, M. S., Murphy, D. B., & Snyder, D. H. (1973). Microtubules: evidence for 13 protofilaments. *Journal of Cell Biology*, *59*(2), 267-275.

Tole, S., & Hébert, J. (2020). Telencephalon patterning. In *Patterning and cell type specification in the developing CNS and PNS* (pp. 23-48). Academic press.

Tolić, I. M. (2018). Mitotic spindle: kinetochore fibers hold on tight to interpolar bundles. *European Biophysics Journal*, 47(3), 191-203.

Tolić-Nørrelykke, I. M. (2008). Push-me-pull-you: how microtubules organize the cell interior. European biophysics journal, 37, 1271-1278.

Tomlinson V, Gudmundsdottir K, Luong P, Leung KY, Knebel A, Basu S. 2010. JNK phosphorylates Yes-associated protein (YAP) to regulate apoptosis. *Cell Death Dis* 1:e29.

Toso, A., Winter, J. R., Garrod, A. J., Amaro, A. C., Meraldi, P., & McAinsh, A. D. (2009). Kinetochore-generated pushing forces separate centrosomes during bipolar spindle assembly. *Journal of Cell Biology*, 184(3), 365-372.

Trimborn, M., Bell, S. M., Felix, C., Rashid, Y., Jafri, H., Griffiths, P. D., ... & Jackson, A. P. (2004). Mutations in microcephalin cause aberrant regulation of chromosome condensation. *The American Journal of Human Genetics*, 75(2), 261-266.

Tseng, C. C. (1995). Human chromosome analysis. In *Tested studies for laboratory teaching. Proc. of the 16th Workshop/Conf. of the association for biology laboratory education (ABLE)* (Vol. 16, pp. 33-56).

Tseng, L. C., & Chen, R. H. (2011). Temporal control of nuclear envelope assembly by phosphorylation of lamin B receptor. *Molecular biology of the cell*, 22(18), 3306-3317.

Tsuji, T., Ficarro, S. B., & Jiang, W. (2006). Essential role of phosphorylation of MCM2 by Cdc7/Dbf4 in the initiation of DNA replication in mammalian cells. Molecular biology of the cell, 17(10), 4459-4472.

Tsunekawa, Y., Britto, J. M., Takahashi, M., Polleux, F., Tan, S. S., & Osumi, N. (2012). Cyclin D2 in the basal process of neural progenitors is linked to non-equivalent cell fates. *The EMBO journal*, *31*(8), 1879-1892.

Tungadi, E. A., Ito, A., Kiyomitsu, T., & Goshima, G. (2017). Human microcephaly ASPM protein is a spindle pole-focusing factor that functions redundantly with CDK5RAP2. *Journal of Cell Science*, 130(21), 3676-3684.

Tybulewicz, V. L., Crawford, C. E., Jackson, P. K., Bronson, R. T., & Mulligan, R. C. (1991). Neonatal lethality and lymphopenia in mice with a homozygous disruption of the c-abl proto-oncogene. *Cell*, *65*(7), 1153-1163.

Uetake, Y., & Sluder, G. (2010). Prolonged prometaphase blocks daughter cell proliferation despite normal completion of mitosis. *Current Biology*, 20(18), 1666-1671.

Uretz, R. B., Bloom, W., & Zirkle, R. E. (1954). Irradiation of parts of individual cells II. Effects of an ultraviolet microbeam focused on parts of chromosomes. *Science*, *120*(3110), 197-199.

Uzbekov, R., & Alieva, I. (2018). Who are you, subdistal appendages of centriole?. Open biology, 8(7), 180062.

Vader, G., Medema, R. H., & Lens, S. M. (2006). The chromosomal passenger complex: guiding Aurora-B through mitosis. *The Journal of cell biology*, *173*(6), 833-837.

Valdez, V.A., Neahring, L., Petry, S., & Dumont, S. (2023). Mechanisms underlying spindle assembly and robustness. *Nature Reviews Molecular Cell Biology*, 24 (8), 523-542.

Valverde, R., Ingram, J., & Harrison, S. C. (2016). Conserved tetramer junction in the kinetochore Ndc80 complex. Cell reports, 17(8), 1915-1922.

Van Essen, D. C. (2002). Surface-based atlases of cerebellar cortex in the human, macaque, and mouse. Annals of the New York Academy of Sciences, 978(1), 468-479.

Varma, D., & Salmon, E. D. (2012). The KMN protein network—chief conductors of the kinetochore orchestra. Journal of cell science, 125(24), 5927-5936.

Varma, D., & Salmon, E. D. (2012). The KMN protein network—chief conductors of the kinetochore orchestra. *Journal of cell science*, *125*(24), 5927-5936.

Vas, A. C., & Clarke, D. J. (2008). Aurora B kinases restrict chromosome decondensation to telophase of mitosis. *Cell Cycle*, 7(3), 293-296.

Vietri, M., Schink, K. O., Campsteijn, C., Wegner, C. S., Schultz, S. W., Christ, L., ... & Stenmark, H. (2015). Spastin and ESCRT-III coordinate mitotic spindle disassembly and nuclear envelope sealing. *Nature*, *522*(7555), 231-235.

Vineethakumari, C., & Lüders, J. (2022). Microtubule anchoring: attaching dynamic polymers to cellular structures. *Frontiers in Cell and Developmental Biology*, *10*, 867870.

Vukušić, K., Ponjavić, I., Buđa, R., Risteski, P., & Tolić, I. M. (2021). Microtubule-sliding modules based on kinesins EG5 and PRC1-dependent KIF4A drive human spindle elongation. *Developmental cell*, *56*(9), 1253-1267.

Walczak, C. E., & Heald, R. (2008). Mechanisms of mitotic spindle assembly and function. *International review of cytology*, 265, 111-158.

Walsh, K. T., & Doe, C. Q. (2017). Drosophila embryonic type II neuroblasts: origin, temporal patterning, and contribution to the adult central complex. *Development*, 144(24), 4552-4562.

Wandke, C., Barisic, M., Sigl, R., Rauch, V., Wolf, F., Amaro, A. C., ... & Geley, S. (2012). Human chromokinesins promote chromosome congression and spindle microtubule dynamics during mitosis. *Journal of Cell Biology*, 198(5), 847-863.

Wang, H., Peng, B., Pandita, R. K., Engler, D. A., Matsunami, R. K., Xu, X., ... & Hegde, M. L. (2017). Aurora kinase B dependent phosphorylation of 53BP1 is required for resolving merotelic kinetochore-microtubule attachment errors during mitosis. *Oncotarget*, *8*(30), 48671.

Wang, Y., Jin, F., Higgins, R., & McKnight, K. (2014). The current view for the silencing of the spindle assembly checkpoint. Cell cycle, 13(11), 1694-1701.

Warecki, B., & Sullivan, W. (2018). Micronuclei formation is prevented by Aurora B-mediated exclusion of HP1a from late-segregating chromatin in Drosophila. Genetics, 210(1), 171-187.

Wasserman, T., Katsenelson, K., Daniliuc, S., Hasin, T., Choder, M., & Aronheim, A. (2010). A novel c-Jun N-terminal kinase (JNK)-binding protein WDR62 is recruited to stress granules and mediates a nonclassical JNK activation. *Molecular biology of the cell*, 21(1), 117-130.

Waterman-Storer, C. M., Desai, A., Bulinski, J. C., & Salmon, E. D. (1998). Fluorescent speckle microscopy, a method to visualize the dynamics of protein assemblies in living cells. Current biology, 8(22), S1.

Watson, R. O., Bell, S. L., MacDuff, D. A., Kimmey, J. M., Diner, E. J., Olivas, J., ... & Cox, J. S. (2015). The cytosolic sensor cGAS detects Mycobacterium tuberculosis DNA to induce type I interferons and activate autophagy. Cell host & microbe, 17(6), 811-819.

Weaver, B. A., & Cleveland, D. W. (2006). Does an euploidy cause cancer?. Current opinion in cell biology, 18(6), 658-667.

Wendell, K. L., Wilson, L. & Jordan, M. A. Mitotic block in HeLa cells by vinblastine: ultrastructural changes in kinetochore-microtubule attachment and in centrosomes. *J. Cell Sci.* 104, 261–274 (1993).

Whalley, H. J., & Malliri, A. (2015). Centrosome separation; a careful balancing act. Cell Cycle, 14(19), 3001-3002.

White, T. O. N. Y. A., & Hilgetag, C. C. (2008). Gyrification and development of the human brain. *Handbook of developmental cognitive neuroscience*, 39-50.

Wieschaus, E., Nüsslein-Volhard, C., & Jürgens, G. (1984). Mutations affecting the pattern of the larval cuticle in Drosophila melanogaster: III. Zygotic loci on the X-chromosome and fourth chromosome. *Wilhelm Roux's archives of developmental biology*, 193, 296-307.

Wildman, D. E., Uddin, M., Romero, R., Gonzalez, J. M., Than, N. G., Murphy, J., ... & Fritz, J. (2011). Spontaneous abortion and preterm labor and delivery in nonhuman primates: evidence from a captive colony of chimpanzees (Pan troglodytes). PloS one, 6(9), e24509.

Wilhelm, T., Olziersky, A. M., Harry, D., De Sousa, F., Vassal, H., Eskat, A., & Meraldi, P. (2019). Mild replication stress causes chromosome mis-segregation via premature centriole disengagement. *Nature communications*, *10*(1), 3585.

Willardsen, M. I., & Link, B. A. (2011). Cell biological regulation of division fate in vertebrate neuroepithelial cells. *Developmental Dynamics*, 240(8), 1865-1879.

Wirtz-Peitz F, Nishimura T & Knoblich JA (2008)Linking cell cycle to asymmetric division: Aurora-A phosphorylates the Par complex to regulate Numblocalization. Cell 135, 161–173

Wodarz, A., & Huttner, W. B. (2003). Asymmetric cell division during neurogenesis in Drosophila and vertebrates. *Mechanisms of development*, *120*(11), 1297-1309.

Wollman, R., Cytrynbaum, E. N., Jones, J. T., Meyer, T., Scholey, J. M., & Mogilner, A. (2005). Efficient chromosome capture requires a bias in the 'search-and-capture' process during mitotic-spindle assembly. *Current Biology*, 15(9), 828-832.

Wong, R. W. (2010). An update on cohesin function as a 'molecular glue' on chromosomes and spindles. *Cell cycle*, *9*(9), 1754-1758.

Woodruff, J. B. et al. The centrosome is a selective condensate that nucleates microtubules by concentrating tubulin. *Cell* 169, 1066–1077.e10 (2017).

Wordeman, L. (2005). Microtubule-depolymerizing kinesins. Current opinion in cell biology, 17(1), 82-88.

Worrall, J. T., Tamura, N., Mazzagatti, A., Shaikh, N., van Lingen, T., Bakker, B., ... & McClelland, S. E. (2018). Nonrandom mis-segregation of human chromosomes. *Cell reports*, *23*(11), 3366-3380.

Wu, J., Larreategui-Aparicio, A., Lambers, M. L., Bodor, D. L., Klaasen, S. J., Tollenaar, E., ... & Kops, G. J. (2023). Microtubule nucleation from the fibrous corona by LIC1-pericentrin promotes chromosome congression. *Current Biology*, *33*(5), 912-925.

Wu, J., Larreategui-Aparicio, A., Lambers, M. L., Bodor, D. L., Klaasen, S. J., Tollenaar, E., ... & Kops, G. J. (2023). Microtubule nucleation from the fibrous corona by LIC1-pericentrin promotes chromosome congression. *Current Biology*, *33*(5), 912-925.

Wynshaw-Boris, A., Pramparo, T., Youn, Y. H., & Hirotsune, S. (2010, October). Lissencephaly: mechanistic insights from animal models and potential therapeutic strategies. In *Seminars in cell & developmental biology* (Vol. 21, No. 8, pp. 823-830). Academic Press.

Xu, S., Sun, X., Niu, X., Zhang, Z., Tian, R., Ren, W., ... & Yang, G. (2017). Genetic basis of brain size evolution in cetaceans: insights from adaptive evolution of seven primary microcephaly (MCPH) genes. BMC Evolutionary Biology, 17, 1-13.

Xu, S., Wu, X., Peng, B., Cao, S. L., & Xu, X. (2020). Primary microcephaly with an unstable genome. Genome Instability & Disease, 1, 235-264.

Xu, X., Lee, J., & Stern, D. F. (2004). Microcephalin Is a DNA Damage Response Protein Involved in Regulation of CHK1 and BRCA1\* ♠ . *Journal of Biological Chemistry*, *279*(33), 34091-34094.

Yamano, H., Gannon, J., Mahbubani, H., & Hunt, T. (2004). Cell cycle-regulated recognition of the destruction box of cyclin B by the APC/C in Xenopus egg extracts. Molecular cell, 13(1), 137-147.

Yang, C., Tang, X., Guo, X., Niikura, Y., Kitagawa, K., Cui, K., ... & Xu, B. (2011). Aurora-B mediated ATM serine 1403 phosphorylation is required for mitotic ATM activation and the spindle checkpoint. *Molecular cell*, *44*(4), 597-608.

Yang, D. W., & Choi, K. W. (2021). Suppression of Patronin deficiency by altered Hippo signaling in Drosophila organ development. *Cell Death & Differentiation*, 28(1), 233-250.

Yau, K. W., van Beuningen, S. F., Cunha-Ferreira, I., Cloin, B. M., van Battum, E. Y., Will, L., ... & Hoogenraad, C. C. (2014). Microtubule minus-end binding protein CAMSAP2 controls axon specification and dendrite development. Neuron, 82(5), 1058-1073.

Yokoyama, H., Koch, B., Walczak, R., Ciray-Duygu, F., González-Sánchez, J. C., Devos, D. P., ... & Gruss, O. J. (2014). The nucleoporin MEL-28 promotes RanGTP-dependent γ-tubulin recruitment and microtubule nucleation in mitotic spindle formation. *Nature communications*, *5*(1), 3270.

Yoon, K., & Gaiano, N. (2005). Notch signaling in the mammalian central nervous system: insights from mouse mutants. *Nature neuroscience*, 8(6), 709-715.

Ypsilanti, A. R., & Rubenstein, J. L. (2016). Transcriptional and epigenetic mechanisms of early cortical development: An examination of how Pax6 coordinates cortical development. Journal of Comparative Neurology, 524(3), 609-629.

Yu, F., Cai, Y., Kaushik, R., Yang, X., & Chia, W. (2003). Distinct roles of Gαi and Gβ13F subunits of the heterotrimeric G protein complex in the mediation of Drosophila neuroblast asymmetric divisions. *Journal of Cell Biology*, 162(4), 623-633.

Yu, K. W., Zhong, N., Xiao, Y., & She, Z. Y. (2019). Mechanisms of kinesin-7 CENP-E in kinetochore—microtubule capture and chromosome alignment during cell division. Biology of the Cell, 111(6), 143-160.

Yu, T. W., Mochida, G. H., Tischfield, D. J., Sgaier, S. K., Flores-Sarnat, L., Sergi, C. M., ... & Walsh, C. A. (2010). Mutations in WDR62, encoding a centrosome-associated protein, cause microcephaly with simplified gyri and abnormal cortical architecture. *Nature genetics*, *42*(11), 1015-1020.

Zeke, A., Misheva, M., Reményi, A., & Bogoyevitch, M. A. (2016). JNK signaling: regulation and functions based on complex protein-protein partnerships. *Microbiology and Molecular Biology Reviews*, *80*(3), 793-835.

Zhang, C. (2014). The WD40 Repeat Protein Mutations: Genetics, Molecular Mechanisms and Therapeutic Implications. Journal of Genetic Syndromes & Gene Therapy, 5(6), 1.

Zhang, R., Roostalu, J., Surrey, T., & Nogales, E. (2017). Structural insight into TPX2-stimulated microtubule assembly. *Elife*, *6*, e30959.

Zhang, T., Oliveira, R. A., Schmierer, B., & Novák, B. (2013). Dynamical scenarios for chromosome bi-orientation. Biophysical journal, 104(12), 2595-2606.

Zhang, W., Yang, S. L., Yang, M., Herrlinger, S., Shao, Q., Collar, J. L., ... & Chen, J. F. (2019). Modeling microcephaly with cerebral organoids reveals a WDR62–CEP170–KIF2A pathway promoting cilium disassembly in neural progenitors. *Nature communications*, *10*(1), 2612.

Zheng, Y., Wong, M. L., Alberts, B., & Mitchison, T. (1995). Nucleation of microtubule assembly by a γ-tubulin-containing ring complex. *Nature*, *378*(6557), 578-583.

Zhong, L., Hu, M. M., Bian, L. J., Liu, Y., Chen, Q., & Shu, H. B. (2020). Phosphorylation of cGAS by CDK1 impairs self-DNA sensing in mitosis. Cell discovery, 6(1), 26.

Zhou, Y., Qin, Y., Qin, Y., Xu, B., Guo, T., Ke, H., ... & Gao, F. (2018). Wdr62 is involved in female meiotic initiation via activating JNK signaling and associated with POI in humans. *PLoS genetics*, *14*(8), e1007463.

Zhu, H., Coppinger, J. A., Jang, C. Y., Yates, J. R., & Fang, G. (2008). FAM29A promotes microtubule amplification via recruitment of the NEDD1–γ-tubulin complex to the mitotic spindle. *Journal of Cell Biology*, *183*(5), 835-848.

Zierhut, C., Yamaguchi, N., Paredes, M., Luo, J. D., Carroll, T., & Funabiki, H. (2019). The cytoplasmic DNA sensor cGAS promotes mitotic cell death. Cell, 178(2), 302-315.

Zombor, M., Kalmár, T., Nagy, N., Berényi, M., Telcs, B., Maróti, Z., ... & Sztriha, L. (2019). A novel WDR62 missense mutation in microcephaly with abnormal cortical architecture and review of the literature. *Journal of Applied Genetics*, 60, 151-162.